Optical hybrid architectures for quantum information processing

Kun Huang

THÈSE DE DOCTORAT DE
L'ÉCOLE NORMALE SUPÉRIEURE DE PARIS EN CO-TUELLE AVEC
L'ÉCOLE NORMALE SUPÉRIEURE DE L'EST DE LA CHINE

Optical Hybrid Architectures for Quantum Information Processing

Présenté par :
Kun Huang

pour obtenir le grade de docteur de l'École Normale Supérieure de Paris et de docteur de l'École Normale Supérieure de l'Est de la Chine

Spécialité : **Optique Quantique**

23 Mai, 2015

M. Tiancai Zhang	*Rapporteur*
M. Alberto Porzio	*Rapporteur*
M. Lei Xu	*Examinateur*
M. Qiang Zhang	*Examinateur*
M. Cheng-Zhi Peng	*Examinateur*
M. Julien Laurat	*Directeur de thèse*
M. Heping Zeng	*Directeur de thèse*

Abstract

The thesis focuses on the experimental investigation of the optical hybrid approach for quantum information processing. Specifically, two traditionally separated approaches, i.e. the discrete and the continuous-variable ones, are combined in the same experiment with two distinct quantum measurements based on photon counting (photon number) and homodyne detection (quadrature components).

The optical hybrid approach is first applied to generate high-fidelity non-Gaussian states, e.g. Fock states and Schrödinger cat states, which correspond to two types of qubit encodings used in optical quantum information. The use of high-efficiency superconducting nanowire single-photon detectors leads to an unprecedented preparation rate, which facilitates the subsequent use of these states. For instance, the two types of states are combined to generate for the first time a hybrid entanglement between particle-like and wave-like optical qubits, as well as the extension to hybrid qutrit entanglement. These novel resources may pave the way to implement heterogeneous networks where discrete and continuous-variable operations and techniques can be efficiently combined. Additionally, we also experimentally demonstrate for the first time the so-called squeezing-induced micro-macro entangled states.

During this PhD, efforts have also been dedicated to implement a high-efficiency and low-noise frequency up-conversion system based on two synchronized fiber lasers. Such quantum frequency converter not only permits to extend the spectra of quantum states to difficultly accessible wavelengths with current technology, but also constitutes a high-performance photon detector especially in the infrared regime. Based on the conversion system, several applications are demonstrated, such as infrared photon-number-resolving detection, and few-photon-level infrared imaging.

Keywords

optical quantum information, Fock state, Schrödinger cat state, non-Gaussian state, hybrid entanglement, frequency up-conversion detection

Résumé

Cette thèse s'intéresse à une approche dite hybride de l'information quantique. Deux approches traditionnellement séparées, variables discrètes et variables continues, sont combinées dans une même expérience nécessitant à la fois comptage de photons (nombre de photons) et détection homodyne (quadratures).

Cette architecture hybride a d'abord été utilisée pour générer des états non-gaussiens de la lumière de grande fidélité, par exemple état de Fock et chat de Schrödinger optique, qui correspondent à deux types d'encodages utilisés en information quantique. L'utilisation de détecteurs supraconducteurs à forte efficacité a permis d'obtenir un taux de préparation sans précédent, ce qui facilite l'utilisation ultérieure de ces états. Ces deux types d'états ont ensuite été combinés pour réaliser pour la première fois une intrication hybride entre qubits optiques de nature différente. Son extension à des qutrits a également été obtenue. Ces nouvelles ressources ouvrent la voie à la mise en œuvre de réseau quantique hétérogène où les opérations et les techniques propres aux variables discrètes et continues peuvent être efficacement combinées.

Ce travail de thèse a également été consacré à la mise en œuvre d'un système de conversion de fréquence à haute efficacité et faible bruit, basé sur deux lasers à fibres synchronisés. Ce convertisseur de fréquence quantique permet non seulement d'étendre les états quantiques à des longueurs d'onde difficilement accessibles avec la technologie actuelle, mais constitue également un détecteur de photons à haute performance, surtout dans le régime infrarouge. Basé sur ce système, plusieurs applications ont ensuite été démontrées, comme la détection infrarouge résolue en nombre de photons et l'imagerie infrarouge ultra-sensible.

Mots clés

information quantique, optique quantique, état de Fock, chat de Schrödinger, état non-gaussien, intrication hybride, conversion de fréquence

摘要

本论文致力于从实验上探究光量子信息科学中一种新兴的研究框架，其整合了传统上分隔已久的两种分别基于离散变量与连续变量的路线，将光子探测（光子数）和平衡零拍探测（光场位相及振幅分量）结合在一个实验当中，充分利用了各自在光量子信息处理中的特点和优势。

在这种混合架构下，我们首先在实验上制备了两种高纯度的非高斯态，即光子数态和薛定谔猫态，他们分别对应着光量子信息中两种不同的量子比特载体。得益于高探测效率的超导纳米线单光子探测器，量子态的制备率达到了前所未有的水平，这极大地促进了其在后续量子信息协议中的应用。比如，基于上述两种量子态，我们首次在实验上实现了一种包含“类粒子”和“类波动”量子比特的杂化纠缠态，并将其拓展到量子三元之间的杂化纠缠态。这种全新的纠缠态为异质光量子信息网络的实现铺平了道路，从而有效地结合基于离散和连续变量的操作和技术。此外，我们也首次在实验上展示了一种光场压缩致使的微观—宏观纠缠态。

除了所述量子态的制备，基于时域同步的光纤激光器，我们还搭建了一套高效率低噪声的频率上转换系统。这套转换系统不仅能够将量子态的频谱延伸到现有技术难以实现的波长，而且其本身也可以作为一个高效率的红外光子探测器。基于这套系统，我们分别实现了红外光子可分辨探测和少光子水平红外灵敏成像。

关键字

光量子信息，光子数态，薛定谔猫态，非高斯态，杂化纠缠态，频率上转换探测

Acknowledgment

The present work is accomplished within the cooperation program between l'École Normale Supérieure de Paris (ENS – Paris) in France and East China Normal University (ECNU) in China. Thus I would like to record my gratitude to those people from both sides who gave me the possibility to complete this thesis.

First and foremost, I owe a tremendous debt of gratitude to my supervisors Prof. Heping Zeng (State Key Laboratory of Precision Spectroscopy, Shanghai) and Prof. Julien Laurat (Laboratoire Kastler Brossel, Paris) for their constant guidance and invaluable support during these years. Thanks to them, I had the opportunity to conduct my academic researches in two remarkable groups where I interacted with so many talented and friendly people.

In 2009, I had the chance to be accepted as a master student in Heping's group and co-supervised by Dr. E Wu who was a young and active physicist. She brought me to the wonderland of optics by helping me to build a solid laser. Even now I can still feel the excitement when I observed the laser oscillation. Then my interests were focused on *single-photon frequency up-conversion*. I want to thank the guys who ever contributed to this topic before and with me: Haifeng Pan, Huafang Dong, Yao Li, Xiaorong Gu, and Qian Zhou, without whom the work presented in Part III of this thesis would not have been possible. I give my best wishes to those still working on this experiment, Xiongjie Li, Ruikai Tang, Wenjie Wu, Jianhui Ma, Huiqin Hu.

I deeply appreciate the helpful instruction and technical supports from so many researchers in the lab, among them Zugeng Wang, Liang'en Ding, Jingxin Ding, Yangqin Chen, Longsheng Ma, Zhenrong Sun, Jianping Yin, Zhiyi Bi, Guang Wu, Wenxue Li, Jian Wu, Sanjun Zhang, Botao Wu, Lijuan Zheng, and Xiuliang Chen.

My gratitude also goes to the rest group members, Ming Yan, Qiang Hao, Min Ren, Yi Jian, Min Li, Yahui Feng, Hao Li, Yan Liang, Hui Zhou, Kangwen Yang, Liping Shi, Gengxu Chen, Yan Liu, and so on. We had lots of fun together, such as sporting, travelling, and dinning. I should in addition acknowledge the administrative staff, Lanlan Huang, Weiying Cai, and Bentai Li, for their patience and kindness.

In 2012, I had the chance to work in Julien's group in LKB on the topic about *optical quantum state engineering*. Especial thanks should go to Jianli Liu and Olivier Morin, who taught me all the details and tricks about the experiment in terms of theoretical and technical aspects. I must extend thanks to Hanna Le Jeannic, Josselin Ruaudel, and Youn-Chang Jeong, who helped me so much to build experimental setup and acquire data, especially during the period of my writing the thesis. I would also like to acknowledge the staff in the electronic workshop, mechanical workshop, and cryogenic workshop, who made it possible for me to successfully carry out the experiments.

I am grateful to my "Parrain" Pierre-François Cohadon, Director Heidmann Antoine, as well as Claude Fabre, Nicolas Treps, Élisabeth Giacobino, Alberto Bramati, and Quentin Glorieux, who were always willing and patient to answer my questions and give helpful advices. I also owe my thanks to the administrative staff in the lab who provided me much convenience and patience particularly when I could not make myself clearly in French.

Many thanks to my other colleagues: members working on *femtosecond quantum optics*, Giulia Ferrini, Jonathan Roslund, Valentin Averchenko, Renné Medeiros de Araújo, Roman Schmeissner, Yin Cai, Zhan Zheng, Pu Jian, Alexandre Brieussel, Valérian Thiel, Clément

Jacquard, and Vanessa Chille; members working on *quantum memories*, Dominik Maxein, Christophe Arnold, Valentina Parigi, Lambert Giner, Lucile Veissier, Adrien Nicolas, Baptiste Gouraud, Pierre Vernaz-Gris, Neil Corzo-Trejo, and Aveek Chandra. You guys gave me lots of wonderful memories in Paris, like picnic along the Seine, dessert in the group meeting, chat over a cup of tea, drinks in the bar, and exotic foods in the restaurant.

I would also like to acknowledge our collaborators Francesco Marsili, and Matthew D. Shaw in Jet Propulsion Laboratory, Sae Woo Nam, and Varun Verma in National Institute of Standards and Technology, who fabricated and provided the state-of-the-art superconducting nanowire single-photon detectors at our working wavelength. It was those detectors that boosted or even enabled the experiments with two-photon conditioning shown in Part II of the thesis.

My gratitude should go as well to the financial supports from the Foundation for the Author of National Excellent Doctoral Dissertation of China and the China Scholarship Council.

I must thank my thesis reviewers for their carefully reading the entire manuscript and making many helpful suggestions to improve the quality of this thesis.

Last but not least, I would like to convey sincere thanks to all my family members for their constant support and enthusiastic encouragement, particularly during the days when I was geographically far away from you. I am especially grateful to Jiazi and Tata, whose companionship has eased a difficult journey. Love you all!

Contents

Introduction

Quantum information science

Historically, the idea of exploiting quantum phenomena in information technology was initiated in the 1970s, and rapidly attracted intensive interests among a small group of pioneer physicists, among others Richard Feynman, Charles Bennett, Paul Benioff, and David Deutsch. The investigation of the foundational problems of quantum mechanics and the physics of computation finally gave birth to a new fascinating field of research: *quantum information science* [1, 2]. Since then, a large variety of quantum protocols and algorithms as well as many revolutionary experimental demonstrations have been proposed and implemented driven by the prospect to develop new processing and communication capabilities from the quantum realm.

Quantum information science spans a wide variety of topics, including *quantum communication*, *quantum computation*, and *quantum metrology*. These three streams of researches have progressed mostly in parallel but deeply connected. More specifically, quantum communication, the art of transferring a quantum state from one place to another [3], has recently reached a level of maturity. For instance, the implementation of quantum cryptography protocols, allowing an absolutely secure exchange of information, has been demonstrated to the extent that commercial products are now available. Besides of information transportation, much attention has also been attracted in information processing to realize quantum computation, which could dramatically improve computational power for particular tasks [4]. Many algorithms have hitherto been proposed to demonstrate the remarkable computing capability beyond any classical computer, such as Shor's algorithm for integer factorization, and Grover's algorithm for data searching. The third direction, quantum metrology, is fast emerging, and would enable to reach an unprecedented precision beyond the classical limit [5].

In general, all forms of information processing can be considered in a quantum mechanical context. For instance the *no-cloning theorem*, which states that the creation of identical copies of an arbitrary unknown quantum state is forbidden, leads to various applications, including quantum cryptography, quantum teleportation, and quantum repeaters. Another example can be highlighted with the *quantum superposition*, which leads to the realization of a qubit state, as used in quantum information processing. The qubit is in a superposition of both logical states at the same time, which powers quantum computation with a unique property so-called parallelism. Additionally *entanglement*, one of the most striking feature in quantum mechanics, is an extremely valuable resource for achieving many tasks such as quantum teleportation [6] or quantum dense coding [7].

This thesis enters into this general context, and focuses on a specific approach for implementing optical quantum information processing (QIP).

Optical hybrid architecture

In practical optical QIP, there are two complementary approaches for encoding information with light, namely the discrete- and the continuous-variable approaches, each exploiting only one aspect of the wave-particle duality of light. Some protocols harness the particle-like discrete nature of light to encode quantum information on qubits, i.e. states of the form $c_0|0\rangle + c_1|1\rangle$, which involve single-photons, and live in a two-dimensional space spanned for example by orthogonal polarizations or the absence or presence of a single-photon [8]. In the

continuous alternative, i.e. wave-like qubits, the encoding is realized with the quadrature components (amplitude or phase) of a light field [9], in an inherently infinite-dimensional space. The qubits can be implemented for instance as arbitrary superpositions of classical light waves with opposite phases, known as optical Schrödinger cat states, $c_0|\alpha\rangle + c_1|-\alpha\rangle$, where $|\alpha\rangle$ is a coherent state with mean photon number $|\alpha|^2$.

Both encodings have advantages and drawbacks. Specifically discrete-variable QIP enables the realization of operations with a nearly unity fidelity, but it usually involves probabilistic implementations and mostly requires post-selection of successful events. On the other side, the continuous-variable approach can benefit from high detection efficiency by homodyne measurement and enables deterministic operations based on the on-demand entanglement resources. However, it typically suffers from intrinsically limited operation fidelity due to the imperfection of the entanglement. A brief comparison between these two encoding methods is summarized in Table 1 in terms of preparation, characterization, and detection [10, 11].

Table 1: Comparison between discrete-variable (DV) and continuous-variable (CV) QIP [11].

	DV QIP	CV QIP
Carrier	Discrete degree of freedom of a photon[a]	Quadratures of a light field
Source	Photons by PDC[b]	Squeezed light by PDC
Basis	Photon number basis: $\{\|n\rangle\}$	Quadrature basis: $\{\|x\rangle\}$
Dimensionality	Finite	Infinite
Encoding	$\|\psi\rangle = \alpha\|0,1\rangle + \beta\|1,0\rangle$	$\|\psi\rangle = \int \psi(x)\|x\rangle dx$
Representation	Density matrix	Wigner function
Detector	Photon detector (measure $\hat{n}$)	Homodyne detector (measure $\hat{x}$)
Difficulty	Two-qubit gate[c]	Non-Gaussian gate[d]

[a] e.g. polarization, orbital angular momentum, photon number, time bin, spatial mode ...
[b] PDC: parametric down-conversion
[c] e.g. CNOT gate
[d] e.g. cubic phase gate

Recently, a large effort has been dedicated to combining both approaches in a so-called *optical hybrid architecture* that overcomes the current limitations of optical QIP [10, 11, 12, 13, 14]. Indeed the integration of the discrete- and continuous-variable toolboxes and technologies has stimulated a series of new proposals and groundbreaking experiments.

Context and outline of the thesis

The general objective of the work during this thesis is to develop the required toolbox in the hybrid approach for quantum information processing, where continuous variables of light and photon counting are mixed. Specifically, we focus on the engineering of high-fidelity optical quantum states (particularly non-Gaussian states) and the development of high-performance photon detectors.

This PhD work has been accomplished in the framework of a co-tutored program between Laboratoire Kastler Brossel (Paris, France) and Laboratory of Precision Spectroscopy (Shanghai, China). Benefiting from the bilateral research resources, we conduct three main works:

- Experimental realization of high-purity non-Gaussian states, such as Fock states and

Schrödinger cat states, which constitute respectively two different photonic qubits in the quantum information processing.

- Laboratory generation of hybrid entanglement between particle-like and wave-like optical qubits, leading to the demonstration of a squeezing-induced micro-macro entangled state.
- Experimental implementation of coincident frequency up-converter based on two synchronized fiber lasers, with applications to infrared single-photon detection, infrared photon-number-resolving detection and ultra-sensitive infrared imaging.

Before presenting the main results of these works, in **Part I** we first introduce some theoretical and experimental tools required to understand the physical mechanisms and the experimental realizations. Specifically, in Chapter 1 we give a general introduction about the quantum theory of light, and provide two formalisms to describe quantum states, i.e. the density matrix and the Wigner function. With the Wigner function, the quantum states can be classified into two categories: Gaussian states and non-Gaussian states. The production of Gaussian states, particularly squeezed states, or two-mode squeezed vacuum states, are theoretically investigated in Chapter 2 based on nonlinear frequency down-conversion. Its complementary process, frequency up-conversion, is also studied as the basis for the implementation of quantum frequency converter. The transformation of Gaussian states into non-Gaussian ones can result from the so-called measurement-induced nonlinearity, as detailed in Chapter 3. Finally, Chapter 4 presents an automatic locking system based on microcontroller fully developed during this thesis. This system serves as a useful and versatile tool for phase and cavity lockings in the various experiments.

Part II describes the experimental demonstrations of quantum state engineering. The first example is the generation of heralded Fock states as shown in Chapter 5. Thanks to the low loss of the whole optical system and the high performance of superconducting single-photon detectors, quantum-optical state engineering up to the two-photon level is experimentally demonstrated. These features are also applied to produce Schrödinger cat states as detailed in Chapter 6. With the combination of the discrete-variable (Fock states) and continuous-variable (cat states) resources, we then experimentally generate for the first time a novel kind of optical entanglement, a so-called optical hybrid entanglement, as illustrated in Chapter 7. Beyond its fundamental significance, such hybrid entanglement opens the promises for heterogeneous network implementation, where discrete and continuous-variable operations and techniques can be efficiently combined. Additionally, based on this resource, we investigate a so-called squeezing-induced micro-macro entangled state, which is reminiscent of the original spirit of the Schrödinger cat state gedanken experiment.

In **Part III**, we report the parallel effort dedicated to the implementation of quantum frequency up-converter, which has promising applications in QIP. First, this up-converter can be used as an efficient photon detector, particularly at the infrared wavelengths. Second, it enables to spectrally translate the quantum state. This functional capability can find applications as frequency converter in future quantum network. Third, the quantum converter also provides an effective way to manipulate quantum states in the spectro-temporal domain. In Chapter 8, a high-efficiency and low-noise coincidence frequency conversion system is presented. Applications based on this conversion system, e.g. infrared photon-number-resolving detection and few-photon-level infrared imaging, are given in Chapter 9.

Publications and awards

Publications

1. K. Huang, H. Le Jeannic, V.B. Verma, M.D. Shaw, F. Marsili, S.W. Nam, E Wu, H. Zeng, O. Morin, J. Laurat, "Experimental quantum state engineering with time-separated heraldings from a continuous-wave light source: a temporal-mode analysis," arXiv:1511.02122 (2015).

2. K. Huang, H. Le Jeannic, J. Ruaudel, V. B. Verma, M. D. Shaw, F. Marsili, S. W. Nam, E Wu, H. Zeng, Y.-C. Jeong, R. Filip, O. Morin, and J. Laurat, "Synthesis of large squeezed coherent-state superpositions with minimal resources," *Physical Review Letters* **115**, 023602 (2015). doi: 10.1103/PhysRevLett.115.023602

3. K. Huang, H. Le Jeannic, J. Ruaudel, O. Morin, and J. Laurat, "Microcontroller-based locking in optics experiments," *Review of Scientific Instruments* **85**, 123112 (2014). doi: 10.1063/1.4903869

4. O. Morin, K. Huang, J. Liu, H. Le Jeannic, C. Fabre, and J. Laurat, "Remote creation of hybrid entanglement between particle-like and wave-like optical qubits," *Nature Photonics* **8**, 570-574 (2014). doi: 10.1038/nphoton.2014.137

5. O. Morin, J. Liu, K. Huang, F. Barbosa, C. Fabre, and J. Laurat, "Quantum State Engineering of Light with Continuous-Wave Optical Parametric Oscillators", *Journal of Visualized Experiments* **87**, e51224 (2014). doi: 10.3791/51224

6. K. Huang, X. Gu, Q. Zhou, H. Pan, E Wu, and H. Zeng, "Efficient generation of mid-infrared photons at 3.16 μm by coincidence frequency downconversion," *Laser Physics* **23**, 045401 (2013). doi: 10.1088/1054-660X/23/4/045401

7. Q. Zhou, K. Huang, H. Pan, E Wu, and H. Zeng, "Ultrasensitive mid-infrared up-conversion imaging at few-photon level," *Applied Physics Letters* **102**, 241110 (2013). doi: 10.1063/1.4811826

8. X. Gu, K. Huang, H. Pan, E Wu, and H. Zeng, "Efficient mid-infrared single-photon frequency upconversion detection with ultra-low background counts," *Laser Physics Letters* **10**, 055401 (2013). doi: 10.1088/1612-2011/10/5/055401

9. K. Huang, X. Gu, H. Pan, E Wu, and H. Zeng, "Few-photon-level two-dimensional infrared imaging by coincidence frequency upconversion," *Applied Physics Letters* **100**, 151102 (2012). doi: 10.1063/1.3703610

10. K. Huang, X. Gu, H. Pan, E Wu, and H. Zeng, "Synchronized fiber lasers for efficient coincidence single-photon frequency upconversion," *IEEE Journal of Selected Topics in Quantum Electronics* **18**, 562 (2012). doi: 10.1109/JSTQE.2010.2102005

11. K. Huang, E Wu, X. Gu, H. Pan, and H. Zeng, "Ultrashort Laser Pulses for Frequency Upconversion", in chapter 16 of book *Laser Pulses - Theory, Technology, and Applications*, edited by Igor Peshko, ISBN 978-953-51-0796-5, October 17, 2012. doi: 10.5772/48541

12. X. Gu, K. Huang, H. Pan, E Wu, and H. Zeng, "Photon correlation in single-photon frequency upconversion," *Optics Express* **20**, 2399 (2012). doi: 10.1364/OE.20.002399

13. K. Huang, X. Gu, M. Ren, Y. Jian, H. Pan, G. Wu, E Wu, and H. Zeng, "Photon-number-resolving detection at 1.04 μm via coincidence frequency upconversion," *Optics Letters* **36**, 9 (2011). doi: 10.1364/OL.36.001722

14. X. Gu, K. Huang, Y. Li, H. Pan, E Wu, and H. Zeng, "Temporal and spectral control of single-photon frequency upconversion for pulsed radiation," *Applied Physics Letters* **96**, 131111 (2010). doi: 10.1063/1.3374330

Conferences

1. K. Huang, O. Morin, H. Le Jeannic, J. Liu, C. Fabre, and J. Laurat, Photons Beyond Qubits, Palacky University, Olomouc, Czech Republic, Apr. 14 -17, 2014.

2. K. Huang, O. Morin, J. Liu, H. Le Jeannic, C. Fabre, and J. Laurat, 3$^{\text{rd}}$ Workshop of the GDR-IQFA, Université Paris 7, Nov. 20-22, 2013.

3. K. Huang, O. Morin, J. Liu, C. Fabre, and J. Laurat, 3$^{\text{rd}}$ workshop of the Sino-French Research Network on "Quantum Manipulation of Atoms and Photons", Palaiseau, France, Sep. 23-27, 2013.

4. K. Huang, X. Gu, H. Pan, E Wu, and H. Zeng, CLEO/QELS, California, U. S., May 6-11, 2012.

5. K. Huang, X. Gu, M. Ren, Y. Jian, H. Pan, E Wu, G. Wu, and H. Zeng, Nonlinear Optics conference, Hawaii, U. S., July 17-22, 2011.

6. K. Huang, X. Gu, M. Ren, Y. Jian, H. Pan, E Wu, and H. Zeng, CLEO/QELS, Maryland, U. S., May 1-6, 2011.

Awards

1. National Scholarship for postgraduate students (2013)

2. Foundation for the Author of National Excellent Doctoral Dissertation of China, East China Normal University (2012)

3. Second prize of 12$^{\text{th}}$ National "Challenge Cup" competition (2011)

4. Award for Excellent Doctors in Academics, East China Normal University, (2011)

5. Second prize of 12$^{\text{th}}$ Shanghai "Challenge Cup" (2011)

Part I

Theoretical and Experimental Tools

1 | Quantum Theory of Light

In this first chapter, we will briefly introduce some basic concepts about the quantum theory of light in order to make the whole thesis self-contained, and the manuscript more accessible to non-specialists. These quantum description and the introduced mathematical notations will also be useful for the explanations and expressions given in the following chapters. Here the quantum states are described with two formalisms: the *density matrix* and the *Wigner function*. From their general definitions, we derive some important mathematical properties. Then *Gaussian operations* will be presented: they enable to obtain various common *Gaussian states* starting from *vacuum*. Finally, we will give some examples of *non-Gaussian states*.

For more details about these concepts, the readers can refer to various textbooks with systematic and rigorous derivations [15, 16, 17, 18, 19].

1.1 Photons

In the following, we provide the quantum formalism enabling the description of light. The photon, with a defined energy $E = h\nu$, exhibits properties of both waves and particles, also known as the *wave-particle duality*.

1.1.1 Creation and annihilation operators

The electromagnetic field is quantized by using the simple harmonic oscillator operators - the *annihilation operator* $\hat{a}$ and the *creation operator* $\hat{a}^\dagger$. We have the well-known single-mode Hamiltonian and commutator,

$$\begin{aligned} \hat{\mathcal{H}} &= \hbar\omega \left(\hat{a}\hat{a}^\dagger + \frac{1}{2} \right) \ , \\ [\hat{a}, \hat{a}^\dagger] &= 1 \ . \end{aligned} \tag{1.1}$$

The product of both operators forms the *photon-number operator*

$$\hat{n} = \hat{a}^\dagger \hat{a} \ . \tag{1.2}$$

The electric field is given by

$$\hat{\mathrm{E}}_{\vec{k}}(\vec{r}, t) = E_0[\hat{a}e^{-i(\omega t - \vec{k}\cdot\vec{r})} + \hat{a}^\dagger e^{i(\omega t - \vec{k}\cdot\vec{r})}] \ , \tag{1.3}$$

where $\vec{k}$ is the the wave vector. Since the annihilation and creation operators are not Hermitian, thus they are not *observables*. When working with real measurements it may be preferable to use another frame of reference to describe the situation. This is the idea of field quadratures to describe the light.

1.1.2 Quadrature operators

For constructing observables of light, we use the following Hermitian *quadrature operators* [1]:

$$\begin{aligned} \hat{x} &= \sigma_0(\hat{a}^\dagger + \hat{a}) \ , \\ \hat{p} &= i\sigma_0(\hat{a}^\dagger - \hat{a}) \ . \end{aligned} \tag{1.4}$$

Conversely, the annihilation/creation operators are thus given by

$$\begin{aligned} \hat{a} &= \frac{\hat{x} + i\hat{p}}{2\sigma_0} \ , \\ \hat{a}^\dagger &= \frac{\hat{x} - i\hat{p}}{2\sigma_0} \ . \end{aligned} \tag{1.5}$$

Using the commutation relation (1.1), we can deduce the commutator between the quadrature operators,

$$[\hat{x}, \hat{p}] = i2\sigma_0^2 \ . \tag{1.6}$$

The Heisenberg uncertainty relation follows and is given by

$$\Delta x \Delta p \geqslant \sigma_0^2 \ , \tag{1.7}$$

[1] Note that here we use the convention σ_0 introduced in [20]. In many other materials, Plank constant $\hbar$ is used. They are identified as $\hbar = 2\sigma_0^2$.

where $\Delta x = \sqrt{\langle \hat{x}^2 \rangle - \langle \hat{x} \rangle^2}$ denotes a standard deviation.

The vacuum state saturates the Heisenberg inequality with the following identity

$$\Delta x = \Delta p = \sigma_0 \ . \tag{1.8}$$

This relation highlights the statistical meaning of σ_0 : it is the standard deviation of the vacuum fluctuation.

It is worth noting that quadrature operators can be arbitrarily chosen via rotation by an angle of θ in phase space

$$\begin{aligned} \hat{x}_\theta &= \cos\theta \hat{x} + \sin\theta \hat{p} \\ &= \sigma_0 (\hat{a} e^{-i\theta} + \hat{a}^\dagger e^{i\theta}) \ . \end{aligned} \tag{1.9}$$

The orthogonal quadrature operator is given by $\hat{p}_\theta = \hat{x}_{\theta+\pi/2}$.

Due to the Hermitian property of the quadrature operator $\hat{x}_\theta$, there exists a series of orthonormal eigenvectors $\{|x_\theta\rangle\}_{x_\theta \in \mathbb{R}}$ satisfying the eigenvalue equation

$$\hat{x}_\theta |x_\theta\rangle = x_\theta |x_\theta\rangle \ , \tag{1.10}$$

and the completeness condition

$$\int_{\mathbb{R}} |x_\theta\rangle\langle x_\theta| \ dx_\theta = \mathbb{1} \ . \tag{1.11}$$

Note that these eigenvectors correspond to a fixed phase θ.

Strictly speaking these eigenstates are not truly normalized, thus they cannot be generated experimentally [19]. Nevertheless, they will appear in many mathematical tricks, for instance, for the introduction of *wave functions* as

$$\psi(x_\theta) = \langle x_\theta | \ \psi \rangle \ . \tag{1.12}$$

The moduli square of the wave function $|\psi(x_\theta)|^2$ has the physical meaning of *quadrature probability distribution* $\mathcal{P}_{|\psi\rangle}(x_\theta)$ (also known as *marginal distribution*), which can be measured using homodyne detection, as will be detailed in Chapter 3.

The general quadrature eigenstate $|x_\theta\rangle$ can be expressed in the Fock state basis,

$$|x_\theta\rangle = \pi^{-1/4} \exp[-\tfrac{1}{2} x_\theta^2 + \sqrt{2} e^{i\theta} x_\theta \hat{a}^\dagger - \tfrac{1}{2} e^{2i\theta} \hat{a}^{\dagger 2}] \, |0\rangle \ , \tag{1.13}$$

from which one can obtain the quadrature representation of any pure state.

1.2 Representations of quantum states

In quantum optics, there are a number of different ways to describe the quantum state of light. In principle, they can be reformulated from one to the other. Usually, for practical convenience, one of them would be preferred in certain applications. In this section, two commonly used formalisms will be introduced, namely the *density matrix* and the *Wigner function*.

1.2.1 Density matrix

A *pure state* can be simply represented by a single state vector $|\psi\rangle$, which is an element of a *Hilbert space* $\mathcal{H}$. However, because of the imperfection in the state preparation or due to environmental decoherence for instance, the state of a quantum system will evolve to a

statistical mixture of pure states, or *mixed state*. For describing mixed state we resort to a more general representation given by the *density matrix* (or the *density operator*):

$$\hat{\rho} = \sum_i P_i \left|\psi_i\right\rangle \left\langle\psi_i\right| \ , \tag{1.14}$$

where P_i is the statistical weight of the pure state $|\psi_i\rangle$, with the probability conservation $\sum_i P_i = 1$.

A physically acceptable density matrix should satisfy some constraints:

$$\begin{aligned} \mathrm{Tr}(\hat{\rho}) = 1 \quad &\Leftrightarrow \quad Normalization \\ \hat{\rho} = \hat{\rho}^\dagger \quad &\Leftrightarrow \quad Hermiticity \\ \langle\psi|\,\hat{\rho}\,|\psi\rangle \geqslant 0 \quad for \quad \forall\ |\psi\rangle \quad &\Leftrightarrow \quad Positivity \end{aligned} \tag{1.15}$$

From these requirements, the density matrix have many properties that lead to important concepts.

Diagonalisation The density matrix can always be diagonalized into some orthogonal basis,

$$\hat{\rho} = \sum_i p_i \left|\psi_i\right\rangle \left\langle\psi_i\right| . \tag{1.16}$$

This can be seen as a weighted sum of probabilities across multiple pure states, where the weights are given by the eigenvalues p_i of the density matrix.

Purity The purity of a quantum state is defined as

$$P = \mathrm{Tr}[\hat{\rho}^2] = \sum_i p_i^2 \ . \tag{1.17}$$

For pure state $P = 1$; otherwise for mixed state, $0 < P < 1$.

von Neumann entropy This is another criterion for purity given by

$$\mathcal{S}_{vN} = -\,\mathrm{Tr}[\hat{\rho}\ln\hat{\rho}] = -\sum_i p_i \ln p_i \ . \tag{1.18}$$

This quantity is equal to 0 for pure states and positive otherwise. Additionally, this quantity is often used as a measure of entanglement for pure states by treating $\hat{\rho}$ as the density matrix for either of two entangled subsystems [2].

Fidelity This quantity enables to measure the similarity between two quantum states, generally defined as [3]:

$$\mathcal{F}(\hat{\rho}_1, \hat{\rho}_2) = \left(\mathrm{Tr}\left[\sqrt{\sqrt{\hat{\rho}_2}\hat{\rho}_1\sqrt{\hat{\rho}_2}}\right]\right)^2 \ . \tag{1.19}$$

[2] Actually, for pure states, the entanglement is directly linked to the purity of the subsystem density matrix (after a partial trace of the full density matrix). A pure state is entangled if and only if the subsystem is in a mixed state.

[3] If one state is pure, $\mathcal{F} = \mathrm{Tr}[\hat{\rho}_1\hat{\rho}_2]$; if both are pure states, $\mathcal{F} = |\langle\psi_1|\psi_2\rangle|^2$ [20]. Additionally, the fidelity is bounded by [21]

$$\begin{aligned} \mathcal{F}(\hat{\rho}_1, \hat{\rho}_2) &\geqslant \mathrm{Tr}(\hat{\rho}_1\hat{\rho}_2) + \sqrt{2}\sqrt{[\mathrm{Tr}(\hat{\rho}_1\hat{\rho}_2)]^2 + \mathrm{Tr}(\hat{\rho}_1\hat{\rho}_2\hat{\rho}_1\hat{\rho}_2)} \ , \\ \mathcal{F}(\hat{\rho}_1, \hat{\rho}_2) &\leqslant \mathrm{Tr}(\hat{\rho}_1\hat{\rho}_2) + \sqrt{[1-\mathrm{Tr}(\hat{\rho}_1^2)][1-\mathrm{Tr}(\hat{\rho}_2^2)]} \ . \end{aligned}$$

The above inequalities are saturated if at least one state is pure.

Marginal distribution It corresponds to the probability distribution (non-negative real number) of quadrature values for a given state

$$\mathcal{P}_{\hat{\rho}}(x_\theta) = \langle x_\theta|\hat{\rho}|x_\theta\rangle \ . \tag{1.20}$$

1.2.2 Wigner function

Besides of the density matrix, it is also possible to represent a given quantum state in phase space by a quasi-probability distribution known as the *Wigner function*. It is called a quasi-probability distribution because it can take negative values. The negativity of the Wigner function is considered as a strong indication of non-classicality.

The Wigner function of a quantum state was firstly introduced by E.P. Wigner in 1932 in the context of quantum mechanical corrections for thermodynamic equilibrium. It can be written as [4]:

$$W_{\hat{\rho}}(x,p) = \frac{1}{2\pi\sigma_0^2}\int e^{iyp/\sigma_0^2}\langle x-y|\hat{\rho}|x+y\rangle\, dy \ . \tag{1.21}$$

For a pure state, the Wigner function can be expressed via the wave function

$$W_{\hat{\rho}}(x,p) = \frac{1}{2\pi\sigma_0^2}\int e^{iyp/\sigma_0^2}\psi^*(x-y)\psi(x+y)\, dy \ . \tag{1.22}$$

With the *parity operator* $\hat{\mathcal{P}} = e^{i\pi\hat{a}^\dagger\hat{a}}$, the Wigner function can also be written in the following form [18]

$$W_{\hat{\rho}}(x,p) = \frac{1}{4\sigma_0^2}W_{\hat{\rho}}(\alpha) = \frac{1}{2\pi\sigma_0^2}Tr[\hat{D}(-\alpha)\hat{\rho}\hat{D}(\alpha)\hat{\mathcal{P}}] \ , \tag{1.23}$$

where $x + ip = 2\sigma_0\alpha$.

From the density matrix, the Wigner function can be calculated as

$$W_{\hat{\rho}}(x,y) = \sum_{k,l}\rho_{kl}W_{|k\rangle\langle l|}(x,y) \ , \tag{1.24}$$

where

$$W_{|k\rangle\langle l|}(x,p) = \frac{(-1)^l}{2\pi\sigma_0^2}\sqrt{\frac{l!}{k!}}\left(\tfrac{x-ip}{\sigma_0}\right)^{k-l}e^{-(x^2+p^2)/2\sigma_0^2}L_l^{k-l}\left(\tfrac{x^2+p^2}{\sigma_0^2}\right) \ , \tag{1.25}$$

with L_l^{k-l} a associated Laguerre polynomial (cf. Appendix A). This equation is true for $k \geqslant l$, otherwise, we can use the following relation

$$W_{|k\rangle\langle l|}(x,p) = W^*_{|l\rangle\langle k|}(x,p) \qquad k \leqslant l \ . \tag{1.26}$$

Thanks to equation (1.25), it is possible to access each element of the density matrix from the Wigner function

$$\rho_{kl} = \mathrm{Tr}[\hat{\rho}|k\rangle\langle l|] = 4\pi\sigma_0^2\iint dxdp\ W_{\hat{\rho}}(x,p)W_{|k\rangle\langle l|}(x,p) \ . \tag{1.27}$$

The equation (1.24) is very useful to calculate numerically the Wigner function associated with a given density matrix. It can also be generalized to more than one modes with two variables x_i, p_i for each mode i, for instance:

$$W_{\hat{\rho}}(x_1,y_1;x_2,y_2) = \sum_{k,l;m,n}\rho_{klmn}W_{|k\rangle\langle l|}(x_1,y_1)W_{|m\rangle\langle n|}(x_2,y_2) \ , \tag{1.28}$$

[4] Originally it was written with the convention using $\hbar$:

$$W_{\hat{\rho}}(x,p) = \frac{1}{2\pi\hbar}\int_{\mathbb{R}} e^{ipy/\hbar}\langle x-y/2|\hat{\rho}|x+y/2\rangle\, dy$$

where ρ_{klmn} is the density matrix element of a two-mode state.

Similarly to the density matrix, the Wigner function of a physical state should respect some basic constraints:

$$\begin{aligned} \iint_{\mathbb{R}^2} W_{\hat{\rho}}(x,p)dxdp = 1 \quad &\Leftrightarrow \quad Normalization \\ W_{\hat{\rho}}(x,p) \in \mathbb{R} \quad &\Leftrightarrow \quad Hermiticity \\ \mathcal{P}_{\hat{\rho}}(x_\theta) \geqslant 0 \quad for \quad \forall\, x_\theta \quad &\Leftrightarrow \quad Positivity \\ |W(x,p)| \leqslant \frac{1}{2\pi\sigma_0^2} \quad &\Leftrightarrow \quad Bound \end{aligned} \tag{1.29}$$

where the marginal distribution is given by

$$\mathcal{P}_{\hat{\rho}}(x_\theta) = \int dp_\theta\, W_{\hat{\rho}}(x_\theta \cos\theta - p_\theta \sin\theta, p_\theta \cos\theta + x_\theta \sin\theta)\ . \tag{1.30}$$

Besides of these relations, the Wigner function should be continuous in the phase space. Unlike the density matrix, it seems that there is no simple sufficient condition for ensuring that a function is the Wigner function of a physical state. One solution is to transform the Wigner function back to the corresponding density matrix, and thus use the sufficient condition (1.15). However this method needs a truncation of the Hilbert space.

Here are some important properties associated with the Wigner function:

Overlap formula This is a general formula for two Hermitian operators.

$$\mathrm{Tr}[\hat{O}_1\hat{O}_2] = 4\pi\sigma_0^2 \iint dxdp\ W_{\hat{O}_1}(x,p)W_{\hat{O}_2}(x,p)\ . \tag{1.31}$$

It is a very powerful tool for many calculations, such as the calculation of fidelity, purity, and the study of conditional measurement.

Value at phase-space origin The value of the Wigner function at the phase-space origin only depends on the diagonal elements of the density matrix:

$$2\pi\sigma_0^2 W_{\hat{\rho}}(0,0) = \sum_k (-1)^k \rho_{kk}\ . \tag{1.32}$$

It is related to the expectation value of the parity operator [5].

Symmetrically ordered operator The quantum mechanical expectation value for an operator function $\mathcal{F}(\hat{x},\hat{p})$ that is symmetrically ordered with respect to $\hat{x}$ and $\hat{p}$ agrees with the corresponding "classical" average, where $W(x,p)$ plays the role of the weight function:

$$\langle \mathcal{F}(\hat{x},\hat{p})\rangle = \iint W(x,p)f(x,p)dxdp\ . \tag{1.33}$$

Here, the classical function f is obtained from the operator function $\mathcal{F}$ by replacing $\hat{x}$ by x and $\hat{p}$ by p.

[5] It can be obtained from $2\pi\sigma_0^2 W_{\hat{\rho}}(0,0) = \mathrm{Tr}[\hat{\rho}\hat{\mathcal{P}}]$.

The relationship can be applied to the operator function based on the symmetrically ordered photon creation and annihilation operators:

$$\left\langle \mathcal{F}(\hat{a}^\dagger, \hat{a}) \right\rangle = \iint W(x,p) f(x,p) dx dp \ . \tag{1.34}$$

The classical function $f(x,p)$ is simply obtained from the following exchange:

$$\hat{a}^\dagger \to \frac{x+ip}{2\sigma_0} \qquad \hat{a} \to \frac{x-ip}{2\sigma_0} \ . \tag{1.35}$$

1.3 Gaussian manipulations

Gaussian manipulations are primary tools for state preparation and analysis in continuous-variable quantum information processing [22, 23]. In this section, we will introduce the concept of *Gaussianity* and the realm of *Gaussian operations* will be presented as well.

1.3.1 Gaussianity

The famous *Hudson-Piquet theorem* [24] establishes an equivalence between the (quantum) non-Gaussian character and the negativity of the Wigner function for pure states:

A necessary and sufficient condition for a pure quantum state being a Gaussian state is that the corresponding Wigner function is positive (true probability distribution).

Although this relation cannot simply extend to mixed states [25], great effort is still dedicated to find connection between Gaussianity and Wigner function properties for a general state. It has been recently proved that for a Gaussian state, the value of the Wigner function at the origin of phase space is bounded by a positive quantity, which is a function only of the average photon number of the state [26]. Specifically, a quantum state is non-Gaussian if

$$W(0,0) < \frac{1}{\pi} \mathrm{e}^{-2\bar{n}(\bar{n}+1)}, \tag{1.36}$$

where $\bar{n}$ is the mean photon number.

1.3.2 Gaussian operations

A quantum operation is said Gaussian when it maps Gaussian states into Gaussian states. Gaussian operations are unitary and thus trace preserving. They can be described by interaction Hamiltonian with at maximum quadratic annihilation/creation operators.

Rotation The rotation operation can be achieved with the so-called *phase shift operator*

$$\hat{U}(\theta) = e^{-i\theta \hat{a}^\dagger \hat{a}} \ . \tag{1.37}$$

It can be realized by changing the phase of the quantum states, e.g. the temporal evolution, which leads to the rotation of its Wigner function in phase space. The rotated Wigner function $W_{\hat{U}\hat{\rho}\hat{U}^\dagger}(x,p)$ and the original one $W_{\hat{\rho}}(x,p)$ are related by

$$W_{\hat{U}\hat{\rho}\hat{U}^\dagger}(x,p) = W_{\hat{\rho}}(x\cos\theta - p\sin\theta, p\cos\theta + x\sin\theta) \ . \tag{1.38}$$

The density matrix element of the phase shift operator in the Fock state basis is given by

$$U_{mn}(\theta) = \langle m|\hat{U}(\theta)|n\rangle = e^{-i\theta n}\delta_{mn} \ , \tag{1.39}$$

where δ_{mn} is the Kronecker delta symbol.

Displacement The displacement operation is achieved with the *displacement operator* defined as:

$$\hat{D}(\alpha) = e^{\alpha\hat{a}^\dagger - \alpha^*\hat{a}} \ . \tag{1.40}$$

Experimentally, it can be realized by mixing a state with a bright coherent light on a highly asymmetric beam-splitter. As it is called, the displacement operation will translate the Wigner function in phase space in the following way

$$W_{\hat{D}\hat{\rho}\hat{D}^\dagger}(x,p) = W_{\hat{\rho}}(x - 2\sigma_0\Re[\alpha],\ p - 2\sigma_0\Im[\alpha]) \ . \tag{1.41}$$

The density matrix element of the displacement operator in the Fock state basis is given by

$$\begin{aligned} D_{mn}(\alpha) &= \langle m|\hat{D}(\alpha)|n\rangle \\ &= \sqrt{\frac{n!}{m!}} e^{-|\alpha|^2/2} \alpha^{m-n} L_n^{m-n}(|\alpha|^2) \ , \end{aligned} \tag{1.42}$$

under the condition of $m \geqslant n$. For $m \leqslant n$, we have $D_{mn}(\alpha) = D^*_{nm}(-\alpha)$.

Beam-splitter The beam-splitter operation between two modes can be written as

$$\hat{B}(\theta) = e^{\theta(\hat{a}^\dagger\hat{b} - \hat{a}\hat{b}^\dagger)} \ , \tag{1.43}$$

where $t = \cos\theta$ and $r = \sin\theta$ are the transmission and reflection coefficients in amplitude (thus t^2 and r^2 for power coefficients).

A beam-splitter is one of the simplest elements in quantum optics experiments. It is also very useful in the theoretical analysis of two-mode systems. Remarkably, the output Wigner function $W'(x_a, p_a; x_b, p_b)$ after a beam-splitter has a simple relationship with the input Wigner function $W(x_a, p_b; x_a, p_b)$:

$$W'(x_a, p_a; x_b, p_b) = W(tx_a + rx_b, tp_a + rp_a; tx_b - rx_a, tp_b - rp_a) \ . \tag{1.44}$$

The beam-splitter operation acts on a two-mode Fock state as

$$\begin{aligned} \hat{B}\,|n_1, n_2\rangle = \sum_{k_1=0}^{n1}\sum_{k_2=0}^{n2} &\sqrt{\frac{(k_1+k_2)!(n_1+n_2-k_1-k_2)}{n_1!n_2!}} \begin{pmatrix} n_1 \\ k_1 \end{pmatrix} \begin{pmatrix} n_2 \\ k_2 \end{pmatrix} \\ &\times (-1)^{k_2} t^{n_2+k_1-k_2} r^{n_1-k_1+k_2} \,|k_1+k_2, n_1+n_2-k_1-k_2\rangle \ , \end{aligned} \tag{1.45}$$

where $\begin{pmatrix} n \\ k \end{pmatrix}$ is the binomial coefficient. Equation (1.45) can be alternatively expressed as [27]

$$\hat{B}\,|n_1, n_2\rangle = \sum_{N_1,N_2} B^{n_1,n_2}_{N_1,N_2}\,|N_1, N_2\rangle \ , \tag{1.46}$$

where

$$\begin{aligned} B^{n_1,n_2}_{N_1,N_2} = &\sum_{k=0}^{n_1}\sum_{l=0}^{n_2} (-1)^{n_1-k} r^{n_1+n_2-k-l} t^{k+l} \\ &\times \frac{\sqrt{n_1!n_2!N_1!N_2!}}{k!l!(n_1-k)!(n_2-l)!} \delta_{N_1,n_2+k-l}\delta_{N_2,n_1-k+l} \ . \end{aligned} \tag{1.47}$$

When the total input photon number is $N = n_1 + n_2$, the output state becomes $(N+1)-$dimensional entangled state. By using the equation (1.46), it is not difficult to calculate the density matrix for the beam-splitter operator in the Fock state basis.

Squeezing The squeezing operation is defined as [6]

$$\hat{S}(\zeta) = e^{\frac{\zeta}{2}(\hat{a}^2 - \hat{a}^{\dagger 2})} , \tag{1.48}$$

where ζ is the *squeezing parameter*. This operation is obtained by parametric interaction. In contrast with all the previous operations, it requires non-linear optics, as will be seen in the next chapter. The squeezing operation will deform the Wigner function as

$$W_{\hat{S}\hat{\rho}\hat{S}^\dagger}(x,p) = W_{\hat{\rho}}(xe^{\zeta},\ pe^{-\zeta}) . \tag{1.49}$$

The density matrix element of the squeezing operation in the Fock state basis is given by

$$\begin{aligned} S_{mn}(\zeta) &= \langle m|\hat{S}(\zeta)|n\rangle \\ &= \frac{\sqrt{m!n!}}{\frac{m+n+1}{2}\cosh\zeta} \sum_{k}^{\min\{m,n\}} (\frac{\sinh\zeta}{2})^{\frac{(m+n-2k)}{2}} \frac{(-1)^{\frac{(m-k)}{2}}}{k!(\frac{m-k}{2})!(\frac{n-k}{2})!} , \end{aligned} \tag{1.50}$$

where

$$k = \begin{cases} 0, 2, 4, \ \ldots & \text{if } m,n \text{ is even} \\ 1, 3, 5, \ \ldots & \text{if } m,n \text{ is odd} . \end{cases}$$

$S_{mn}(\zeta) = 0$ when $|m-n|$ is odd.

1.4 Gaussian states

Gaussian states are at the heart of quantum information processing with continuous variables, which are used in a wide variety of tasks and applications, including quantum communication, quantum cryptography, quantum computation, quantum teleportation, and quantum state and channel discrimination [23]. With the Gaussian operations, one can map a Gaussian state into another. Specifically, all pure Gaussian states can be obtained by applying these operations on a vacuum state.

1.4.1 Coherent state

The coherent state is the most common state used in the lab. It can be generated by a laser operating largely above threshold. Here are some basic properties about the single-mode coherent state.

Definition

$$|\alpha\rangle = \hat{D}(\alpha)|0\rangle \qquad (\alpha = |\alpha|e^{i\phi} \in \mathbb{C}) . \tag{1.51}$$

Fock state expansion

$$|\alpha\rangle = e^{-|\alpha|^2/2} \sum_{n=0}^{+\infty} \frac{\alpha^n}{\sqrt{n!}} |n\rangle . \tag{1.52}$$

Wave function

$$\langle x_\theta|\alpha\rangle = \frac{1}{\sqrt[4]{2\pi\sigma_0^2}} e^{i|\alpha|\sin(\phi-\theta)x_\theta/\sigma_0} e^{-[x_\theta/2\sigma_0 - |\alpha|\cos(\phi-\theta)]^2} . \tag{1.53}$$

[6] If $\zeta = |\zeta|e^{i\theta}$ is a complex number, the operator is written as $\hat{S}(\zeta) = \exp[\frac{\zeta}{2}\hat{a}^2 - \frac{\zeta^*}{2}\hat{a}^{\dagger 2}]$. With a phase-shift operator we have $\hat{S}(\zeta) = \hat{U}^\dagger(\theta/2)\hat{S}(|\zeta|)\hat{U}(\theta/2)$.

Wigner function

$$W_{|\alpha\rangle}(x,p) = \frac{1}{2\pi\sigma_0^2} e^{-(x-2\sigma_0\Re[\alpha])^2/2\sigma_0^2 - (p-2\sigma_0\Im[\alpha])^2/2\sigma_0^2} \ . \tag{1.54}$$

1.4.2 Squeezed vacuum state

The simplest single-mode squeezed state $|\zeta\rangle$ can be generated by applying the squeezing operator on the vacuum state $|0\rangle$.

Definition

$$|\psi_{sq}\rangle = \hat{S}(\zeta)|0\rangle \qquad (\zeta = |\zeta|e^{i\phi} \in \mathbb{C}) \ . \tag{1.55}$$

Fock state expansion

$$|\psi_{sq}\rangle = \sqrt[4]{1-\lambda^2} \sum_{n=0}^{\infty} \sqrt{\binom{2n}{n}} \left(\frac{\lambda}{2}\right)^n |2n\rangle \ , \tag{1.56}$$

where $\lambda = \tanh\zeta$. We can see that the squeezed vacuum state only contains even-photon number states [7].

Wave function

$$\langle x|\psi_{sq}\rangle = \frac{1}{(s\pi)^{1/4}} e^{-x^2/2s} \ , \tag{1.57}$$

where $s = e^{-2\zeta}$ is the *squeezing factor*. It is often given in a logarithmic scale:

$$s_{dB} = -10\log_{10} s = -10\log_{10}\left(\frac{1-\lambda}{1+\lambda}\right) = \frac{20}{\ln 10}\zeta \ . \tag{1.58}$$

Wigner function

$$W_{sq}(x,p) = \frac{1}{2\pi\sigma_0^2} e^{-\frac{x^2}{2\sigma_x^2} - \frac{p^2}{2\sigma_p^2}} \ , \tag{1.59}$$

where $\sigma_x^2 = s\sigma_0^2$ and $\sigma_p^2 = \frac{1}{s}\sigma_0^2$.

The Wigner function of a squeezed vacuum state is plotted in figure 1.1. We can notice that it corresponds to the Wigner function of the vacuum state squeezed along one axis and "anti-squeezed" along the orthogonal axis. This is the result of the Heisenberg inequality $\sigma_x\sigma_p \geqslant \sigma_0^2$.

1.4.3 Two-mode squeezed vacuum state

This two-mode state is also called *two-mode squeezed vacuum* since it can be simply obtained by mixing two squeezed vacua on a 50:50 beam-splitter and vice versa.

[7] This leads to a strong photon bunching effect, which is usually quantified by the second-order correlation function $g^{(2)}(0) = \left\langle \hat{a}^\dagger\hat{a}^\dagger\hat{a}\hat{a}\right\rangle / \left\langle \hat{a}^\dagger\hat{a}\right\rangle^2$. For the squeezed vacuum state we have $g^{(2)}(0) = 3 + 1/\sinh^2(\zeta)$.

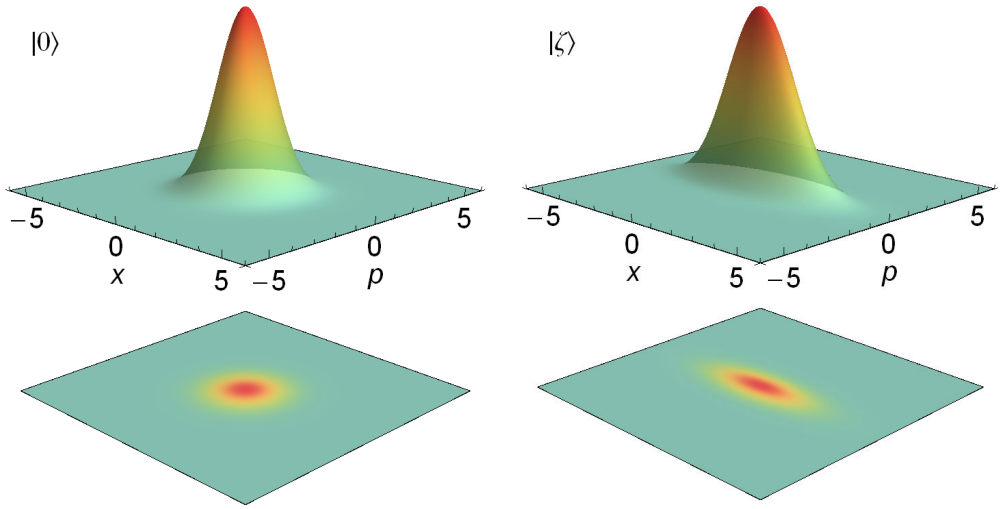

Figure 1.1: Wigner function of vacuum state on the left and squeezed vacuum state of 4 dB on the right.

Definition

$$|\psi_{sq}\rangle_{ab} = \hat{S}_{ab}(\zeta)|0\rangle \qquad (\zeta = |\zeta|e^{i\phi} \in \mathbb{C}) \ . \tag{1.60}$$

where the *two-mode squeezing operator* is defined as [8]

$$\hat{S}_{ab}(\zeta) = e^{\zeta(\hat{a}\hat{b} - \hat{a}^\dagger\hat{b}^\dagger)} \ .$$

The two-mode squeezing operator can be equivalently written as the mixing of two squeezing operators by a balanced beam-splitter:

$$\hat{S}_{ab}(\zeta) = \hat{B}(\frac{\pi}{4})\hat{S}_a(\zeta)\hat{S}_b(-\zeta)\hat{B}^\dagger(\frac{\pi}{4}) \ .$$

Fock state expansion

$$|\psi_{sq}\rangle_{ab} = \sqrt{1-\lambda^2}\sum_{n=0}^{\infty}\lambda^n|n\rangle_a|n\rangle_b \ . \tag{1.61}$$

Wigner function

$$W(x_a, p_a, x_b, p_b) = \frac{1}{(2\pi\sigma_0^2)^2}e^{-\frac{(x_a-x_b)^2}{4\sigma_0^2 s} - \frac{(x_a+x_b)^2}{4\sigma_0^2/s} - \frac{(p_a-p_b)^2}{4\sigma_0^2/s} - \frac{(p_a+p_b)^2}{4\sigma_0^2 s}} \ . \tag{1.62}$$

If we only consider one local mode, i.e. we lose the information about one of them, the resulting state is thus obtained by a partial trace:

$$\int_a W_{\hat{S}_{ab}(\zeta)} = \frac{1}{\pi}\frac{1}{\sigma_x^2+\sigma_p^2}e^{-(x^2+p^2)/(\sigma_x^2+\sigma_p^2)} \ , \tag{1.63}$$

which is actually a thermal state as described now.

[8] Here we assume that ζ is a real number for simplicity.

1.4.4 Thermal state

As shown above, a thermal state can be obtained by tracing over one mode of a two-mode squeezed vacuum. Since the two-mode squeezed vacuum is a Gaussian state, the thermal state is thus necessarily Gaussian.

Density matrix

$$\hat{\rho}_{th} = \sum_n \frac{1}{n_{th}+1}\left(\frac{n_{th}}{n_{th}+1}\right)^n |n\rangle\langle n| \ , \tag{1.64}$$

where n_{th} is the mean photon number.

Wigner function

$$W(x,p) = \frac{1}{2\pi\sigma_{th}^2} e^{-(x^2+p^2)/2\sigma_{th}^2} \ . \tag{1.65}$$

The variance of this state is $\sigma_{th}^2 = (2n_{th}+1)\sigma_0^2$, which is larger than the vacuum fluctuation.

1.4.5 Covariance matrix

All the states discussed above are Gaussian states and consequently share many common properties. Indeed all the Gaussian states can be produced through the four mentioned Gaussian operations. In the general case, one can write:

$$\hat{\rho}_{\text{gauss}} = \hat{D}(\alpha)\hat{S}(\zeta)\hat{\rho}_{th}\hat{S}^\dagger(\zeta)\hat{D}^\dagger(\alpha) \ , \tag{1.66}$$

which leads to a general Wigner function [9]

$$W_{\text{gauss}}(x,p) = \frac{1}{2\pi\sigma_x\sigma_p} e^{-\frac{(x-x_0)^2}{2\sigma_x^2} - \frac{(p-p_0)^2}{2\sigma_p^2}} \ . \tag{1.67}$$

Remarkably, any Gaussian state can be fully described with a real, symmetric and positive *covariance matrix* $\mathbf{\Sigma}$, which only contains first and second moments:

$$\mathbf{\Sigma}_{mn} = \Re[\overline{(\mathbf{X}_m - \overline{\mathbf{X}}_m)(\mathbf{X}_n - \overline{\mathbf{X}}_n)}] \ , \tag{1.68}$$

where

$$\mathbf{X} = \begin{pmatrix} \hat{x_1} \\ \hat{p_1} \\ . \\ . \end{pmatrix} \ , \quad \overline{\mathbf{X}} = \begin{pmatrix} \langle\hat{x_1}\rangle \\ \langle\hat{p_1}\rangle \\ . \\ . \end{pmatrix} \ . \tag{1.69}$$

For a single-mode Gaussian state with zero mean values, its covariance matrix simply reads

$$\mathbf{\Sigma} = \begin{pmatrix} \langle\hat{x}^2\rangle & \langle\frac{1}{2}\{\hat{x},\hat{p}\}\rangle \\ \langle\frac{1}{2}\{\hat{x},\hat{p}\}\rangle & \langle\hat{p}^2\rangle \end{pmatrix} \ . \tag{1.70}$$

1.5 Non-Gaussian states

Recently, non-Gaussian states of light attract more and more attention in the quantum computing and communication communities. Indeed, it has been shown that many operations require non-Gaussian states and operations [28]. For instance, non-Gaussian operations are required to distill Gaussian entanglement [29]. In this section, some commonly seen non-Gaussian states are introduced.

[9] With the help of rotation operation, it can cover all the single-mode Gaussian states.

1.5.1 Fock states

Fock states (also known as a *number states*) contain a well-defined number of photons, which can be generated from the vacuum state by iterative application of the creation operator [10].

Definition

$$|n\rangle = \frac{(\hat{a}^\dagger)^n}{\sqrt{n!}}|0\rangle \ . \tag{1.71}$$

Wave function

$$\langle n|x_\theta\rangle = e^{in\theta}\frac{1}{(\sqrt{2\pi}\sigma_0 2^n n!)^{1/2}} H_n\left(\frac{x}{\sigma_0\sqrt{2}}\right) e^{-x^2/4\sigma_0^2} \ , \tag{1.72}$$

with H_n the n-th Hermite polynomial.

Wigner function

$$W_{|n\rangle}(x,p) = \frac{(-1)^n}{2\pi\sigma_0^2} e^{-(x^2+p^2)/2\sigma_0^2} L_n\left(\tfrac{x^2+p^2}{\sigma_0^2}\right) \ . \tag{1.73}$$

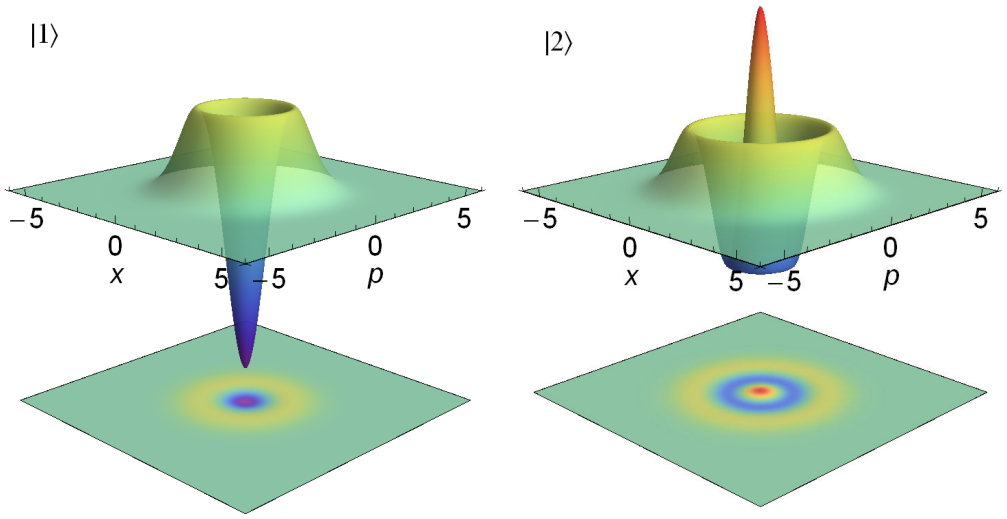

Figure 1.2: Wigner function of Fock states $|1\rangle$ (left) and $|2\rangle$ (right).

The corresponding plots are given in figure 1.2. From these Wigner functions, it is easy to see that the Fock states are phase invariant and as a consequence the marginal distributions do not depend on the phase.

1.5.2 Qubit state

A qubit is a quantum system having two distinct, that is, orthogonal, logical states. We label these states with a zero and a one, $|0\rangle$ and $|1\rangle$. And the *qubit state* can be expressed in the following form

$$|\psi\rangle = \cos(\frac{\theta}{2})\,|0\rangle + e^{i\varphi}\sin(\frac{\theta}{2})\,|1\rangle\,, \tag{1.74}$$

[10] Here we only consider *excited Fock states* with $n \geqslant 1$ for non-Gaussian states.

corresponding to a point with spherical polar coordinates θ and φ in the Bloch sphere. In particular, here we consider a photonic qubit where $|1\rangle$ and $|0\rangle$ are two Fock states, so the information is encoded in presence or absence of a single photon.

Definition We rewrite the state in the following form with two real numbers α and β ($\alpha^2 + \beta^2 = 1$) and a relative phase ϕ:

$$\alpha|0\rangle + \beta e^{i\phi}|1\rangle \ . \tag{1.75}$$

Wave function

$$\langle x_\theta|\psi\rangle = \frac{e^{-x_\theta^2/4\sigma_0^2}}{(\sqrt{2\pi}\sigma_0)^{1/2}}\left(\alpha + \beta\frac{x_\theta}{\sigma_0}e^{i(\theta+\phi)}\right). \tag{1.76}$$

Wigner function

$$W_{|\psi\rangle}(x,p) = \frac{1}{2\pi\sigma_0^2}e^{-(x^2+p^2)/2\sigma_0^2}\left[\alpha^2 + \beta^2\left(\tfrac{x^2+p^2}{\sigma_0^2} - 1\right) + 2\alpha\beta\tfrac{x}{\sigma_0}\right] \ . \tag{1.77}$$

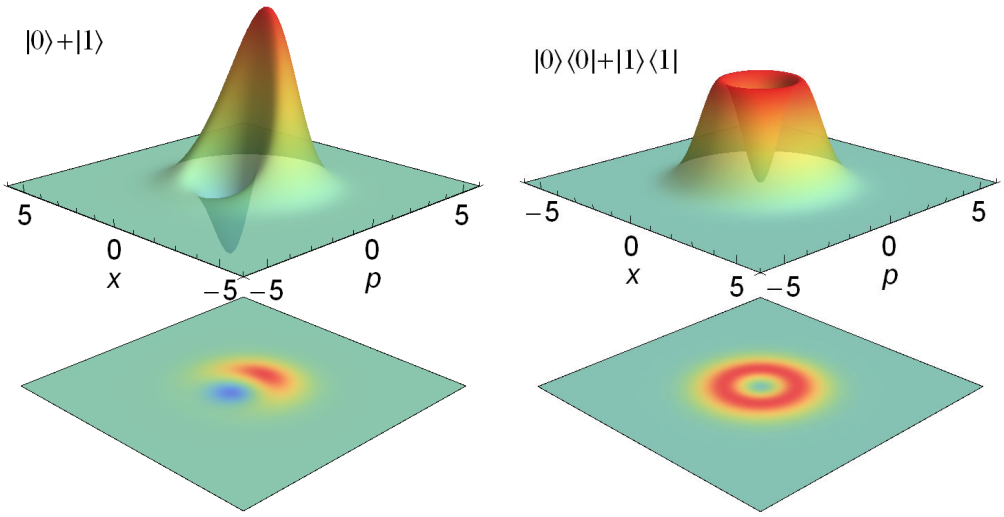

Figure 1.3: Wigner function of qubit state with equal weights (left) and equal mixture of vacuum and single-photon state (right).

The plot given in figure 1.3 corresponds a qubit state with equal weights ($\alpha = \beta = 1/\sqrt{2}$). The Wigner function of the qubit state is phase dependent, unlike the one of a statistical mixture of vacuum and single-photon state. Additionally the marginal distribution along the $p-$direction is asymmetric while the one along the $x-$direction is symmetric [11]. Such behavior is due to the cross terms (or coherence terms) $|1\rangle\langle 0|$ and $|0\rangle\langle 1|$.

Note that the negative part of the Wigner function of such a qubit state is preserved as long as $\beta > 0$. Since the state is pure, the *Hudson-Piquet theorem* states that it is indeed non-Gaussian. In contrast, the statistically mixed state of vacuum and single photon can

[11] As will be presented in Chapter 5, this property shows up quite often in the single-photon generation experiment due to the contamination by backscattered photons.

not keep the negativity of its Wigner function after 50% of loss [12]. However we can not immediately judge that it is Gaussian or not since it is a mixed state. In this case we can resort to a recently proposed witness for the quantum non-Gaussian character, which is only based on the knowledge of photon number probabilities, yet it can detect a wide class of states with positive Wigner functions that are not mixtures of Gaussian states [30]. It can been proven that the single-photon state after finite losses always keeps the non-Gaussian property.

1.5.3 Schrödinger cat state

Schrödinger's cat is a thought experiment, sometimes described as a paradox, devised by the Austrian physicist *Erwin Schrödinger* in 1935. It described a cat apparently held in a superposition of alive and dead states. Many researchers now refer the Schrödinger's cat state to a quantum state in a superposition of two highly distinguishable classical states. Here the Schrödinger cat state is considered as *coherent state superposition* (CSS), specifically, superposition of two coherent states with same amplitudes but opposite phases.

Definition

$$|cat_{\pm}\rangle = \tfrac{1}{N_{\pm}}(|\alpha\rangle \pm |-\alpha\rangle) \ , \tag{1.78}$$

where $|\alpha\rangle$ is a coherent state with an amplitude α and $\mathcal{N}_{\pm} = \sqrt{2(1 \pm e^{-2|\alpha|^2})}$ are the normalization factors. $|cat_{+}\rangle$ and $|cat_{-}\rangle$ denote the even and odd cat states, respectively.

Fock state expansion

$$\begin{aligned} |cat_{+}\rangle &= \frac{2}{\mathcal{N}_{+}} e^{-|\alpha|^2/2} \sum_{n=0}^{+\infty} \frac{\alpha^{2n}}{\sqrt{(2n)!}} |2n\rangle \\ |cat_{-}\rangle &= \frac{2}{\mathcal{N}_{-}} e^{-|\alpha|^2/2} \sum_{n=0}^{+\infty} \frac{\alpha^{2n+1}}{\sqrt{(2n+1)!}} |2n+1\rangle \ . \end{aligned} \tag{1.79}$$

We can see that the even (odd) cat state only contains even (odd) photon number states.

Wigner function

$$\begin{aligned} W_{|cat_{\pm}\rangle}(x,p) &= \frac{e^{-(x^2+p^2)/2\sigma_0^2}}{2\pi\sigma_0^2(1 \pm e^{-2\alpha^2})} \left[e^{-2\alpha^2} \cosh(2\alpha x/\sigma_0) \pm \cos(2\alpha p/\sigma_0) \right] \\ &= \frac{1}{1 \pm e^{-2\alpha^2}} \left[\frac{1}{2} W_{|\alpha\rangle}(x,p) + \frac{1}{2} W_{|-\alpha\rangle}(x,p) \pm W_{|0\rangle}(x,p) \cos(2\alpha p/\sigma_0) \right] \ , \end{aligned} \tag{1.80}$$

where the amplitude α is assumed to be real.

As shown in figure 1.4, the associated Wigner functions exhibit negativities. Also we can notice that the interference fringes occur in the $p-$quadrature direction due to the interference terms between $|\alpha\rangle$ and $|-\alpha\rangle$. This property makes the Schrödinger cat state strongly differ from a statistical mixture of two coherent states. The fringes become more pronounced when the amplitude increases. It is worth noting that for Schrödinger cat states with small amplitudes (also called "kitten" states), the even kitten state can be faithfully approximated with a squeezed vacuum with an appropriate squeezing; the odd kitten state

[12] Such state can been seen as a single-photon state after losses. When the losses exceed 50%, its Wigner function will lose its negativity, as shown in figure 1.3.

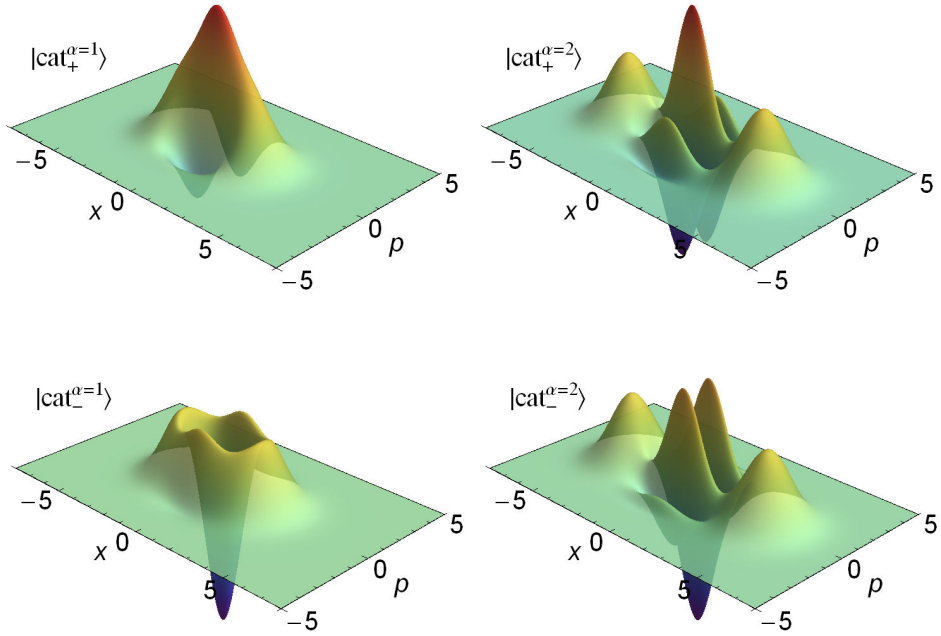

Figure 1.4: Wigner functions of the even cat states $|cat_+\rangle$ in the top line and odd cat states $|cat_-\rangle$ in the bottom line, for an amplitude $\alpha = 1$ on the left and $\alpha = 2$ on the right. The interference fringes between the two coherent state peaks at α and $-\alpha$ quickly become more pronounced when the amplitude increases.

is close to a squeezed single-photon state [13]. In Chapter 6 we will use protocols based on these approximations to experimentally generate Schrödinger kitten states.

1.6 Conclusion

In this chapter we gave a general description of quantum states following two different formalism: the density matrix and the Wigner function. Importantly the quantum states have been classified in two complementary classes: Gaussian states and non-Gaussian states. Gaussian states can be obtained with only Gaussian operations, while the realization of non-Gaussian states should resort to non-Gaussian operations, such as Kerr effect or photon subtraction. Both classes will be experimentally demonstrated in this thesis work. In the next chapter, we will first introduce the generation of Gaussian states, specifically squeezed vacuum states resulting from nonlinear frequency conversion.

[13] Squeezed single-photon state can be reformulated as single-photon-subtracted squeezed vacuum. Specifically, $\hat{a}\hat{S}(\zeta)|0\rangle = -\sinh(\zeta)\hat{S}(\zeta)|1\rangle$.

2 | Nonlinear Frequency Conversion

The invention of the laser triggers the fast development of nonlinear optics, which studies the response of media to strong optical fields. Nowadays nonlinear effects are investigated and applied over a wide range of energies and powers, from single-photons to zettawatts and above, and over broad spectral regimes, from THz to Gamma-ray frequencies. In this chapter we will only focus on *nonlinear frequency conversion* based on three-wave mixing, a well-known nonlinear process that leads to the generation of new optical frequencies. Such nonlinear interaction plays the key role in quantum optics experiments for quantum state preparation and manipulation.

We first give a general theoretical description of optical nonlinear conversion processes. Then several specific cases will be discussed, including *spontaneous down-conversion*, *coherent up-conversion* and *coherent down-conversion*. Since these processes have been widely studied in many textbooks [31, 32, 15] and PhD works [20, 33, 34], the aim of this chapter is to present and emphasize some important points for our further experiments, and provide a conceptual and experimental toolbox.

2.1 Introduction

The optical frequency conversion is a second-order process based on a nonlinear medium with a $\chi^{(2)}$ susceptibility. It can be divided into two complementary categories: *frequency down-conversion*, where a high frequency photon is "split" into two lower frequency photons with energy conservation; or *frequency up-conversion*, where two photons are "fused" into one of higher frequency. Since these processes always involve three modes, they are usually called *three-wave mixing*. The three-wave mixing can efficiently happen when the two following requirements are fulfilled:

$$\begin{aligned} \omega_3 &= \omega_1 + \omega_2 && \text{energy conservation} \\ \mathbf{k}_3 &= \mathbf{k}_1 + \mathbf{k}_2 && \text{momentum conservation,} \end{aligned}$$

where $\omega_{1,2,3}$ are the angular frequencies of the fields, and $\mathbf{k}_{1,2,3}$ the corresponding wave vectors. The second requirement is usually called *phase matching*. Typically the phase matching can be obtained by one of the two following methods:

- *Birefringence phase matching* : We can rewrite the phase matching condition as $\Delta k = n_1\omega_1 + n_2\omega_2 - n_3\omega_3 = 0$, where $n_{1,2,3}$ are the refractive indexes. Thanks to the birefringence feature of the medium (different refractive indexes for two polarizations), the difference due to dispersion can be compensated by the difference in phase velocity of orthogonally polarized waves. Practically, this can be obtained by rotating the crystal to a given angle (*angle tuning*), setting the crystal to a given temperature (*temperature tuning*), or both.
- *Quasi-phase matching* (QPM) : If no particular effort is made to match the refractive indexes, the conversion process will gradually shift to its complementary process after a so-called *coherence length*. As a result, there is no net nonlinear effect after propagation of twice the coherence length. In QPM materials, the nonlinear coefficient $\chi^{(2)}$ is periodically inverted every coherence length, so that the undesired process is suppressed and the desired process continues. QPM has many practical advantages: for instance, all the involved optical fields can propagate collinearly and can have the same polarization. This not only permits a much longer interaction length, but also enable to access the largest nonlinear coefficient of the material.

For a perfect nonlinear medium without loss and absorption, the Hamiltonian of three-wave mixing can be expressed as

$$\hat{\mathcal{H}} = i\hbar g(\hat{a}_1^\dagger \hat{a}_2^\dagger \hat{a}_3 + \hat{a}_1 \hat{a}_2 \hat{a}_3^\dagger) \ , \tag{2.1}$$

where g is a coupling constant determined by the second-order susceptibility of the nonlinear material. The first coupling term ($\hat{a}_1^\dagger \hat{a}_2^\dagger \hat{a}_3$) corresponds to the down-conversion process while the Hermitian conjugate term corresponds to the opposite process, i.e. up-conversion. Interestingly, regardless of these processes, there are conversion laws about the photon number operator $\hat{N}_i = \hat{a}_i^\dagger \hat{a}_i$. It is easy to check that $\hat{N}_1 - \hat{N}_2$, $\hat{N}_1 + \hat{N}_3$, $\hat{N}_2 + \hat{N}_3$ and $\hat{N}_1 + \hat{N}_2 - 2\hat{N}_3$ are invariant during the evolution of the system. These conservation laws are also called the *Manley-Rowe relations* and tell us that the photons in mode 1 and 2 are always pairwise created (or destroyed) as a consequence of a photon creation (or destruction) in mode 3. Such an intriguing behavior will be more elaborated in the next section.

2.2 Spontaneous down-conversion

It can be rigorously called *spontaneous parametric down-conversion* (also known as *SPDC* or *parametric fluorescence*). This is a very special case among the three-wave mixing processes

since classically it seems to only involve one pump field. The down-converted photon pairs are indeed created from the vacuum, a phenomenon that can only be explained by quantum optics. In this section, we will show that the down-converted photons pairs are strongly correlated.

2.2.1 Theoretical description

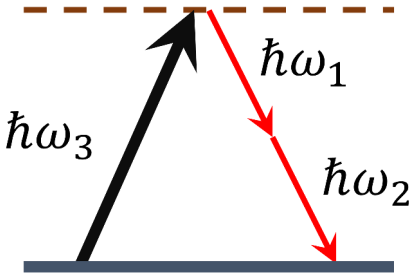

Figure 2.1: Simple scheme for spontaneous parametric down-conversion. Disappearance of one pump photon leads to the simultaneously creation of two photons, usually called signal and idler.

In order to investigate the dynamics of spontaneous down-conversion as shown in figure 2.1, we resort to the interaction Hamiltonian as

$$\hat{\mathcal{H}}_{int} = i\hbar g \hat{a}_1^\dagger \hat{a}_2^\dagger \hat{a}_3 - h.c. \ , \tag{2.2}$$

where $h.c.$ denotes the Hermitian conjugate. In the non-degenerate case, the down-converted photons often refer to "signal" and "idler" photons for historical reasons. In the case of a strong coherent pump field, there is negligible depletion of the pump power. Hence the amplitude of the pump field can be classically treated as $\langle \hat{a}_3 \rangle = \alpha$. With this assumption the Hamiltonian can be simplified as

$$\hat{\mathcal{H}}_{int} = i\hbar\kappa \hat{a}_1^\dagger \hat{a}_2^\dagger - h.c. \qquad \text{where } \kappa = g\alpha \ , \tag{2.3}$$

therefore, resulting in:

$$\frac{d}{dt}\hat{a}_{1,2} = -\frac{i}{\hbar}[\hat{a}_{1,2}, \mathcal{H}_{int}] = \kappa \hat{a}_{2,1}^\dagger \ . \tag{2.4}$$

This leads to the evolution equations for this parametric process:

$$\begin{aligned} \hat{a}_1(t) &= \hat{a}_1(0)\cosh(\zeta) + \hat{a}_2^\dagger(0)\sinh(\zeta) \ , \\ \hat{a}_2(t) &= \hat{a}_2(0)\cosh(\zeta) + \hat{a}_1^\dagger(0)\sinh(\zeta) \ . \end{aligned} \tag{2.5}$$

where $\zeta = \kappa t$ (we will see later it is actually the squeezing parameter).

Using the expressions for the quadrature operators (with the convention $\sigma_0 = 1$):

$$\begin{aligned} \hat{x} &= \hat{a}^\dagger + \hat{a} \\ \hat{p} &= i(\hat{a}^\dagger - \hat{a}) \ , \end{aligned} \tag{2.6}$$

we can get the following correlations between the two-mode quadrature observables

$$\begin{aligned} \hat{x}_1(t) \pm \hat{x}_2(t) &= [\hat{x}_1(0) \pm \hat{x}_2(0)]e^{\pm\zeta} \\ \hat{p}_1(t) \pm \hat{p}_2(t) &= [\hat{p}_1(0) \pm \hat{p}_2(0)]e^{\mp\zeta} \ . \end{aligned} \tag{2.7}$$

Initially, the two modes are both in vacuum states and the quadrature observables in these modes are uncorrelated. But after a certain interaction time, there appear correlation between the position observables and anti-correlation between the momentum observables. This property is the basis of the famous *EPR paradox* [35], thus the generated state is also called *EPR* state.

We can write down the evolution operator for this spontaneous down-conversion process:

$$\hat{S}_{12}(\zeta) = e^{-\frac{\hat{\mathcal{H}}t}{i\hbar}} = e^{\zeta(\hat{a}_1\hat{a}_2 - \hat{a}_1^\dagger\hat{a}_2^\dagger)} \ , \tag{2.8}$$

which is usually called *two-mode squeezing operator*, as introduced in Chapter 1.

For better illustrating the squeezing feature, we can consider the simpler degenerate case. With $\hat{a}_1 = \hat{a}_2 = \hat{a}$ we obtain

$$\hat{a}(t) = \hat{a}(0)\cosh(\kappa t) + \hat{a}^\dagger(0)\sinh(\kappa t) \ . \tag{2.9}$$

Similarly, we can get the evolution of the quadrature operators as:

$$\begin{aligned} \hat{x}(t) &= \hat{x}(0)e^{-\zeta} \\ \hat{p}(t) &= \hat{p}(0)e^{\zeta} \ , \end{aligned} \tag{2.10}$$

from which we deduce a so-called *squeezing factor* $s = e^{-2\zeta}$. The evolution operator in this case becomes the squeezing operator $\hat{S}(\zeta) = e^{\zeta(\hat{a}^2 - \hat{a}^{\dagger 2})}$, also presented in Chapter 1.

Additionally, we can use the intensity correlation function $g^{(2)}(0)$ to study the photon statistics of the down-converted light. For the light produced from an initial vacuum state, we have

$$\begin{aligned} g^{(2)}(0) &= \frac{\langle \hat{a}^\dagger(t)\hat{a}^\dagger(t)\hat{a}(t)\hat{a}(t)\rangle}{\langle \hat{a}^\dagger(t)\hat{a}(t)\rangle^2} \\ &= 3 + \frac{1}{\sinh^2\zeta} \ . \end{aligned} \tag{2.11}$$

This expression indicates that the generated squeezed vacuum state exhibits *photon bunching effect* ($g^{(2)}(0) > 1$). This feature is well expected as the state must contain pairs of photons.

2.2.2 Optical parametric oscillator

Obtaining a strong nonlinear effect usually requires a large nonlinear coefficient and an intense pump power. Therefore, one possible way to enhance the nonlinear effect is to use nonlinear mediums with QPM structures or resort to new nonlinear materials. The other way is to enhance the pump power either by using a pulsed pump or utilizing a cavity for pump recycling. To work in the continuous-wave regime, the second solution is required. By inserting a nonlinear crystal into a resonant cavity, one forms a so-called *optical parametric oscillator* (or OPO). Figure 2.2 shows an OPO sketch.

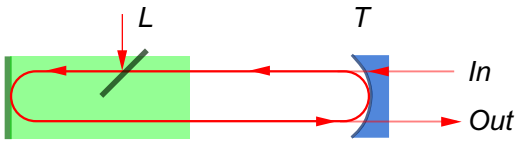

Figure 2.2: Loop of the fields inside the OPO cavity. L denotes the intra cavity losses, T stands for the transmittance of the output coupler. "In" represents the input field (a priori vacuum) and "Out" denotes the output field.

To describe the dynamical relationships of the fields inside the cavity, we use the following notations:

— T intensity transmission of the output coupler

— L intra-cavity loss

— τ round-trip time

— $\mathfrak{g}$ effective nonlinear gain

For the degenerate case and under the assumption of a strong coherent pump field, the dynamical relationship after one round-trip is given by [20]

$$\tau\frac{d\hat{a}(t)}{dt} = -(T'/2)\hat{a}(t) + \mathfrak{g}|\alpha|\hat{a}^\dagger(t) + \sqrt{L}\hat{a}_L(t) + \sqrt{T}\hat{a}_{\text{in}}(t) \ , \tag{2.12}$$

where $T' = L+T$, $\hat{a}$ the signal mode in the cavity, $\hat{a}_p$ the pump mode, $\hat{a}_L$ the mode coupled to the vacuum by the loss, and $\hat{a}_{\text{in}}$ the input mode outside of the cavity. The first and second terms in the right side of the equation correspond to annihilate and create a photon in the signal mode, respectively. Therefore, there exists a pumping threshold α_{th} where the gain compensates the cavity losses: $-T'/2 + \mathfrak{g}|\alpha|_{\text{th}} = 0$. Consequently, we can introduce a parameter $\varepsilon = |\alpha|/|\alpha|_{\text{th}} = |\alpha|2\mathfrak{g}/T'$ defined as the ratio of the pump to the threshold, which can be interpreted as the pumping strength.

In order to investigate the noise spectrum of the OPO output, we use the following rotation to obtain the quadrature observable

$$\hat{x}(t) = e^{-i\theta}\hat{a}(t) + e^{i\theta}\hat{a}^\dagger(t) \ , \tag{2.13}$$

where $\theta = \omega t + \phi_p/2$ and use the convention $\sigma_0 = 1$. This yields to the loop equation for the quadrature observable:

$$\tau\frac{d\hat{x}(t)}{dt} = -T'/2\hat{x}(t) + \mathfrak{g}|\alpha|\hat{x}(t) + \sqrt{L}\hat{x}_L(t) + \sqrt{T}\hat{x}_{\text{in}}(t) \ . \tag{2.14}$$

After a Fourier transformation, we get

$$(1 + \varepsilon - i\omega/\omega_c)\,\hat{x}(\omega) = \tfrac{\sqrt{L}}{T'/2}\hat{x}_L(\omega) + \tfrac{\sqrt{T}}{T'/2}\hat{x}_{\text{in}}(\omega) \ , \tag{2.15}$$

where $\omega_c = T'/(2\tau)$ corresponds to the bandwidth of the cavity.

The following relation enables us to access the quadrature of the output mode

$$\hat{x}_{\text{out}} = \sqrt{T}\hat{x} - \sqrt{1-T}\hat{x}_{\text{in}} \ . \tag{2.16}$$

With the help of equations (2.15), (2.16) and the fact $\hat{x}_L(\omega)$, $\hat{x}_{\text{in}}(\omega)$ act on vacuum, we can finally obtain the spectral density of noise $s_x = \langle\hat{x}_{\text{out}}(\omega)\hat{x}_{\text{out}}(-\omega)\rangle$:

$$\begin{aligned} s_x(\omega) &= 1 + \eta\frac{4\varepsilon}{(1-\varepsilon)^2 + 4(\omega/\omega_c)^2} \\ s_p(\omega) &= 1 - \eta\frac{4\varepsilon}{(1+\varepsilon)^2 + 4(\omega/\omega_c)^2} \ , \end{aligned} \tag{2.17}$$

where $\eta = T/(T+L)$ is the *escape efficiency* of the OPO. This very important quantity gives the probability for a generated photon to go out of the cavity and not to disappear due to the losses.

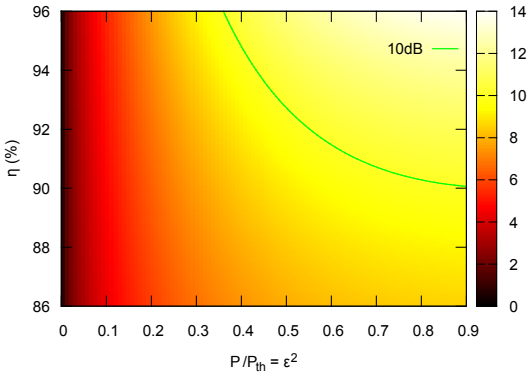

Figure 2.3: Squeezing map as a function of the normalized pump power P/P_{th} and escape efficiency η. The green contour line shows the boundary for obtaining 10 dB squeezing. The analysis frequency ω is 0.

Figure 2.3 gives the squeezing map versus the pump power and escape efficiency at zero analysis frequency. The green line shows the boundary for obtaining 10 dB squeezing. It is important to stress that the escape efficiency impose the limit for the squeezing that one can maximally obtain by increasing the pump power. For instance, to get 10 dB, the escape efficiency should be higher than 90%. This is clear with the help of equation (2.17), $s_-^{max} = s_-(\omega = 0, \varepsilon = 1) = 1 - \eta$. In addition, we can also notice that for a low escape efficiency, the squeezing increase slowly with the pump power. The evolution is more significant for larger escape efficiency.

Another important aspect for squeezed state is its purity, which is defined as $P = 1/\sqrt{s_+ s_-}$ as for any Gaussian states. As shown in figure 2.4, the purity of the state decreases with the pump power. When the pump power goes to the threshold, the purity degrades to zero since the anti-squeezing diverges to $+\infty$. Also, it is worth noting that larger escape efficiency provides higher purity for a given pump power.

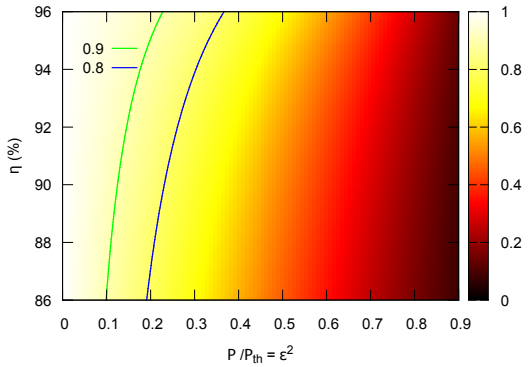

Figure 2.4: Purity map of squeezed light as a function of the normalized pump power P/P_{th} and escape efficiency η . The analysis frequency ω is 0.

In a nutshell, high escape efficiency indicates a "good" OPO.

2.2.3 Building an OPO

In terms of cavity design, there exits many methods to conceive OPOs for generating squeezed light. Bow-tie configuration is used in many experiments as it offers many degrees of freedom for alignment and phase matching, many injection and output ports and single-direction propagation. Ref. [36] employed this cavity configuration and observed 9 dB squeezing at 860 nm. Due to the relative long cavity length (a nonlinear crystal and four mirrors are needed), the squeezing bandwidth is however very often limited around 10 MHz. For obtaining a broader bandwidth but also reduced losses, monolithic OPO provides a solution where both end surfaces of the crystal are polished and mirror-coated. Addi-

tionally, it has extremely low intracavity losses due to the absence of extra optical elements in the cavity. So far the highest squeezing level was reported to be -11.5 dB in R. Schnabel's group with a bandwidth of about 170 MHz [37]. However, it is quite challenging for a monolithic OPO to simultaneously satisfy the conditions of cavity resonance and phase matching. Therefore, as a compromised case, a semi-monolithic configuration is often used in the experiment, where the cavity is formed by one of the crystal ends and a curved bulk coupling mirror [38]. We use this specific scheme both for type-I and type-II [1] OPOs as shown in figure 2.5.

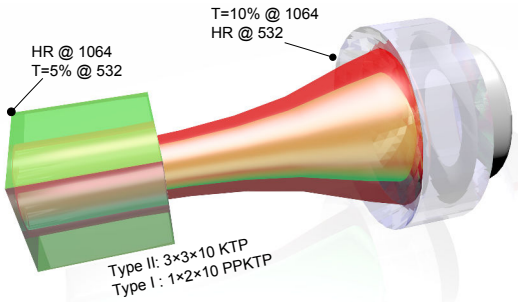

Figure 2.5: Configuration of a semi-monolithic OPO. The cavity is formed by one end face of crystal and a curved output mirror with a radius of curvature of 38 mm.

Coating The OPO is made of a semi-monolithic linear cavity. One face of the crystal is directly coated with an intensity reflection of 95% for the 532 nm pump and high reflection at 1064 nm. A mirror with 38-mm radius of curvature is used for output coupler, which has a reflection of 90% for the infrared and is highly reflective for the pump. Therefore, the free spectral range $\mathcal{I}$ is about 4 GHz. With an estimation of 0.5% of intracavity losses, we can obtain a cavity finesse $\mathcal{F} = 60$, which finally gives us the cavity bandwidth $\Delta = 60$ MHz. Additionally the escape efficiency is thus given by $\eta = T/(T + L) \approx 95\%$.

Pump source The pump source at 532 nm is from a continuous-wave frequency-doubled Nd:YAG laser at 1064 nm. Actually, both the pump light and seed light are directly accessible from our laser system [2].

Phase matching As explained at the beginning of this chapter, there are two possible ways to realize phase matching with birefringent crystals: angle tuning and temperature tuning. In our case of a semi-monolithic configuration, it is not possible to tilt the crystal to obtain the phase matching. As described in [20, 33], phase-matching condition around the room temperature can be realized by optimizing the crystal cutting angle. Usually the acceptable bandwidth of phase matching is about 10°C, which makes it possible to simultaneously achieve the aforementioned cavity resonance with the help of other degrees of freedom.

Resonance The OPOs used in our experiment are resonant for all the interacting fields, resulting in a threshold as low as 50 mW. Specifically, for type-I OPO, the cavity is set on resonance both for the signal and the pump by adjusting the cavity length via a PZT and the crystal temperature. For type-II OPO, there are three involved modes: signal and idler with orthogonal polarizations, and the pump. The triple resonance is thus more difficult to achieve since it needs another degree of freedom. As the cavity is semi-monolithic, the angle of the crystal is fixed for all the beams with a normal incidence. Fortunately, by tuning the temperature of the crystal in the Nd:YAG laser, we can modify the output laser frequency,

[1] Type-I phase matching: $o \longleftrightarrow e + e$ Type-II phase matching: $e \longleftrightarrow o + e$
[2] Diabolo Laser from Innolight

which gives the possibility to obtain the triple resonance. However this method has two problems. First the tuning process is slow. Second the tuning range is limited (about 6 GHz/K). Indeed for some crystals, the triple resonance condition cannot be found, it is then necessary to change the incident point on the crystal.

Locking Since the cavity is resonant for all modes, in principle we can use any of them to lock the cavity. We choose to use the pump to lock the cavity, otherwise it would be necessary to inject an additional infrared seed beam. The length of the cavity is locked by using the Pound-Drever-Hall technique (12 MHz phase modulation frequency). Thanks to the microcontroller-based hybrid locking system (which will be detailed in Chapter 4), the cavity locking is totally automatic.

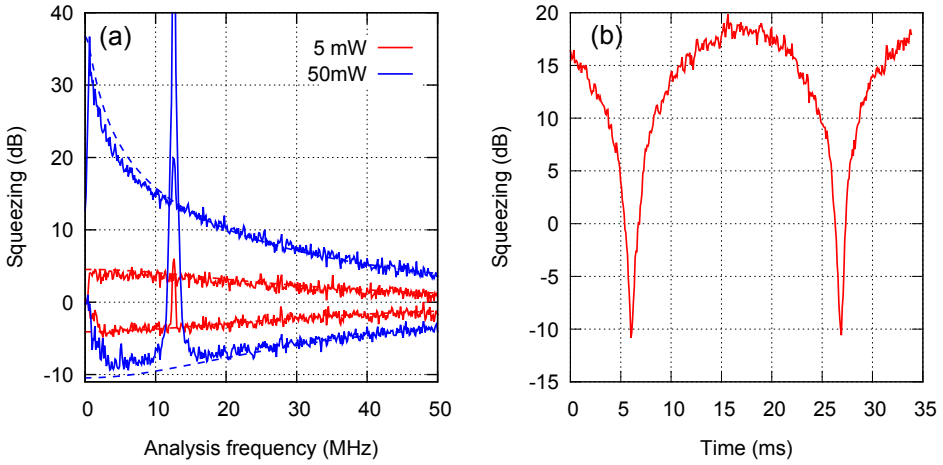

Figure 2.6: (a) Squeezing and anti-squeezing versus analysis frequency for different values of the pump power. The dashed line is theoretical fitting using equation (2.17) with parameters $\eta = 91\%$ and ω_c=65 MHz. All traces are normalized to the vacuum noise. (b) Arches of squeezing when the phase of the local oscillator is scanned, at pump power P= 40 mW. The trace is recorded at a Fourier frequency of F = 4 MHz with a resolution bandwidth RBW = 300 kHz and a video bandwidth VBW = 3 kHz, and it is normalized to the vacuum noise.

Results The highest measured squeezing in our experiment occurs close to the threshold $P_{\text{th}} = 50$ mW. Figure 2.6(a) shows the corresponding squeezing and anti-squeezing as a function of the analysis frequency. The theoretical curves are fitted according to equation (2.17), with a global efficiency of $\eta = 91\%$ and a bandwidth of ω_c=65 MHz. The recorded arches of squeezing at an analysis frequency of 4 MHz are shown in figure 2.6(b) when the phase of local oscillator is scanned. The measured squeezing as high as 10.5 dB indicates overall losses below 10%. After correction for the propagation and detection losses of 93%, we estimate a squeezing of 16.5 dB at the output of the OPO.

It is worth noting that even though many state engineering protocols don't need so high level of squeezing (3dB is very often enough), the maximum squeezing obtained here is not useless. Indeed the maximum squeezing an OPO can obtain indicates how "good" an OPO is as it is related to the escape efficiency, as stressed previously. Better is an OPO, purer is the output squeezing at a specific level. In figure 2.6(a), we also give the case of $P = 5$ mW, showing a high-purity 3 dB squeezing over a bandwidth of 30 MHz. Such a pure squeezed state will be an essential source for our experiments.

2.3 Coherent frequency up- and down-conversion

Besides of generating squeezed light, nonlinear frequency conversion has also great potential for manipulating and controlling quantum states. For instance, *coherent frequency up-conversion* is essentially a *sum frequency generation* (SFG) process where a signal photon is translated to the one with a higher frequency while completely preserving all the quantum characteristics [39]. Such coherent conversion can be used as a photonic quantum information interface, which plays a critical role in the development of future quantum networks [40]. For example, photons at telecommunications wavelengths of 1310 nm and 1550 nm are preferable to transmit information in optical fibers for distribution over long distances. However, efficient quantum memories typically are realized with alkaline atoms, which require wavelengths near 800 nm. Hence in order to bridge the spectral gap between the channels for quantum communication and nodes for storage and quantum processing, quantum interfaces are required. Here we will introduce a photonic interface based on coherent frequency up-conversion.

2.3.1 Coherent up-conversion

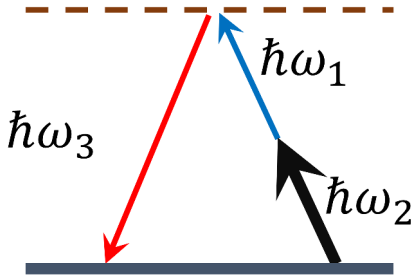

Figure 2.7: Simple scheme of coherent frequency up-conversion process where a single photon at ω_1 is annihilated with the creation of a higher energy photon at ω_3. Since the pump at ω_2 is strong, this process can be seen as a one-to-one conversion.

Figure 2.7 depicts a simple scheme of the coherent frequency up-conversion process where a single photon at ω_1 is annihilated with the creation of a higher energy photon at ω_3. Since the pump field at ω_2 is strong, this process can be seen as a one-to-one conversion. For describing the evolution of this conversion process, we can revisit the equation (2.1) and focus on the up-conversion part of the interaction Hamiltonian:

$$\hat{\mathcal{H}}_{int} = i\hbar g \hat{a}_1 \hat{a}_2 \hat{a}_3^\dagger - h.c. \ . \tag{2.18}$$

If the pump field is very strong with negligible depletion, we can classically treat the operator for pump mode as $\langle \hat{a}_2 \rangle = \alpha$. With this assumption the Hamiltonian can be simplified as

$$\hat{\mathcal{H}}_{int} = i\hbar\kappa \hat{a}_1 \hat{a}_3^\dagger - h.c. \qquad \text{where } \kappa = g\alpha \ . \tag{2.19}$$

The evolution equation is thus given by

$$\frac{d}{dt}\hat{a}_{1,3} = -\frac{i}{\hbar}[\hat{a}_{1,3}, \mathcal{H}_{int}] = \kappa \hat{a}_{3,1} \ . \tag{2.20}$$

This leads to the evolution equations for this conversion process:

$$\begin{aligned} \hat{a}_1(t) &= \hat{a}_1(0)\cos(\kappa t) + \hat{a}_3(0)\sin(\kappa t) \\ \hat{a}_3(t) &= \hat{a}_3(0)\cos(\kappa t) - \hat{a}_1(0)\sin(\kappa t) \ . \end{aligned} \tag{2.21}$$

Compared to equations (2.5) for spontaneous parametric down-conversion, here there is no creation operator in the evolution equation, which means that no spurious "noisy" photon is generated during the process. After an interaction time fulfilling $\kappa t_c = \pi/2$, we can get $\hat{a}_1(t_c) = \hat{a}_3(0)$ and $\hat{a}_3(t_c) = \hat{a}_1(0)$, which shows a complete state transfer from one frequency to the other.

Let us elaborate this property with a simple example. Assuming initially there is no photon in the SFG mode 3, and a single-photon state in the signal mode 1, hence the initial state can be expressed as $|\psi\rangle = |1,0\rangle_{1,3} = \hat{a}_1^\dagger|0,0\rangle_{1,3}$. After an amount of time t_c, the finally state is $|\psi\rangle_{t_c} = \hat{a}_3^\dagger|0,0\rangle_{1,3} = |0,1\rangle_{1,3}$. Clearly the single photon state at low frequency ω_1 is completely transferred to the one at higher frequency ω_3 .

Interestingly, from equation (2.21) we can notice that the coherent up-conversion process is actually a beam splitter with a transmittance $t = \cos\kappa t$ and a reflectance $r = \sin\kappa t$ [41]. Continuing with the above example, we can see that generally after a time t the final state is $|\psi\rangle_t = (t\hat{a}_1^\dagger + r\hat{a}_3^\dagger)|0,0\rangle_{1,3} = t|0,1\rangle_{1,3} + r|1,0\rangle_{1,3}$. It is a single-photon entangled state spanning between two colors.

With an initial state $|\psi\rangle = |\phi\rangle_1 \otimes |0\rangle_3$, the evolution of the average photon number in the signal mode 1 is given by

$$\begin{aligned} N_1(t) &= \langle\psi|\hat{a}_1^\dagger(t)\hat{a}_1(t)|\psi\rangle \\ &= t^2\langle\phi|\hat{a}_1^\dagger(0)\hat{a}_1(0)|\phi\rangle \\ &= t^2 N_1^0 \ , \end{aligned} \tag{2.22}$$

where N_1^0 denotes the average photon number of the input signal. Similarly, the average photon number for the SFG mode 3 is

$$N_3(t) = r^2 N_1^0 \ . \tag{2.23}$$

It is easy to check $N_1(t) + N_3(t) = N_1^0$. Hence a *conversion efficiency* can be defined as

$$\eta = \frac{N_3(t)}{N_1^0} = r^2 = \sin^2\kappa t = \sin^2(\sqrt{\frac{P}{P_c}}) \ , \tag{2.24}$$

where P_c is the pump power for the complete conversion. The evolution of average photon number with the pump power is illustrated in figure 2.8. We notice that the conversion efficiency shows an oscillation behavior with the increase of pump power.

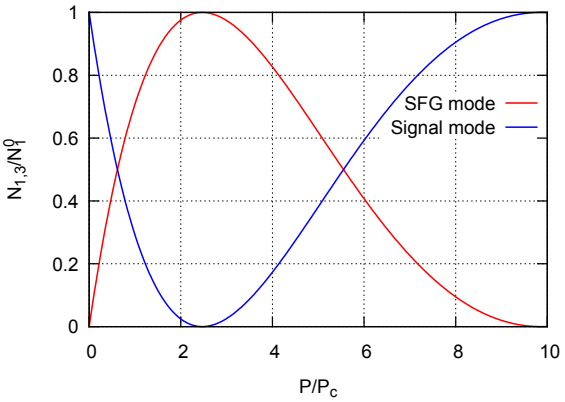

Figure 2.8: The correlation between average photon numbers in SFG mode 3 and signal mode 1.

The joint probability P_{13} of simultaneously detecting a photon in mode 1 and mode 3 at

the frequency converter is given by

$$\begin{aligned} P_{13} &\propto \langle \hat{a}_1^\dagger(t)\hat{a}_3^\dagger(t)\hat{a}_3(t)\hat{a}_1(t)\rangle \\ &= (\langle \hat{n}_0^2\rangle - \langle \hat{n}_0\rangle)\eta(1-\eta) \ , \end{aligned} \tag{2.25}$$

which depends on the conversion efficiency and has a maximum value at 50% efficiency.

Additionally the *intensity cross-correlation function* at zero delay is obtained by

$$g_{13}^{(2)}(0) = \frac{\langle \hat{n}_1\hat{n}_3\rangle}{\langle \hat{n}_1\rangle\langle \hat{n}_3\rangle} = \frac{\langle \hat{n}_0^2\rangle - \langle \hat{n}_0\rangle}{\langle \hat{n}_0\rangle^2} = g_0^{(2)}(0) \ , \tag{2.26}$$

where $g_0^{(2)}(0)$ is the intensity auto-correlation function [3] for the initial state in the single mode. Note that the cross-correlation function does not depend on the conversion efficiency. It is expected by noticing that the frequency conversion process acts as a beam-splitter. The cross-correlation function $g_{13}^{(2)}(0)$ between the converted and unconverted mode is equivalent to the auto-correlation function $g^{(2)}(0)$ of the input quantum state. Since $g^{(2)}(0)$ is invariant to the beam-splitting ratio (cf. Appendix B), hence $g_{13}^{(2)}(0)$ is independent of conversion efficiency. In particular, if the input state is a single-photon state, $g_{13}^{(2)}(0) = 0$; if the input is a coherent state, $g_{13}^{(2)}(0) = 1$.

2.3.2 Multimode regime

In this section, we will consider a more general case where both pump and signal have multi-longitudinal modes. This is the case of coincidence pumping frequency up-conversion that will be used in one of our experiments (cf. Chapter 8). In this case, the frequency conversion process becomes much more complicated due to the commutative coupling between the pump and signal modes. The corresponding Hamiltonian can be reformulated as

$$\hat{\mathcal{H}}_{int} = i\hbar g \sum_{ij} \alpha_i(\hat{a}_{1j}\hat{a}_{3ij}^\dagger + h.c.) \ , \tag{2.27}$$

where we assume that the nonlinear coupling coefficient is constant and all the modes are in the phase-matching window. α_i is the pump filed related to each longitudinal mode numbered by i; $\hat{a}_{1j}$ is the annihilation operator of signal photons related to longitudinal mode labeled by j; and $\hat{a}_{3ij}^\dagger$ is the creation operator of SFG photons related to the longitudinal modes of both pump and signal fields. Then the dynamics of the involved modes is given by the coupled mode equations as

$$\begin{aligned} \frac{d}{dt}\hat{a}_{1j} &= -\frac{i}{\hbar}[\hat{a}_{1j}, \mathcal{H}_{int}] = g\sum_i \alpha_i \hat{a}_{3ij} \\ \frac{d}{dt}\hat{a}_{3ij} &= -\frac{i}{\hbar}[\hat{a}_{3ij}, \mathcal{H}_{int}] = g\alpha_i \hat{a}_{1j} \ . \end{aligned} \tag{2.28}$$

It is convenient to introduce the following annihilation operators corresponding to the supermodes of signal and SFG fields [42, 43]:

$$\begin{aligned} \hat{a}_1 &= \sum_j \hat{a}_{1j} \\ \hat{a}_3 &= \sum_{ij} c_i \hat{a}_{3ij} \ , \end{aligned} \tag{2.29}$$

[3] The intensity auto-correlation function at zero is defined as

$$g^{(2)}(0) = \frac{\langle \hat{a}^\dagger(t)\hat{a}^\dagger(t)\hat{a}(t)\hat{a}(t)\rangle}{\langle \hat{a}(t)^\dagger\hat{a}(t)\rangle^2} = \frac{\langle \hat{n}^2\rangle - \langle \hat{n}\rangle}{\langle \hat{n}\rangle^2} \ .$$

where $c_i = \alpha_i/\alpha$ and $\alpha^2 = \sum_i \alpha_i^2$ ($\alpha \in \mathbb{R}$), which means that each probability amplitude is weighted by its corresponding pump field amplitude. This leads to the evolution equations for the conversion process:

$$\begin{aligned} \hat{a}_1(t) &= \hat{a}_1(0)\cos(\kappa t) + \hat{a}_3(0)\sin(\kappa t) \\ \hat{a}_3(t) &= \hat{a}_3(0)\cos(\kappa t) - \hat{a}_1(0)\sin(\kappa t) \ , \end{aligned} \tag{2.30}$$

which is exactly the same as equation (2.21) in the single-mode regime. It indicates that we can coherently manipulate the SFG output field by classical modification of the pump fields. This is very desirable for quantum state engineering and control. Indeed it has been shown that with proper dispersion engineering of the converter, a quantum pulse gate can be realized [41]. Additionally, using a pump field with specific phase chirping, one can effectively compress a chirped single photon while keeping the quantum properties and coherence [44].

In the next section, we will introduce a complementary process for quantum state manipulation, i.e. coherent frequency down-conversion.

2.3.3 Coherent down-conversion

Although experimental demonstrations of coherent up-conversion are very successful since the late 90's [39], the opposite process, i.e. coherent down-conversion, has been proposed and experimentally demonstrated only very recently [45, 46]. As we already know, there is a mismatch between the atomic transition wavelength for quantum memory and optical transmission wavelength for information distribution in optical fiber [47, 48]. Quantum interface based on coherent down-conversion can turn to be a critical resource for building a quantum network [49, 50].

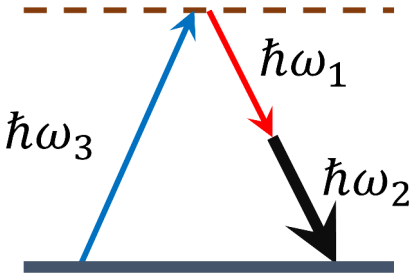

Figure 2.9: Simple scheme of coherent down up-conversion process where a single photon at ω_3 is annihilated with the creation of a higher energy photon at ω_1. Since the pump at ω_2 is strong, the spontaneous emission for frequency down-conversion is negligible, which leads to a noiseless frequency down-conversion.

It is commonly believed that frequency down-conversion is noisy and cannot preserve quantum coherence because the appearance of the $\hat{a}^\dagger$ terms in equation (2.5) leads to spontaneous quantum noise. Therefore quantum frequency down-conversion cannot be realized with three-wave mixing process. However, there is another operation regime as shown in figure 2.9. Here we inject a strong field at lower frequency ω_2 instead of higher frequency ω_3 as in spontaneous down-conversion process. This process will not be encountered as a parametric amplification for signal field due to the gain saturation. In the other words, the amplification of the strong signal field at ω_2 requires more energy from the pump field at ω_3, which eventually will be depleted.

For describing this specific case, we can use the Hamiltonian of three-wave mixing (2.1) and focus on the down-conversion part:

$$\hat{\mathcal{H}}_{int} = i\hbar g \hat{a}_1^\dagger \hat{a}_2^\dagger \hat{a}_3 - h.c. \ . \tag{2.31}$$

In our case, the approximation $\langle \hat{a}_2 \rangle = \alpha$ is valid, which results in

$$\hat{\mathcal{H}}_{int} = i\hbar\kappa \hat{a}_1^\dagger \hat{a}_3 - h.c. \qquad \text{where } \kappa = g\alpha \ . \tag{2.32}$$

The first term in this equation shows that the annihilation of a photon at ω_3 will lead to the creation of a photon at ω_1 with lower energy. If we write down the full expression of the interaction Hamiltonian, we can realize that it is the same as the one used for coherent up-conversion (2.19). Indeed we just emphasize the different parts of this coupling Hamiltonian that originally includes the two processes, up- and down-conversion. Therefore, it is natural to obtain the same dynamics equations:

$$\hat{a}_1(t) = \hat{a}_1(0)\cos(\kappa t) + \hat{a}_3(0)\sin(\kappa t)$$
$$\hat{a}_3(t) = \hat{a}_3(0)\cos(\kappa t) - \hat{a}_1(0)\sin(\kappa t)\ .$$

Interestingly we can show that the conversion direction depends on the initial state. As we already demonstrated, if the initial state is in $|\psi\rangle = |1,0\rangle_{1,3}$, we will get $|\psi\rangle_{t_c} = |0,1\rangle_{1,3}$. This is the up-conversion process. Now if we set the initial state in $|\psi\rangle = |0,1\rangle_{1,3}$, then we have $|\psi\rangle_{t_c} = |1,0\rangle_{1,3}$, which is the down-conversion process. This is not difficult to understand if we notice the photon-number oscillation behavior during the up-conversion process as shown in figure 2.8. When the pump power reaches the complete up-conversion conversion point at P_c, the reverse process, down-conversion, will start.

Coherent down-conversion not only allows a quantum conversion of a state to lower frequency, but also permits a realization of a full quantum frequency translation that we will present right now.

2.3.4 Quantum frequency translation

Ideally, *quantum frequency translation* (QFT) should satisfy the following requirements [51]:

— Allow translation by any small or large frequency shift (usually in the visible and near infrared regimes).

— Preserve the full quantum properties of the original state, e.g., coherence, and entanglement.

— Must be highly efficient while not introducing additional spurious "noise" photons.

QFT based on the three-wave mixing (either coherent up-conversion or coherent down-conversion) can only satisfy the latter two requirements. For example, if we rely on a quantum memory [4] that absorbs and emits at a 795-nm wavelength, and we want to store photons at 808 nm [5], it is not possible to directly use the above mentioned converter due to the small difference between the signal and target frequencies. One solution is to use *four-wave mixing* (FWM) where the two pump fields are designed to have a frequency difference equal to that by which one aims to translate the quantum state of interest [51]. An alternative solution is to combine the aforementioned coherent up- and down-conversion as illustrated in figure 7.1.

The signal photon at ω_{in} is first converted to an intermediate photon at ω_i by coherent up-converter with a pump field at ω_{p1}. Subsequently a down-converter pumped at ω_{p2} translates the intermediate photon to a target frequency at ω_{out}. Therefore the frequency shift $\Delta\omega$ between input and output photons is equal to the frequency difference between the two pump fields, i.e. $\Delta\omega = \omega_{out} - \omega_{in} = \omega_{p1} - \omega_{p2}$. Therefore, we can engineer the frequencies of pump fields to finely translate the signal state by a small frequency shift. Such fine frequency translation of quantum states can find useful applications in practical quantum networks.

[4] using atomic Rb ensembles

[5] Typical laser wavelength from Ti:sapphire oscillator. This laser is used in many experiments for generating entangled photon-pairs.

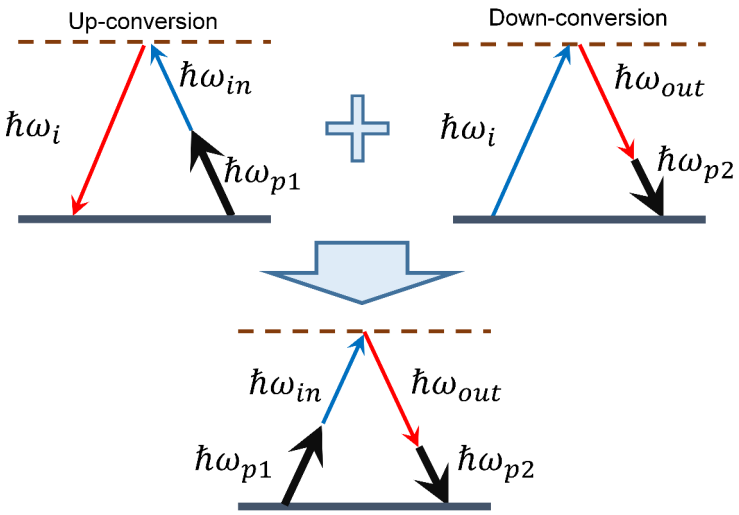

Figure 2.10: Illustration of quantum frequency converter with the combination of a coherent up-converter and a coherent down-converter. After an up-converter the signal photon at ω_{in} is converted to an intermediate photon at ω_i which is then down-converted to the target photon at ω_{out}. The small frequency shift can be realized by finely tuning the frequencies of the two pump fields.

2.4 Conclusion

In this chapter we have introduced some basic concepts about nonlinear frequency conversion and discussed the corresponding main properties for frequency down-conversion and up-conversion. The spontaneous down-conversion is the core process of an OPO which enables the generation of squeezed vacuum states. These squeezed states can be used as initial Gaussian sources for the subsequent generation of non-Gaussian states (e.g. Fock states and Schrödinger cat states) with the help of conditioning measurement. This is the focus of the next chapter.

Besides of preparing quantum states, nonlinear frequency conversion can also be used as an essential tool for quantum state manipulation. Specifically, coherent up- and down-conversion allow to translate the quantum states into a higher or lower frequency while maintaining the quantum properties. Combination of these two coherent processes gives the possibility to implement a quantum frequency translator, which will play an important role as quantum interface in quantum information processing. The experimental implementation of coherent converters will be given in part III.

3 | Quantum Theory of Measurements

Quantum measurement not only gives some information about a system, but also modifies the system. Therefore, in many quantum information protocols measurements play an important role for both characterizing and engineering quantum states. In this chapter, it will be shown that with linear optical elements and photon detectors, non-Gaussian states can be obtained through measurement-induced interaction [52]. Here the quantum measurements are described with the well-known *Positive Operator Valued Measures* (POVM). The formalism provides a powerful and general description of both the probabilities associated with measurement outcomes and the quantum states of the measured system after the observation [1, 53].

We will start with an introduction of the POVM formalism, which is then used to describe two types of detectors: *photon detectors* that give "clicks" related to photon numbers, and *homodyne detectors* that provide photocurrents related to quadratures. Next, a general strategy at the heart of this work , i.e. *conditional state preparation*, will be presented in detail. Finally we will present a typical technique for quantum state tomography based on *Maximum likelihood algorithm*.

3.1 Positive Operator Valued Measures

Quantum measurements are usually described by a collection of *measurement operators* $\{\hat{M}_m\}$ where each index m refers to a possible measurement outcome. The measurement operator acting on a state $|\psi\rangle$ will result in the state [1]

$$|\psi_m\rangle = \frac{\hat{M}_m|\psi\rangle}{\sqrt{\mathcal{P}(m)}} , \tag{3.1}$$

where $\mathcal{P}(m)$ is the probability for obtaining the result m, which is given by

$$\mathcal{P}(m) = \langle\psi|\hat{M}_m^\dagger \hat{M}_m|\psi\rangle . \tag{3.2}$$

There is a special measurement operator, called a *projector* $\hat{P}_m$, which is defined as

$$\hat{P}_m = |\psi_\lambda\rangle\langle\psi_\lambda| , \tag{3.3}$$

where $\{|\psi_\lambda\rangle\}$ are the eigenstates of an observable with each eigenvalue λ. Hence, if one measures λ and the eigenvalue is not degenerate, the state after the measurement will be in the eigenstate $|\psi_\lambda\rangle$. This kind of measurement refers to *projective measurement* (or *von Neumann measurement*).

In practice, if we are only interested in determining the probability of possible measurements, it is very convenient to define a set of Hermitian operators, i.e. *Positive Operator Valued Measures* (POVM). Based on measurement operators, each POVM element is defined as

$$\hat{\Pi}_m = \hat{M}_m^\dagger \hat{M}_m . \tag{3.4}$$

Therefore the measurement probability is given by

$$\mathcal{P}(m) = \mathrm{Tr}[\hat{\Pi}_m \hat{\rho}] . \tag{3.5}$$

These POVM operators follow the completeness relation for the conservation of probability:

$$\sum_m \hat{\Pi}_m = \hat{\mathbb{1}} . \tag{3.6}$$

3.2 Photon detectors

Photon detector is a device that can detect at least a single photon. These detectors are basically characterized by two parameters: *quantum efficiency* and *dark counts* [2]. Practically, the quantum efficiency often strongly depends on the wavelength. On the other hand, the noise is intrinsic to the detector: it does not depend on the impinging light. A "good" detector should have a high efficiency and low dark counts.

The Wigner functions of POVM elements associated with the photon detectors can take negative values, thus demonstrating the non-Gaussian property. In this sense, these detectors are usually categorized as *non-Gaussian detectors* [22, 54]. In the following, we present different photon detectors and give expressions of their POVM elements.

[1] These expressions can be extended to the density matrix formalism

$$\hat{\rho}_m = \frac{\hat{M}_m \hat{\rho} \hat{M}_m^\dagger}{\mathcal{P}(m)} .$$

[2] Background light can also contribute to unwanted photon-detection events and hence is practically included into this parameter.

3.2.1 Photon number resolved detectors

Photon number resolved detectors(PNRDs) are also called *photon counters* since they can distinguish photon numbers of the incident light. In the ideal case of unity quantum efficiency and no dark counts, the POVM operator associated to the measurement k is the projector $|k\rangle\langle k|$ in the Fock state basis. For realistic detectors with quantum efficiency η and dark noise ν [3], the corresponding operator $\hat{\Pi}_n$ can be rewritten as a sum of projectors [4]:

$$\hat{\Pi}_n = \sum_{k=0}^{\infty} r_{k,n} |k\rangle\langle k| \ , \tag{3.7}$$

where the coefficient $r_{k,n}$ corresponds to the probability to have the outcome "n" when measuring the state $|k\rangle$. This non-negative term can be expressed as:

$$r_{k,n} = \sum_{m=0}^{\min\{n,k\}} \mathrm{C}_k^m \eta^m (1-\eta)^{k-m} P(n-m) \ , \tag{3.8}$$

where $P(n)$ gives the probability to have n noisy photons (assuming a Poisson distribution [5])

$$P(n) = \frac{\nu^n}{n!} e^{-\nu} \ . \tag{3.9}$$

The corresponding Wigner function of the POVM element (assuming no dark noise) is finally given by

$$W_{\hat{\Pi}_n} = \frac{-\frac{x^2+p^2}{2\sigma_0^2}\frac{\eta}{2-\eta}}{2\pi\sigma_0^2} \frac{(-\eta)^n}{(2-\eta)^{n+1}} L_n[\frac{x^2+p^2}{(2-\eta)\sigma_0^2}] \ , \tag{3.10}$$

where L_n is the n-th Laguerre polynomial.

3.2.2 on/off detectors

These so-called *on/off detectors* have only two possible outcomes. Avalanche photodiode (APD) belongs to this type, as it can only tell if no photon or at least one photon. Ideally, the output "off" corresponds to the projector on the vacuum state, i.e. $\hat{\Pi}_{\text{off}} = |0\rangle\langle 0|$. In reality, the "off" measurement is generally described with POVM operator as

$$\hat{\Pi}_{\text{off}} = \sum_{k=0}^{\infty} r_{k,\text{off}} \ |k\rangle\langle k| \ , \tag{3.11}$$

where the coefficient reads

$$r_{k,\text{off}} = e^{-\nu}(1-\eta)^k \ . \tag{3.12}$$

The POVM operator of "on" measurement is thus given by $\hat{\Pi}_{\text{on}} = \mathbb{1} - \hat{\Pi}_{\text{off}}$ due to the completeness of the POVM set.

The corresponding Wigner functions for the two POVMs are given by [20, 22]

$$\begin{aligned} W_{\hat{\Pi}_{\text{off}}} &= \frac{1}{2\pi\sigma_0^2}\frac{e^{-\nu}}{2-\eta} e^{-\frac{x^2+p^2}{2\sigma_0^2}\frac{\eta}{2-\eta}} \\ W_{\hat{\Pi}_{\text{on}}} &= W_{\mathbb{1}} - W_{\hat{\Pi}_{\text{off}}} = \frac{1}{2\pi\sigma_0^2}\left(\frac{1}{2} - \frac{e^{-\nu}}{2-\eta} e^{-\frac{x^2+p^2}{2\sigma_0^2}\frac{\eta}{2-\eta}}\right) \ . \end{aligned} \tag{3.13}$$

[3] The dark noise is defined as the mean photon number of noise counts in the detection windows.

[4] For phase insensitive detector, the density matrix of a POVM element only has diagonal terms [55, 56].

[5] If considering a thermal dark noise, we have

$$P(n) = \frac{\nu^n}{(\nu+1)^{n+1}} \ .$$

3.2.3 Two-photon detection

Optical quantum state engineering usually requires detectors with photon-number-resolving ability. By using only on/off detectors, it is also possible to emulate photon-number resolution via spatial multiplexing [57] or time multiplexing [58].

As depicted in figure 3.1, we consider a device made of a 50:50 beam-splitter and two on/off detectors. When there are two photons in the incident light, they have 50% probability to be split by the beam-splitter. Each photon is then detected by the on/off detector. In the case of small average photon number of the incident light, coincidence events indicate two incident photons. The ability of heralding two-photon state will be essential in the conditional preparation of quantum states discussed in the next section of this chapter. With N detectors, such spatial multiplexing device can potentially distinguish photon numbers up to N.

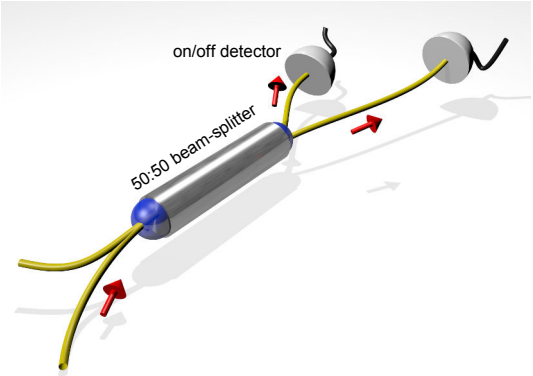

Figure 3.1: Two-photon detector based on spatial multiplexing. The measured beam is sent to a 50:50 beam-splitter with two single-photon detector connected at each output. This device can be treated as a single detector with POVM elements $\hat{\Pi}_m$.

The POVM elements of this two-photon detector are given by

$$\hat{\Pi}_0 = \sum_n e^{-2\nu}(1-\eta)^n |n\rangle\langle n| \ , \tag{3.14}$$

$$\hat{\Pi}_1 = 2\sum_n \left(e^{-\nu}(1-\eta/2)^n - e^{-2\nu}(1-\eta)^n\right) |n\rangle\langle n| \ , \tag{3.15}$$

$$\hat{\Pi}_{\geqslant 2} = \sum_n \left(1 + e^{-2\nu}(1-\eta)^n - 2e^{-\nu}(1-\eta/2)^n\right) |n\rangle\langle n| \ , \tag{3.16}$$

where η and ν are the quantum efficiency and dark noise of each on/off detector. These POVM operators satisfy the completeness relation $\hat{\Pi}_0 + \hat{\Pi}_1 + \hat{\Pi}_{\geqslant 2} = \mathbb{1}$.

Note that there is another commonly used method for distinguishing two photons via temporal multiplexing. Specifically, such scheme relies on a time delay τ in one output of a beam-splitter. After recombining the two outputs with another 50:50 beam-splitter, light can be detected with a on/off detector. Consequently, if there are two photons in the incident light, they have a chance to be temporally separated with a time delay τ in the detected port. Hence, the on/off detector can count the two photons at two different time windows at an interval of τ. The scheme provides a simple and efficient solution in the pulsed regime [58]. However such time-multiplexed detector is not suitable in continuous-wave regime due to the random arrival time of photons.

Now we turn to another kind of detector, the homodyne detector, which is the central instrument in the continuous-variable toolbox.

3.3 Homodyne detector

Homodyne detector is devised to provide the measurement of a single-mode quadrature x_θ for characterization of an optical quantum state or conditional preparation of quantum states. We will see that the Wigner function of its POVM element is Gaussian, thus the homodyne detector can be categorized as a *Gaussian detector* [22].

3.3.1 Basic properties

The scheme is illustrated in figure 3.2. A signal under investigation $\hat{\rho}_s$ is mixed with a classical field $|\alpha\rangle$ (*local oscillator*) by a balanced (50/50) beam-splitter [6]. The phase of the local oscillator is adjusted by a PZT for accessing quadrature values with different phases θ. The two interfering modes after the beam splitter are then detected by a pair of identical photodetectors (typically linear photodiodes). Finally the difference of the generated photocurrents is obtained by an electronic subtraction. This difference is directly linked to the field quadrature with a scaling factor.

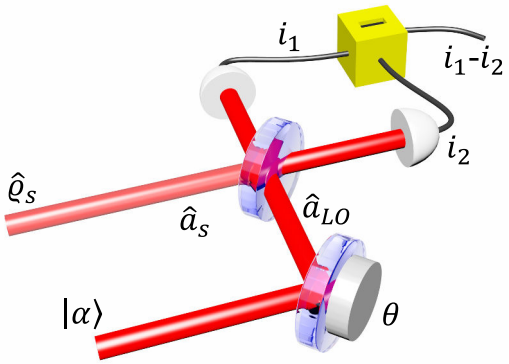

Figure 3.2: A scheme of balanced homodyne detector. The signal beam under investigation is mixed with a bright coherent state (*local oscillator*) on a 50:50 beam-splitter. The two outputs are measured with a pair of identical photodiodes. The subtraction of the photocurrents is proportional to the field quadrature value. To access the various phases of quadrature measurements, the phase of the local oscillator is scanned via a PZT.

Now we will present a simple calculation for highlighting the main features about the homodyne detector. The two-mode interaction between the signal $\hat{\rho}_s$ and the classical local oscillator on a beam-splitter is given by

$$\begin{aligned} \hat{a}_1 &= (\hat{a}_{LO} + \hat{a}_s)/\sqrt{2} \ , \\ \hat{a}_2 &= (\hat{a}_{LO} - \hat{a}_s)/\sqrt{2} \ . \end{aligned} \tag{3.17}$$

The two output modes after the beam-splitter are measured with photodiodes. The resulting photocurrents are proportional to the incident photon numbers, thus $\hat{i} \propto \hat{n}$:

$$\hat{n}_{1,2} = \tfrac{1}{2}(\hat{a}^\dagger_{LO}\hat{a}_{LO} + \hat{a}^\dagger_s\hat{a}_s \pm \hat{a}^\dagger_{LO}\hat{a}_s \pm \hat{a}^\dagger_s\hat{a}_{LO}) \ . \tag{3.18}$$

The subtraction of the two photocurrents results in a signal proportional to

$$\hat{n}_1 - \hat{n}_2 = \hat{a}_{LO}\hat{a}^\dagger_s + \hat{a}^\dagger_{LO}\hat{a}_s \ . \tag{3.19}$$

In the approximation of strong coherent state, the local oscillator can be classically treated as $\langle \hat{a}_{LO} \rangle = \alpha e^{i\theta}$, leading to

$$\hat{n}_1 - \hat{n}_2 \approx \alpha e^{i\theta}\hat{a}^\dagger_s + \alpha e^{-i\theta}\hat{a}_s \ . \tag{3.20}$$

[6] For the purpose of accessing quadrature values, here we consider the balanced homodyne detector. Note that unbalanced homodyne detector is also commonly used in quantum optics experiment as an alternative way to measure the statistics (moments) of the field quadratures [22].

The homodyne signal is thus given by

$$i_1 - i_2 \propto \alpha \hat{x}_\theta \ , \tag{3.21}$$

which is proportional to a quadrature observable with an amplifying factor depending on the magnitude α of the local oscillator. The larger is α, the better is the sensitivity of the measurement. Additionally, the phase of the measured quadrature can be adjusted by changing the phase of the local oscillator.

It is worth mentioning that the homodyne detector only detects the optical states having the same spatialtemporal mode defined by the local oscillator [7]. Therefore high visibility V between the signal and local oscillator is required for achieving large detection efficiency η_{vis}. Specifically $\eta_{vis} = V^2$.

3.3.2 POVM of homodyne detector

For a perfect homodyne detector, the POVM elements are given by

$$\hat{\Pi}(x_\theta) = |x_\theta\rangle\langle x_\theta| \ , \tag{3.22}$$

where $\hat{x}_\theta|x_\theta\rangle = x_\theta|x_\theta\rangle$. For a given phase, the POVM elements associated with the outcome x_θ satisfy the completeness relation:

$$\int \hat{\Pi}(x_\theta)dx_\theta = \int |x_\theta\rangle\langle x_\theta|dx_\theta = \mathbb{1} \ . \tag{3.23}$$

The density matrix element in the Fock basis is given by

$$\Pi_{nm} = \langle n|\hat{\Pi}(x_\theta)|m\rangle = \langle n|x_\theta\rangle\langle x_\theta|m\rangle \ , \tag{3.24}$$

which can be computed with the wave function of Fock state

$$\langle n|x_\theta\rangle = e^{in\theta}\frac{1}{(\sqrt{2\pi}\sigma_0 2^n n!)^{1/2}} H_n\left(\frac{x}{\sigma_0\sqrt{2}}\right) e^{-(x/\sigma_0\sqrt{2})^2/2} \ , \tag{3.25}$$

where H_n is the n-th Hermite polynomial.

The corresponding Wigner function is thus written as:

$$W_{\hat{\Pi}(x_\theta)}(x,p) = \frac{1}{2\pi\sigma_0^2}\frac{1}{2}\delta(x\cos\theta + p\sin\theta - x_\theta) \ . \tag{3.26}$$

Practically, the detection efficiency of homodyne detector is never 100% due to many factors, for instance the limited visibility of the interference, limited quantum efficiency of the photodiodes. The losses can be modeled as an imaginary beam-splitter (with an intensity transmission η) before a perfect detector. For an initial state $\hat{\rho}_0$, the state after the beam splitter can be obtained from the so-called generalized Bernoulli transformation:

$$\langle m|\hat{\rho}_\eta|n\rangle = \sum_{k=0}^{\infty} B_{m+k,m}(\eta)B_{n+k,n}(\eta)\langle m+k|\hat{\rho}_0|n+k\rangle \ , \tag{3.27}$$

where

$$B_{n+k,n} = \sqrt{\binom{n+k}{n}\eta^n(1-\eta)^k} \ . \tag{3.28}$$

[7] This important feature can be obtained with a more rigorous and comprehensive model [59]

In this case, the probability of obtaining a quadrature value x_θ is given by

$$\begin{aligned}\mathcal{P}_\eta(x) &= \langle x_\theta|\hat{\rho}_\eta|x_\theta\rangle \\ &= \sum_{m,n=0}^{\infty}\sum_{k=0}^{\infty} B_{m+k,m}(\eta)B_{n+k,n}(\eta)\langle n|x_\theta\rangle\langle x_\theta|m\rangle\langle m+k|\hat{\rho}_0|n+k\rangle \ .\end{aligned} \tag{3.29}$$

Therefore, the POVM element of a lossy homodyne detector is given by

$$\hat{\Pi}_\eta(x_\theta) = \sum_{m,n,k} B_{m+k,m}(\eta)B_{n+k,n}(\eta)\langle n|x_\theta\rangle\langle x_\theta|m\rangle|n+k\rangle\langle m+k| \ . \tag{3.30}$$

The corresponding Wigner function reads as:

$$W_{\hat{\Pi}_\eta(x_\theta)}(x,p) = \frac{1}{2\pi\sigma_0^2}\frac{1}{2}\frac{1}{\sqrt{2\pi\sigma_0^2(1-\eta)}}\exp\left(-\frac{(x_\theta-\sqrt{\eta}(x\cos\theta+p\sin\theta))^2}{2\sigma_0^2(1-\eta)}\right) \ . \tag{3.31}$$

3.4 Conditional state preparation

A unique property of quantum measurement is that it allows to modify states by appropriately choosing a measurement strategy. This kind of method for state engineering is thus called *conditional state preparation* for highlighting the probabilistic but heralded character of this technique.

3.4.1 Composite system

Conditional preparation of a quantum state always involves at least two-mode composite system, the conditional mode and the signal mode. In particular, measurement is made on one part of a bipartite correlated system; the action of this measurement is to project the other part to a target state as shown in figure 3.3.

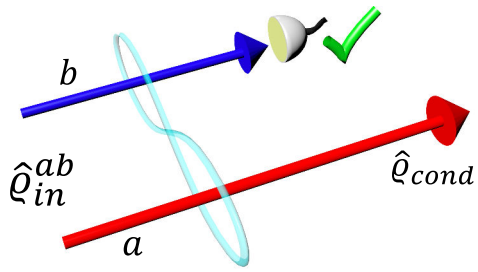

Figure 3.3: Conceptual scheme of a conditional preparation. A measurement is performed on one mode of an entangled state. The measurement outcome then heralds the preparation of a new state.

We start with a two-mode state $\hat{\rho}_{\mathrm{in}a,b}$. On one of the mode, we perform a measurement $\hat{\Pi}_a$. When the measurement apparatus gives the desired answer, the other mode will be projected into $\hat{\rho}_{\mathrm{cond},b}$. Using measurement theory based on the introduced POVM formalism, this conditional state can be written as

$$\hat{\rho}_{\mathrm{cond},b} = \frac{\mathrm{Tr}_a[\hat{\Pi}_a\otimes\mathbb{1}_b\hat{\rho}_{ab}]}{\mathrm{Tr}[\hat{\Pi}_a\otimes\mathbb{1}_b\hat{\rho}_{ab}]} \ , \tag{3.32}$$

where Tr_a demotes the partial trace over mode a, and $\hat{\rho}_{\mathrm{cond},b}$ is called *reduced density matrix*.

Similar to the expression based on the density matrix, we have an equivalent one based on the Wigner function:

$$W_{\hat{\rho}_{\mathrm{cond},b}}(x_b,p_b) = \frac{\iint_{\mathbb{R}^2} dx_a dp_a W_{\hat{\Pi}_a}(x_a,p_a)W_{\hat{\rho}_{ab}}(x_a,p_a,x_b,p_b)}{\iiiint_{\mathbb{R}^4} dx_a dp_a dx_b dp_b W_{\hat{\Pi}_a}(x_a,p_a)W_{\hat{\rho}_{ab}}(x_a,p_a,x_b,p_b)} \ , \tag{3.33}$$

where the partial integration takes the place of partial trace. As we use the product of $W_{\hat{\Pi}_a}(x_a, p_a)$ and $W_{\hat{\rho}_{ab}}$, one of them needs to exhibit negativity if we want to prepare a state with negative values at the end.

3.4.2 Beam-splitter model

The simplest example for conditional state preparation of light can rely on a beam-splitter for mixing two optical modes. Combination of beam-splitters with detectors in one output mode indeed provides a promising way for engineering quantum states of traveling optical fields.

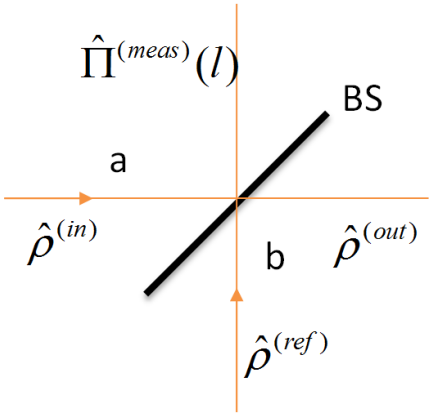

Figure 3.4: Simple scheme for conditional preparation of quantum state.

Les us consider the scheme shown in figure 3.4. A single mode $\hat{\rho}^{(in)}$ is mixed with a reference mode $\hat{\rho}^{(ref)}$ at a beam-splitter with r (amplitude reflectance) and t (amplitude transmittance), and a measurement $\hat{\Pi}^{(meas)}(l)$ is performed on the output reference mode. Since the two output modes are entangled in general, the measurement will influence the output signal mode $\hat{\rho}^{(out)}$. The reduced output state can be expressed in the more general case as:

$$\hat{\rho}^{(out)} = \frac{Tr_b[\hat{\Pi}^{(meas)}(l)\hat{B}\hat{\rho}^{(in)} \otimes \hat{\rho}^{(ref)}\hat{B}^\dagger]}{p(l)} , \tag{3.34}$$

where the conditional probability $p(l)$ of obtaining the result l is

$$p(l) = Tr_{a,b}[\hat{\Pi}^{(meas)}(l)\hat{B}\hat{\rho}^{(in)} \otimes \hat{\rho}^{(ref)}\hat{B}^\dagger] . \tag{3.35}$$

For simplicity, we assume that all the involved states are pure states [8]. So the output state is a pure state that can be written as:

$$|\psi^{(out)}\rangle = \frac{\hat{Y}|\psi^{(in)}\rangle}{\|\hat{Y}|\psi^{(in)}\rangle\|} , \tag{3.36}$$

where

$$\hat{Y} = \langle\psi^{(meas)}|\hat{B}|\psi^{(ref)}\rangle , \tag{3.37}$$

is the non-unitary *conditional beam-splitter operator*. The success probability is thus given by

$$p(\psi^{(meas)}) = \|\hat{Y}|\psi^{(in)}\rangle\|^2 = \langle\psi^{(in)}|\hat{Y}^\dagger\hat{Y}|\psi^{(in)}\rangle . \tag{3.38}$$

[8] For the calculation on mixed states, please refer to the seminal paper [60]

Let us take a very simple example where $|\psi^{(meas)}\rangle = |n\rangle$ and $|\psi^{(ref)}\rangle = |0\rangle$. In this case the non-unitary operator is given by [9]

$$\hat{Y} = \langle n|\hat{B}|0\rangle = \frac{(-r)^n}{t^n\sqrt{n!}}\hat{a}^n t^{\hat{n}} \ . \tag{3.39}$$

In the case of highly asymmetric beam splitter ($t \to 1$), we have $\hat{Y} \to \hat{a}^n$, which corresponds to a photon subtraction operation.

3.4.3 Calculation based on density matrix

Generally, it is not easy to analytically calculate the non-unitary beam-splitter operator, especially in the case of mixed states. An alternative way for obtaining the conditional state is to truncate the involved states into a finite-dimension Hilbert space, and then to use matrix manipulation and simple linear algebra.

Therefore, the first step is to represent all the involved quantum states, quantum channels and quantum measurements by density matrices with truncated Fock state dimensions. As shown in equation (1.46), the beam-splitter operator on the two-mode Fock state results in

$$\hat{B}|n_1, n_2\rangle = \sum_{N_1,N_2} B^{n_1,n_2}_{N_1,N_2}|N_1, N_2\rangle \ , \tag{3.40}$$

where

$$\begin{aligned} B^{n_1,n_2}_{N_1,N_2} = &\sum_{k=0}^{n_1}\sum_{l=0}^{n_2}(-1)^{n_1-k} r^{n_1+n_2-k-l} t^{k+l} \\ &\times \frac{\sqrt{n_1!n_2!N_1!N_2!}}{k!l!(n_1-k)!(n_2-l)!}\delta_{N_1,n_2+k-l}\delta_{N_2,n_1-k+l} \ . \end{aligned} \tag{3.41}$$

Rewriting the involved states in the Fock states basis, we also have

$$\begin{aligned} \hat{\rho}^{(in)} &= \sum_{\mu,\nu}\rho^{(in)}_{\mu,\nu}|\mu\rangle\langle\nu| \ , \\ \hat{\rho}^{(ref)} &= \sum_{\mu',\nu'}\rho^{(ref)}_{\mu',\nu'}|\mu'\rangle\langle\nu'| \ , \\ \hat{\rho}^{(in)}_{ab} &= \hat{\rho}^{(in)} \otimes \hat{\rho}^{(ref)} = \sum_{\mu,\nu,\mu',\nu'}\rho^{(in)}_{\mu,\nu}\rho^{(ref)}_{\mu',\nu'}|\mu,\mu'\rangle\langle\nu,\nu'| \ , \\ \hat{\rho}^{(meas)}_{ab} &= \hat{I} \otimes \sum_{j,k}\rho^{(meas)}_{j,k}|j\rangle\langle k| = \sum_{i,j,k}\rho^{(meas)}_{j,k}|i,j\rangle\langle i,k| \ . \end{aligned} \tag{3.42}$$

With the above matrix forms, the second step is to compute the matrix product and partial trace according to equation (3.34). Finally the matrix element of the output mode is given

[9] For the general case, $|\psi^{(meas)}\rangle = |n\rangle$ and $|\psi^{(ref)}\rangle = |m\rangle$, it is shown that the mode in the output channel is prepared in either a photon-subtracted (when $m < n$) or a photon-added (when $m > n$) Jacobi polynomial state [61].

by [10]

$$\begin{aligned}\rho^{(out)}_{m,n} &= \langle m|\hat{\rho}^{(out)}|n\rangle \\ &= \sum_{l}\sum_{\mu,\nu,\mu',\nu'}\sum_{i,j,k}\rho^{(in)}_{\mu,\nu}\rho^{(ref)}_{\mu',\nu'}\rho^{(meas)}_{j,k} \\ &\times \langle m,l|\hat{B}|\mu,\mu'\rangle\langle\nu,\nu'|\hat{B}^{\dagger}|i,j\rangle\langle i,k|n,l\rangle \\ &= \sum_{l,j}\sum_{\mu=0}^{m+l}\sum_{\nu=0}^{n+j} B^{m,l}_{\mu,m+l-\mu}B^{n,j}_{\nu,n+j-\nu}\rho^{(in)}_{\mu,\nu}\rho^{(ref)}_{m+l-\mu,n+j-\nu}\rho^{(meas)}_{j,l} \ ,\end{aligned} \tag{3.43}$$

where the last step is achieved by noting that non-zeros terms only exist for $m+l=\mu+\mu'$, $n+j=\nu+\nu'$, $i=n$, and $k=l$.

Now let us discuss some specific cases:

1. If there is no measurement in the mode b, then the measurement can be described by an identity operator
$$\hat{\rho}^{(meas)} = \hat{I} \ . \tag{3.44}$$
Inserting the matrix element of the operator
$$\rho^{(meas)}_{j,k} = \delta_{j,k} \tag{3.45}$$
into equation (3.43), we can get
$$\rho^{(out)}_{m,n} = \sum_{l}\sum_{\mu=0}^{m+l}\sum_{\nu=0}^{n+l} B^{m,l}_{\mu,m+l-\mu}B^{n,l}_{\nu,n+l-\nu}\rho^{(in)}_{\mu,\nu}\rho^{(ref)}_{m+l-\mu,n+l-\nu} \ . \tag{3.46}$$

2. If there is no input for the reference mode b, that is
$$\hat{\rho}^{(ref)} = |0\rangle\langle 0| \ . \tag{3.47}$$
Inserting
$$\rho^{(ref)}_{\mu',\nu'} = \begin{cases} 1, & \mu'=\nu'=0 \\ 0, & others \end{cases} \tag{3.48}$$
into equation (3.43), we can get
$$\rho^{(out)}_{m,n} = \sum_{l,j} B^{m,l}_{m+l,0}B^{n,j}_{n+j,0}\rho^{(in)}_{m+l,n+j}\rho^{(meas)}_{j,l} \ . \tag{3.49}$$

3. If there is no measurement and no reference in mode b, we can insert equations (3.45) and (3.48) into equation (3.43), resulting in
$$\rho^{(out)}_{m,n} = \sum_{l} B^{m,l}_{m+l,0}B^{n,l}_{n+l,0}\rho^{(in)}_{m+l,n+l} \ , \tag{3.50}$$
where
$$B^{m,l}_{m+l,0} = \sqrt{\begin{pmatrix} m+l \\ m \end{pmatrix}\eta^m(1-\eta)^l} \ . \tag{3.51}$$
$\eta = t^2$ is the power transmittance of the beam splitter. This transformation is called *generalized Bernoulli transformation*. Actually, this simplest case describes the evolution of a quantum state after losses modeled by a fictitious beam-splitter.

[10] Note that here we omit the normalization factor, which can be found back using the requirement of unitary trace of the density matrix. The normalization factor is also interpreted as the heralding probability.

We can see that some realistic assumptions can help to simplify the computation processes. Actually, even for the general case, the calculation is easy and fast with the help of simple programming. With the above proposed method, we can directly access to certain matrix entries of interest instead of calculating the whole density matrix. This is favorable for some cases, for instance, if we are only interested in the photon-number distribution of the output conditional state.

Note that the simplest way for obtaining the output density matrix is to directly handle the computation based on matrix operation, which can avoid the complex summation shown in equation (3.43). It makes the programming even simpler since most of programming languages already provide powerful libraries about linear algebra.

3.4.4 Qmixer

Based on numerical calculation with truncated density matrices, we developed during this PhD work a simple but very useful software, aiming at providing a theoretical tool for studying quantum state evolution under conditional measurements. The software is named "Qmixer" because the core of the calculation model is a beam-splitter (two-mode mixer).

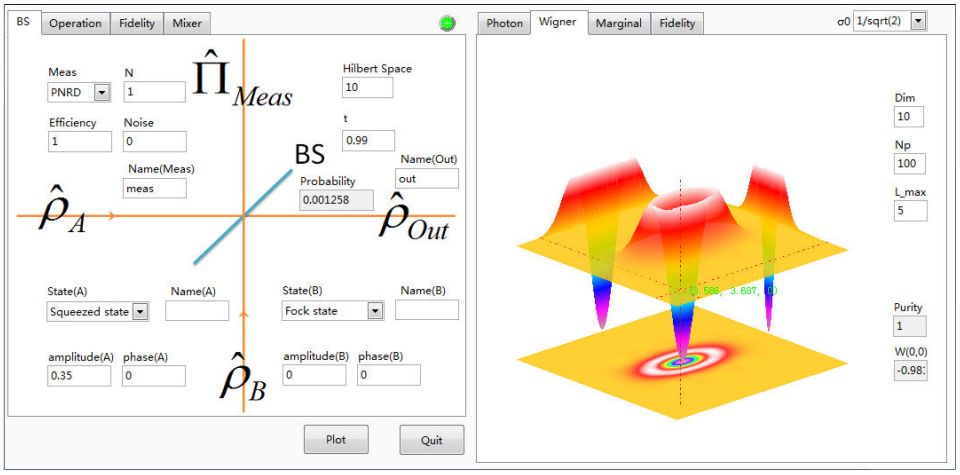

Figure 3.5: Interface of Qmixer, a versatile tool developed during this PhD for studying quantum state evolution under conditional measurements. The example shown in the figure is single-photon subtraction from a squeezed vacuum state.

As shown in figure 3.5, Qmixer is programmed with LabView as it provides a very simple way to access various graphical interfacing tools. The software user interface mainly consists of two parts: parameters setting (left panel) and results display (right panel). In each panel, there are several sub-panels for specific purposes. In the following, we will present the user interface of Qmixer.

Left panel In this panel, we can set the parameters according to our needs. It contains four sub-panels: "BS", "Operations", "Fidelity" and "Mixer".

- In "BS" panel, we can set parameters of the beam-splitter model, such as incident quantum states ($\hat{\rho}_A$ and $\hat{\rho}_B$), involved quantum measurement ($\hat{\Pi}_{Meas}$), beam-splitter power transmission (t) and truncated photon number (Hilbert space dimension). Some commonly used quantum states (Fock states, coherent states, squeezed states and cat states) and quantum measurements (APD, PNR detector, Homodyne detector) can be conveniently selected from the drop-down list.

- In "Operations" panel, we can apply any of the single-mode Gaussian operations (rotation, displacement and squeezing) to a quantum state.
- In "Fidelity" panel, we can compute the fidelity between a quantum state of interest and a target state.
- In "Mixer" panel, we can synthesize a statistical mixture of two states with user-defined weights.

Right panel In this panel, we can display the results associated with the user's settings in the left panel. It contains four sub-panels: "Photon", "Wigner", "Marginal" and "Fidelity".

- In "Photon" panel, it shows the photon number distribution of the output conditional state.
- In "Wigner" panel, it gives the Wigner function of the output state and some important values for the state such as state purity and the value at the origin of the Wigner function. Note that we can also change the normalization convention σ_0.
- In "Marginal" panel, it displays the marginal distribution of the output state with a user-defined projection angle.
- In "Fidelity" panel, it provides the plot of the fidelity as a function of certain parameters (e.g. state amplitude) set in the left "Fidelity" sub-panel.

Qmixer provides therefore a simple but very useful tool to model our experiments related to conditional measurement. For more details and examples, readers can refer to Appendix D.

3.5 MaxLik for quantum state tomography

Quantum state tomography is a technique for extracting the full information of a quantum state by subjecting it to an ensemble of quantum measurements. As we know, a quantum state can be completely described by its density matrix (or equivalently by its Wigner function). For quantum optics in free space, the reconstruction of quantum sates is usually implemented by a set of quadrature values from homodyne measurements. In this case, the measurements of the quadrature $\hat{x}_\theta$ give the marginal distribution $\mathcal{P}(x_\theta) = \int dy_\theta W(x_\theta, y_\theta)$. The next step is to reconstruct the Wigner function W.

There exit several algorithms for quantum tomography [59], such as inverse Radon transformation, pattern functions, and Maximum-likelihood algorithm (MaxLik algorithm) . The most commonly used technique henceforth is the MaxLik algorithm due to three main advantages [62]. First, MaxLik algorithm enables us to compensate the optical losses; second, it allows us to incorporate the positivity and unity-trace constraints into the reconstruction procedure, thus always leading to a physically state; third, it gives the highest accuracy (with an intrinsic numerical noise defined by the Cramer-Rao bound). Nevertheless, MaxLik algorithm also has some limitations, such as the truncation of the Hilbert space and the requirement of more computational resources. Here we will give a brief introduction about this MaxLik algorithm, which has been extensively used during this PhD work.

The measurement outcomes of the homodyne detection can be organized as $\{\theta_j, x_j, f_j\}$ where f_j is the frequency of occurrence for each outcome $\{\theta_j, x_j\}$. The likelihood is then given by

$$\mathcal{L}(\hat{\rho}) = \prod_j \mathcal{P}(\theta_j, x_j)^{f_j} \ , \tag{3.52}$$

where $\mathcal{P}(\theta_j, x_j) = \mathrm{Tr}[\hat{\Pi}(\theta_j, x_j)\hat{\rho}]$ is the probability to obtain the result $\{\theta_j, x_j\}$ for a quantum state $\hat{\rho}$ and $\hat{\Pi}(\theta_j, x_j)$ is the POVM element of homodyne detector (cf. equation (3.22)).

In order to find a state $\hat{\rho}$ that maximizes the likelihood as the name of MaxLik algorithm suggests, an iteration operator is thus introduced:

$$\hat{R}(\hat{\rho}) = \sum_j \frac{f_j}{\mathcal{P}(\theta_j, x_j)} \hat{\Pi}_j(\theta_j, x_j) \ . \tag{3.53}$$

Since the experimental data $\{\theta_j, x_j\}$ is discrete, one can always reduce the bin size such that f_j only takes the values of either 0 or 1. As a result, the iteration operator is simply given by

$$\hat{R}(\hat{\rho}) = \sum_j \frac{\hat{\Pi}_j(\theta_j, x_j)}{\mathcal{P}(\theta_j, x_j)} \ . \tag{3.54}$$

The most compatible density matrix $\hat{\rho}$ can be found by the following iterations:

$$\hat{\rho}^{(k+1)} = \mathcal{N}\left[\hat{R}(\hat{\rho}^{(k)})\ \hat{\rho}^{(k)}\ \hat{R}(\hat{\rho}^{(k)})\right] \ , \tag{3.55}$$

where $\mathcal{N}$ denotes the normalization factor to a unitary trace. The initial state is given by a normalized unitary matrix $\hat{\rho}^{(0)} = \mathcal{N}[\mathbb{1}]$. For each iteration the likelihood given by the currently estimated density matrix will monotonically increase. At last it will approach to the maximum-likelihood density matrix $\hat{\rho}_0$. In this case, we have $f_j \propto \mathcal{P}_j$ and $\sum_j \hat{\Pi}_j \propto \mathbb{1}$. Hence $\hat{R}(\hat{\rho}_0) \propto \mathbb{1}$, i.e.

$$\hat{R}(\hat{\rho}_0)\ \hat{\rho}_0\ \hat{R}(\hat{\rho}_0) \propto \hat{\rho}_0 \ . \tag{3.56}$$

One important feature for the MaxLik algorithm is the possibility to incorporate the loss. In a practical experiment, due to the propagation loss and imperfect quantum efficiency of homodyne detector, the quadrature distribution will be distorted. Therefore, to estimate the state before the losses, the projector $\hat{\Pi}(\theta, x)$ should be replaced by (cf. equation (3.30))

$$\hat{\Pi}_\eta(\theta, x) = \sum_{m,n,k} B_{m+k,m}(\eta) B_{n+k,n}(\eta) \langle n|\theta, x\rangle\langle\theta, x|m\rangle |n+k\rangle\langle m+k| \ . \tag{3.57}$$

It is worth mentioning that the MaxLik algorithm can be extended to the reconstruction of a two-mode state [20], which is intensively used in our experiments for hybrid entanglement generation in Chapter 7.

3.6 Conclusion

In this chapter, we introduced the basic concepts of the POVM formalism, which was then used to describe two types of detectors: photon detector and homodyne detector. The click detectors belong to the non-Gaussian detector family usually used in the conditional preparation of non-Gaussian states while the homodyne detector as a Gaussian detector is typically used for quantum state tomography together with the technique of Maximum likelihood algorithm. All the performed experiments in part II will involve these two types of measurements for conditional preparation and state characterization.

4 | Automatic Locking System

The locking of optical cavities or interferometer phases is very often requested in quantum optics experiments. This task is traditionally achieved with analog systems based on various techniques, such as the Pound-Drever-Hall (PDH) locking, the dither-and-lock, or the tilt-locking method. Although such analog locking systems are very mature, yet certain other desirable features, such as automatic relocking when the lock is lost or sequential locking by a sample-and-hold behavior, can quickly make the analog design cumbersome. However, with the advances of digital locking systems, these features can be easily accomplished in software, enabling rapid development and modification. In this chapter, we will present a microcontroller-based locking system that does not require any modulations or external error signals [63]. The implementation of the locking system can enable, for instance, long-term data acquisition or just simpler functioning on a daily basis.

The algorithm for digital locking will be first presented as well as a simple model for characterizing the locking behavior. Next we will demonstrate the performances for locking optical cavities with a moderate finesse (100) and a high finesse (1000). The possible combination of this technique with analog devices will also be discussed. Finally integration of locking system into a compact box and implementation of an user interface for remote monitor will be presented.

4.1 Introduction

Digital locking has attracted more and more attention in optics experiments [64, 65, 66, 67] since its first demonstration in laser frequency stabilization at the end of 1990s [68, 69]. Especially, the application of digital system has been recently boosted by the rapid development of high-speed and low-cost field programmable gate arrays (FPGA) and microcontroller units (MCU). For example, Ref. [70] generated a modulation signal by a FPGA programmed with LabView, which was then applied to an electro-optic modulator in a Pound-Drever-Hall scenario. The FPGA enabled automatic relocking and included some inbuilt locking analysis tools. Similarly, in Ref. [71], a microcontroller unit was also used in such a scenario to lock a fiber laser to an optical cavity. In these implementations, the logic unit is usually combined with traditional locking processes. It enables the digitalization and processing of the signal, replacing the usual PID control and lock-in-amplifier, and adds novel capabilities and further scalability.

There are ongoing discussions between choosing a FPGA or a conventional MCU for locking purpose. Generally speaking, FPGA can be much faster. However, for many lockings, fast digital controller is not necessary since the frequency bandwidth of the system is usually limited by the sensors, actuators and/or transducers. For instance, the bandwidth of typical piezoelectric transducers (PZT) used for controlling the optical path length is only tens of kHz, which makes FPGAs largely exceed the needs. Last but not least, microcontrollers can be programmed in C language, which makes them easily accessible by relatively inexperienced users.

Here, we present a microcontroller-based locking system that does not require any modulation or external error signal [63]. The microcontroller chip used in our experiment is the ADuC7020 from Analog Devices, which already contains five 12-bit ADCs (with sampling rate of 1 MHz) and four 12-bit DACs (with voltage output settling time of 10 μs) [72]. Additionally the evaluation board (EVALADUC7020QSZ, around 50 euros) is commercially available, thus making its use very simple as no additional electrical soldering is required.

4.2 Algorithm and model

The core process for locking is based on a maximum (or minimum) -searching algorithm without requirement of any modulation or external error signal, which makes the way to lock extremely simple and intuitive. In this section we will detail the implemented algorithms and show the performances obtained for locking a Mach-Zehnder interferometer.

4.2.1 Searching algorithm

As a first example, we consider the case of a 1.5 m-arm Mach-Zehnder interferometer, as illustrated in figure 4.1(a). The interference signal is measured by a photodiode and this photocurrent is sent to the MCU. After processing, the output of the unit is fed back to the PZT actuator.

A flowchart of the program execution is given in figure 4.1(b). The voltage on the PZT is increased with a constant step unless the signal value (Y1) is smaller than the previous one, which would lead to a sign-flip of the sweep. As a result, the locked signal can always stay at its maximal value. To avoid high-frequency noise the signal is averaged over a user-defined numbers of ADC sampling (typically 50).

Importantly, in such long-arm interferometers, fluctuations can lead to a change of the paths by many wavelengths, larger than the limited range of typical actuators. In order to keep the locking, one has thus to shift back the position of the PZT. Usual analog

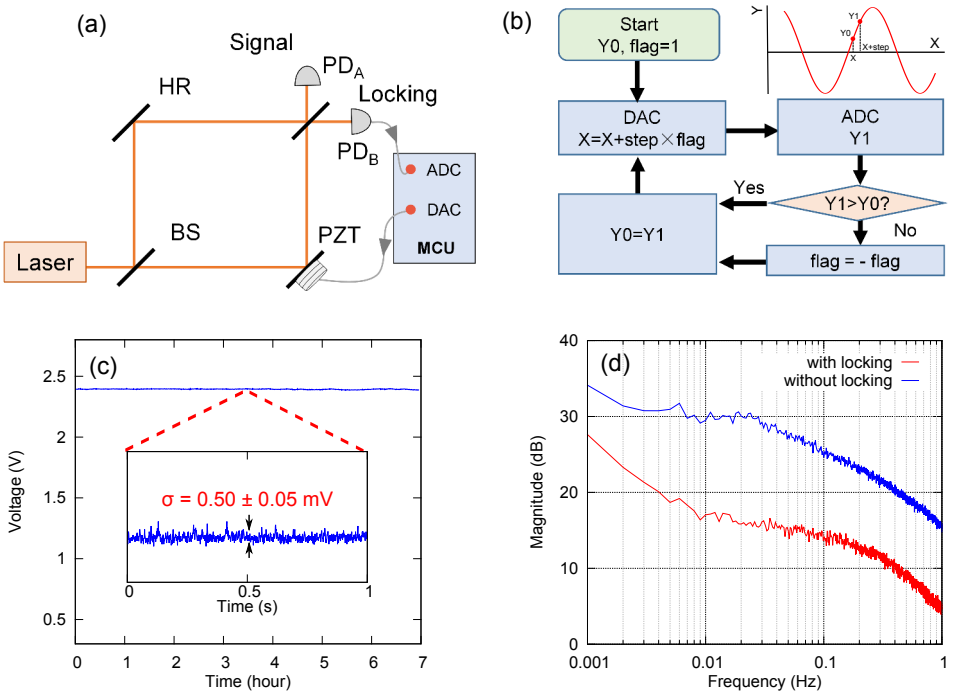

Figure 4.1: (a) Experimental setup: locking a 1.5-meter-arm Mach-Zehnder interferometer with a microcontroller unit. HR stands for high-reflective mirror, BS for beam-splitter, PZT for piezoelectric transducer and PD for photodiode. (b) Flowchart of the program execution for the maximum-searching algorithm. (c) Long-term stability. The inset gives a one-second zoom and the associated standard deviation. (d) Noise spectrum at low frequencies with and without locking.

PID controllers do not have this kind of feature, and would need elaborated developments. In contrast, this can be easily achieved by a programmable device. The recentering can indeed be trivially taken into account with simple codes in the locking program. Specifically, when the detected peak position is near the ends of the DAC output range, the output is shifted back to the center (not shown on the flowchart). As a result, the phase can be automatically relocked around the center of the DAC range. After a certain time (usually a few milliseconds), a stable locking is recovered. Such automatic locking enables a very long-term stability, as shown in figure 4.1(c) for a 7-hour recording. Typically, recentering occurred once per hour.

The inset in figure 4.1(c) corresponds to a one-second zoom. The standard deviation (with a sampling rate of 250 kHz) is 0.50 ± 0.05 mV, which can be translated into a phase fluctuation of $1.7° \pm 0.1°$ ($1.5°$ if corrected from detector noise). Over 1 hour, the standard deviation raises to 1.7 ± 0.3 mV, corresponding to $3.1° \pm 0.2°$. The MCU-based locking enables thus a very good phase stability on the short as well as on the long time scales, compatible with most applications, including for instance the use of high squeezing levels [36, 73, 74] in demanding quantum optics and quantum information experiments.

4.2.2 Simple model and set parameters

A simple model can be used to estimate the locking performances based on this algorithm. The phase stability is indeed limited by the ADC resolution ϵ of the microcontroller. In our case, with a number of bits N =12 and a maximum reference voltage $V_0 = 2.5$ V, the

resolution is given by $\epsilon = V_0/2^{12} \simeq 0.61$ mV. Only the voltage fluctuations larger than ϵ can be detected, leading to a minimum detectable phase change $\Delta\theta_0$.

To minimize this value, the best strategy is to use the full dynamic range, and thus having a fringe with close to unity visibility, i.e. a detected voltage $V = V_0 \sin^2(\varphi/2)$. In this case, the minimum detectable phase change is given by:

$$\Delta\theta_0 \simeq 2\sqrt{\frac{\epsilon}{V_0}} = 2\sqrt{2^{-N}} \simeq 1.8^\circ \ . \tag{4.1}$$

For step sizes in the algorithm leading to phase changes smaller than this value, the locking noise, i.e. the measured standard deviation, is expected to be constant, with a value slightly smaller than ϵ. In the general case of a non-unit visibility, V_0 has to be replaced by the fringe amplitude (2.2 V in our case). One way to increase the locking performance would be to combine two 12-bit ADCs to obtain a 24-bit system [71]. Another possibility is to use a logarithmic amplifier in order to increase the resolution around the set point.

We now consider step sizes leading to phase changes larger than the previous one. The resulting phase increment depends on the number of bits N of the DAC, the number n of fringe periods for a full scan and an integer M defined by the user:

$$\Delta\theta = M.\frac{2\pi n}{2^N} \ . \tag{4.2}$$

When the phase step $\Delta\theta$ is larger than $\Delta\theta_0$, the phase fluctuation scales with $\Delta\theta$. The noise is thus driven by the steps. For proper functioning, this regime should be avoided.

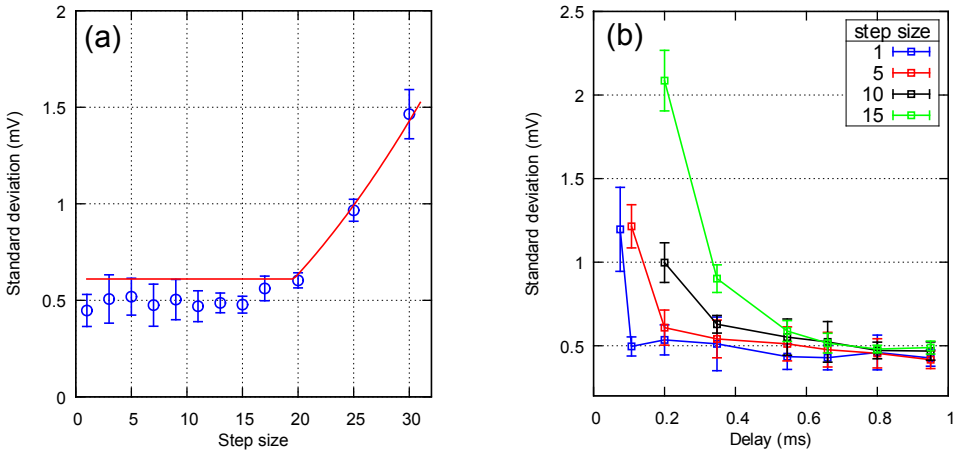

Figure 4.2: (a) Standard deviation as a function of the step size given by the integer M. The solid line is a guide for the eyes, following the model given in the text. (b) Standard deviation as a function of the delay between the output (DAC) and the acquisition (ADC).

For a full characterization of the locking system, and to illustrate this simple model, we studied in a systematic way the behavior obtained for various parameters in the algorithm. Figure 4.2(a) shows the standard deviation for one second as a function of the step size. As predicted, the measured voltage noise exhibits first a plateau and then scales as the square of the step. If the step size is increased further, a stable locking cannot be obtained anymore.

One parameter more difficult to include in this simple model is the temporal delay between the output (DAC) and read (ADC) blocks. With a fixed step size, the delay plays an important role in the locking behavior as shown in figure 4.2(b). Specifically, when

the delay is too long, the bandwidth is too much reduced and cannot compensate for the fluctuations. When the delay is too short, there is not enough time for the PZT to respond. Because the locking algorithm relies on the comparison of the two sequential signal values, the improper response of PZT will produce some disturbance for each step, finally altering the locking. A 1 ms-delay is typically added in the program. A bandwidth around a few kHz is achieved here, limited by the PZT.

4.3 Cavity locking

The microcontroller-based locking is now applied to a more complicated task, i.e. the locking of optical cavities. Two cavities with moderate and high finesse, respectively around 100 and 1000, will be considered, requiring two different execution programs.

4.3.1 Low-finesse cavity

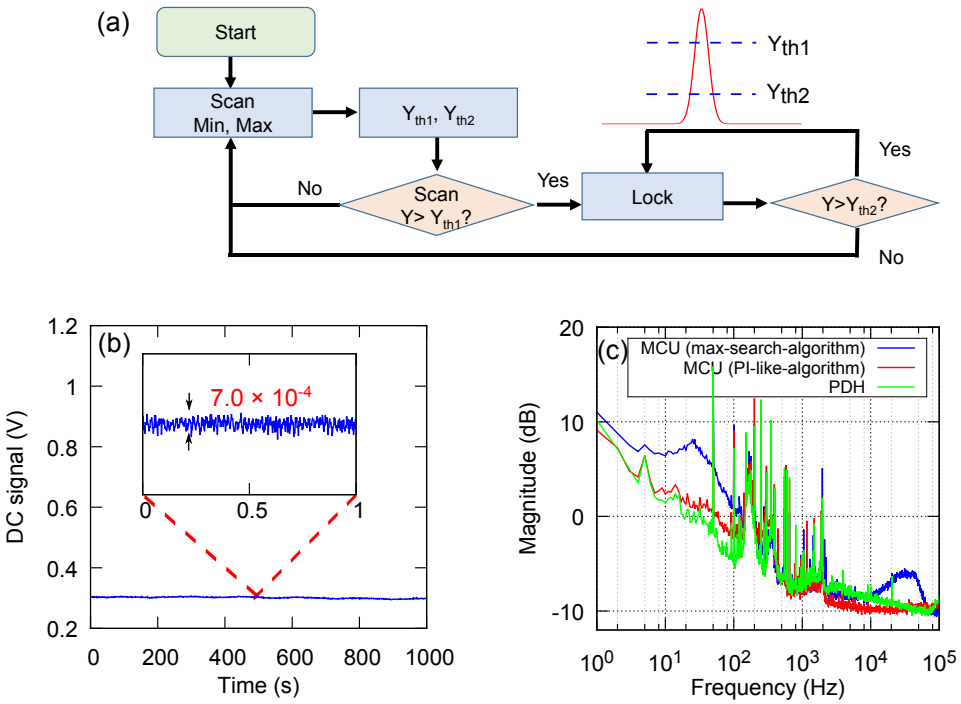

Figure 4.3: (a) Flowchart of the program execution to lock a low-finesse cavity, including peak searching and automatic relocking. (b) Long-term stability. The inset gives a one-second zoom. The standard deviation is normalized to the cavity peak height. (c) Noise spectra for maximum-searching locking, PI-like locking and for locking with the standard analog Pound-Drever-Hall technique.

The locking of a cavity specifically requires a scanning mode to first identify the peak heights and positions. This function can be easily realized with simple programming for the generation of triangle signal. The flowchart of the program execution is given in figure 4.3(a). The microcontroller first sweeps the cavity length and subsequently defines a high and low threshold (Y_{th1} and Y_{th2}). It then sweeps again the length to reach an initial start

point above the high threshold. If the locked signal becomes smaller than the low threshold, the microcontroller will get out of the locking mode and go back to the scanning mode.

To test this method, we used an optical parametric oscillator [74]. The finesse for the pump is around 100 and the 4 cm-long cavity was previously locked by the PDH technique [75], with a phase-modulation at 12 MHz. Figure 4.3(b) confirms the long-term stability and the inset shows a one-second zoom. The standard deviation normalized to the peak height is equal to 7.0×10^{-4}, similar to what is obtained here with the PDH locking (6.6×10^{-4}). For 15 minutes, the normalized standard deviation raises to 4×10^{-3}.

To obtain this result, the locking algorithm has been slightly modified. Indeed, with the maximum-searching algorithm presented previously in Section 4.2.1, the standard deviation is a bit larger (8.0×10^{-4}). This simple approach is however sufficient for many applications. Here, the control has been improved by implementing some proportional feedback using more sophisticated programming. For instance, one can numerically calculate the corresponding derivative of the signal, or simply use the signal difference between the sequential steps, as the gain of the feedback signal. We call this method the PI-like algorithm. The measured noise spectra are finally given in figure 4.3(c) for the three different techniques.

4.3.2 High-finesse cavity

Compared to a low-finesse cavity, locking a high-finesse cavity is more challenging due to the limited resolution of the ADC. For instance, for a finesse of 1000, the number of sampling points to cover the whole peak is around $4096/1000 \simeq 4$ which is obviously insufficient to lock the cavity. To overcome this problem, one can combine two 12-bit ADCs in order to obtain a 24-bit ones as mentioned previously. Another way to address the problem is to use two different scanning modes, namely a long scan and a short scan, as explained now.

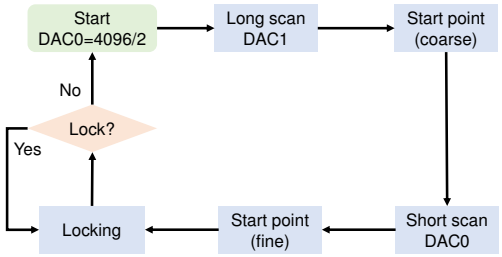

Figure 4.4: Flowchart of the program execution to lock a high-finesse cavity. This scheme includes two different scanning modes controlled by two outputs in order to use the full DAC resolution.

The flowchart of the program execution is given in figure 4.4. One output of the DAC (DAC1) is used for the long scan, which spans over more than a free spectral range in order to identify the rough peak position. Another output (DAC0) is used for the short scan around the peak position identified by the long scan mode and also used for the locking. The two outputs are summed with different gains. Such uneven allocation of sampling over the free spectral range enables the full use of the DAC resolution. Since there are four DACs available in the microcontroller development board, this method can be easily implemented without the need of any additional electronic building.

Figure 4.5 gives an example of the process for locking a 0.5 mm-long cavity [38] with a finesse of 1000. Note that in order to make the re-lock process faster when the cavity is unlocked, the program goes firstly to the short-scan mode instead of directly using the long-scan one. If the short scan still cannot find the peak after 10 sweeps then the program jumps to the long-scan mode.

The performances are displayed in figure 4.6. Figure 4.6(a) provides the temporal stability using the PI-like algorithm for the locking, while figure 4.6(b) gives the spectra for PI-like, maximum-searching and analog dither-and-lock (DTH) techniques. For one second,

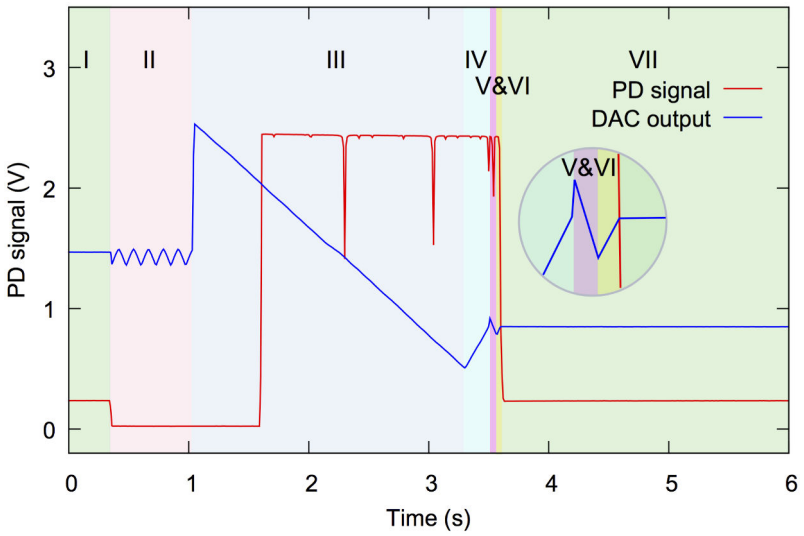

Figure 4.5: Experimental locking process of a cavity with a finesse equal to 1000. The light is measured in reflexion. (I) Cavity is locked. (II) Light is blocked to disrupt the lock and the program goes thus to the short-scan mode. (III) As the short-scan did not enable the relocking in this specific example, the long-scan is started in order to learn the rough peak position. (IV) The output is set at a rough start point determined in the previous step. (V) A short-scan is started to find the precise peak position. (VI) The output is set to the precise start point. (VI) Locking is on.

the standard deviation normalized to the peak height is found to be 4.8×10^{-3} for the PI-like, which is slightly better than the 5.6×10^{-3} given by DTH. The direct maximum-searching provides a standard deviation of 6×10^{-3}. For 15 minutes, the normalized standard deviation reaches 8×10^{-3}. These results show the suitability and efficiency of the microcontroller-based locking with high-finesse cavities.

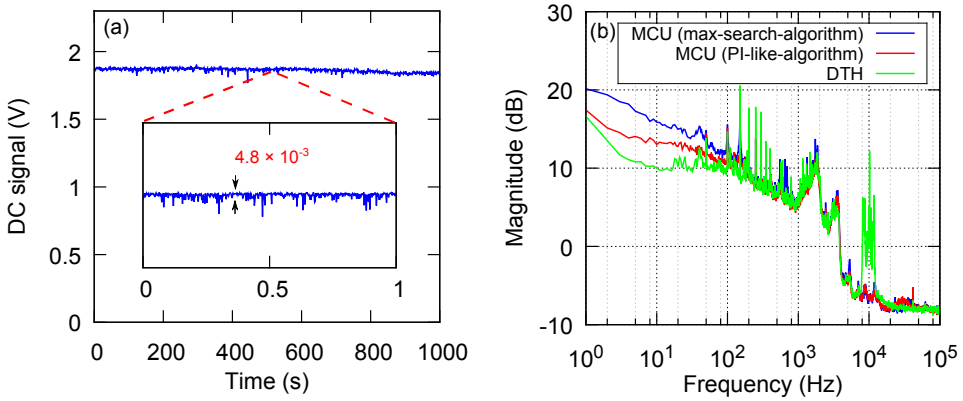

Figure 4.6: (a) Long-term stability for the high-finesse cavity. The inset gives a one-second zoom. The standard deviation is normalized to the cavity peak height. (b) Noise spectrum for maximum-searching locking, PI-like locking and the traditional analog dither-and-lock technique.

As an additional illustration of functions easily implemented by programming, figure 4.7

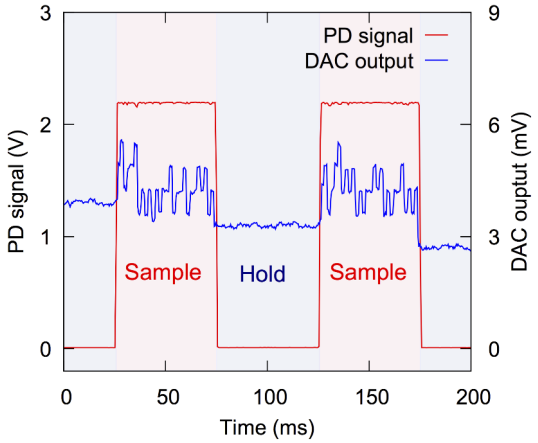

Figure 4.7: Sequential locking for the high-finesse cavity. The light is switched off by mechanical shutters during 50 ms between locking periods. The DAC output holds the last value. This sequential functioning is very useful in many experiments where data acquisitions have to be done in the absence of strong lights, such as in experiments involving photon counting.

finally shows the temporal trace obtained for a sequential locking. The cavity is locked for 50 ms and the light is then blocked. The unit keeps the last output value for a specified time, until the light is switched on again. This sample-and-hold functioning is central to many experiments: for instance, it enables to lock an experiment and then to proceed to acquisition in the photon-counting regime where locking lights have to be off [76].

4.3.3 Hybrid locking

The MCU-based locking as shown previously exhibits almost equivalent performances in many lockings for our experiment. To obtain these results, there are two factors needed to be considered:

1. The feedback of the the locking system should be fast enough. In our case, the feedback bandwidth is mainly limited by the slow response of PZT actuators. With special design of the PZT-actuated mirror, it is possible to achieve a 180 kHz servo bandwidth [77].

2. The interferometer phase or cavity length should show a good passive stability. MCU-based locking based on maximum-searching algorithm cannot compensate fast deviations in an effective way. This condition can be reached with an optimized cavity design for better isolation from mechanical noise and temperature fluctuations.

When the above two conditions are not fulfilled, one can either employ a more sophisticated algorithm or resort to a more robust analog locking system. Here we will introduce a compromised solution where we use analog devices for the locking and the MCU for the re-locking (or initialization). This kind of *hybrid locking* enables us to benefit the robustness of analog locking system and automatic re-locking feature by digital control.

The simple flowchart of hybrid locking system is shown in figure 4.8. When the analog locking is lost, we use the MCU to output a digital signal for resetting the PID, and then output a triangle analog signal for sweeping the cavity. Once the peak is identified, we use the MCU to turn on the PID again. Since the PID parameters are already optimized, the locking of the cavity can be engaged without difficulty. Actually, this is similar to what we usually do when there is no MCU. Instead of using MCU, we manually reset PID and then find back the peak for initializing the locking. The functionality of MCU here in hybrid locking system is to monitor and initialize the locking.

The hybrid locking system is used in our experiment to lock an OPO cavity, which is doubly resonant for the pump at 532 nm and the seed light at 1064 nm as shown in figure 4.8. The error signal of the PDH locking is obtained from the demodulation of the reflected

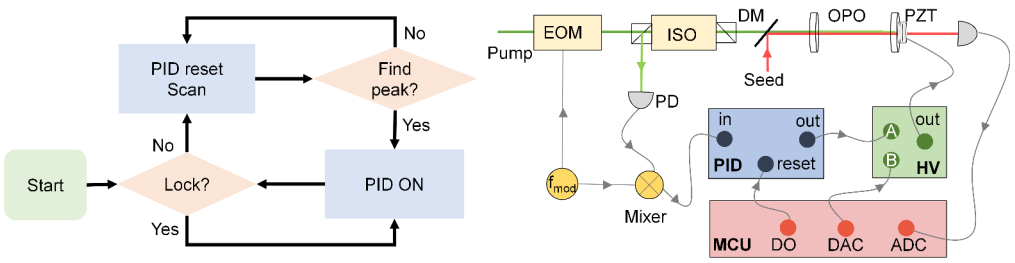

Figure 4.8: (Left) A flowchart for hybrid locking. (Right) Hybrid locking for a double resonant OPO. ISO: isolator; DM: dichroic mirror; IF: interference filter; PD: photodiode; HV: high voltage box. A and B in the high voltage box are two input channels, which will be summed up before amplification. Channel A has a variable attenuation.

phase-modulated pump light. Hence, once the OPO cavity is locked, it must be resonant for pump light. However, the cavity may not be resonant for the seed light due to the different wavelengths.

Figure 4.9 shows the responses of the cavity to the pump and seed when the cavity is scanned with a triangle waveform from a function generator. The peaks of the seed occur at the same position with every other peaks of pump after optimization of the crystal temperature and the laser frequency. As depicted in figure 4.8, the transmitted seed light from the OPO cavity is therefore used to monitor the status of the locking instead of directly using the pump.

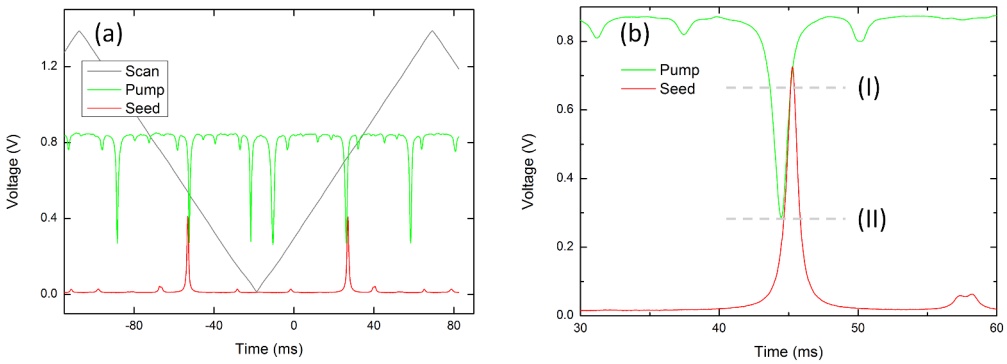

Figure 4.9: (a) Responses of the OPO cavity to the pump and seed when the cavity is scanned with a triangle waveform from a function generator. (b) The peaks for the pump and seed when the phase-matching temperature is optimized. I and II denote the threshold levels for switching to the locking mode.

It is worth noting that the threshold for identifying the seed peak should be carefully set in the experiment. When the cavity is tuned (by changing the temperature of crystal) to be perfectly doubly resonant, then we unlock and sweep the cavity. We find that the relative positions between the pump and seed peaks are slightly different when the cavity is locked or unlocked. When the cavity is locked, the pump power inside the cavity is enhanced, which may lead to thermal effects. As a result, if the threshold is set to be the level I (c.f. figure 4.9) as usual, the cavity might not be locked since the peak of pump is far away from the resonant point. Instead we use the level II for the threshold, which corresponds the peak of pump. Note that the cavity can only be locked at the position located at left side of the

seed peak.

Interestingly, with the same monitored signal from the seed we can also lock the phase between the pump and the seed with fringes due to the parametric interaction. Such phase locking can be conveniently realized with the aforementioned MCU-based digital locking based maximum-searching algorithm. Note that in this scenario, the threshold for identifying the locking status should be set carefully as the parametric interaction will alter the peak value.

4.4 Integration and remote monitor

In order to make the MCU locking system more accessible for daily use, we integrate the "naked" MCU board into a control box. Figure 4.10 shows one of these locking boxes recently used in our lab. The switches, buttons, LEDs, and BNC connectors make it very easy to operate. For example, it enables us to switch from scanning mode to locking mode, and vice versa; to know the locking status via LEDs; to record the locking status with a TTL output; to remotely control (sampling & hold) with a TTL input. With these features, the integrated locking box would facilitate more complex quantum experiments which need many cavities and phase lockings. For the details about the configuration of these boxes, readers can refer to the Appendix E.

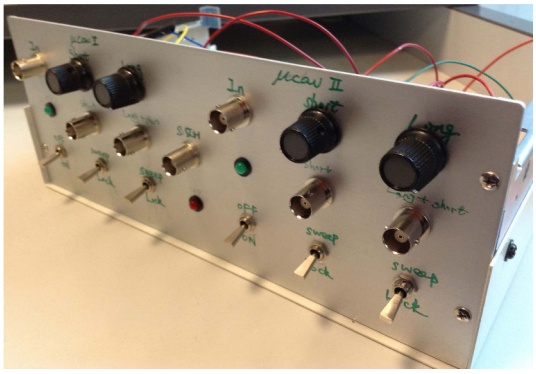

Figure 4.10: Integration box of MCU-based automatic locking system.

In order to realize remote monitor and control of the lockings operating in the lab, we use a Labjack (low cost USB/Ethernet/WiFi based measurement and automation device) [1] to collect the information of each locking and then display the locking status on a computer screen at distance as shown in figure 4.11. These lockings are implemented with the different aforementioned methods. The continuous band indicates a status of locking while the dropping line indicates a loss of locking. Note that it is the infrared light from the transmission of the filtering cavity that is used for locking the OPOs and micro-cavities in the down stream. Therefore, in figure 4.11 it is expected that when the filtering cavity is not locked, all the downstream cavities get unlocked.

[1] Here we use LabJack U6, which offers 14 Analog Inputs, 2 Analog Outputs (12-Bit, 0-5 Volts), 20 Digital I/O. Command/response (software timed) analog input and output typically take 1-4 ms depending on number of channels and communication configuration.

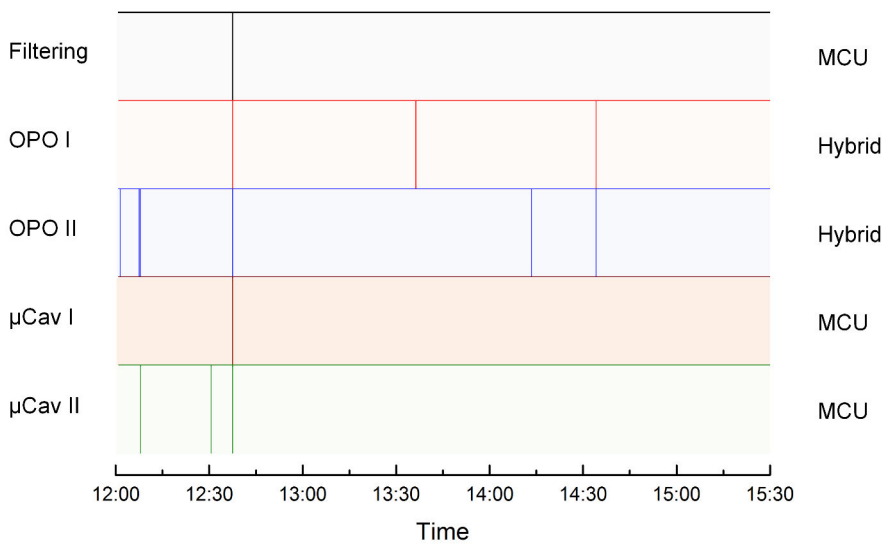

Figure 4.11: Remote monitor of the locking status of the various locking systems. These lockings are implemented with different methods. The continuous bands indicate a state of locking while the dropping line indicates a loss of locking. When the filtering cavity is not locked, all the downstream cavities will get unlocked.

4.5 Conclusion

In this chapter we have presented a microcontroller-based locking system that allows for automatic and sequential locking and is easily scalable. Its applicability to various lockings, including interferometers and optical cavities, has been well demonstrated, offering comparable performances compared to traditional analog locking systems. For some cases that MCU could not achieve desirable performances, a hybrid locking system was proposed, where MCU played the role of monitoring and initiating the locking. Additionally the information of locking status was collected in one location, which not only enabled remote monitor and control of locking, but also allowed to post-process the acquired data. All the experiments implemented in Part II have benefited from such automatic locking system.

Part II

Hybrid Entanglement Generation

5 | Heralded Fock States

Single-photon source only emits one photon at a time, excluding the effect of multi-photon components that occurs with the attenuated coherent light. This anti-bunching effect makes it as a critical source for investigating many quantum phenomena. Single photons are also regarded as ideal carriers for encoding information in *quantum key distribution* (QKD) protocols due to low decoherence and easy transmission. Additionally, single photons are at the heart of linear-optical quantum computation (LOQC) for instance the seminal proposal by Knill, Laflamme and Milburn [28]. More generally, Fock states are the key ingredients in many optical quantum state engineering protocols. For example, they are used as quantum-optical catalysis for generating nonclassical states of light by means of linear optics [78]. Besides, high-fidelity large squeezed Schödinger cat states can be generated using Fock states as initial resources [79].

In this chapter, we will first present the generation of high-fidelity Fock states up to two photons based on a type-II optical parametric oscillator. Then, a novel way to synthesize quantum superposition of the form $\alpha|0\rangle + \beta|2\rangle$ will be introduced as well as its experimental realization. Finally we will investigate a two-photon generation heralded by two-photon detection with a temporal delay between the events and highlight the importance of temporal modes when working in the continuous-wave regime.

5.1 Single-photon state generation

The way to produce single photons can be divided into two categories: deterministic, and probabilistic but heralded. In principle, deterministic emission can be realized using single emitters such as atoms [80], Nitrogen-vacancy center [81], Quantum dot [82]. However, till so far these sources are often limited by the low collection efficiency. As a result, they have a low probability to actually get a single photon on demand. The other way to obtain single-photon source is to use a probabilistic but heralded scheme. One possibility is to use photon pairs emitted in two distinct modes: the detection of a single photon in one mode heralds the generation of a single photon in the other mode [83].

Commonly such photon pairs can be obtained with spontaneous down-conversion as explained in Chapter 2, either by pulsed single-pass configuration [84, 85, 86] or by continuous-wave OPOs [87]. For the latter case, two methods can be used to obtain the two distinct modes. The first one is based on tapping a very small fraction of a squeezed vacuum [88], leading intrinsically to a low count rate. The other method consists in using non-degenerate modes emitted by the OPO. With a type-I nonlinear interaction, signal and idler have the same polarization, thus the only degree of freedom is the frequency. The two correlated modes can be then two modes with frequencies separated by multiples of the cavity free spectral range, as demonstrated in [89]. However, this configuration requires a frequency shift of the local oscillators for the homodyne tomography. Here we use another possibility with a type-II interaction, hence the frequency-degenerate signal and idler modes have orthogonal polarizations and can be easily separated [38].

5.1.1 Principle and model

We start with a two-mode squeezed vacuum state with a squeezing parameter λ [1]:

$$|\psi_{sq}\rangle_{ab} = (1-\lambda^2)^{1/2} \sum_{n=0}^{\infty} \lambda^n |n\rangle_a |n\rangle_b \ , \tag{5.1}$$

where a and b denote the two correlated modes. These modes have orthogonal polarizations at the output of a type II OPO and can be spatially separated with a polarizing beam-splitter. Due to the photon-number correlation, detection of n-photons in one mode will project the other mode into the corresponding Fock state $|n\rangle$. Such conditional preparation of Fock states is thus probabilistic but heralded.

Unfortunately, in reality many imperfections will degrade the fidelity of the generated state. In order to understand and model our experiment, three experimental defects will be discussed:

- conditional detector: photon-number resolution, efficiency, and dark noise
- light source: squeezing level and purity
- general optical losses in the setup

In the following, we are going to consider the defects of each part more or less independently, in order to estimate the importance of each of them. The goal is not to give here a precise and exhaustive model of this experiment but more a study of the "symptomatic" effects of the different parts. For this purpose, we are going to use the POVM formalism (cf Chapter 3) where the heralded sate is given by:

$$\hat{\rho}_{\mathrm{cond},b} = \mathrm{Tr}_a[\hat{\Pi}_a \otimes \mathbb{1}_b \hat{\rho}_{ab}] / \mathrm{Tr}_{a,b}[\hat{\Pi}_a \otimes \mathbb{1}_b \hat{\rho}_{ab}] \ . \tag{5.2}$$

[1] linked to squeezing factor by $\sigma_x^2/\sigma_0^2 = s = (1-\lambda)/(1+\lambda)$.

Practically we will employ the "Qmixer" (cf. Section 3.4.4) to numerically calculate the fidelity of the generated state depending on various parameters [2]. For the details about this simulation, readers can refer to Appendix D (Qmixer). When necessary, analytical expressions will be given for better illustrating the physical meaning.

Conditional detector The detector used in our experiment is not perfect in terms of photon-number-resolving ability, detection efficiency and dark noise. Figure 5.1 shows the fidelity of the conditionally prepared single-photon state and two-photon state as a function of squeezing levels of the initial source. Here we consider two types of detectors, APD and PNRD, with limited detection efficiency and no dark noise. For both types of detectors, the fidelity of the heralded single-photon state decreases as the input squeezing increase. For APD-type detectors, they can not distinguish photon numbers larger than one. Thus the firing of detectors in the conditional path will herald high photon-number states. It seems that such a problem can be effectively solved by using PNRDs. However, due to the limited detection efficiency, they can not neither perfectly distinguish the high photon-number components. Even though they enable to reach a higher fidelity compared to APDs, yet this advantage will fade out as squeezing goes smaller. This is because the high-photon number components $|n\rangle\langle n|$ in the initial state are scaled as λ^n. The dark noise of the detectors is omitted here, which is quite fair since we use very low-noise superconducting single-photon detectors (SSPDs) in our experiment.

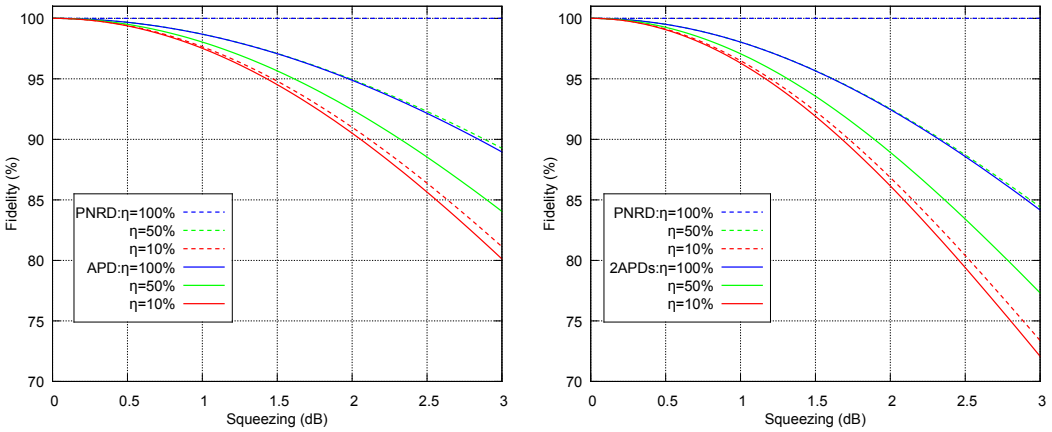

Figure 5.1: Fidelity of the conditionally prepared single-photon state (left) and two-photon state (right) as a function of squeezing levels of the initial EPR source. These plots are done with two types of detectors, APD and PNRD, with various detection efficiencies. Here we consider detectors without dark noise.

Light source In the above discussion, the squeezing is assumed perfectly pure. Actually for an OPO, the purity of squeezing degrades as the pump power increases (cf. Section 2.2). Figure 5.2 shows the fidelity of the conditional state as a function of anti-squeezing of the initial source when the squeezing level is fixed. We can see that as the anti-squeezing increases, the purity of squeezing will decease accordingly. As a result, the fidelity of the prepared Fock state will degrade. Indeed the degradation of squeezing purity is due to the losses. Specifically the output squeezed state can be regarded as a perfect one after a given

[2] We can also resort to the version based on the Wigner function, as did in [20] for obtaining corresponding analytical results.

loss η:

$$\begin{aligned} s'_x &= (1-\eta) + \eta s_x \\ s'_p &= (1-\eta) + \eta s_p \ . \end{aligned} \tag{5.3}$$

Therefore, the loss on the initial squeezing can be seen as an equivalent one on the state prepared from a pure squeezed state.

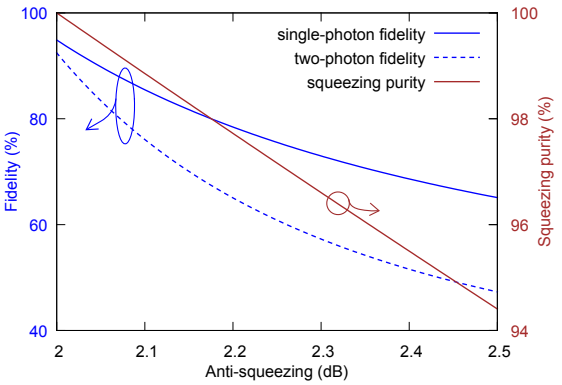

Figure 5.2: Fidelity of conditionally prepared Fock state as a function of anti-squeezing of the initial source when the squeezing level is fixed to be -2 dB. The conditioning detector is a perfect on/off detector.

Losses Losses on the Fock state $|n\rangle$ will result in a statistical mixture of Fock states with lower photon numbers:

$$|n\rangle \xrightarrow{Losses} \sum_{k=0}^{n} \binom{n}{k} \eta^k (1-\eta)^{n-k} |k\rangle\langle k| \ , \tag{5.4}$$

where $\binom{n}{k}$ is binomial coefficient and η is the power transmission. This equation gives the fidelity of η^n for Fock states $|n\rangle$, which is plotted in figure 5.3.

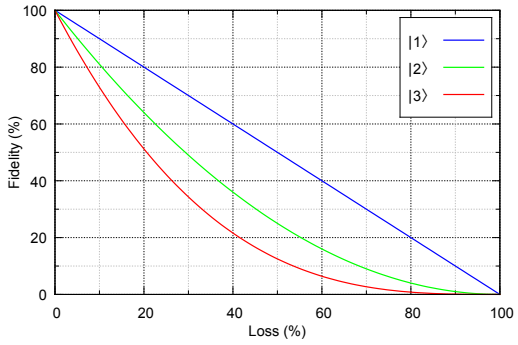

Figure 5.3: Decoherence of Fock states $|n\rangle$ under losses.

Clearly Fock states with higher photons suffers more from the losses. For instance, to achieve fidelity above 50%, the losses should be less that 50%, $\sim 30\%$ and $\sim 20\%$ for states $|1\rangle$, $|2\rangle$ and $|3\rangle$, respectively. The losses here can occur in any stages, including the state preparation, propagation and characterization.

We now turn to the experimental realization.

5.1.2 Experimental setup

The experimental setup is sketched in figure 5.4. The two-mode squeezed vacuum state is generated by a semi-monolithic OPO, as detailed in Chapter 2. Then the two orthogonally polarized modes are spatially separated with a polarizing beam-splitter. One mode is directed to the conditioning path where the light is detected by a SSPD after a series of spectral filtering. The detection event will herald the presence of a single-photon state in the other mode, which is then characterized by quantum state tomography via a homodyne detection. The isolator in the signal path is used to eliminate the backscattered photons from entering into the conditional path. All the measurements are acquired and processed by an oscilloscope/computer. In the following, we will get into more details about each part of the experimental setup.

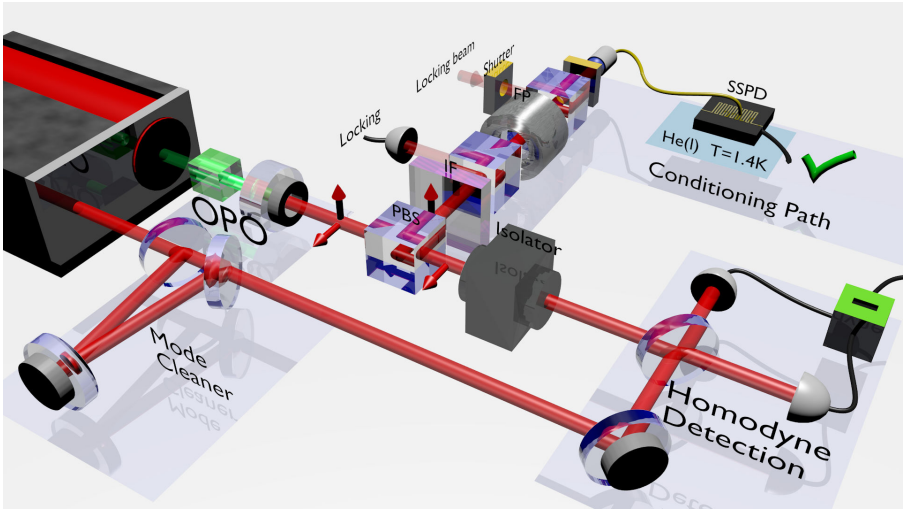

Figure 5.4: Experiment setup for generating single-photon state. A two-mode squeezed state is prepared by a type-II OPO operating far below the threshold. The signal and idler modes are separated via a polarizing beam-splitter. The idler light is sent through a set of spectral filtering including an interferential filter (IF) and a Fabry-Pérot cavity (FP) before being detected by a superconducting single-photon detector. The detection event in the conditional path heralds a single-photon state, which is then characterized by homodyne measurement.

Conditioning path In the conditional path there are two main stages: frequency filtering and single-photon detection. Here we give a brief discussion about their configurations and the effects on the prepared state.

- *Filtering stage*: The down-converted photon pairs out of an OPO can occur in any combination of two frequencies $\omega_0 - n\Delta$ and $\omega_0 + n\Delta$ within the phase-matching window, where ω_0 is the central frequency of down-converted light, Δ is the free spectral range of the OPO cavity and n is an integer. Since the optical frequency of the local oscillator in the homodyne detection is ω_0, it can only detect the mode at this specific degenerate frequency. In the other words, detection of a photon at $\omega_0 - n\Delta$ ($n \neq 0$) will herald a vacuum state [3] at ω_0 since the actual single photon is at $\omega_0 + n\Delta$

[3] Strictly speaking it should be a thermal state, but quite closed to vacuum due to the very low pump power of the OPO.

being ignored by the homodyne detector. Therefore, in order to make sure that the photons detected in the conditioning path come from the degenerate frequency, it is necessary to eliminate those photons at other frequencies. The filtering stage consists of an interferential filter and a μCavity (450-μm cavity length), which finally gives a -25 dB rejection of the non-degenerate modes (cf. [38] for more details).

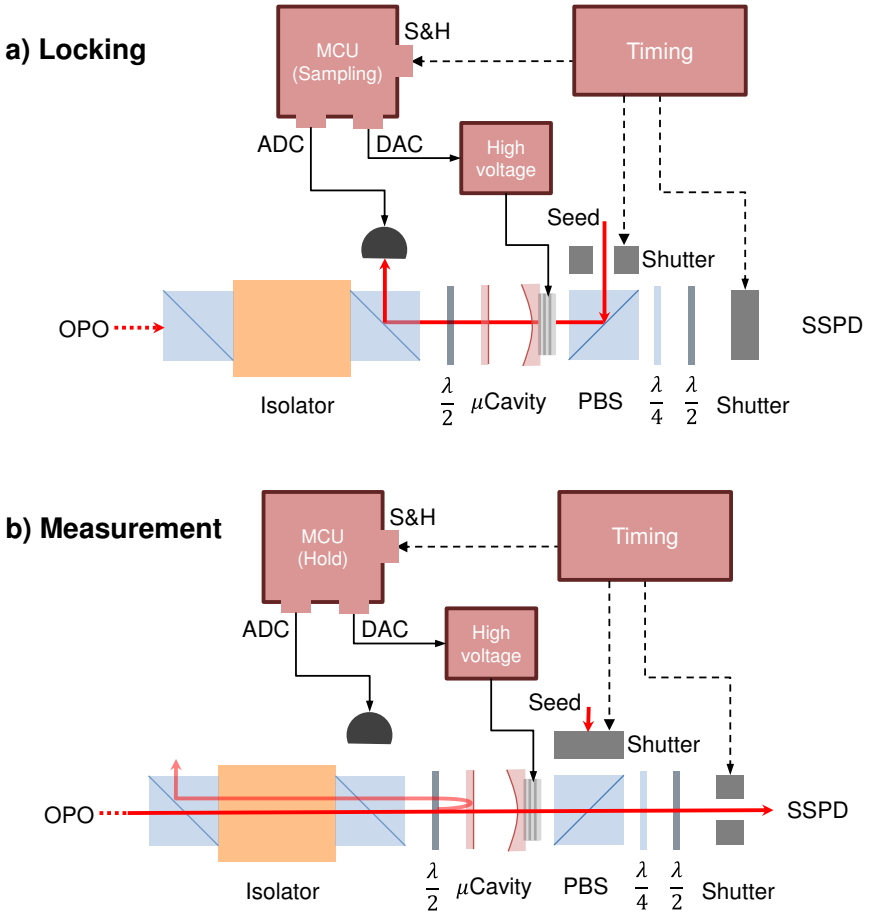

Figure 5.5: Steps for experiment running. (a) During the locking period, the shutter for the seed is open while the path to the SSPD is blocked. The microcontroller is set to be in the "sampling" mode, thus completing locking feedback. (b) In the measurement time, the status of the two shutters are exchanged and the microcontroller is set to be in the "hold" mode. It will output constantly the very last value onto the PZT thus "freezing" the cavity to stay on resonance.

■ *Conditional detector*: In the experiment we use a superconducting single-photon detector (SSPD). it enables high detection efficiency at 1064 nm (70%), negligible dark counts ($<$ 10 Hz) and low timing jitter (30 ps). In principle, heralded preparation of single-photon states does not require an efficient detector when the pump power is very low, as can be seen in figure 5.1. However in practice, highly efficient detector is favorable for increasing the preparation rate. Moreover, higher count rates will improve the signal to noise ratio for the conditioning because the dark noise of the detector will give out false triggers, thus degrading the fidelity of the generated state. Timing jitter of the detector is also important due to the fact that the heralded single-photon state

in our experiment is temporally spread within a temporal mode defined by the OPO cavity ($\sim$ 20 ns). If the timing of the heralded detection has a large uncertainty, then the generated state will have a poor overlap with the given temporal mode centered at a fixed position, thus degrading the fidelity of the heralded single-photon state. For more details about SSPDs, readers can refer to the Appendix F.

- *Sampling and locking*: The μCavity used in the conditional path is locked with a microcontroller, as detailed in Chapter 4. In order to avoid any extended cavity with the OPO, an optical isolator (not shown in figure 5.4) is inserted in the conditional path. Additionally, to eliminate the scattered photons from the locking beam, the experiment is designed to operate in a cyclic fashion as shown in figure 5.5 with a locking period and a measurement period. In the "locking" period, the shutter [4] for the seed is open while the path to SSPD is blocked. The microcontroller is set to be in the "sampling" mode, thus completing locking. In the "measurement" period, the status of the two shutters are exchanged and the microcontroller is set to be in the "hold" mode. It will constantly output the very last value onto the PZT thus "freezing" the cavity to keep it on resonance.

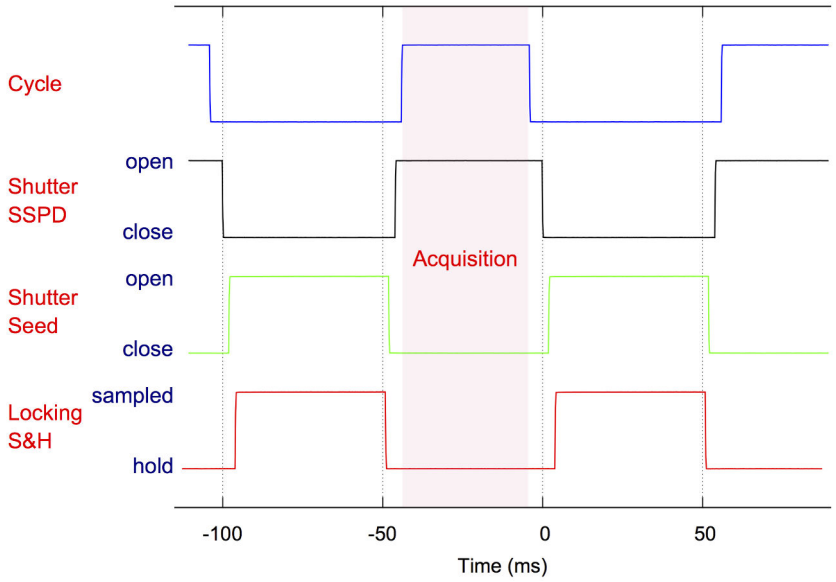

Figure 5.6: Diagram of timing setting for control signals.

- *Timing*: Since the experiment is operated alternately between "locking" and "measurement" periods, hence controlling the timing of various TTL signals are necessary. Figure 5.6 shows the timing setting for those signals. The temporal delays between the signals are set in purpose. From "locking" to "measurement", first the microcontroller is set to be in "hold" before closing the shutter for the seed to make sure that a proper value for cavity resonance is taken. Then the shutter for SSPD can be opened since the seed beam is already blocked. From "measurement" to "locking", these steps should be reversed, namely in the following order: close the shutter for SSPD, open the shutter for seed and set microcontroller to be in "sampling" mode. Note that there is another periodical signal called "cycle" as shown in figure 5.6, which is used for as triggers

[4] The shutter used here is a mechanical beam blocker (SR475 from *Stanford Research System*), which has a 3-mm aperture and can operate up to 100 Hz.

together with pulsed signal from the SSPD for heralding the single-photon generation. This "cycle" triggering signal can be replaced directly by the "shutter SSPD" signal if we can properly estimate the rising time and falling time of the shutter.

Signal path The heralded single-photon state will propagate into this path. Therefore the loss in this channel should be as low as possible: for instance we should use very good anti-reflection coatings (typically $\sim 1\%$) for optics elements in the path, or simply use less elements. The total intensity transmittance of propagation η_{prop} is estimated to be 93% mainly limited by the required optical isolator. The other origin of losses is the detection efficiency of the homodyne detection. To achieve high-fidelity states, there are two critical points:

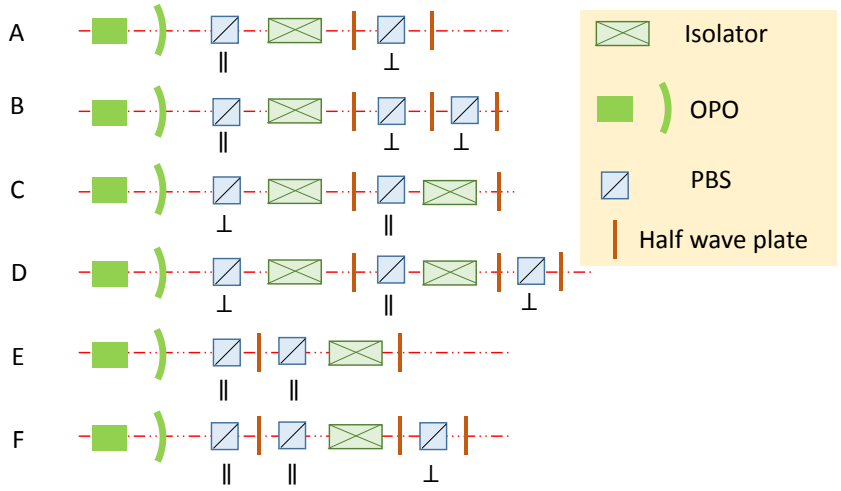

Figure 5.7: Various configurations for the optical isolator have been tested to reduce the backscattered photons from homodyne detection. $\perp$ denotes the isolation of photons with a polarization orthogonal to the one of the local oscillator in homodyne detection, while $\parallel$ denotes the isolation of photons with the same polarization. The configuration F gives out the best isolation performance since majority of the backscattered photons are in the same polarization as the local oscillator one.

- *Isolator configuration*: There is an optical isolator in the signal path, which is necessary in the experiment in order to get rid of the backscattered photons from the homodyne detection. The scattering effect can occur from any surfaces impinged with a high power local light, such as lenses after the beam splitter (not shown in the figure 5.4) and photodiodes. Since the scattered photons in normal direction of surfaces are perfectly mode-matched with the signal, thus they can efficiently propagate into the conditional path. Even worse, these scattered photons are indistinguishable with the real heralding photons. This coherent contamination results in asymmetric marginal distributions [20]. Two ways are used to reduce the scattering: tilting the elements' surfaces to avoid normal incidence and using Ion-Beam-Sputtered (IBS) coating. Various configurations for the optical isolator have been tested as shown in figure 5.7. The best isolation performance is obtained with the configuration F since majority of backscattered photons are in the same polarization as the local oscillator one.

- *Homodyne detection*: The homodyne detection includes a local oscillator provided by the output of a "mode cleaner" cavity (with a finesse of 1000) and a pair of InGaAs pho-

todiodes [5] with a quantum efficiency $\eta_{phot} = 97\%$. There are mainly three parts limiting the detection efficiency of homodyne detector: mode-matching between the signal and local oscillator, quantum efficiency of photodiodes, and distance between shot noise and electronic background. The efficiency due to the mode overlap η_{vis} is quadratically linked to visibility of the oscillator-signal interference V: $\eta_{vis} = V^2 = 0.98^2 \approx 0.96$. An electronic noise being N dB below the vacuum noise at the central frequency leads to an effective efficiency $\eta_{noise} = 1 - 10^{-N/10}$ [90]. The spectrum of our homodyne detector with a 6-mW local oscillator is given in figure 5.8. The distance between the short noise and electronic noise is more than 20 dB at low analysis frequency and 16 dB at the frequency of 50 MHz. Considering an OPO bandwidth about 50 MHz, it translates to an effective efficiency of $\eta_{noise} = 96\%$. All the contributions finally lead to an overall detection efficiency: $\eta_{HD} = \eta_{phot} \times \eta_{vis} \times \eta_{noise} \simeq 90\%$.

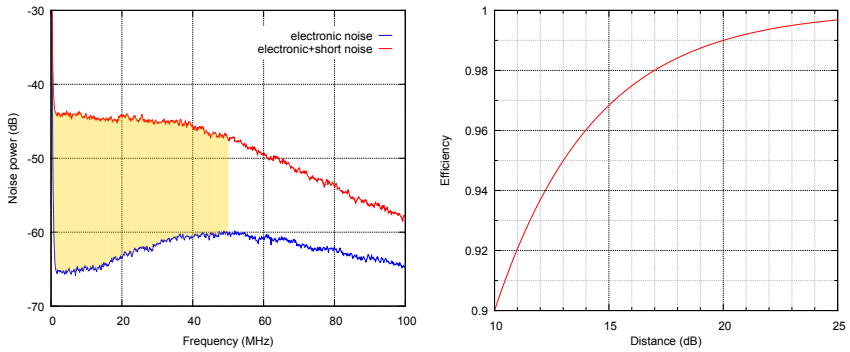

Figure 5.8: (Left) Spectrum of the homodyne detection. The yellow region highlights the 50 MHz bandwidth of the OPO cavity. (Right) Effective efficiency as a function of the distance between the shor noise and electronic noise.

We now explain how the data are acquired and finally processed.

Data acquisition and processing Each detection event in the conditional path heralds the preparation of a single photon in the signal path, which is then sent to the homodyne detection. The output homodyne signal is recorded automatically by a designed software and then post-processed for obtaining corresponding quadrature values. Here we will detail these two steps: data acquisition and data processing.

- *Data acquisition*: The homodyne signal is acquired with a high-speed oscilloscope (Lecroy WaveRunner 610Zi) remotely controlled by a master computer via a LAN connection [6]. The sampling rate is set to 10 Gs/s. For each trigger, it will register 100-ns homodyne signal called a "segment". The time of acquisition window is large enough comparing to the temporal mode of the heralded single-photon state (~ 20 ns). The oscilloscope is run in a so-called "sequence mode". N (typically 1000) segments are accumulated in the oscilloscope memory before data transferring.

[5] Fermionics, 500-μm diameter of detection area

[6] Actually there is another operation mode used in our experiment. Instead of transferring data from the oscilloscope to a computer via LAN connection, we can directly run the software in the oscilloscope and transfer data from a shared memory managed by the operating system. This operation mode can strongly minimize the time of data transferring (cf. Appendix in [20]). However for experiments that require the some phase information, we will use another oscilloscope (Lecroy WaveSurfer 434). In this case, these two oscilloscopes should be synchronized and this can only be realized with the technique based on LAN connection. In this manuscript, we only use this general technique for all the experiments mentioned afterwards.

- *Data processing*: Due to the limited bandwidth of the OPO cavity, the heralded photon is spread in a given temporal mode of a finite duration. The generated single photon is defined by the creation operator:

$$\hat{A}_f^\dagger = \int f(t)\hat{a}^\dagger(t)dt \ , \tag{5.5}$$

where $f(t)$ is the temporal mode function and $\hat{a}^\dagger(t)$ represents the instantaneous creation operator at time t.

The output signal from the homodyne detector is continuous and each measurement corresponds to a quadrature measurement at time t, which is given by

$$\hat{I}_-(t) \propto \alpha_{LO}(t)[\hat{a}(t)e^{-i\theta} + \hat{a}^\dagger(t)e^{i\theta}] \ . \tag{5.6}$$

To infer the quadrature value of the state, we can multiply the instantaneous signal from the homodyne detection with the mode function and integrate it over time:

$$\int f(t)\hat{I}_-(t)dt \propto \alpha_{LO}[\hat{A}_f e^{-i\theta} + \hat{A}_f^\dagger e^{i\theta}] \propto \hat{X}_\theta \ , \tag{5.7}$$

where we consider a local oscillator with a constant amplitude. This approach works if the temporal response of the acquisition electronics (typically on a scale of nanoseconds) is fast compared to the duration of the mode of interest [7].

In the ideal case of very low pump power and no additional filtering in the conditioning path, the temporal mode is given by a double-decaying exponential profile, $f(t) = \sqrt{\pi\gamma}e^{-\pi\gamma|t|}$, where γ is the FWHM bandwidth of the OPO cavity. In practice the temporal mode function can be arbitrarily chosen for maximizing the single-photon fidelity. The effect of temporal modes on the reconstructed state is presented in the next section.

5.1.3 Results and discussion

Since the single-photon state is phase invariant, the phase of each measured quadrature is not required for the state tomography. In this experiment, the phase of the local oscillator is thus scanned for obtaining a random distribution of the phases. The accumulated quadrature measurements (typically 50,000 data points) after post-processing with an appropriate temporal mode are used for the state reconstruction with a C++ written MaxLik algorithm. For the state generated in the experiment, a truncation of the Fock space up to $|6\rangle$ is enough, and 200 iterations of the algorithm gives a reasonable accuracy.

High fidelity single-photon state The diagonal elements of the reconstructed density matrix is given in figure 5.9 as well as the corresponding Wigner function. Without any correction, the obtained single-photon component reaches 78.0%. By taking into account the detection loss of 15%, a single-photon fidelity of 91.5% is inferred. Thanks to the low pumping power (1 mW for a threshold of 80 mW), the two-photon component is limited to 1%. Benefited from the highly efficient SSPD (70%) the heralding rate for single-photon generation reaches 300 kHz.

[7] For pulsed parametric down-conversion, the temporal mode is defined by the pulse shape. In this case, $\alpha_{LO}(t) \propto f(t)$, and hence $\int \hat{I}_-(t)dt \propto \hat{X}_\theta$. Because of the slow electronics' response, the integration occurs in this setting automatically. The output of the homodyne detector is an electrical pulse whose shape is determined by the response function, and magnitude is proportional to the quadrature. Here the bandwidth of homodyne detection has to be larger than the repetition rate of the pulses (typically ∼100 MHz) in order to distinguish the adjacent pulses.

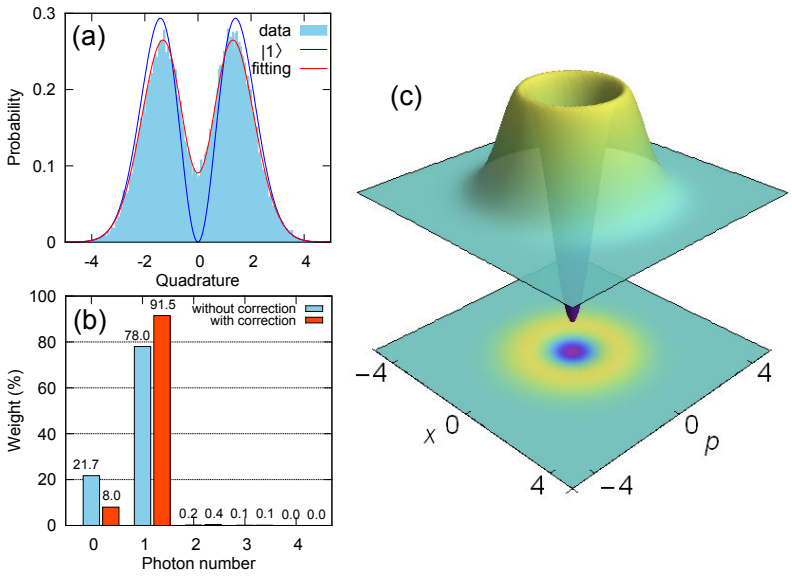

Figure 5.9: High-fidelity single-photon state. (a) Marginal distribution from 50,000 quadrature measurements with average phases. The red solid line is a fit of the experimental data while the blue solid line indicates a perfect single-photon state. (b) Photon-number distribution of the generated state, with and without correction for the 15% detection loss. (c) Corresponding Wigner function without loss correction.

Fidelity and temporal modes For the low pumping assumption, the heralded single-photon state in a temporal mode $f(t)$ can be expressed as

$$|\Psi\rangle = \int f(t)\hat{a}^\dagger(t)dt \ . \tag{5.8}$$

If we apply another mode function, say $g_1(t)$, in the multiplication with the homodyne signal, then what kind of measurement results can we get?

We can always find a series of norm-orthogonal functions $g_k(t)$ among which the first one is $g_1(t)$. They satisfy the orthogonality and completeness relations:

$$\begin{aligned} \int g_k(t)g_{k'}^*(t)dt &= \delta_{kk'} \ , \\ \sum_k g_k(t)g_k(t') &= \delta(t-t') \ . \end{aligned} \tag{5.9}$$

Then we can decompose the single-photon state in this basis:

$$|\Psi\rangle = \int \sum_k c_k g_k(t)\hat{a}^\dagger(t)dt = \sum_k c_k|1\rangle_k \ , \tag{5.10}$$

where $|1\rangle_k$ means there is one photon in the mode g_k and vacuum in the other modes and the coefficient c_k is given by

$$c_k = \int f(t)g_k^*(t)dt \ . \tag{5.11}$$

So the corresponding density matrix is given by

$$\hat{\rho} = \sum_{k,k'} \rho_{kk'}|1\rangle_{kk'}\langle 1| \ , \tag{5.12}$$

where

$$\rho_{kk'} = c_k c_k^* = |c_k|^2 \ . \tag{5.13}$$

If we only focus on the state in the mode $g_1(t)$, then we can trace over the other modes, which results in

$$\hat{\rho}' = \rho_{11}|1\rangle_{11}\langle 1| + (1-\rho_{11})|0\rangle_{11}\langle 0| \ . \tag{5.14}$$

Clearly the single photon fidelity is given by

$$\mathcal{F} = |c_1|^2 = \left| \int f(t) g_1^*(t) dt \right|^2 , \tag{5.15}$$

which is determined by the overlap between the actual temporal mode and the mode on which we project.

Particularly, when there is only temporal mismatch between the temporal modes (i.e. temporal delay), the temporal modes are given by:

$$\begin{aligned} f(t) &= \sqrt{\pi\gamma} e^{-\pi\gamma|t|} \\ g(t) &= \sqrt{\pi\gamma} e^{-\pi\gamma|t-\Delta t|} \ . \end{aligned} \tag{5.16}$$

Thus the fidelity reads as

$$\begin{aligned} I &= e^{-\pi\gamma|\Delta t|}(1+\pi\gamma\,|\Delta t|) \\ \mathcal{F} &= I^2 \ . \end{aligned} \tag{5.17}$$

In the other case where these only exits a spectral mismatch (i.e. temporal duration), we can consider the following temporal modes:

$$\begin{aligned} f(t) &= \sqrt{\pi\gamma} e^{-\pi\gamma_2|t|} \\ g(t) &= \sqrt{\pi\gamma} e^{-\pi\gamma_1|t|} \ . \end{aligned} \tag{5.18}$$

The fidelity can thus be obtained as

$$\mathcal{F} = \frac{4\gamma_1\gamma_2}{(\gamma_1+\gamma_2)^2} \ . \tag{5.19}$$

Figure 5.10 shows the experimental results for these two cases where the fitted lines are given by assuming an OPO bandwidth of 53 MHz.

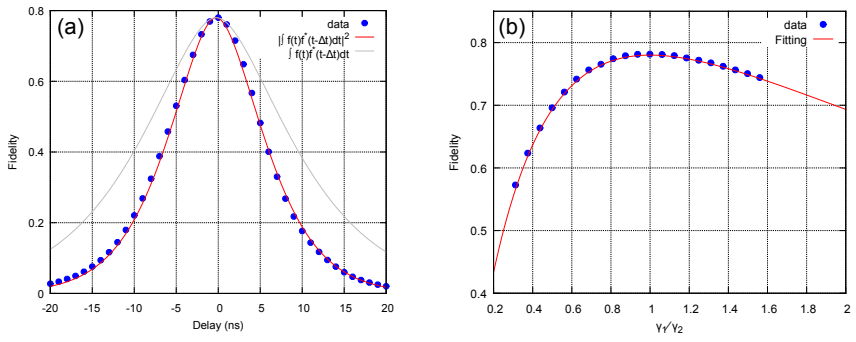

Figure 5.10: Effect on single-photon fidelity in the cases of temporal mismatch (a) and spectral mismatch (b). The fitting curves are given by using an OPO cavity bandwidth of 53 MHz.

5.2 Two-photon state generation

As introduced at the beginning of this chapter, the detection of two photons in the conditional path will herald the generation of two-photon Fock state. The effects of various imperfections in the experiment are shown in figures 5.1, 5.2 and 5.3. Generally speaking, the two-photon state is more sensitive to the losses. In this section, we will present the experimental realization of high-fidelity two-photon Fock state. The photon statistics in the conditional path will also be discussed, such as the photon bunching effect of the heralding photons.

5.2.1 Experimental setup

The experimental setup is presented in figure 5.11. It is very close to the one used for single-photon generation except for the conditional detector. The two-photon detector is realized by two SSPDs after a 50:50 beam-splitter. The coincident gate is configured in the oscilloscope. The accepted coincidence window between the two heralding triggers is set to be 1 ns, which imposes a negligible effect on the fidelity of conditional state. Given coincidence event in the conditioning path, the heralded state is then characterized by quantum state tomography performed via a homodyne detection. Note that in order to increase the heralding rate, the pump power is increased up to 2 mW which is still far below the threshold (about 80 mW).

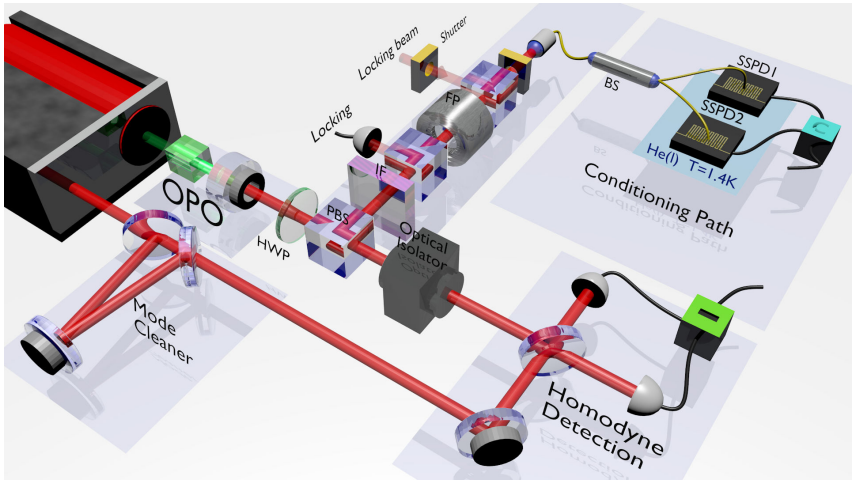

Figure 5.11: Experiment setup for generating two-photon Fock state. The two-photon detection in the conditional path is realized with two SSPDs after a 50:50 beam-splitter.

5.2.2 High fidelity two-photon state

The homodyne signal is acquired and processed using the same way as in single-photon case. Figure 5.12 presents the results of a high-fidelity two-photon Fock state obtained in our experiment: the histogram of the measured quadrature values, the diagonal elements of the reconstructed density matrix and the corresponding Wigner function. Due to the very low pump power, the three-photon component is limited around 3%. The two-photon component is 58.3% without any corrections. To the best of our knowledge, this is the highest value reported to date. By taking into account the detection losses of 15%, we infer a value as high as 79.0%. Assuming of a single-photon fidelity of 78%, the expected

two-photon fidelity is $(78\%)^2 \approx 60\%$ which is in good agreement with the value obtained in our experiment. The two-photon state is indeed more sensitive to the losses. Thanks to the highly efficient SSPDs, the heralding count rate reaches 150 Hz and the total acquisition time only takes around 20 minutes for accumulating 50,000 quadrature measurements.

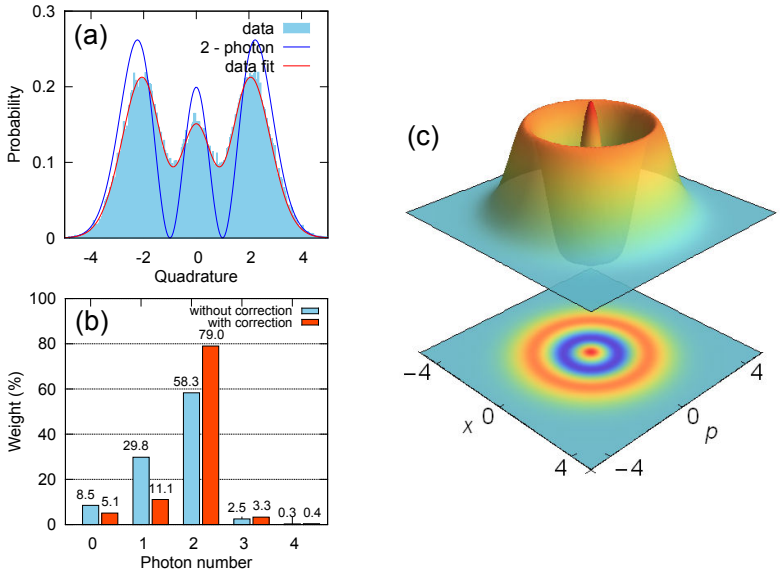

Figure 5.12: Generation of high-fidelity two-photon Fock state. (a) Marginal distribution from 50,000 quadrature measurements with phase averaging. The red solid line is a fit of the experimental data while the blue solid line indicates a perfect two-photon state. (b) Photon-number distribution of the generated state, with and without correction for detection losses of 15%. (c) Corresponding Wigner function without loss correction.

5.2.3 Properties of the photon statistics

The down-conversion process is a stochastic process, or rather a *Poisson process*. For such a process, the interval time between each pair of consecutive down-conversion events follows an exponential distribution and all of these inter-arrival times are independent from each other. To investigate this photon statistics, we use only one SSPD in the conditional path. Given the dead time between segment acquisition ($\approx 1\ \mu s$) in our oscilloscope, the measured count rate is attenuated to about 1.3 kHz. Figure 5.13(a) presents the probability density as a function of the inter-arrival time between two events. The fitting line is given by

$$P(t) = \lambda^2 t e^{-\lambda t}\ , \tag{5.20}$$

with a mean value of $2/\lambda$. The parameter λ used in the fitting is $1/0.36$(ms), thus giving a mean interval time of 0.72 ms. The average count rate is inferred to be about 1.4 kHz which is consistent to the measured value.

Another aspect about photon statistics is the photon-bunching effect in the conditional

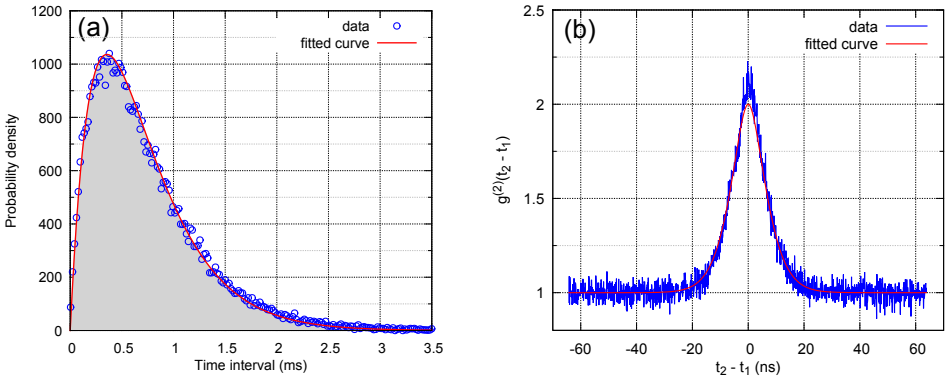

Figure 5.13: (a) Probability density as a function of inter-arrival times between two consecutive events in the down-conversion process. (b) Second-order correlation function $g^{(2)}(|t_2 - t_1|)$ in the conditional path.

path. Theoretically, the second-order correlation function $g^{(2)}$ is given by [91]:

$$\begin{aligned} g^{(2)}(t_2 - t_1) &= \frac{\langle \hat{a}^\dagger(t_1)\hat{a}^\dagger(t_2)\hat{a}(t_2)\hat{a}(t_1)\rangle}{\langle \hat{a}^\dagger(t_1)\hat{a}(t_1)\rangle \langle \hat{a}^\dagger(t_2)\hat{a}(t_2)\rangle} \\ &= 1 + (\frac{e^{-\mu|t_2-t_1|}}{2\mu} - \frac{e^{-\lambda|t_2-t_1|}}{2\lambda})^2/(\frac{1}{2\mu} - \frac{1}{2\lambda})^2 \ , \end{aligned} \tag{5.21}$$

where

$$\begin{aligned} \lambda &= \pi\gamma + \varepsilon \\ \mu &= \pi\gamma - \varepsilon \ , \end{aligned} \tag{5.22}$$

ε is the nonlinear gain coefficient and γ is the FWHM bandwidth of the OPO cavity. In the approximation of low pumping power ($\varepsilon \ll \gamma$), we have

$$g^{(2)}(t_2 - t_1) = e^{-2\pi\gamma|t_2-t_1|}(1 + \pi\gamma\,|t_2 - t_1|)^2 + 1 \ . \tag{5.23}$$

From the above equation we can notice that $g^{(2)}(t_2 - t_1)$ increases from 1 to 2 when $|t_2 - t_1|\gamma$ decreases from infinity to zero, which means that the trigger events are bunched in time. Such bunching effect will favor our two-photon experiment.

Figure 5.13(b) shows the measured $g^{(2)}(t_2 - t_1)$ with two SSPDs in the conditional path. The fitting curve is obtained with the parameter $\gamma = 50$ MHz. The slight mismatch of $g^{(2)}(0)$ is due to the imperfect separation of the signal and idler modes. In ideal case, the state in conditional path is a thermal state, thus giving $g^{(2)}(0) = 2$. For the general case, we detail it in the next section.

5.3 Engineering of two-photon superposition states

The slight deviation of $g^{(2)}(0)$ leads us to notice that mixing the signal and idler modes can provide a way to engineer states of the form $\alpha|0\rangle + \beta|2\rangle$. In the section, we will discuss about this technique from basic principles to the experimental implementation.

5.3.1 General protocol

As shown in figure 5.14(a), we start with a two-mode squeezed vacuum state $|\psi\rangle$ from a type-II OPO:

$$|\psi\rangle \propto \sum_n \lambda^n |n,n\rangle_{a,b} = \sum_n \lambda^n \frac{\hat{a}^{\dagger n}\hat{b}^{\dagger n}}{n!}|0,0\rangle_{a,b} \ , \tag{5.24}$$

where λ is the squeezing parameter, $\hat{a}^\dagger$ and $\hat{b}^\dagger$ are creation operators for the orthogonal modes a and b, respectively.

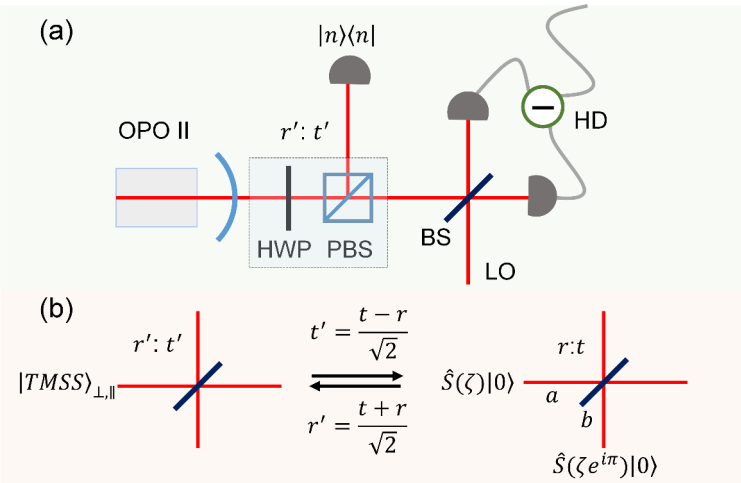

Figure 5.14: (a) General scheme for generating states of the form $\alpha|n-2\rangle+\beta|n\rangle$, which is a superposition of two Fock states with the same parity. (b) Two equivalent ways for calculation with a 45° rotation in phase space. Note that the two-mode squeezed state (TMSS) is equivalent to two squeezed states.

A half-wave plate (HWP) and a polarization beam splitter form a polarization-dependent beam splitter with an amplitude reflectance r' and transmittance t'. In the Heisenberg picture, the evolution of operators are given by

$$\begin{aligned} \hat{a}^\dagger &= t'\hat{a}^\dagger + r'\hat{b}^\dagger \\ \hat{b}^\dagger &= t'\hat{b}^\dagger - r'\hat{a}^\dagger \ . \end{aligned} \tag{5.25}$$

In the limit of small squeezing parameter $\lambda \to 0$ and small reflectivity $r' \to 0$, the state heralded by a n-photon detection in the conditional path is given by

$$|\phi_n\rangle \propto \sqrt{n(n-1)}r'|n-2\rangle + \lambda|n\rangle \ , \tag{5.26}$$

which is a superposition of two highest Fock states with the same parity depending on the conditional photon number n. By adjusting the reflectivity r', arbitrary weights can be obtained. Note that the relative phase between the superposition terms can be controlled with a birefringent material, which leads to the preparation of quantum bits.

Equivalently, the two-mode squeezed vacuum state can produced via two single-mode squeezed vacuum states as shown in figure 5.14(b). The corresponding squeezing parameters have the same magnitudes but opposite phases. This fact can simplify our calculation to model this state preparation. Therefore the conditional states can be computed as following:

$$\hat{\rho} \propto \mathrm{Tr}[\hat{B}(r)|\psi\rangle\langle\psi|\hat{B}^\dagger(r)\hat{\Pi}] \ , \tag{5.27}$$

where $\hat{B}$ is the beam-splitter mixing operator, the input state is $|\psi\rangle = \hat{S}(\zeta)|0\rangle_a \otimes \hat{S}(\zeta e^{i\pi})|0\rangle_b$, and the measurement operator is $\hat{\Pi} = |n\rangle\langle n|$. Using this rotation picture of our state preparation, it is very easy to use the "Qmixer" software to numerically simulate the conditional states.

5.3.2 $g^{(2)}(0)$ in the conditioning path

In particular, we consider here the case $n = 2$. As shown in figure 5.14(b), two squeezed vacua are brought to interfere on a beam-splitter with an amplitude reflectance r and transmittance t. This kind of two-mode mixing can be conveniently described with the Wigner function, giving the output state as

$$W'_{ab}(x_a, p_a; x_b, p_b) = \frac{1}{(2\pi)^2} e^{-\frac{(tx_a + rx_b)^2}{2s} - \frac{(tp_a + rp_b)^2}{2/s} - \frac{(tx_b - rx_a)^2}{2/s} - \frac{(tp_b - rp_a)^2}{2s}} , \tag{5.28}$$

where $s = e^{-2\zeta}$ is the squeezing factor.

If we only focus on the state in the conditional path [8], we can trace out the mode a leading to

$$W'_b(x, p) = \frac{1}{2\pi\sigma_x\sigma_p} e^{-\frac{x^2}{2\sigma_x^2} - \frac{p^2}{2\sigma_p^2}} , \tag{5.29}$$

where

$$\sigma_x^2 = sr^2 + t^2/s , \qquad \sigma_p^2 = st^2 + r^2/s . \tag{5.30}$$

The resulting state is still a Gaussian state with

$$\langle x^2 \rangle = \sigma_x^2 , \qquad \langle p^2 \rangle = \sigma_p^2 , \tag{5.31}$$

which gives the average photon number

$$\langle \hat{n} \rangle = \frac{\langle x^2 \rangle + \langle p^2 \rangle - 2}{4} = \frac{1}{4}(s + \frac{1}{s} - 2) . \tag{5.32}$$

For Gaussian states with zero offset, the second-order correlation function (cf. Appendix B) is given by [9]

$$g^{(2)}(0) = (\frac{\sigma_x^2 - \sigma_p^2}{\sigma_x^2 + \sigma_p^2 - 2})^2 + 2 = \frac{(t^2 - r^2)^2}{\lambda^2} + 2 , \tag{5.34}$$

where $\lambda = (1 - s)/(1 + s) = \tanh\zeta$.

Clearly, when $t = 0$ or $r = 0$ the $g^{(2)}(0)$ corresponds to a squeezed vacuum state; when $t = r = 1/\sqrt{2}$ the $g^{(2)}(0)$ corresponds to a thermal state. This can explain that the $g^{(2)}(0)$ shown in figure 5.13(b) is slightly higher than 2 as this value is very sensitive to the mixing of the two modes.

[8] If we trace out the mode b, what we get is

$$W'_a(x, p) = \frac{1}{2\pi\sigma_x\sigma_p} e^{-\frac{x^2}{2\sigma_p^2} - \frac{p^2}{2\sigma_a^2}} ,$$

which is just the 90°-rotation of $W'_b(x, p)$.

[9] If we use the coefficients in the left scheme shown in figure 5.14, then we have

$$g^{(2)}(0) = (\frac{2t'r'}{\lambda})^2 + 2 . \tag{5.33}$$

5.3.3 Superposition between $|0\rangle$ and $|2\rangle$

The previously demonstrated two-photon Fock state has been obtained in the condition of perfect alignment of HWP ($r' = 0$). As shown in the protocol, a superposition of vacuum and two-photon Fock state can be synthesized by adjusting the HWP angle. Figure 5.15 demonstrates the evolution of the heralded states with the angle of HWP. It is clearly shown that the weights of superposition terms can be conveniently controlled. The superposition can be understood in the following way: the two photons in the conditional path are ether both from the idler mode or one from idler mode and the other one from signal mode. The former heralds a two-photon state while the latter heralds a vacuum state. The distinguishability of these two events leads to a coherently superposed state. This novel method for state engineering does not need ancilla beams [92, 93]. It is also worth mentioning that the proposed protocol takes the advantage of the polarization non-degeneracy of the type-II OPO. The PBS used to mix the two modes will erase the polarization information for the signal and idler photons entering the conditional path. For experiments based on OPOs with frequency non-degeneracy [89, 94], the mixing of signal and idler modes will not result in a superposition state due to the spectral distinguishability.

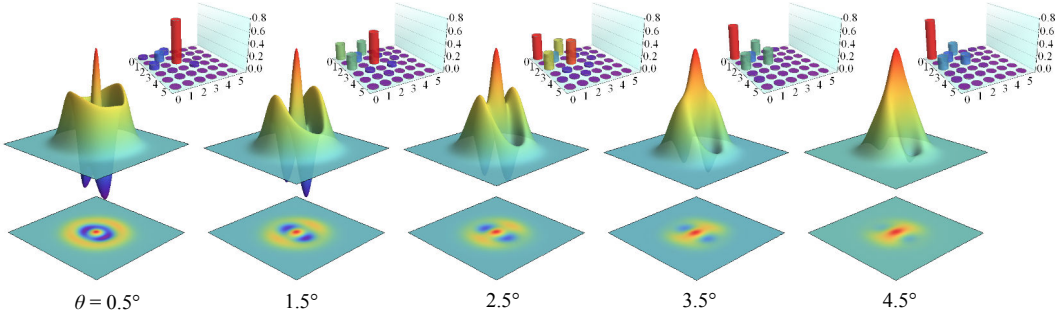

Figure 5.15: Evolution of the heralded states with incremental values of the half-wave plate angle θ. The Wigner functions are phase sensitive due the superposition property of the generated states. The Absolute values of density matrices are also shown in the top-right corner, which clearly demonstrate the dynamic change of superposition weights. The results are corrected for 15% losses.

The angle tuning of HWP not only enables to engineer the states, but also changes the heralding probability. Since the average photon number in the conditioning path is independent on the HWP angle (cf. equation (5.32)), the joint probability in the coincidence measurement only relies on the second-order correlation function $g^{(2)}(0)$ of the state in the conditioning path. According to equation (B.17), the value of $g^{(2)}(0)$ increases with larger HWP angle, thus giving a higher heralding probability.

Note that the superposition state is phase dependent, hence the reconstruction of the density matrix requires the phase information of the quadrature values. The technique for obtaining this information will be detailed in Chapter 6.

5.3.4 Approximation of Schrödinger cat state

It is well known that superposition of Fock states with the same parity can approximate Schödinger's cat states $|\alpha\rangle \pm |-\alpha\rangle$. Furthermore, if one can arbitrarily synthesize the superposition coefficients, large amplitude of the target states can be obtained. Let us consider the following state

$$|\phi_n\rangle = b_n|n\rangle + b_{n-2}|n-2\rangle + \dots \ , \tag{5.35}$$

and the targeted squeezed Schödinger's cat given by

$$|\mathrm{Scat}_{\pm}^{\alpha}\rangle = \frac{1}{\sqrt{2(1 \pm e^{-2\alpha^2})}} \hat{S}(\zeta)(|\alpha\rangle \pm |-\alpha\rangle) \ . \tag{5.36}$$

With the photon number distribution of a squeezed coherent state

$$\hat{S}(\zeta)|\alpha\rangle) = \sqrt[4]{(1-\lambda^2)} e^{\frac{(\lambda-1)\alpha^2}{2}} \sum_{n=0}^{\infty} \sqrt{\frac{\lambda^n}{2^n n!}} \mathrm{H}_n(\pm\sqrt{\frac{1-\lambda^2}{2\lambda}}\alpha)|n\rangle \tag{5.37}$$

where $\lambda = \tanh\zeta$, we can express the squeezed Schödinger's cat in the Fock state basis

$$|\mathrm{Scat}_{\pm}^{\alpha}\rangle = c_n|n\rangle + c_{n-2}|n-2\rangle + \dots \ . \tag{5.38}$$

Therefore the fidelity between them is described as

$$\mathcal{F} = |\langle \mathrm{Scat}_{\pm}^{\alpha}|\phi_n\rangle|^2 = (b_n c_n + b_{n-2}c_{n-2} + \dots)^2 \ , \tag{5.39}$$

which is maximized when the coefficients are proportional to each other (*Cauchy-Schwarz inequality*)

$$\mathcal{F}_{max} = c_n^2 + c_{n-2}^2 + \dots \ . \tag{5.40}$$

The fidelity between engineered states and cat states are plotted in figures 5.16. The fidelity is optimized by the squeezing and size of the targeted squeezed cat state. This method enables to reach a cat size $|\alpha|^2 \approx 3$ for n=2 or $|\alpha|^2 \approx 5$ for n=3 with a fidelity above 98%.

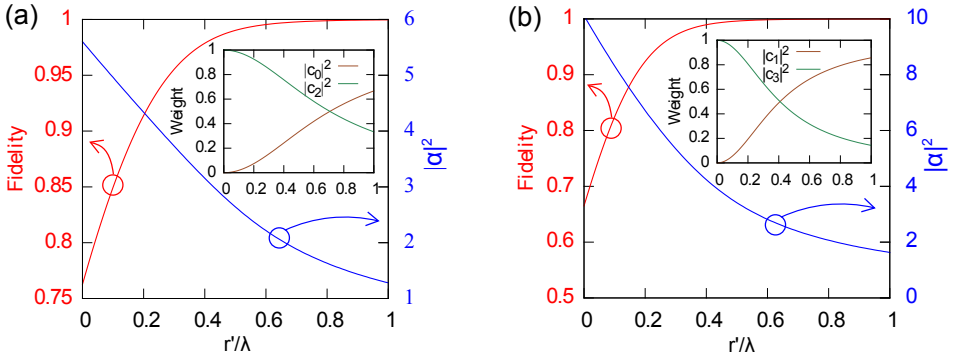

Figure 5.16: Fidelity between photon-number superposition state and cat state as a function of r'/λ. (a) Fidelity with an even cat state $\mathcal{F} = |\langle \mathrm{Scat}_{+}^{\alpha}|\phi_2\rangle|^2$. (b) Fidelity with an odd cat state $\mathcal{F} = |\langle \mathrm{Scat}_{-}^{\alpha}|\phi_3\rangle|^2$. The fidelity is maximized by the squeezing and size of the targeted squeezed cat state. The inset shows the evolution of photon-number distribution.

Figure 5.17 shows the experimentally obtained fidelity between the engineered states (cf. figure 5.15) and ideal squeezed cat states. For HWP angle $\theta = 1.5°$, a fidelity $\mathcal{F} = 0.67 \pm 0.01$ is obtained for a size $|\alpha|^2 = 3$ and a squeezing of 4 dB. The generated state thereby exhibits the highest amplitude and fidelity reported to date for free-propagating cat states. Furthermore, the demonstrated scheme is very versatile. Indeed, by simply adjusting the HWP angle, the properties of the state can be engineered. For instance, as can be seen in figure 5.17(b), the state generated with $\theta = 2.5°$ exhibits a maximal fidelity $\mathcal{F} = 0.68 \pm 0.01$ for a state $|\alpha|^2 = 1.9$ and a squeezing of 3 dB. Given the loss in the experiment, the corrected

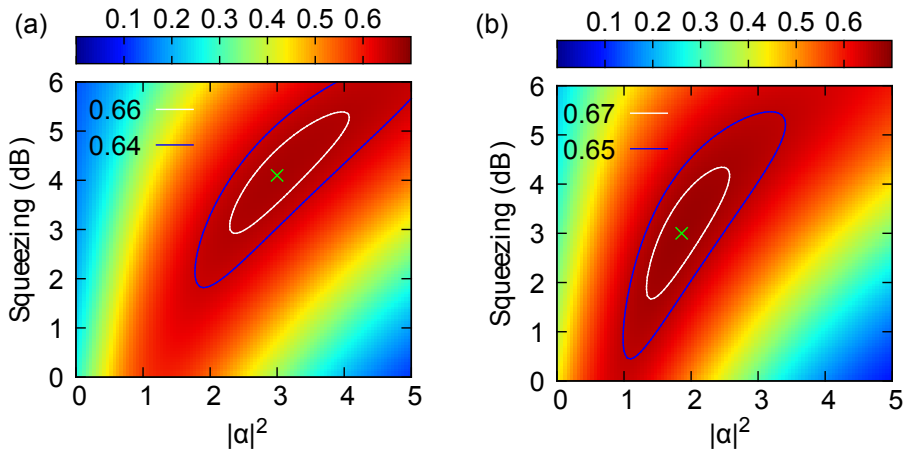

Figure 5.17: Fidelity between the generated state and an ideal squeezed even coherent-state superposition, for (a) $\theta = 1.5°$ (b) $\theta = 2.5°$. The plots give the calculated fidelity as a function of the size $|\alpha|^2$ of the superposition and the squeezing in dB. The green crosses indicate the maximal fidelities. For $\theta = 1.5°$, the fidelity reaches 0.67 with an even cat state with a size $|\alpha|^2 = 3$ and a 4-dB squeezing.

fidelity is expected to reach a value around 80%, similarly to the one obtained for the two-photon state displayed in figure 5.12. The discrepancy mainly comes from the strong phase sensitivity of such states.

Note that the demonstrated state engineering relied on two-mode squeezed vacuum and a conditioning operation performed on one of the two modes. No ancilla beam was required, in contrast to previous works relying on coherent-state-injected photon detectors [92, 95]. Additionally only two conditional detections were used in our experiment, instead of three conditionings shown in [79]. Therefore the protocol demonstrated here indeed enables the heralded generation of large-size squeezed cat states with the minimal required resources.

5.4 Heralding photons with temporal separation

In contrast to the single-photon state scheme, the generation of two-photon states involves two conditioning photon-detection events. Till so far, in the above experiments the delay between the two detection events was set to zero. In this section, we will investigate how the generated states can be affected by the temporal separation of the conditional detections. To avoid any confusion, we emphasize here that the HWP is aligned to be in the "perfect" position such that the signal and idler modes are separated without any mixing.

5.4.1 Temporal modes

Generally speaking, in the approximation of low pump power, the generated state conditioned on the n-photon detection is given by [91]

$$|\Psi_n\rangle \propto \prod_{i=1}^{n} \int dt g_i(t) \hat{a}^\dagger(t) |0\rangle \ . \tag{5.41}$$

Specifically, the heralded two-photon state cab be written as:

$$|\Psi_2\rangle = \frac{1}{\sqrt{N}} \iint dt dt' g_1(t) g_2(t') \hat{a}^\dagger(t) \hat{a}^\dagger(t') |0\rangle \ , \tag{5.42}$$

where

$$g_i(t) = \sqrt{\pi\gamma} e^{-\pi\gamma|t-t_i|} \tag{5.43}$$

are the single-photon wave packets corresponding to two temporally separated trigger photons.

The normalization constant N can be determined by the normalization of the state [10],

$$N = 1 + I^2 \ , \tag{5.44}$$

where I is the overlap between the two temporal modes

$$I = \int g_1(t) g_2(t) dt = e^{-\pi\gamma|t_1-t_2|}(1 + \pi\gamma|t_1 - t_2|) \ . \tag{5.45}$$

If we use a specific mode $f_1(t)$ as our interest mode, what can we measure at the end from the homodyne signal? To answer this question, we can construct a series of normal-orthogonal functions $f_k(t)$ among which $f_1(t)$ is the first mode. So the two-photon state can be rewritten as:

$$\begin{aligned} |\Psi_2\rangle &= \frac{1}{\sqrt{N}} \sum_{m,n} C_{mn} [\int dt f_m(t) \hat{a}^\dagger(t)][\int dt' f_n(t') \hat{a}^\dagger(t')] |0\rangle \\ &= \frac{1}{\sqrt{N}} \sum_{m,n} C_{mn} \hat{A}_m^\dagger \hat{A}_n^\dagger |0\rangle \\ &= \frac{1}{\sqrt{N}} [\sum_m \sqrt{2} C_{mm} |2\rangle_{f_m} + \sum_{m>n} (C_{mn} + C_{nm}) |1\rangle_{f_m} |1\rangle_{fn}] \ , \end{aligned} \tag{5.46}$$

where the decomposition coefficients are

$$C_{mn} = [\int f_m^*(t) g_1(t) dt][\int f_n^*(t') g_2(t') dt'] = \alpha_m \beta_n \ . \tag{5.47}$$

If we consider a temporal mode of interest $f_1(t)$ equal to $g_1(t)$, we can obtain $C_{mn} = \delta_{1,m}\beta_n$. After tracing over other modes, the measurement probabilities for different photon-number states are given by

$$P_2 = \frac{2}{N} |C_{11}|^2 = \frac{2|\beta_1|^2}{1 + I^2} = \frac{2I^2}{1 + I^2} \ , \tag{5.48}$$

$$\begin{aligned} P_1 &= \frac{1}{N} \sum_{m>1} |C_{m1} + C_{1m}|^2 \\ &= \frac{1}{N} \sum_{m>1} |C_{1m}|^2 = \frac{1}{N} \sum_{m>1} |\beta_n|^2 \\ &= \frac{1}{N}(1 - |\beta_1|^2) = \frac{1 - I^2}{1 + I^2} \ . \end{aligned} \tag{5.49}$$

[10] We use the relation

$$\begin{aligned} &\langle 0| \hat{a}(t'_2) \hat{a}(t'_1) \hat{a}^\dagger(t_1) \hat{a}^\dagger(t_2) |0\rangle \\ =& \langle 0| \hat{a}(t'_2) [\hat{a}^\dagger(t_1) \hat{a}(t'_1) + \delta(t_1 - t'_1)] \hat{a}^\dagger(t_2) |0\rangle \\ =& \delta(t_1 - t'_2)\delta(t_2 - t'_1) + \delta(t_1 - t')\delta(t_2 - t'_2) \ . \end{aligned}$$

Since the target mode is always occupied by one heralded single photon, the probability to find no photon in this mode is thus zero, which is confirmed by:

$$P_0 = 1 - P_1 - P_2 = 0 \ . \tag{5.50}$$

For more general cases, as shown in equation (5.49) the probability to find just one photon in the target mode is very complicated due to the coherent superposition between two probability amplitudes (C_{mn} and C_{nm}).

Note that the mode $f_1(t) = g_1(t)$ is not the optimal temporal mode, because we can find other modes that will give a higher two-photon fidelity. To demonstrate this point, we can reformulate the state $|\Psi_2\rangle$ with two orthogonal mode functions, symmetric and antisymmetric, which are constructed in the following way:

$$\begin{aligned} f_1(t) &= \frac{1}{\sqrt{2(1+I)}}[g_1(t_1) + g_2(t_2)] \ , \\ f_2(t) &= \frac{1}{\sqrt{2(1-I)}}[g_1(t_1) - g_2(t_2)] \ . \end{aligned} \tag{5.51}$$

Therefore the resulting state can be expressed as

$$\begin{aligned} |\Psi_2\rangle &= \frac{1+I}{2\sqrt{(1+I^2)}}[\int dt f_1(t)\hat{a}^\dagger(t)]^2 |0\rangle - \frac{1-I}{2\sqrt{(1+I^2)}}[\int dt f_2(t)\hat{a}^\dagger(t)]^2 |0\rangle \\ &= \frac{1+I}{\sqrt{2(1+I^2)}}|2,0\rangle_{1,2} - \frac{1-I}{\sqrt{2(1+I^2)}}|0,2\rangle_{1,2} \ . \end{aligned} \tag{5.52}$$

It indicates that the two photons can be either in the mode $f_1(t)$ or in mode $f_2(t)$. The two-photon fidelity in mode $f_1(t)$ can be easily obtained from the norm square of the coefficient

$$F = \frac{(1+I)^2}{2(1+I^2)} \ . \tag{5.53}$$

It can be proved that $F \geqslant P_2$. Recall that P_2 is the two-photon fidelity using $g_1(t)$ as the temporal mode, which is given by equation (5.48).

Actually, it has been shown that for low gain pump, the mode $f_1(t)$ is the optimal mode for obtaining the highest two-photon fidelity. Figure 5.18 depicts the four modes functions $g_1(t)$, $g_2(t)$, $f_1(t)$, and $f_2(t)$.

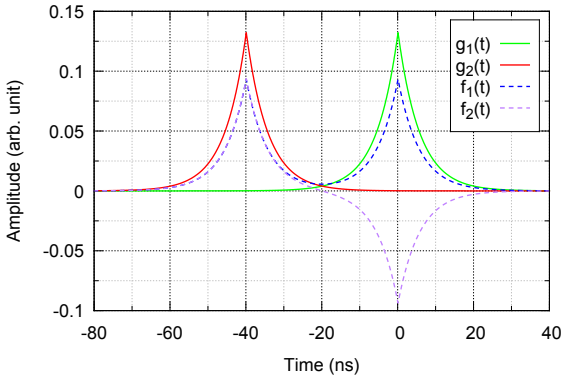

Figure 5.18: Mode functions $g_1(t)$, $g_2(t)$, $f_1(t)$, and $f_2(t)$.

5.4.2 Results and discussion

For illustrating the experimental effect of temporal modes on the conditional states, the conditional detections from the two SSPDs are set to have a 40-ns delay. The acquired

homodyne signal is then processed with the four aforementioned temporal modes shown in figure 5.18.

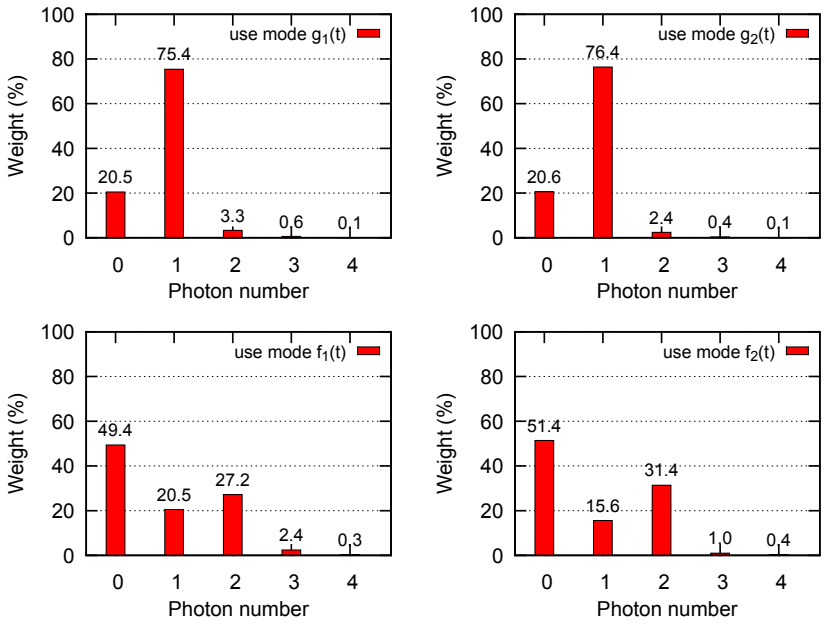

Figure 5.19: Photon-number distributions of reconstructed states by choosing different temporal mode functions $g_1(t)$, $g_2(t)$, $f_1(t)$, and $f_2(t)$, respectively. The state tomography is done without loss correction.

Figure 5.19 shows photon-number distributions of the reconstructed states by choosing different temporal mode functions $g_1(t)$, $g_2(t)$, $f_1(t)$, and $f_2(t)$, respectively. Due to the losses, the single-photon fidelity is about 76% which gives an expected optimal two-photon fidelity about $76\%^2 \approx 58\%$ when heralded by zero-delay coincident triggers. In the experiment, the two trigger times are well separated by 40 ns, which is much larger than the coherence time of the heralded photons (about 20 ns). According to equation (5.53), the expected two-photon fidelity in the symmetric mode $f_1(t)$ and asymmetric mode $f_2(t)$ will decrease to half compared to the case of $t_1 - t_2 = 0$. It leads to a two-photon fidelity of $58\%/2 = 29\%$, which is in good agreement with what we measure.

The above example illustrated how the reconstructed states are affected by using different temporal modes. In the next example, we will demonstrate how, with the same temporal mode, the reconstructed states are affected by using various temporal delays for the coincident triggers.

In our experiment, the homodyne signal is acquired given coincident clicks with a given delay Δt. If we use a temporal mode $g_1(t)$ centered at the same time with one click, what we expect is thus given by (cf. Section 5.4.1)

$$\hat{\rho} = P_1|1\rangle\langle 1| + P_2|2\rangle\langle 2| \ , \tag{5.54}$$

where P_1 and P_2 are given by

$$\begin{aligned} P_1 &= \frac{1 - I^2}{1 + I^2} \ , \\ P_2 &= \frac{2I^2}{1 + I^2} \ . \end{aligned} \tag{5.55}$$

Recall that I is defined by

$$I = e^{-\pi\gamma\Delta t}(1 + \pi\gamma\Delta t) \ . \tag{5.56}$$

After taking account into the losses on the state (modeled with a fictitious beam-splitter with a power transmittance η), the resulting state $\hat{\rho}'$ is thus written as

$$\hat{\rho}' = P_2\eta^2|2\rangle\langle 2| + [P_2 2\eta(1-\eta) + P_1\eta]|1\rangle\langle 1| + [P_2(1-\eta)^2 + P_1(1-\eta)]|0\rangle\langle 0| \ . \tag{5.57}$$

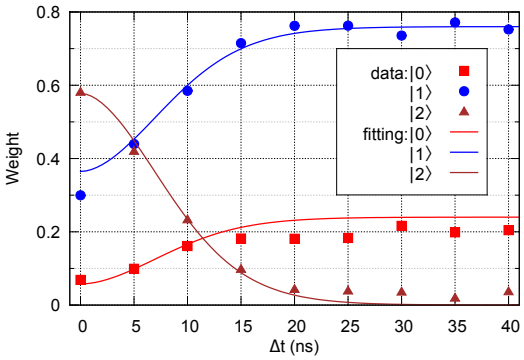

Figure 5.20: Reconstructed states as a function of the temporal separation Δt between the coincident triggers. The fitting parameters are the OPO FWHM bandwidth $\gamma = 53$ MHz and the overall intensity transmission $\eta = 0.76$.

Figure 5.20 shows the reconstructed states as a function of the temporal separation Δt between the coincident triggers. The fitted curves are obtained by using the parameters γ = 53 MHz and $\eta = 0.76$. The slight discrepancy may be due to the high photon-number components.

Note that in the experiment, all the data is acquired once, which covers the trigger delays up to 70 ns. Therefore we can continuously post-select the temporal delay between triggers within this range. The total data number is 1000,000 and the selected data number with any trigger separation is above 15,000 that is enough to realize the accurate state tomography.

5.5 Conclusion

In conclusion, we have experimentally generated high-fidelity heralded Fock states based on the type-II optical parametric oscillator operated below threshold. 78.0% single-photon fidelity and 58.3% two-photon fidelity have been achieved, mainly limited by the losses in the detection part. Thanks to the highly efficient SSPDs, the heralding count rates for single-photon generation is close to MHz, which permits tomography as well as optimization of the experimental setup in real time [96]. For two-photon state generation, the heralding rate reaches 150 Hz. The obtained states will benefit to quantum optical engineering and information processing that require Fock states with high fidelity and importantly in a well-defined spatial mode. For instance, these states will be used in the generation of hybrid entanglement, which will be presented in Chapter 7.

Additionally, we proposed a novel method to engineer quantum states with the form of $\alpha|n\rangle + \beta|n-2\rangle$. As a proof of principle, we experimentally demonstrated a superposition of vacuum and two-photon Fock state. Arbitrary weights of the superposition terms can be synthesized by only rotating the HWP. The generated states can be optimized to approximate large-amplitude squeezed even cat states [97, 98, 99].

Finally we have experimentally investigated that in our continuous-wave experiment the temporal separation between conditioning detections indeed largely affected the generated states. Another example will be given in the next chapter as a large-size cat state can be generated with a time-separated two-photon subtraction from a squeezed vacuum.

6 | Schrödinger Cat States

Schrödinger's cat is a gedanken experiment that originally described a cat existing in a superposition of alive and dead states. Nowadays, the term Schrödinger's cat usually refer to a quantum superposition between two highly distinguishable classical states. A typical example in quantum optics is a coherent state superposition (CSS), i.e. $|\alpha\rangle \pm |-\alpha\rangle$. As shown in Chapter 1, the CSS exhibits the quantum interference feature that cannot be observed with a statistical mixture of coherent states. Even with a modest amplitude α, the coherent states $|\alpha\rangle$ and $|-\alpha\rangle$ are almost orthogonal [1]. This property attracts great attention in continuous-variable quantum computation where qubits can be encoded with such states [100, 101]. Additionally, CSSs can also be useful in high-precision measurements [102, 103].

In this chapter, we will first demonstrate the generation of an odd cat state, which is then transformed to an even cat states by a π-phase gate. At the end, larger-size cat states will be generated using time-separated two-photon subtraction. In contrast to the previous chapter, here the state generation is based on conditional preparation operated on the single-mode squeezed vacuum from a type-I OPO.

[1] The overlap between two coherent states $|\langle\alpha| - \alpha\rangle|^2 = e^{-4|\alpha|^2}$ is already below 2% for $|\alpha|^2 > 1$

6.1 Generation of odd cat states

Generation of Schrödinger cat states is a nontrivial task, since it requires large nonlinearity. The nonlinearity in principle can be provided by cross-Kerr effect [104, 105], yet with currently available material and technology, realization of a pronounced Kerr effect at the single-photon level is still very challenging. To overcome this difficulty, measurement-induced nonlinearity is used at the expense of probabilistic implementation [106, 107]. Specifically, the cat state can be generated with photon subtraction from a squeezed vacuum state [108]. This protocol has been successfully demonstrated in many experiments [99, 109, 110, 111, 112]. For a review of methods for producing optical cat states, readers can refer to [113].

6.1.1 Principle and model

■ Basic principle

As introduced in Chapter 1, the Schrödinger cat state is given by the superposition of two coherent states with opposite phases:

$$|cat_{\pm}^{\alpha}\rangle = \frac{|\alpha\rangle \pm |-\alpha\rangle}{\sqrt{2(1 \pm e^{-2|\alpha|^2})}} , \tag{6.1}$$

where $|\alpha\rangle$ is a coherent state with an amplitude α. $|cat_{-}^{\alpha}\rangle$ is called an odd cat state because it only contains odd photon-number states in the Fock state expansion. Similarly, $|cat_{+}^{\alpha}\rangle$ is thus called an even cat state.

Generation of an odd cat state can be approximated with a superposition of photon-number states with only odd parity. A commonly used strategy is to subtract a single photon from a squeezed vacuum state, as initially proposed by Dakna *et al.* [108]. The single-photon subtraction from a squeezed vacuum results in [2]

$$\begin{aligned} |1\mathrm{PS}\rangle &\triangleq \frac{\hat{a}\hat{S}(\zeta)|0\rangle}{\|\hat{a}\hat{S}(\zeta)|0\rangle\|} = \hat{S}(\zeta)|1\rangle \\ &= \frac{(1-\lambda^2)^{3/4}}{\lambda} \sum_{n=1} \frac{\sqrt{(2n)!}}{n!} (\lambda/2)^n \sqrt{2n} |2n-1\rangle , \end{aligned} \tag{6.2}$$

where $\lambda = \tanh\zeta$. The resulting state is actually a squeezed single photon.

The fidelity between a single-photon-subtracted state $|1\mathrm{PS}\rangle$ and an odd cat state $|cat_{-}^{\alpha}\rangle$ is given by [114]

$$\begin{aligned} \mathcal{F}_1 &= \left\| \langle cat_{-}^{\alpha} | 1\mathrm{PS} \rangle \right\|^2 \\ &= \frac{(1-\lambda^2)^{3/2} \alpha^2 e^{\lambda\alpha^2}}{\sinh \alpha^2} . \end{aligned} \tag{6.3}$$

For a specific amplitude α, the maximum fidelity is obtained by an optimized squeezing parameter λ_{opt} given by

$$\lambda_{\mathrm{opt}} = \frac{\sqrt{9+4\alpha^4} - 3}{2\alpha^2} . \tag{6.4}$$

Figure 6.1 gives the contour plot of the fidelity between $|1\mathrm{PS}\rangle$ and $|cat_{-}^{\alpha}\rangle$. By optimizing the squeezing, the approximation is valid up to $|\alpha|^2 = 1.4$ with $\mathcal{F} > 99\%$. Note that the overlap between two coherent states $|\langle\alpha| - \alpha\rangle|^2 = e^{-4|\alpha|^2}$ is below 2% for $|\alpha|^2 > 1$.

[2] Single-photon addition to a squeezed vacuum will result in the same state, which is clear by noting that $\hat{a}^\dagger \hat{S}|0\rangle \propto \hat{S}\hat{S}^\dagger \hat{a}^\dagger \hat{S}|0\rangle = \hat{S}(\hat{a}^\dagger \cosh r - \hat{a} \sinh r)|0\rangle \propto \hat{S}|1\rangle$.

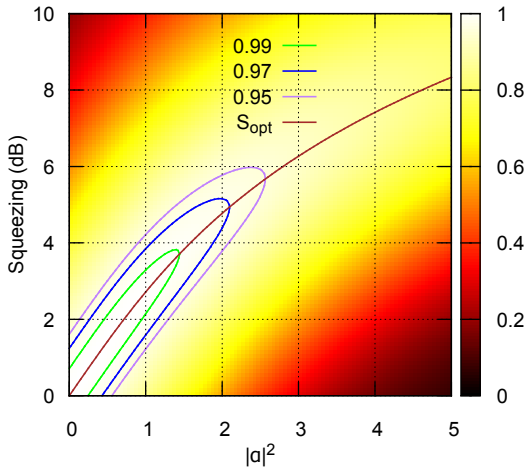

Figure 6.1: Contour plot of the fidelity between single-photon-subtracted squeezed vacuum and odd Schrödinger cat state. S_{opt} indicates the optimal squeezing that maximizes the fidelity for a given cat size $|\alpha|^2$.

■ Model of the experiment

Figure 6.2 presents an experimental scheme for generating an odd cat state based on photon subtraction from a squeezed vacuum produced by a type-I OPO. In the experiment, the photon-subtraction operation is realized with a highly asymmetric beam splitter (cf. Section 3.4.2). Indeed, with an approximation of a small reflection r ($r = \sin\theta \approx \theta$), the beam-splitter operator can be written as $\hat{B} = e^{\theta(\hat{a}\hat{b}^\dagger - \hat{a}^\dagger\hat{b})} \approx 1 + \theta(\hat{b}^\dagger\hat{a} - \hat{b}\hat{a}^\dagger)$. Then we have

$$\hat{B}\hat{S}|0\rangle_a|0\rangle_b \approx \hat{S}|0\rangle_a|0\rangle_b + \theta\hat{a}\hat{S}|0\rangle_a|1\rangle_b \ . \tag{6.5}$$

Therefore, detecting one photon in the conditioning mode b leads to a single-photon subtraction from the signal mode a, i.e. $\hat{a}\hat{S}|0\rangle_a$.

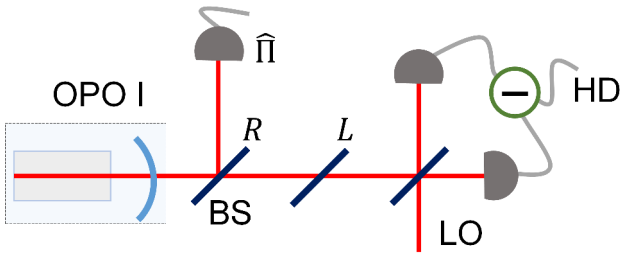

Figure 6.2: Experimental scheme for generating an odd cat state based on photon subtraction from a squeezed vacuum prepared by a type-I OPO. The beam splitter (BS) with an intensity reflectivity R is used to tap a part of squeezing for the conditional measurement (with a measurement operator $\hat{\Pi}$). The losses in the signal path is modeled with the other BS with an intensity reflectivity L. The finally generated state is then characterized by a homodyne detection (HD).

Practically, there are three aspects needed to be taken into account in the experiment. The first one is the tapping ratio R. It can not be very small or it will dramatically decrease the heralding probability. However, a large tapping ratio will introduce large losses. The second one is the losses L in the signal path including the propagation losses and efficiency of homodyne detection. The third one is the realistic photon detector in the conditional path with limited efficiency and unavoidable dark counts.

In order to model all this defects, the "Qmixer" software introduced in Section 3.4.4 is used to obtain numerical simulations. Therefore the conditioning states can be computed as following:

$$\hat{\rho} \propto \mathrm{Tr}[\hat{B}(\theta)|\psi\rangle\langle\psi|\hat{B}^{\dagger}(\theta)\hat{\Pi}] \ , \tag{6.6}$$

where $\hat{B}(\theta)$ is the beam-splitter operator with a tapping ratio $R = \sin^2\theta$; the input state is $|\psi\rangle = \hat{S}(\zeta)|0\rangle_a \otimes |0\rangle_b$; and the measurement operator of a realistic APD is given by

$$\hat{\Pi} = \mathbb{1} - \sum_{k=0}^{\infty} e^{-\nu}(1-\eta)^k \ |k\rangle\langle k| \ .$$

For the details about parameter setting in "Qmixer" for modeling the cat state generation, readers can refer to the Appendix D.

For the experiments of Fock state generation, the "quality" of prepared states can be easily judged from the photon number. However, assessing the "quality" of the generated cat states is more complicated. One way is to calculate the fidelity with ideal odd cat states. The other way is to compare the negativity of the Wigner function. The latter method is based on the fact that the negativity of the Wigner function will degrade in the case of imperfect experimental conditions [115, 20]. These two methods are linked with a statement that the negativity of the Wigner function at the origin of phase space is presented if the fidelity exceeds 50% [116].

Figure 6.3(a) presents the Wigner function at the origin of phase space [3] as a function of the tapping ratio R for different losses L in the signal path. The simulation is done with a pure 3-dB squeezed vacuum state and a perfect APD. We can see that as the increase of tapping ratio, the negativity of the Wigner function will gradually disappear. It is the result of the combined effect of non-photon-number resolving of the conditional detector and limited tapping ratio.

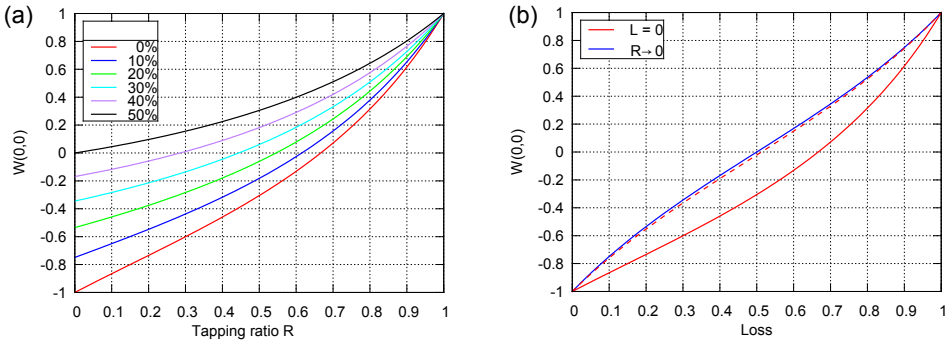

Figure 6.3: (a) Wigner function at the origin of phase space $W(0,0)$ as a function of the tapping ratio R for different losses L in the signal path. The simulation is done with a pure 3-dB squeezed vacuum state and a perfect APD. (b) In the limit cases of $L = 0$ (red solid line) and $R \to 0$ (blue solid line), $W(0,0)$ is given as a function of losses (R or L). The solid curves are given for an APD with a unity efficiency while the dashed red line is given for an APD with an efficiency of 10%.

Interestingly, in the case of no losses in the signal path ($L = 0\%$), even when the tapping ratio reaches 50% the negativity is still maintained. It means that in general we cannot simply regard the tapping ratio as losses on the state. This feature is emphasized in figure

[3] Here we use the normalized version $2\pi\sigma_0^2 W(0,0)$, which gives a value at the origin between -1 to 1 and is independent from the choice of conventions.

6.3(b). It is worth noting that for an APD with an efficiency as low as 10% (dashed red line), the tapping ratio R and the loss L in the signal path almost impose the same impact on the state. We also note that in the limit of $R \to 0$, the conditional state is independent of the detection efficiency of the heralding detector. In this case, the probability of high photon-number states in the conditional path is negligible since the reflection of n photons scales as R^n.

So far the dark noise of the conditioning detector has not been considered for simplicity. Indeed the dark noise induces some "false" events. These "false" triggers will herald squeezed vacuum states, which are orthogonal to the odd cat states, thus degrading the fidelity. Therefore, in practice the dark counts have to be as small as possible compared to the counts of "true" events.

Now we turn to the experimental realization for the generation of an odd cat state.

6.1.2 Experimental realization

The corresponding experimental setup is presented in figure 6.4. A type-I OPO is used to prepare the initial light, a high-purity 3 dB squeezed vacuum state (cf. figure 2.6). A small fraction ($\approx 5\%$) is tapped by a beam-splitter towards the conditioning path. Practically, the variable beam-splitter is made of a half-wave plate and a polarizing beam-splitter. In order to get rid of the non-degenerate spectral mode, an interferential filter and a Fabry-Perot cavity are employed in the conditioning path as detailed in Chapter 5. Finally the filtered light is detected by a superconducting single-photon detector (SSPD) with an efficiency as high as 70%. The detection of a single photon will probabilistically apply a single-photon subtraction on the squeezed vacuum. The heralded state in the signal path is finally characterized by a homodyne detection. The measured homodyne signals are post-processed with a defined temporal mode for extracting the corresponding quadrature values which are used for the quantum state tomography.

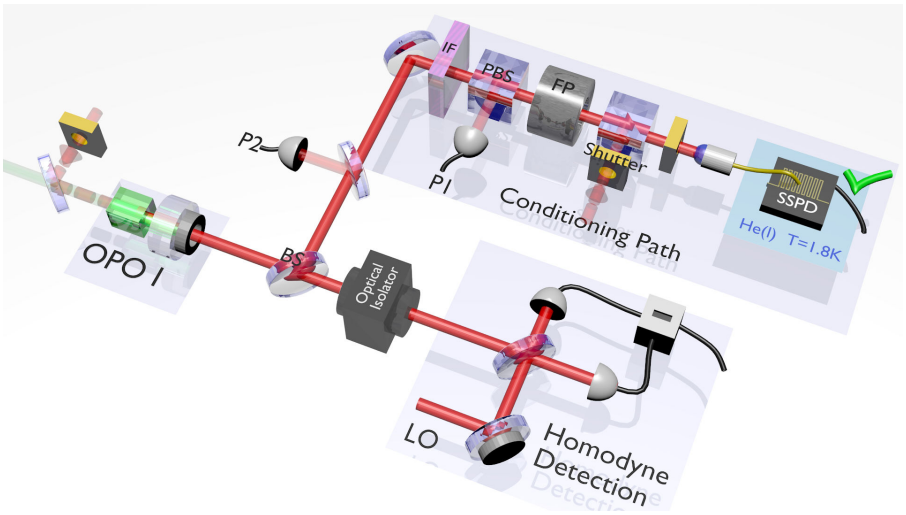

Figure 6.4: Experimental setup for the odd cat state generation. The initial source is a high-purity 3 dB squeezed vacuum state from a type-I OPO. Via a beam-splitter (BS), a small portion ($\approx 5\%$) of squeezing is tapped towards the conditioning path. After a set of frequency filtering, only photons at the carrier frequency can be detected by a superconducting single-photon detector (SSPD) with an efficiency as high as 70%. Given a detection event in the conditioning path, the heralded state in the signal path is recorded by a homodyne detection (HD). The measured homodyne signals are then post-processed with a defined temporal mode to extract the corresponding quadrature values, which are finally used for the optical quantum tomography.

Since the cat state is phase dependent in phase space, thus the state tomography requires the phase information of the measured quadrature values. The next section explains how this phase information can be acquired [4].

6.1.3 Phase information

In order to get the phase information of the quadrature measurement, a weak coherent light (seed beam, 5 mW) is injected into the OPO cavity as shown in figure 6.4. The seed beam will be amplified or deamplified by the pump depending on their relative phase. When the phase of the seed is scanned, we can observe a sinusoid signal in the photodiode P2 (Thorlabs PDA10CS). The relative phase between the seed and the pump is then locked with the microcontroller-based locking introduced in Chapter 4.

Since the polarization of the seed is the same as the signal one, only a small part ($\approx 5\%$) of the seed light goes to the conditional path. Furthermore, the tapping ratio of the beam-splitter in the conditional path is typically $\approx 10\%$, thus even smaller part of seed light is detected by the photodiode P2. To obtain a large enough signal for the locking, the photodiode P2 is chosen to have a large amplification gain and a low offset.

The majority of the seed light goes into the signal path and then interferes with the local oscillator in the homodyne detection. The output of the homodyne detection is divided into the DC part and AC part. The AC part is used for quadrature measurement while the DC part is used for inferring the relative phase between the seed and the local oscillator. Specifically, the DC part is given by

$$i_1 - i_2 = 2\alpha_{seed}\alpha_{LO} cos(\phi_{seed} - \phi_{LO}) \ . \tag{6.7}$$

In the experiment, the phase of the local oscillator is swept via a PZT. Then the resulting interference fringe is fitted with a sine function. Taking into account the PZT nonlinearity, we keep the terms up to second order, i.e. $at^2 + bt + c$. The parameters a and b are intrinsic to the PZT and remain constant when the scanning parameters (e.g. scanning frequency, amplitude and offset) are kept unchanged. Hence they can be used in the whole measurements for one state tomography. The parameter c corresponds to the phase drift (e.g. due to mechanical relaxation, thermal expansion of the optical elements in the path) and varies slowly.

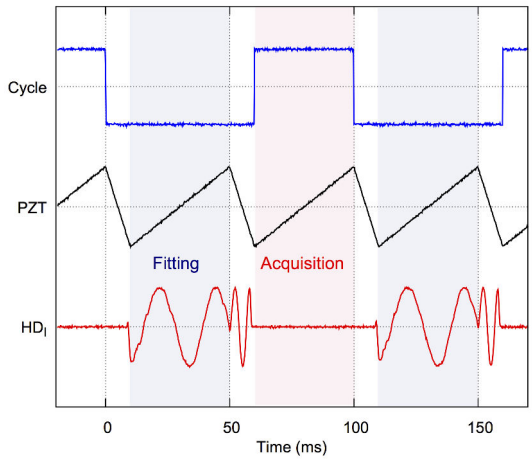

Figure 6.5: Phase estimation based on the interference fringes between the seed light and the local oscillator.

Similar to the experiment for Fock state generation, the experiment here is also run in a cyclic fashion with two steps (cf. figure 5.6): μCavity locking and data acquisition.

[4] Note that for the optical quantum tomography of the superposition state $\alpha|0\rangle + \beta|2\rangle$ demonstrated in Chapter 5, we already implemented the phase acquisition part in the experiment.

To generate cat states, an extra part of phase fitting is implemented within the μCavity locking window as shown in figure 6.5. Specifically, the scanning voltage V of PZT and the fringes from DC part of homodyne detector are recorded, then fitted with a sine function $\sin(AV^2 + BV + C)$. In the period of data acquisition, the seed light is blocked. For each conditioning trigger, the AC part of homodyne detection and the corresponding scanning voltage are acquired, which are post-processed to give the measured field quadrature and the corresponding phase.

Due to slow variation of the local oscillator phase, it is not necessary to do the fitting for each experimental cycle. In practice, the phase fitting is implemented at the beginning of each sequence acquisition in the oscilloscope. Each sequence contains 1000 segments, and each segment corresponds to one trigger event. In our experiment, the phase is very stable during the experiment as shown in figure 6.6. In principle, the phase information can be extracted directly from the variance of the quadrature measurements even without the seed light [20]. However this strategy is only valid under the condition that the phase is stable over the acquisition time for one tomography. For many long-term experiments (30 minutes to 3 hours) as we will present later, the seed light is used in order to obtain an accurate phase information.

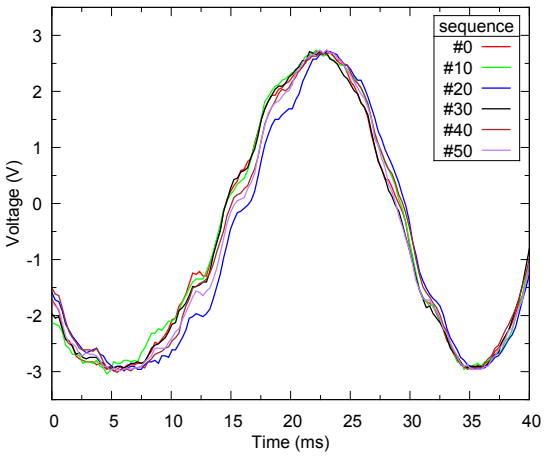

Figure 6.6: Stable interference fringes between the seed and local oscillator during one tomography containing data acquisition of 50 sequences. Only interference fringes for every 10 sequence are given. The total acquisition time for one tomography is about 2 minutes.

6.1.4 Results and discussion

The experimental results are summarized in figure 6.7. The generated odd cat state here is a squeezed single-photon state. Indeed the Wigner function not only exhibits a pronounced negative region at the origin, but also shows squeezing in the p-quadrature direction (cf. contour plot in figure 6.7(c)). Due to this squeezing property, the Wigner function is apparently phase dependent. The two "ears" in the Wigner function of the odd cat state is due to the losses. It is worth noting that the losses no only degrades the negativity of the Wigner function, but also deforms its shape. Here we obtain a negativity of $2\pi\sigma_0^2 W(0,0) = -0.37$ and $2\pi\sigma_0^2 W(0,0) = -0.62$ without and with correction of 15% losses, respectively.

The Wigner function at the origin is directly linked to the photon number distribution as $2\pi\sigma_0^2 W(0,0) = \sum_n (-1)^n \rho_{nn}$. For a perfect odd cat state, it only contains odd photon-number states. However, due to the losses the pure odd cat state becomes a statistical mixture of an odd cat state and an even cat state with smaller amplitudes (cf. equation (6.12)), which leads to the appearance of all the photon numbers as shown in figure 6.7(b). After correcting 15% losses, we can clearly see the oscillation behavior of the photon numbers.

The fidelity between the experimentally generated state and an ideal odd cat state is given

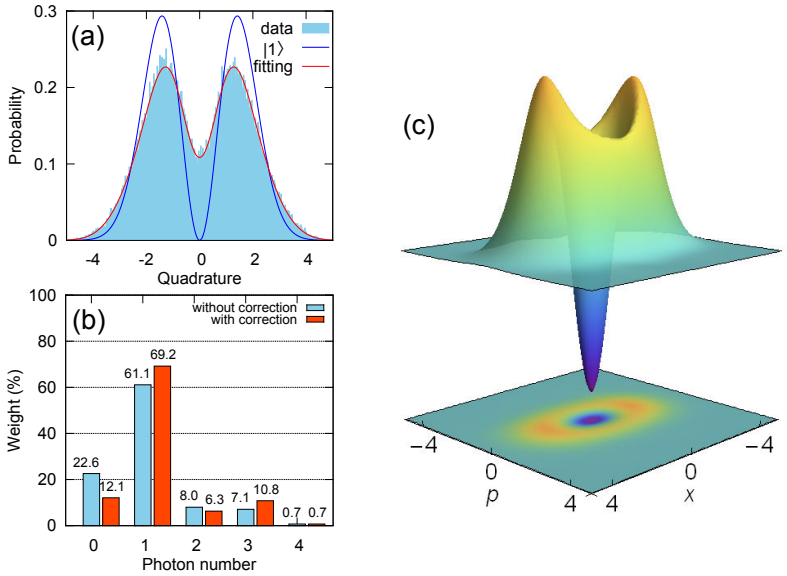

Figure 6.7: Experimental results for odd cat state generation. (a) Marginal distribution from 50,000 quadrature measurements with average phases. The blue solid line is a fit of the experimental data while the red solid line indicates an ideal single-photon state. (b) Photon-number distribution of the generated state, with and without correction for detection losses of 15%. (c) Corresponding Wigner function without loss correction.

in figure 6.8 as a function of the cat size. The fidelity is maximal for a cat size $|\alpha|^2 \approx 1$. Specifically, without any correction, the fidelity is 67.5% for $|\alpha|^2 = 1$; with correction of 15% losses, the fidelity reaches 80.0% for the same size.

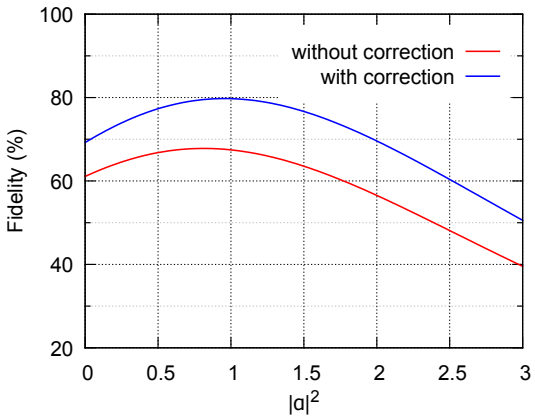

Figure 6.8: Fidelity between the experimentally generated state and an ideal odd cat state as a function of the cat size $|\alpha|^2$.

To achieve larger-size odd cat states, one can extend the scheme to three-photon subtraction from a squeezed vacuum state [111, 112]. It will become very demanding due to two aspects: requirement of higher squeezing as the initial resource and much lower success probability due the three-fold coincidence. To overcome this difficulty, there are some proposals for cat state amplification by combining two small cat states [117, 118]. Note that mixing two small odd cat states with sizes α and β will result in an even cat state with an amplified size $\sqrt{\alpha^2 + \beta^2}$.

6.2 π-phase gate for generating even cat state

In the Bloch sphere, a coherent state qubit can be expressed in the form $|\psi_{\theta,\phi}\rangle = \mathcal{N}_{\theta,\phi}(\cos\frac{\theta}{2}|\alpha\rangle + e^{i\phi}\sin\frac{\theta}{2}|-\alpha\rangle)$ with spherical coordinates θ and ϕ. Therefore starting from an odd cat state, generation of an even cat can be realized with a π-phase rotation along the equator of Bloch sphere [119]. Such rotation is described by a π-phase gate operation, which can be realized by a photon subtraction [120].

6.2.1 Theoretical calculation

■ Fidelity of even cat states

An even cat state $|cat_+^\alpha\rangle$ with a small amplitude can be well approximated by a squeezed vacuum state $\hat{S}|0\rangle$. The fidelity is given by

$$\begin{aligned}\mathcal{F}_0 &= \left\| \langle cat_+^\alpha | \hat{S}|0\rangle \right\|^2 \\ &= \frac{\sqrt{1-\lambda^2}e^{\lambda\alpha^2}}{\cosh\alpha^2} \ .\end{aligned} \tag{6.8}$$

For a specific amplitude α, the maximum fidelity is obtained by an optimized squeezing parameter λ given by

$$\lambda_{\text{opt}} = \frac{\sqrt{1+4\alpha^4}-1}{2\alpha^2} \ . \tag{6.9}$$

The fidelity as a function of the squeezing and the cat size $|\alpha|^2$ is shown in a figure 6.9 (left). We can see that for small sizes $|\alpha|^2 \lesssim 1$, the fidelity is above 95%.

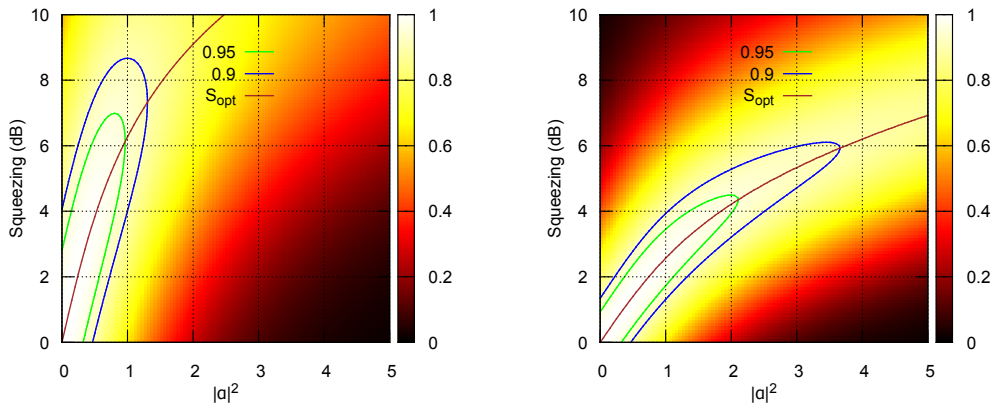

Figure 6.9: Contour plots of the fidelity with ideal even Schrödinger cat states for a squeezed vacuum state (left) and a two-photon subtracted squeezed vacuum state (right). S_{opt} indicates the optimal squeezing to maximize the fidelity with a given cat size $|\alpha|^2$.

To obtain an even cat state with a larger size, one can apply a two-photon subtraction

onto a squeezed vacuum [5]:

$$\begin{aligned} |\text{2PS}\rangle &\triangleq \frac{\hat{a}^2\hat{S}(\zeta)|0\rangle}{\|\hat{a}^2\hat{S}(\zeta)|0\rangle\|} = \mathcal{N}[-\cosh\zeta\sinh\zeta\hat{S}(\zeta)|0\rangle + \sqrt{2}\sinh^2\zeta\hat{S}(\zeta)|2\rangle] \\ &= \frac{(1-\lambda^2)^{5/4}}{\lambda\sqrt{1+2\lambda^2}}\sum_{n=1}^{\infty}\frac{\sqrt{2n!}}{n!}\left(\frac{\lambda}{2}\right)^n\sqrt{2n(2n-1)}\;|2(n-1)\rangle\;, \end{aligned} \tag{6.10}$$

where $\lambda = \tanh\zeta$.

The fidelity between a two-photon subtracted state $|\text{2PS}\rangle$ and an odd cat state $|cat_+^\alpha\rangle$ is given by

$$\begin{aligned} \mathcal{F}_2 &= \left\|\langle cat_+^\alpha|\text{2PS}\rangle\right\|^2 \\ &= \frac{(1-\lambda^2)^{5/2}(1+\lambda\alpha^2)^2e^{\lambda\alpha^2}}{(1+2\lambda^2)\cosh\alpha^2}\;. \end{aligned} \tag{6.11}$$

The fidelity as a function of the squeezing and the cat size $|\alpha|^2$ is shown in figure 6.9 (right). The cat size $|\alpha|^2$ can reach a value of 2 while the fidelity stays above 95%. Moreover, the optimal squeezing for maximizing the fidelity is lower compared to the one in the approximation based on the squeezed vacuum.

■ Cat state decoherence

It is well known that the cat state is extremely sensitive to losses. Here we dedicate more discussion to the decoherence effect of the cat state. Recall that the cat state is given by

$$|cat_\pm^\alpha\rangle = \frac{|\alpha\rangle \pm |-\alpha\rangle}{\sqrt{N_\pm(\alpha)}}\;,$$

where $N_\pm(\alpha) = 2 \pm 2e^{-2\alpha^2}$.

Typically the main source of decoherence in the experiment is the optical loss and can be modeled as a fictitious beam-splitter. The cat state after the beam splitter (with an amplitude reflection r and transmission t) is given by:

$$\begin{aligned} \hat{B}|cat_\pm^\alpha\rangle_a \otimes |0\rangle_b &\propto \hat{B}(\hat{D}_a(\alpha) \pm \hat{D}_a(-\alpha))|0,0\rangle_{a,b} \\ &= \hat{B}(\hat{D}_a(\alpha) \pm \hat{D}_a(-\alpha))\hat{B}^\dagger\hat{B}|0,0\rangle_{a,b} \\ &= (\hat{D}_a(t\alpha)\hat{D}_b(r\alpha) + \hat{D}_a(-t\alpha)\hat{D}_b(-r\alpha))|0,0\rangle_{a,b} \\ &= |t\alpha, r\alpha\rangle_{a,b} + |-t\alpha, -r\alpha\rangle_{a,b}\;, \end{aligned}$$

where $\hat{D}(\alpha)$ is the displacement operator, and the normalization factor is omitted for clarity. Apparently, the resulting two-mode state is an entangled coherent state. Tracing out the unwanted mode b will result in a mixed state in the signal mode a given by

$$\hat{\rho}(\alpha,\eta) = (1-P_\pm)|cat_\pm^{\sqrt{\eta}\alpha}\rangle\langle cat_\pm^{\sqrt{\eta}\alpha}| + P_\pm|cat_\mp^{\sqrt{\eta}\alpha}\rangle\langle cat_\mp^{\sqrt{\eta}\alpha}|\;, \tag{6.12}$$

[5] Generally, a n-photon subtracted squeezed vacuum state is generally given by [121]

$$|\text{nPS}\rangle \triangleq \frac{\hat{a}^n\hat{S}(\zeta)|0\rangle}{\|\hat{a}^n\hat{S}(\zeta)|0\rangle\|} \propto \hat{S}(\zeta)\text{H}_n(-\sqrt{\frac{\tanh\zeta}{2}}\hat{a}^\dagger)|0\rangle\;,$$

where H_n is the Hermite polynomials.

where

$$P_{\pm} = \frac{N_{\mp}(\sqrt{\eta}\alpha)}{2N_{\pm}(\alpha)}(1 - e^{-2(1-\eta)\alpha^2}) \ . \tag{6.13}$$

From equation (6.12), we can find that the amplitude of the coherent states is decreased from α to $\sqrt{\eta}\alpha$ due to the losses. Additionally, the decoherence of the cat state results in a parity flip with a certain chance: for instance, the even cat state becomes an odd cat state with a probability of P_+. The flipping probability dramatically increases with a larger amplitude α [122].

The degradation of the fidelity due to the decoherence can be finally given by

$$\begin{aligned} \mathcal{F}(\alpha, \eta) &= \langle cat_{\pm}^{\alpha} | \hat{\rho}(\alpha, \eta) | cat_{\pm}^{\alpha} \rangle \\ &= (1 - P_{\pm}) \frac{4e^{-(1+\eta)\alpha^2}}{N_{\pm}(\alpha) N_{\pm}(\sqrt{\eta}\alpha)} (e^{\sqrt{\eta}\alpha^2} \pm e^{-\sqrt{\eta}\alpha^2})^2 \ . \end{aligned} \tag{6.14}$$

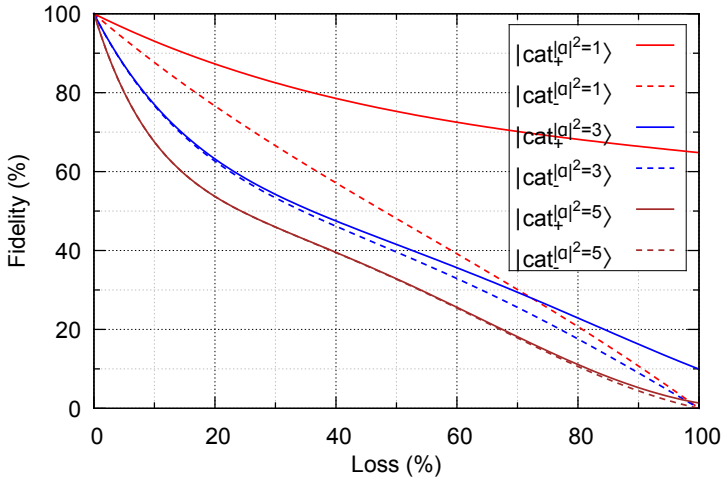

Figure 6.10: Fidelity degradation of cat as a function of the loss for different cat sizes and cat parities. For large cat states, the fidelity is very sensitive to the losses.

Figure 6.10 shows the dependence of this fidelity on the loss for different size $|\alpha|^2$ and cat parities. For a small size (e.g. $|\alpha|^2 = 1$), the odd cat state is much more sensitive to the loss than the even cat state. The even cat state can be approximated by a squeezed vacuum state while the odd cat states is closed to a squeezed single-photon state. Indeed maintaining the negativity of Wigner function is indeed more challenging. Additionally, for a small-size odd cat state, the dependence of fidelity on the loss is almost linear, which is very similar to the behavior of single-photon state. Actually in the approximation of small α, the odd cat state $|cat_{-}^{\alpha}\rangle \propto |\alpha\rangle - |-\alpha\rangle \approx (|0\rangle + \alpha|1\rangle) - (|0\rangle - \alpha|1\rangle) \approx |1\rangle$.

For a relatively large size (e.g. $|\alpha|^2 = 5$), the behavior of fidelity degradation becomes similar for even and odd cat states and both of them are extremely sensitive to the loss. For a 10% loss, the fidelity will decrease to 67.5%. Indeed for a large α, the fidelity quickly drops to 1/2 even for a small loss (cf. equation (6.13)), hence the initial pure cat state becomes a mixed state $1/2(|cat_{+}^{\alpha}\rangle\langle cat_{+}^{\alpha}| + |cat_{-}^{\alpha}\rangle\langle cat_{-}^{\alpha}|)$.

Next we will present the experimental realization for generating even cat states based on the two-photon-subtracted squeezed vacuum.

6.2.2 Experimental realization

The two-photon-subtracted squeezed vacuum can be generated by a π-phase gate on the previously generated odd cat state. The corresponding experimental setup shown in figure 6.11 is similar to the one used for generating the odd cat state. The seed beams for the locking are not shown here for simplicity. The tapping ratio of the two beam-splitters is set to be 5%. The π-phase gate is realized with an additional single-photon subtraction by a SSPD. Given a coincident event (with a coincident window of 2 ns), an even cat state is heralded in the signal path and then characterized by a homodyne detection. Thanks to the efficient SSPDs, accumulation of 50,000 quadrature measurements only takes about 1 hour.

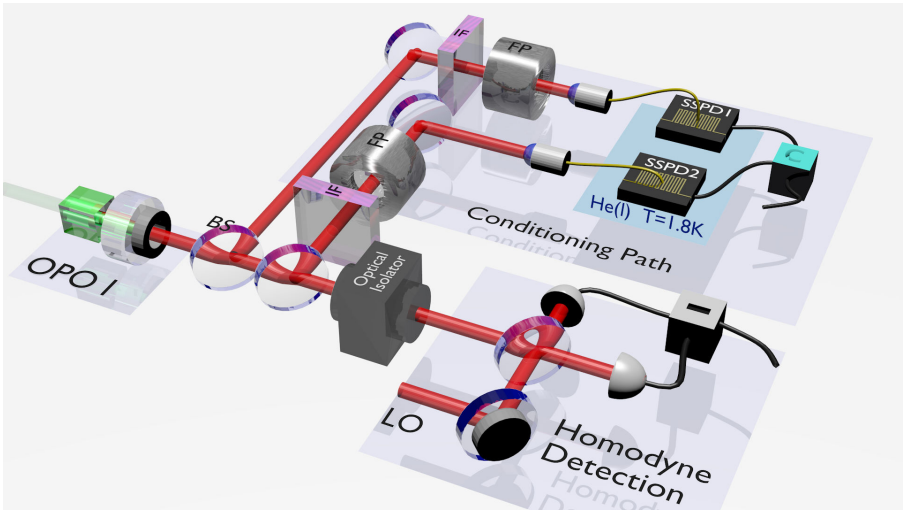

Figure 6.11: Experimental realization of an even cat state with a π-phase gate on the previously generated odd cat state. The π-phase gate is implemented by an additional single-photon subtraction. Given a coincident event, the even cat state is heralded and then characterized by a homodyne detection.

6.2.3 Results and discussion

The marginal distribution is built from 50,000 acquired quadratures as shown in figure 6.12(a). The distribution is very similar to the one obtained for a squeezed vacuum state. The generated state exhibits a photon-number oscillation as shown in 6.12(b). Ideally an even cat state only contains even photon numbers, similar to the squeezed vacuum. Additionally, for an even cat state, its Wigner function is squeezed as show in the contour plot of figure 6.12(c). Note that even for a small cat size ($|\alpha|^2 \approx 1$), the Wigner function of the cat state already demonstrates some regions with slight negative values, which is a direct signature of the non-Gaussianity.

Figure 6.13 gives the fidelity between the generated state with an ideal even cat state as a function of the cat size. The fidelity is above 70% for cat sizes $|\alpha|^2 \lesssim 1.5$ without any correction. Particularly, the fidelity for the size $|\alpha|^2 = 1$ reaches 80% and 85% without and with correction of 15% losses. The loss correction does not greatly improve the fidelity, in contrast to the case of odd cat states as shown in figure 6.8. Indeed for small sizes, the even cat states have much slower degradation of fidelity due to the loss than odd cat states (cf. figure 6.10).

We also compute the overlap between the generated even cat state here and the previously

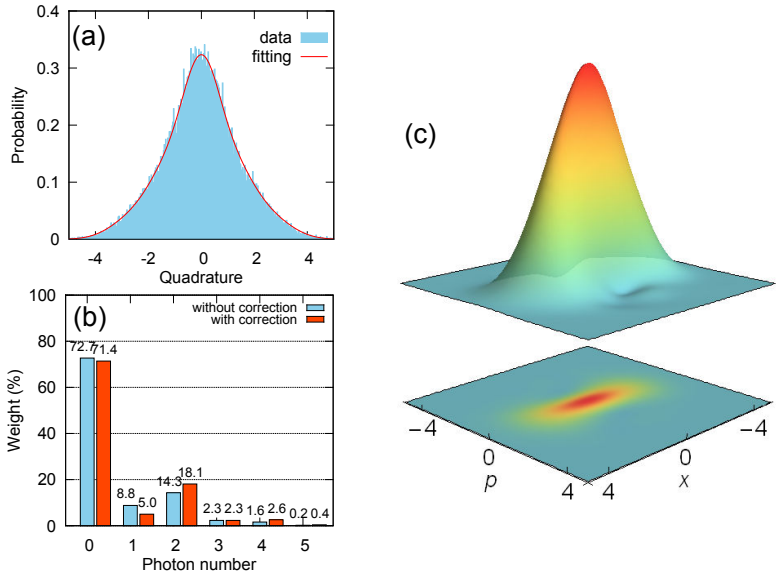

Figure 6.12: Generation of odd cat states. (a) Marginal distribution from 50,000 quadrature measurements. The red solid line is a fit of the experimental data. (b) Photon-number distribution of the generated state, with and without correction for 15% detection losses. (c) Corresponding Wigner function without loss correction.

obtained odd cat state according to the fidelity defined by

$$\mathcal{F}(\hat{\rho}_1, \hat{\rho}_2) = \left(\mathrm{Tr} \left[\sqrt{\sqrt{\hat{\rho}_2}\hat{\rho}_1\sqrt{\hat{\rho}_2}} \right] \right)^2 . \tag{6.15}$$

The fidelity can be also interpreted as a measure of "orthogonality" between the two states. In our experiment, the "orthogonality" is 0.63 (without correction) and 0.42 (with correction). The result is surprising since the fidelities of the prepared odd and even cat state is 80% and 85% for $|\alpha|^2 = 1$.

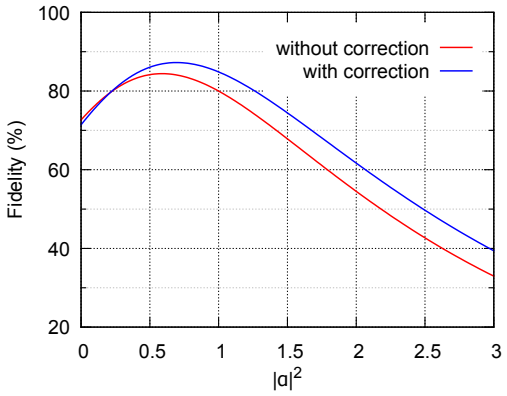

Figure 6.13: Fidelity between the experimentally generated state and an ideal even cat state as a function of the cat size.

In order to investigate the "orthogonality" dependance with the loss, in figure 6.14 we list several groups of useful states: cat states, coherent states, and qubit states. Indeed "orthogonality" between an even cat state and an odd cat state degrades extremely fast even

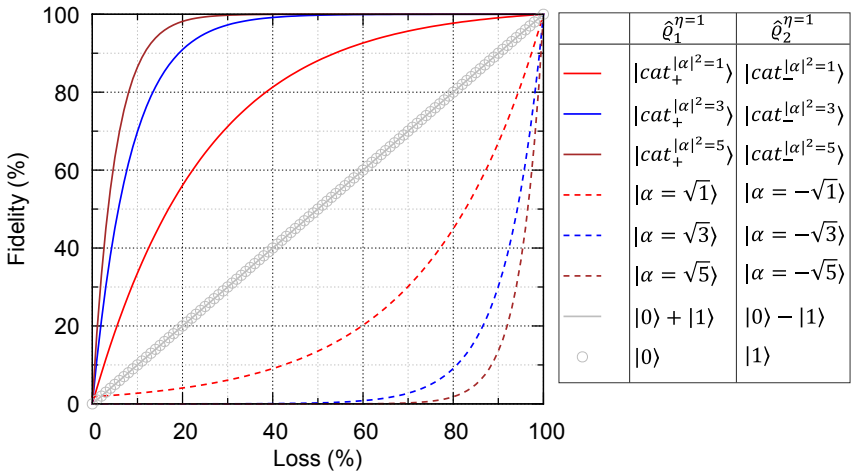

Figure 6.14: The overlap between two states $\hat{\rho}_1$ and $\hat{\rho}_2$ as a function of the loss.

for a small cat size $|\alpha|^2 = 1$. In the presence of only 20% loss, the overlap (in terms of fidelity) is already about 60%.

Contrast to cat states, "orthogonality" between two coherent states with same amplitudes but opposite phases is very resistant to the loss. Moreover, larger is the amplitude, stronger is the immunity to the loss. In principle, coherent states to cat states only need a Hadamard gate [123]. Yet Hadamard gate for coherent state qubits cannot be implemented just with Gaussian operations due to the no-go theorem that distilling Gaussian states with Gaussian operations is impossible [29]. Indeed the non-Gaussian state (especially for the one with negative Wigner function) is more sensitive to the loss. Interestingly, we can find that in figure 6.14 the solid curves corresponding to cat states and the dashed lines corresponding to coherent states have a 2-fold rotational symmetry to the point (0.5,0.5) [6].

Besides of the qubit based on continuous-variables, we also study the behavior of the qubit based on discrete variable, e.g. a superposition of vacuum and single-photon state. The decoherence behaviors are exactly the same for two pairs of orthogonal states $|0\rangle + |1\rangle$, $|0\rangle - |1\rangle$ and $|0\rangle$, $|1\rangle$.

6.3 State engineering with time-separated conditioning

In our experiments, the conditional state preparation is implemented with a continuous OPO cavity. Generally, the heralding photon-detection events can occur in random times, a distinct feature compared to the pulsed scheme. Consequently, one can exploit temporal delays between the heralding events to engineer the quantum states. One example has been already demonstrated in Chapter 5 for investigating the effect of time-separation conditioning on the heralded two-photon Fock state. Here we will give another example applied to two-photon subtracted squeezed vacuum. It will lead to the generation of a large-size cat state of traveling light, which would be an essential resource in various quantum information applications [100, 101].

[6] This symmetry holds for not too small sizes of coherent state amplitudes, e.g. $|\alpha|^2 \geqslant 1$.

6.3.1 Towards larger cat states

As mentioned before, the two-photon-subtracted squeezed vacuum state is given by

$$|2\text{PS}\rangle \propto \hat{a}^2\hat{S}(\lambda)|0\rangle = \beta\hat{S}(\lambda)(\lambda\hat{a}^{\dagger 2} - 1)|0\rangle \ = \beta\hat{S}(\lambda)(\sqrt{2}\lambda|2\rangle - |0\rangle) \ , \tag{6.16}$$

where $\beta = \lambda/(1-\lambda^2)$.

As shown in the previous experiment, $|2\text{PS}\rangle$ is already a good approximation to an even cat state. If one wants to go beyond the cat size, one possible way is to engineer the superposition weights shown in equation (6.16). As mentioned in Section 5.3.3, the optimal superposition coefficients for maximizing the fidelity are proportional to those of the even cat states $|cat_+^\alpha\rangle$, thus giving a superposition state as [97]

$$|\psi_2\rangle \propto \hat{S}(\lambda)(\frac{(1-\lambda^2)\alpha^2 - \lambda}{\sqrt{2}}|2\rangle - |0\rangle) \ . \tag{6.17}$$

With a given squeezing, $|\psi_2\rangle$ optimizes the superposition coefficients according to the cat size. As shown in figure 6.15(a), the fidelity is above 95% for a wide range up to $|\alpha|^2 = 5$. Particularly, for a 3-dB squeezing level, the fidelity can be maintained above 95% up to $|\alpha|^2 = 3$.

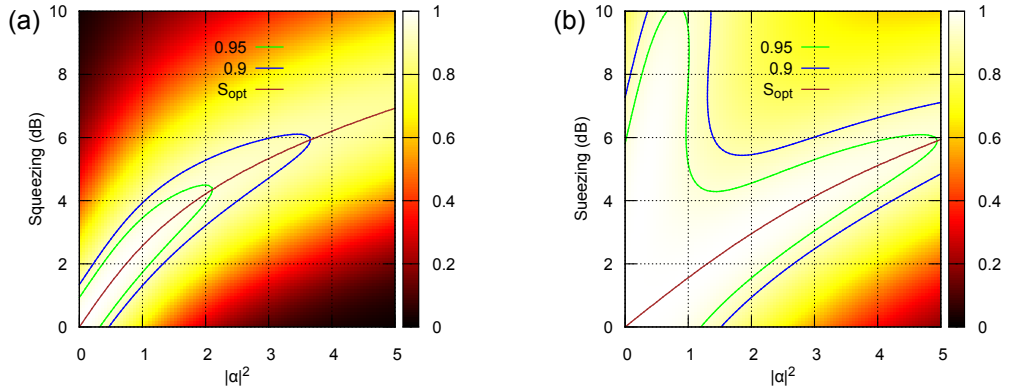

Figure 6.15: Contour plots of the fidelity compared to ideal even Schrödinger cat states for $\mathcal{F}_2 = \left\|\langle cat_+^\alpha|2\text{PS}\rangle\right\|^2$ (a) and $\mathcal{F}_2 = \left\|\langle cat_+^\alpha|\psi_2\rangle\right\|^2$ (b). S_{opt} indicates the optimal squeezing to maximize the fidelity with a given cat size $|\alpha|^2$.

Such state engineering can be realized with a two-photon subtraction from a continuous-wave squeezed vacuum by controlling the temporal separation between two triggers [99]. The theoretical investigation about this protocol can be found in [97, 98]. Here we only present a brief summary of the main results.

We consider that the two-photon-subtraction events occur at time t_1 and t_2, respectively. The corresponding temporal wave packets in the signal path are thus given by $\psi(t-t_{1,2}) = \sqrt{\pi\gamma}e^{-\pi\gamma|t-t_{1,2}|}$. As detailed in Section 5.4.1, the heralded state can be characterized by two orthogonal modes $\Psi_\pm(t) = [\psi(t-t_1) \pm \psi(t-t_2)]/\sqrt{2(1 \pm I_\Delta)}$ with $I_\Delta = e^{-\pi\gamma|t_1-t_2|}(1 + \pi\gamma|t_1-t_2|)$. The temporal two-mode model can be translated into a spatial one as illustrated in figure 6.16. The symmetric mode $\Psi_+(t)$ acts as the main mode to be measured while the asymmetric mode $\Psi_-(t)$ serves as an ancilla. Therefore such state engineering scheme is also named *ancilla-assisted photon subtraction* [99].

The two coincident photon detections can only occur when the two single photons are both from either $\Psi_+(t)$ or $\Psi_-(t)$ due to the Hong-Ou-Mandel interference effect. The two

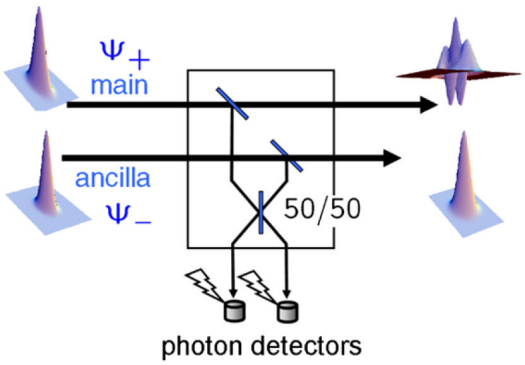

Figure 6.16: Schematic of the ancilla-assisted photon subtraction. *Extracted from* [99].

subtraction events are indistinguishable, thus resulting in a superposition state:

$$|\Phi\rangle = (\hat{a}_+^2 - \hat{a}_-^2)\hat{S}_+(\lambda_+)\hat{S}_-(\lambda_-)|0\rangle_+|0\rangle_- \ , \tag{6.18}$$

where the subscripts $\pm$ denote the modes $\Psi_\pm$. The $\lambda_\pm$ represent the effective squeezing in each mode, which are determined by the temporal separation Δ, OPO bandwidth γ and the pump power.

Typically, for $\gamma\Delta \lesssim 1$, the squeezing parameter λ_- is relatively small. With equation (6.16) and neglecting terms proportional to λ_-^2 and higher, we can get

$$|\Phi\rangle \approx \beta_+\hat{S}_+(\lambda_+)(\lambda_+\hat{a}_+^{\dagger 2} - 1 + \frac{\lambda_-}{\beta_+})|0\rangle_+\hat{S}_-(\lambda_-)|0\rangle_- \ , \tag{6.19}$$

where $\beta_+ = \lambda_+/(1-\lambda_+^2)$.

Compared to equation (6.16), the ancillary mode provides an extra degree of control for adjusting the superposition weights in the main mode. Experimentally, the parameter λ_- can be tuned by changing the time separation Δ. As a result the photon statistics in the main mode can be modified. Particularly the weights of small photon-number components are effectively reduced aiming at achieving larger cat size.

6.3.2 Experimental realization

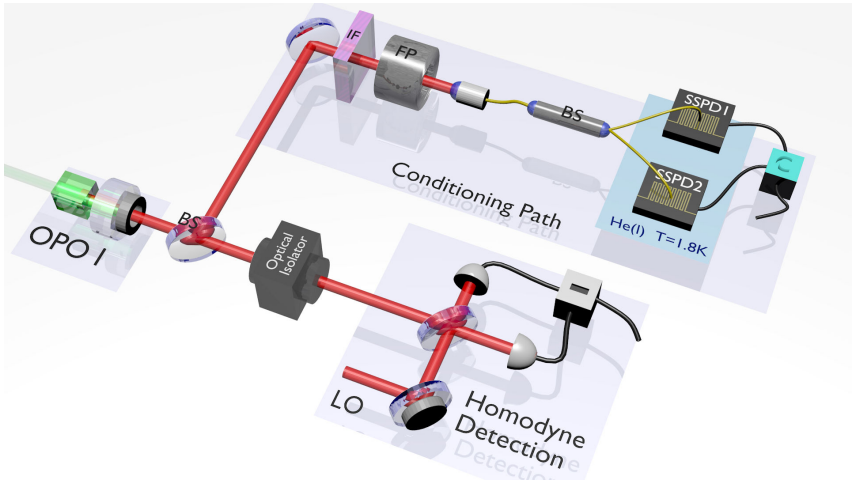

Figure 6.17: Experimental setup for generating large even cat states via ancilla-assisted photon subtraction. The cat size can be increased by playing with the time separation between the coincident detections in the conditional path.

The corresponding experiment setup for generating large even cat states is simply the extension of the single-photon-subtraction experiment shown in figure 6.4. As depicted in figure 6.17, the conditioning beam is divided by a fiber beam-splitter into two parts that are detected by two SSPDs. Given a coincidence between the two detections, the heralded state in the signal path is characterized with a homodyne detection. The time separation can be encoded into the trigger configuration of an advanced oscilloscope (Teledyne LeCroy, WaveRunner 610 Zi). Practically, to investigate the effect of time separation of the conditioning triggers, we acquire all the quadrature values corresponding to a wide coincident window (e.g. $\Delta \leqslant 60$ ns). Then we can post-process the experimental data to select a specific time separation. The symmetric temporal mode Ψ_+ is used to extract the quadrature values corresponding to the state in this temporally spread wave packet.

6.3.3 Results and discussion

In the experiment, we use a nearly pure 3 dB squeezed vacuum as the initial source, and the tapping ratio is set to be about 10% for increasing the conditioning coincident rate. The data acquisition takes 4 hours for accumulating 1000,000 quadrature measurements covering all the coincident delays $\Delta \leqslant 60$ ns. The reconstructed Wigner functions as well as photon-number distributions are given in figure 6.18 for the time separations of $\Delta = 0$ ns and $\Delta = 10$ ns, respectively. These Wigner functions are reconstructed without any losses corrections. As expected, the Wigner function of two-photon subtracted state with $\Delta = 0$ is the same with the one obtained by a π-phase gate on an odd cat state as demonstrated in the previous experiment (cf. figure 6.12).

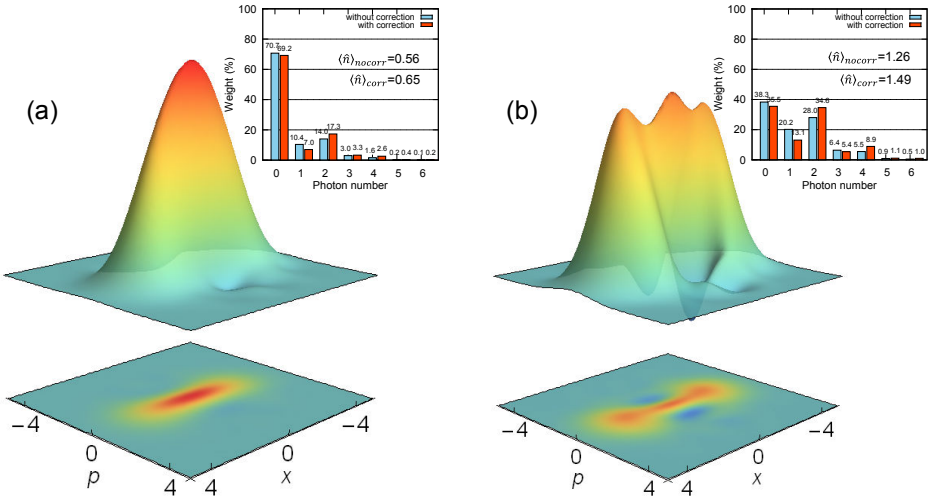

Figure 6.18: Wigner functions of the generated states without any correction in the main mode Ψ_+ for two different temporal separations of coincident detections, $\Delta = 0$ ns (a) and $\Delta = 10$ ns (b), respectively. The corresponding photon-number distributions are shown in the up-right corners as well as the average photon numbers. The initial source has a pure 3 dB squeezing.

For the case of $\Delta = 10$ ns, the Wigner function shows two distinct peaks (cf. the contour plot in figure 6.18(b)), which correspond to the peaks for $|\pm\alpha\rangle$. With a time separation of coincident triggers, the even-photon number distribution extends to $n = 4$. The increase of state energy can also been seen from the increase of the average photon number from 0.65 ($\Delta = 0$ ns) to 1.49 ($\Delta = 10$ ns) with correction of 15% losses. This reveals the mechanism

of such ancilla-assisted photon subtraction for modification of photon numbers.

The fidelity compared to an ideal even cat state is shown in figure 6.19. We can see that the fidelity is enhanced for a large cat size $|\alpha|^2 \gtrsim 1.7$. For instance, the fidelity increase from 60% ($\Delta = 0$ ns) to 70% ($\Delta = 10$ ns) for $|\alpha|^2 = 2.0$ with correction of 15% losses. For such a large size, the fidelity is limited due to the strong sensitivity to the residual losses (cf. figure 6.10).

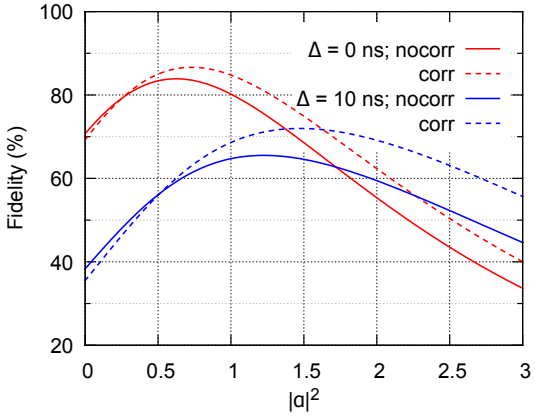

Figure 6.19: Fidelity between the experimentally generated state and an ideal even cat state as a function of cat size for the time separations of $\Delta = 0$ ns and $\Delta = 10$ ns, respectively. Here we use a nearly pure 3 dB squeezed vacuum as the initial source.

The effect of ancilla-assisted photon subtraction becomes more pronounced with a higher initial squeezing level. The results presented in figure 6.20(b) are obtained with a squeezing of -4 dB/5 dB. With a time separation $\Delta = 10$ ns, the Wigner function clearly shows two distinct positive peaks as a signature of the macroscopic nature of a large-size cat state.

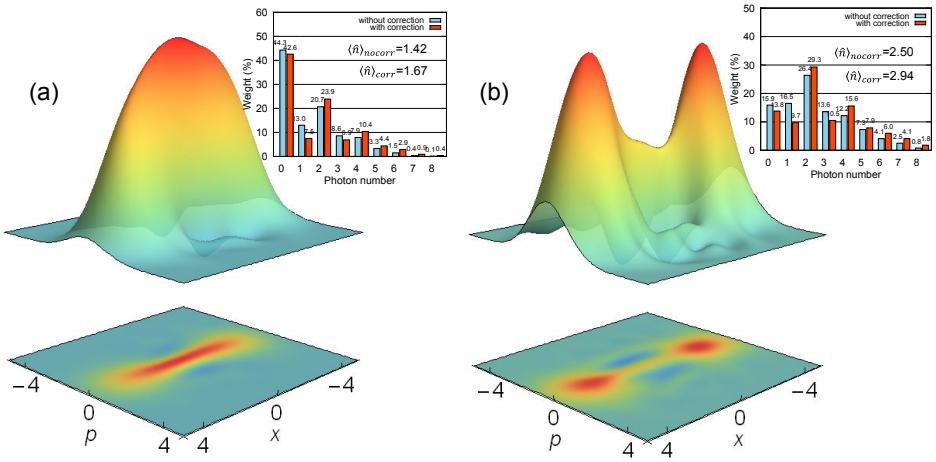

Figure 6.20: Wigner functions of the generated states without any correction in the main mode Ψ_+ for two different temporal separations of coincident detections, $\Delta = 0$ ns (a) and $\Delta = 10$ ns (b), respectively. The corresponding photon-number distributions are shown in the up-right corners as well as the average photon numbers. The initial source has a squeezing/anti-squeezing of -4 dB/5 dB.

As given in figure 6.21, the fidelity is above 50% for the cat size $|\alpha|^2$ from about 1.5 to 3.0 without loss correction. Indeed generating a large cat state $|\alpha|^2 \gtrsim 3$ with a modest fidelity $\mathcal{F} \approx 60\%$ is extremely challenging since it require a total losses $\mathcal{L} \lesssim 20\%$ (cf. figure 6.10).

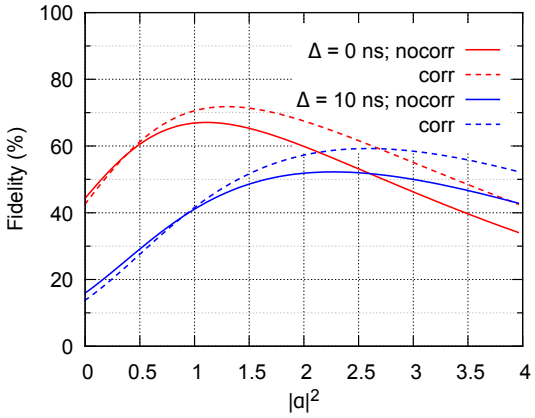

Figure 6.21: Fidelity between the experimentally generated state and ideal even cat state as a function of cat size for time separations of $\Delta = 0$ ns and $\Delta = 10$ ns, respectively. Here we use a -4 dB/5 dB squeezed vacuum as the initial source.

6.4 Conclusion

In conclusion, we have experimentally demonstrated the generation of a high-fidelity odd cat state ($\mathcal{F} = 80\%$ for $|\alpha|^2 = 1$ after correction). With an additional subsequent photon subtraction, a π-phase gate has been implemented for producing a high-fidelity even cat state ($\mathcal{F} = 85\%$ for $|\alpha|^2 = 1$ after correction). Additionally a larger-size even cat state ($\mathcal{F} \approx 60\%$ for $|\alpha|^2 \approx 3$ after correction) was obtained using the technique of time-separated conditioning. These cat states, together with the Fock states presented in the previous chapter, will be the essential sources for generating hybrid entangled states as will be shown in the next chapter.

7 | Hybrid entangled states

In optical quantum information processing, there exit two different approaches, namely the discrete- and the continuous-variable ones. They make use of either aspect of the wave-particle duality of light [124, 125]. In the discrete-variable approach, the information is carried by photonic qubits based on single photons as expressed as $c_0|0\rangle + c_1|1\rangle$, which live in a finite dimensional Hilbert space [8]. In the continuous alternative, encoding is implemented in the field quadratures, for instance as a superpositions of two coherent states with opposite phases, $c_0|\alpha\rangle + c_1|\alpha\rangle$. Such qubits are also called qumodes and span an infinite Hilbert space [126]. Both encodings have advantages and drawbacks [10].

Recently, there has been a significant progress in combining both approaches with a view to realizing a hybrid architecture that overcomes the current limitations [12, 11, 127]. In this endeavor, hybrid entanglement between particle-like and wave-like qubits, i.e. of the form $|0\rangle|\alpha\rangle + |1\rangle|-\alpha\rangle$, becomes a crucial resource to link two computational bases of different nature. Here we devise and experimentally demonstrate a scheme to generate such hybrid entanglement with measurement-induced nonlinearity [76].

In this chapter, first we will highlight the motivation for generating hybrid entangled states by giving an example of a hybrid converter. Then a proposed scheme for generating a hybrid particle-like and wave-like qubit will be theoretically investigated and experimentally realized. Beyond the demonstration of hybrid qubit state, a hybrid qutrit entanglement will also be experimentally generated using the same scheme but with two-photon heralding detections. Finally, we will extend our scheme with an additional local photon subtraction and experimentally demonstrate a so-called squeezing-induced micro-macro state.

7.1 Hybrid qubit entanglement

Generation of a hybrid entanglement between discrete-variable states (single photons) and continuous-variable states (coherent states) has special interest in fundamental quantum mechanics. In quantum optics, single photons are treated as quantum particle while coherent states are considered as the most classical field [17]. Entangling these two states is therefore reminiscent of the original idea of the Schrödinger cat state. Besides this conceptual interest, such hybrid entangled state also has a great potential in quantum key distribution protocols [128], nearly deterministic quantum teleportation [129], and loophole-free Bell inequality test [130].

7.1.1 An example: the hybrid qubit converter

In order to highlight its importance as an essential resource in the optical hybrid quantum information approach, here we give an example of hybrid converter enabling the mapping from discrete qubits to coherent state qubits.

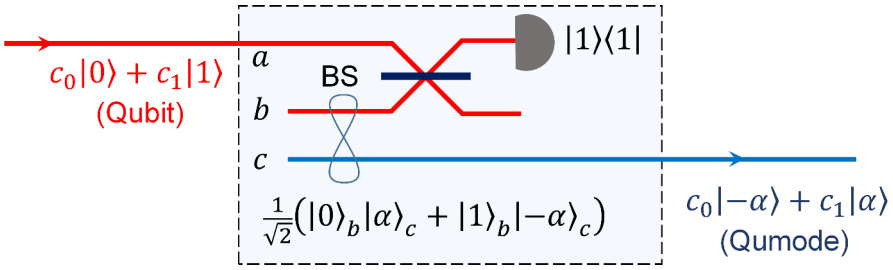

Figure 7.1: Scheme of a qubit-qumode converter using the hybrid entangled state.

The scheme is presented in figure 7.1. An intuitive picture can be given for this mapping process. The detected single photon can either originates from mode a or mode b since the simultaneous presence of single photons in both modes will result in the Hong-Ou-Mandel bunching effect. If the single photon comes from the input qubit state, then the heralded state will be $c_1|\alpha\rangle$; or the single photon is from the hybrid state, $c_0|-\alpha\rangle$ will be obtained. Due to the indistinguishibility between these two events, a superposition state is expected as $c_0|-\alpha\rangle + c_1|\alpha\rangle$.

Rigorously, this result can be obtained with the following calculation. As shown in figure 7.1, a single-rail qubit $c_0|0\rangle + c_1|1\rangle$ based on single photon is prepared in mode a as the input of a qubit-qumode converter. In this converter, the essential teleportation resource is a hybrid entangled state $|0\rangle_b|\alpha\rangle_c + |1\rangle_b|-\alpha\rangle_c$. Via a 50:50 beam-splitter, the modes a and b are mixed according to the operator evolutions:

$$\hat{a}_a^\dagger \to \frac{\hat{a}_a^\dagger + \hat{a}_b^\dagger}{\sqrt{2}} \qquad \hat{a}_b^\dagger \to \frac{\hat{a}_b^\dagger - \hat{a}_a^\dagger}{\sqrt{2}} \ .$$

The resulting three-mode state is given by

$$\begin{aligned} |\psi\rangle \propto\ & c_0|0,0,\alpha\rangle + \frac{c_0}{\sqrt{2}}(|0,1,-\alpha\rangle - |1,0,-\alpha\rangle) \\ & + \frac{c_1}{\sqrt{2}}(|1,0,\alpha\rangle + |0,1,\alpha\rangle) + c_1(|0,2,-\alpha\rangle - |2,0,-\alpha\rangle) \ . \end{aligned} \tag{7.1}$$

If we take a single-photon projection measurement on the mode b and trace out the mode a, then we can obtain

$$|\phi\rangle \propto c_0|-\alpha\rangle + c_1|\alpha\rangle \ , \tag{7.2}$$

which is the qubit (also called qumode) in the basis of coherent states $|\pm\alpha\rangle$.

Note that the reverse conversion from qumode to qubit can be realized by using Bell-state measurements for coherent-state qubits [131, 132]. In these converters, the hybrid entanglement is the critical resource for mapping the two computational bases.

7.1.2 Scheme for hybrid entanglement generation

Traveling hybrid entangled states can be deterministically generated with a cross-Kerr type interaction between a single photon and a coherent state [104, 105]. However till so far there are still many problems for obtaining a clean and suitable interaction of this kind [133]. Therefore, a measurement-induced nonlinearity is proposed to generate such an entangled state at a distance, in a similar way than the Duan-Lukin-Cirac-Zoller protocol in the discrete-variable regime [134], or the remote generation of quasi-Bell states in the continuous-variable framework [135]. The scheme relies on a probabilistic preparation heralded by the detection of a single photon in an indistinguishable fashion. The fragile components remain local, and only single photons propagate between the two distant nodes. In this way, a lossy channel affects the count rate but not the fidelity of the resulting state. Therefore, the proposed method is very suitable to establish entanglement connection over a long distance.

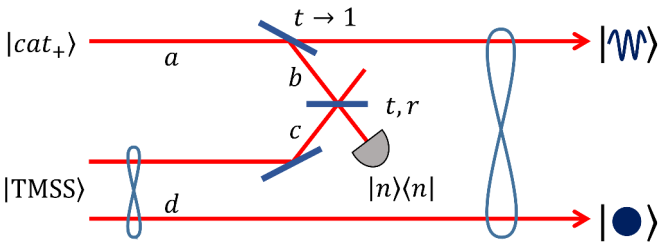

Figure 7.2: Scheme for measurement-induced generation of the hybrid entangled state. The small fraction subtracted from an even cat state is mixed with one mode of a weak two-mode squeezed vacuum state via a beam splitter. The detection of n photons will herald the generation of hybrid entanglement.

The experimental scheme is illustrated in figure 7.2. It requires as initial resources an even cat state and a two-mode squeezed vacuum state. First we tap a small fraction of the cat state with an amplitude reflectivity $\sin\theta \approx \theta \ll 1$, which results in

$$\begin{aligned} \hat{B}(\theta)|cat_+\rangle_a|0\rangle_b &= e^{\theta(\hat{a}\hat{b}^\dagger - \hat{a}^\dagger\hat{b})}|cat_+\rangle_a|0\rangle_b \\ &\approx 1 + \theta\hat{a}\hat{b}^\dagger|cat_+\rangle_a|0\rangle_b \ . \end{aligned} \tag{7.3}$$

On the other side, we have a week two-mode squeezed vacuum state ($\lambda \ll 1$) which can be approximated as

$$\begin{aligned} |\text{TMSS}\rangle &\approx |0\rangle_c|0\rangle_d + \lambda|1\rangle_c|1\rangle_d \\ &= (1 + \lambda\hat{c}^\dagger\hat{d}^\dagger)|0\rangle_c|0\rangle_d \ . \end{aligned} \tag{7.4}$$

The modes b and c are then spatially combined by a beam splitter with an amplitude reflection r and a transmission t, leading to the transformation $\hat{b}^\dagger \to t\hat{b}^\dagger + r\hat{c}^\dagger$ and $\hat{c}^\dagger \to t\hat{c}^\dagger - r\hat{b}^\dagger$. Moreover we have to consider the phase evolution during the propagation by simply doing the replacement $\hat{b}^\dagger \to e^{i\varphi_1}\hat{b}^\dagger$ and $\hat{c}^\dagger \to e^{i\varphi_2}\hat{c}^\dagger$. This leads to

$$(1 + e^{i\varphi_1}\theta r\hat{a}\hat{c}^\dagger + e^{i\varphi_1}\theta t\hat{a}\hat{b}^\dagger)(1 + e^{i\varphi_2}\lambda t\hat{c}^\dagger\hat{d}^\dagger - e^{i\varphi_2}\lambda r\hat{b}^\dagger\hat{d}^\dagger)|cat_+\rangle_a|0\rangle_b|0\rangle_c|0\rangle_d \ . \tag{7.5}$$

We only keep first-order terms in θ and λ, and the terms containing $\hat{b}^\dagger$. This yields to

$$(-e^{i\varphi_2}\lambda r\hat{b}^\dagger\hat{d}^\dagger + e^{i\varphi_1}\theta t\hat{a}\hat{b}^\dagger)|cat_+\rangle_a|0\rangle_b|0\rangle_c|0\rangle_d \ , \tag{7.6}$$

By detecting one photon in mode b and tracing out mode c, the state is reduced to

$$\lambda r|cat_+\rangle_a|1\rangle_d - e^{i\Delta\varphi}\theta t\hat{a}|cat_+\rangle_a|0\rangle_d \ , \tag{7.7}$$

where $\Delta\varphi = \varphi_1 - \varphi_2$.

As $\hat{a}|cat_+\rangle = \alpha|cat_-\rangle$ [1], the heralded state can be rewritten as

$$\theta t\alpha|0\rangle_d|cat_-\rangle_a + \lambda r|1\rangle_d|cat_+\rangle_a \ , \tag{7.8}$$

where we assume of $\Delta\varphi = \pi$ for simplicity.

The superposition weighs can be balanced with the beam-splitter ratio for obtaining a maximally hybrid entangled state [2]:

$$\boxed{|\Psi\rangle = \frac{1}{\sqrt{2}}(|0\rangle_d|cat_-\rangle_a + |1\rangle_d|cat_+\rangle_a)} \ , \tag{7.9}$$

In the limit of large α, the above entangled state can also be expressed with the rotated qubit basis in the discrete mode d, e.g. $\{|+\rangle = (|0\rangle + |1\rangle)/\sqrt{2}, |-\rangle = (|0\rangle - |1\rangle)/\sqrt{2}\}$:

$$|\Psi\rangle = \frac{1}{\sqrt{2}}(|+\rangle_d|\alpha\rangle_a - |-\rangle_d|-\alpha\rangle_a) \ . \tag{7.10}$$

7.1.3 Model of the experiment

■ Density matrix

In our experiment, we use the squeezed vacuum $\hat{S}(\zeta)|0\rangle$ to emulate the even cat state. This is a good approximation for $\alpha \sim 1$. In this case, equation (7.7) provides:

$$\hat{S}(\zeta)\left(\lambda r|1\rangle_{II}|0\rangle_I + \theta t\sinh\zeta|0\rangle_{II}|1\rangle_I\right) \ , \tag{7.11}$$

where we use the identity $\hat{a}\hat{S}(\zeta)|0\rangle = -\sinh\hat{S}(\zeta)|1\rangle$ and the subscripts a, d are replaced by I, II to emphasize that the states are experimental prepared by a type-I OPO and a type-II OPO, respectively.

Since the local squeezing operation will not change the entanglement neither the negativity of the Wigner function, thus it is convenient to consider the following state for investigating the main properties:

$$\lambda r|1\rangle_{II}|0\rangle_I + \theta t\sinh\zeta|0\rangle_{II}|1\rangle_I \ . \tag{7.12}$$

Moreover, we can use the following definition to further simplify the expression:

$$\mu = \frac{\lambda r}{\theta t\sinh\zeta} = \sqrt{\frac{n_{II}}{n_I}} = \sqrt{\frac{N_{II}}{N_I}} = \sqrt{\varepsilon} \ , \tag{7.13}$$

[1] Rigorously, we have

$$\hat{a}\,|cat_+\rangle = \alpha\frac{N_-}{N_+}\,|cat_-\rangle \ ,$$

where $\dfrac{N_-}{N_+} = \sqrt{\dfrac{1-e^{-2|\alpha|^2}}{1+e^{-2|\alpha|^2}}} \in (0,1)$. And for a not too small α, the ratio is close to 1.

[2] Note that to obtain the state $|0\rangle_d|\alpha\rangle_a + |1\rangle_d|-\alpha\rangle_a$, one can use a Hadamard gate that can be realized with a non-gaussian ancilla and projective measurements [120].

where $n_{I(II)}$ is the average photon number from each mode, and μ can be easily determined experimentally with photon counts $N_{I(II)}$ from each mode.

Finally we can investigate the state given by the following expression:

$$\boxed{|\Psi\rangle = \frac{1}{\sqrt{1+\mu^2}}(|0,1\rangle_{II,I} + \mu|1,0\rangle_{II,I})} \,. \tag{7.14}$$

Assuming that $\eta_{I(II)}$ is the intensity transmittance in mode I (II), the state after these losses is finally given by:

$$\hat{\rho} = \frac{1}{1+\varepsilon} \times \left[\begin{array}{cc|cc} (1-\eta_I)+(1-\eta_{II})\varepsilon & 0 & 0 & 0 \\ 0 & \eta_I & \sqrt{\eta_I\eta_{II}\varepsilon} & 0 \\ \hline 0 & \sqrt{\eta_I\eta_{II}\varepsilon} & \eta_{II}\varepsilon & 0 \\ 0 & 0 & 0 & 0 \end{array}\right] \,. \tag{7.15}$$

Figure 7.3 shows a hybrid representation of the density matrix for the case of single-photon balancing ($\mu = 1$) and no losses ($\eta_I = \eta_{II} = 1$). Here we use the Wigner function (well adapted to continuous-variable states) to present the reduced density matrices $\langle k|\hat{\rho}|l\rangle$ ($|k\rangle$ and $|l\rangle$ indicating discrete-qubit states). Note that here we omit the local squeezing in the mode I. In fact, the diagonal blocks are corresponding to the single-photon subtracted squeezed vacuum ($\langle 0|\hat{\rho}|0\rangle$) and squeezed vacuum ($\langle 1|\hat{\rho}|1\rangle$) which in principle live in an infinite Hilbert space. Such hybrid representation provides a visual and illustrative way for the hybrid states containing discrete and continuous modes.

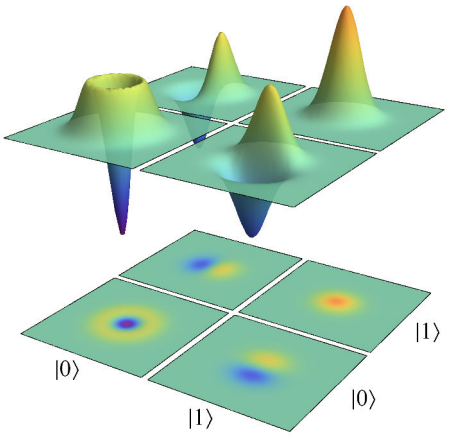

Figure 7.3: Hybrid presentation of the single-photon heralded hybrid entangled state. $\mu = 1$, $\eta_I = 1$ and $\eta_{II} = 1$. The blocks provide the Wigner functions associated with the reduced density matrices $\langle k|\hat{\rho}|l\rangle$ with $k, l \in \{0, 1\}$. The components with $k \neq l$ being not hermitian, the corresponding Wigner functions are not necessarily real, but conjugate. The plot gives therefore the real part for $k > l$ and the imaginary part for $k < l$.

■ Negativity of Wigner function

The $\langle 0|\hat{\rho}|0\rangle$ corresponds to the state when the conditioning single photon comes from the mode I. Generally, the negativity of its Wigner function (defined as the origin value of the Wigner function) is given by [3]:

$$WN = \frac{(1-2\eta_I)+(1-\eta_{II})\varepsilon}{1+\varepsilon-\eta_{II}\varepsilon} \,. \tag{7.17}$$

[3] If we globally look at the Wigner function negativity in the two-mode hybrid representation, then we should consider the balancing factor between the diagonal blocks, which results in

$$WN_2 = \frac{(1-2\eta_I)+(1-\eta_{II})\varepsilon}{1+\varepsilon} \,. \tag{7.16}$$

Specifically, the negativity for the single-photon balancing case, i.e. $\mu = 1$, is

$$WN|_{\varepsilon=1} = \frac{2 - \eta_{II} - 2\eta_I}{2 - \eta_{II}} \ . \tag{7.18}$$

The boundary of negativity is defined by

$$WN|_{\varepsilon=1} \leq 0 \Leftrightarrow \frac{\eta_I}{2 - \eta_{II}} \geq \frac{1}{2} \ . \tag{7.19}$$

This shows that it is experimentally challenging to show negativity in such two-mode experiments as both local efficiencies matter. To achieve negativity of the Wigner function, the losses (assuming symmetric losses in both channels) should be less than 1/3. Figure 7.4 shows the negativity of the Wigner function of the state $\langle 0|\hat{\rho}|0\rangle$ as function of the losses in both modes and the balancing parameter.

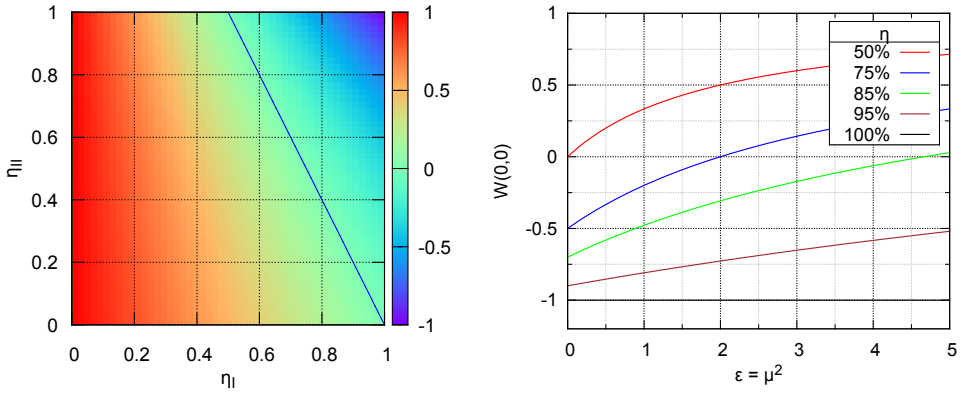

Figure 7.4: (Left) Negativity of the Wigner function of the state $\langle 0|\hat{\rho}|0\rangle$ as a function of the intensity transmittance of the two modes in the condition of single-photon balancing $\mu = 1$. The blue solid line indicates the boundary of negativity. (Right) Negativity of the Wigner function as a function of the balancing factor with the assumption of symmetric losses in the two modes.

■ Negativity of Entanglement

To quantitatively assess the generated entanglement, we compute the negativity [4] given by $\mathcal{N} = \left(||\rho^{T_A}||_1 - 1\right)/2$ [136], where T_A stands for the partial transposition. Here, we have used the useful form

$$\mathcal{N}(\hat{\rho}) = \frac{1}{2}\sum_i (|\lambda_i| - \lambda_i) \ , \tag{7.20}$$

where λ_i are the eigenvalues of the partial transpose. We remind that for a qubit the maximal value of the negativity is 0.5 given this definition.

The density matrix of the entangled state (cf. equation (7.15)) enables to calculate the negativity of entanglement as:

$$EN = \frac{\sqrt{4\eta_I\eta_{II}\varepsilon + [(1-\eta_I) + (1-\eta_{II})\varepsilon]^2} - [(1-\eta_I) + (1-\eta_{II})\varepsilon]}{2(1+\varepsilon)} \ . \tag{7.21}$$

[4] we can also use the *logarithmic negativity* $E_N(\hat{\rho}) = \log_2 \|\rho^{T_A}\|_1 = \log_2(2\mathcal{N} + 1)$.

In the case of single-photon balancing and symmetric losses in the two modes, we have

$$EN|_{\varepsilon=1,\eta_I=\eta_{II}=\eta} = \frac{\sqrt{\eta^2+(1-\eta)^2}-(1-\eta)}{2} \ . \tag{7.22}$$

Figure 7.5 plots the negativity of entanglement as a function of the intensity transmittance of the two modes and balancing factor.

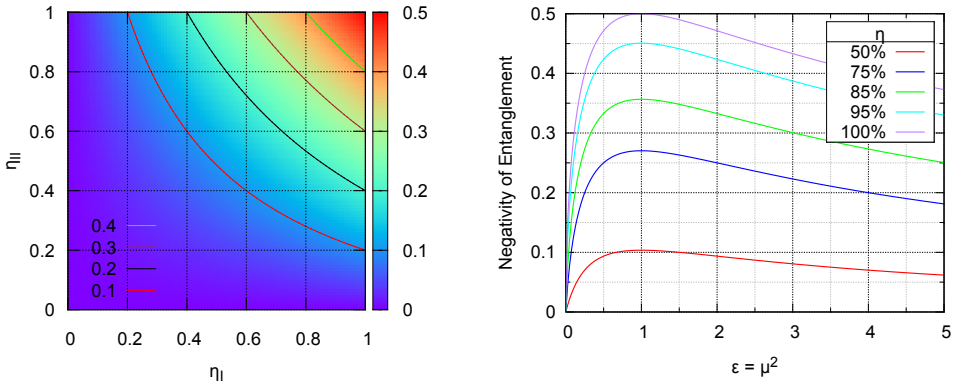

Figure 7.5: (Left) Negativity of entanglement as a function of the intensity transmittance of the two modes in the condition of single-photon balancing, $\mu = 1$. (Right) Negativity of entanglement as a function of the balancing factor with the assumption of symmetric losses in the two modes.

We now turn to the experimental realization.

7.1.4 Experimental setup

As shown in figure 7.6, the experimental setup for generating hybrid entanglement consists of three parts: preparation of the discrete-variable source (Alice), preparation of the continuous-variable source (Bob), and common conditioning path (Router). On Bob's site, a single-mode squeezer (type-I OPO) is used to generate a 3-dB squeezed vacuum, which has a nearly unity fidelity with an even cat state $|cat_+\rangle$ with a small size $|\alpha|^2 \lesssim 1$. Via a highly asymmetric beam-splitter ($R = 5\%$), a single-photon subtraction can be realized for producing an odd cat state (cf. Chapter 6). On Alice's side, a week two-mode squeezed vacuum state is prepared with a two-mode squeezer (type-II OPO) operating very far below threshold (around 100 times below). The output signal and idler modes have orthogonal polarizations, which are spatially separated via a polarization beam-splitter (PBS). Single-photon detection in the idler mode heralds a presence of single-photon state in the signal mode (cf. Chapter 5). The Router combines the two conditional paths in an indistinguishable fashion. After a set of spectral filtering, the heralding photons are finally detected by a superconducting single-photon detector (SSPD) working at cryogenic temperature (≈ 1.8 K). Given a detection event, which heralds entanglement generation, the hybrid entangled state is characterized by two high-efficiency homodyne detections.

Entanglement is very sensitive to the indistinguishablility of heralding modes. In the experiment, the OPOs are designed to have the same configuration (e.g. coating of mirror, and cavity length) to match the output spectral bandwidth. In the conditioning path, a PBS is used to erase the polarization information of the two orthogonally-polarized heralding modes. Thanks to a μCavity (Fabry-Perot cavity) in the filtering stage, the spectral and spatial modes are made to be indistinguishable.

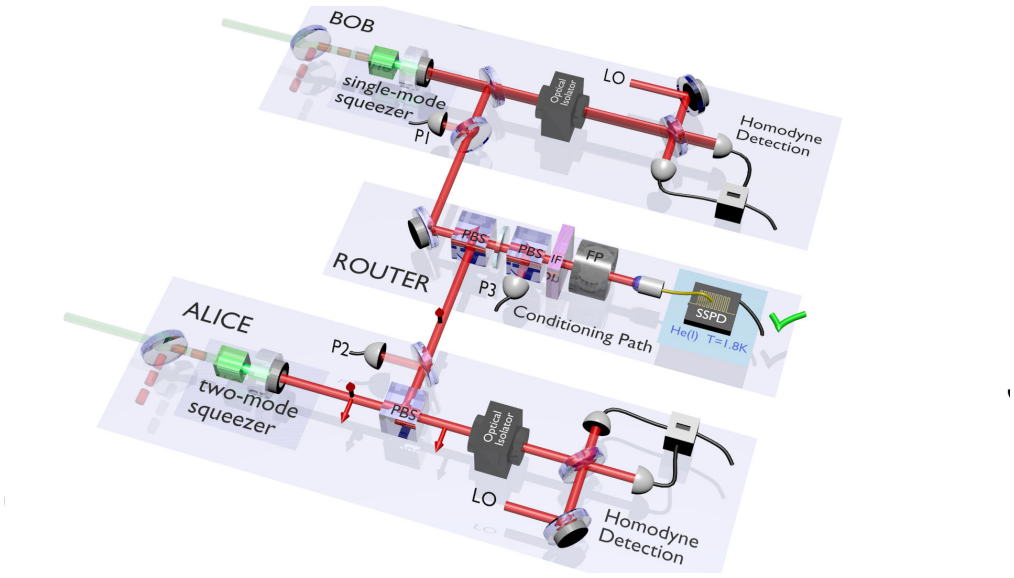

Figure 7.6: Experimental setup for the generation of hybrid entanglement between particle-like and wave-like optical qubits. Alice and Bob locally prepare the required resources with a two-mode squeezer (type-II OPO) and a single-mode squeezer (type-I OPO), respectively. The idler beam in Alice node and the small tapped part of Bob's squeezed vacuum are mixed at a central station (Router) in an indistinguishable way, which enables the generation of entanglement given a conditioning detection by a superconducting single photon detector (SSPD). The heralded entangled state is characterized by two high-efficiency homodyne detectors. Photodiodes P1, P2 and P3 are used for phase control and stabilization. The beam-splitter ratio in the central station enables to choose the relative weights in the superposition. FP stands for Fabry-Perot cavity, IF for interferential filter, PBS for polarizing beam-splitter and LO for local oscillator.

Besides of indistinguishablility, the relative phase between the superposed states has to be controlled. The drift of the superposition phase will indeed result in a statistical mixture of the form $|1\rangle\langle 1|\otimes|cat_+\rangle\langle cat_+|+|0\rangle\langle 0|\otimes|cat_-\rangle\langle cat_-|$. In the experiment, auxiliary seed beams are injected into both OPOs as phase references. The active stabilization is implemented with the microcontroller-based automatic locking system presented in Chapter 4.

Similar to the experiments for generating Fock states and cat states, the experiment here is also conducted in a cyclic fashion: 50 ms are used for phase locking and μCavity locking with the presence of seed beams, and the subsequent 50 ms are used for data acquisition with seed beams blocked (cf. Section 6.1.3).

7.1.5 Results and discussion

In order to achieve a maximally entangled state, the detection probabilities from the two conditioning modes are balanced by adjusting the beam-splitter ratio in the central station. The heralded entangled state is reconstructed by a two-mode maximum likelihood algorithm with the accumulated 200,000 data points (100,000 quadrature values for each modes).

The obtained quantum states without and with correction of 15% detection losses are shown in figures 7.7(a) and (b), respectively. We can see that the discrete mode of the hybrid entangled state is contained in the qubit subspace spanned by $|0\rangle, |1\rangle$. Higher photon-number

components are here limited to 2%. The diagonal elements $\langle 0|\hat{\rho}|0\rangle$ and $\langle 1|\hat{\rho}|1\rangle$, correspond respectively to a photon-subtracted squeezed vacuum (odd cat state) and to a squeezed vacuum (even cat state) while the non-zero off-diagonal terms demonstrate the coherence of the superposition. Without any correction, the odd cat state $\langle 0|\hat{\rho}|0\rangle$ exhibits a notable negativity of Wigner function with $W(0,0) = -0.14$ (ideally -1).

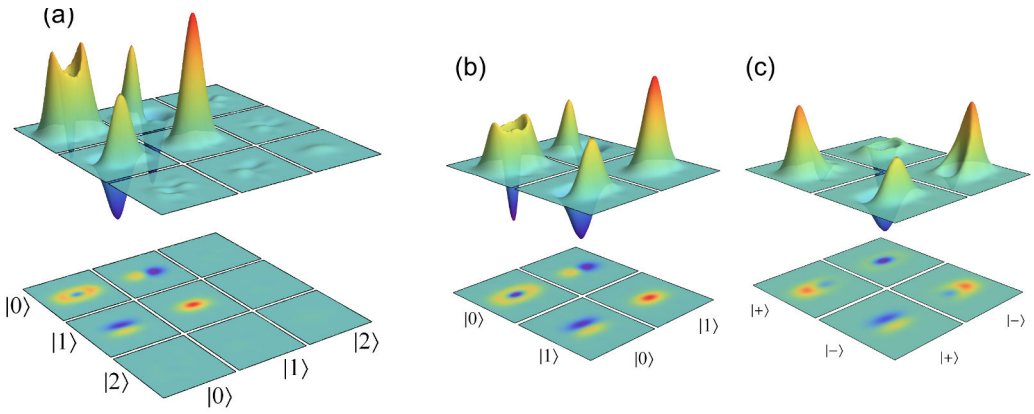

Figure 7.7: Experimental quantum state tomography of maximally entangled sates without (a) and with (b) correction for 15% detection losses. (c) Hybrid representation in the rotated basis of discrete mode. Wigner functions are associated with the reduced density matrices $\langle k|\hat{\rho}|l\rangle$ with $k, l \in \{+, -\}$, corrected for detection losses.

Corrected for detection losses, we can obtain a fidelity of 74% with the target state $|0\rangle_A|cat_-^{|\alpha|=1}\rangle_B - |1\rangle_A|cat_+^{|\alpha|=1}\rangle_B$ (62% for uncorrected case). According to equation (7.20), the negativity of entanglement is also computed to 0.37 (corrected) and 0.26 (uncorrected). Ideally the value is 0.5 for a maximally entangled qubit. The generated state can also be represented using rotated projection basis [5] as shown in figure 7.7(c). In the contour plots, the two projections $\langle +|\hat{\rho}|+\rangle$ and $\langle -|\hat{\rho}|-\rangle$ exhibit an opposite displacement in phase space, corresponding with large fidelity to two coherent states $|\alpha\rangle$ and $|-\alpha\rangle$.

One can also observe that the projected states are not completely round as they are expected. This feature arises from the initial approximation of an even cat state by a squeezed vacuum. Consequently, the projection states are actually squeezed qubit states $\hat{S}(|0\rangle \pm |1\rangle)$. To go beyond this approximation, Bob can perform a local single-photon subtraction to initially prepare an odd cat state, as will be later detailed in Section 7.4 in this chapter.

Additionally, with a slight extension of the experimental setup presented above, we can generate a hybrid qutrit entanglement as detailed now.

7.2 Hybrid qutrit entanglement

The experimental scheme shown in figure 7.2 can be readily extended to generate hybrid qutrit entanglement by using a two-photon detection as heralding. The generated hybrid entangled state would occupy a higher dimensional Hilbert space, i.e. the discrete modes span the $\{|0\rangle, |1\rangle, |2\rangle\}$ space. In this section, we will present a theoretical model as well as its experimental realization for the hybrid qutrit entanglement.

[5] $|+\rangle = (|0\rangle + |1\rangle)/\sqrt{2}$ and $|-\rangle = (|0\rangle - |1\rangle)/\sqrt{2}$.

7.2.1 Principles and model

■ Principles

We will continue to use the scheme shown in figure 7.2. In order to consider a two-photon detection in the conditioning path, the approximation of the beam-splitter operator in equation (7.3) should be extended to the second order as:

$$\hat{B}(\theta) = e^{\theta(\hat{a}\hat{b}^\dagger - \hat{a}^\dagger\hat{b})} \approx 1 + \theta(\hat{a}\hat{b}^\dagger - \hat{a}^\dagger\hat{b}) + \frac{\theta^2(\hat{a}\hat{b}^\dagger - \hat{a}^\dagger\hat{b})^2}{2} \ . \tag{7.23}$$

Similarly, the two-mode squeezed vacuum state in equation (7.4) is approximated by

$$\begin{aligned} |\text{TMSS}\rangle &= |0\rangle_c|0\rangle_d + \lambda|1\rangle_c|1\rangle_d + \lambda^2|2\rangle_c|2\rangle_d \\ &= (1 + \lambda\hat{c}^\dagger\hat{d}^\dagger + \frac{\lambda^2}{2}\hat{c}^{\dagger 2}\hat{d}^{\dagger 2})|0\rangle_c|0\rangle_d \ . \end{aligned} \tag{7.24}$$

Following the same procedure as detailed in Section 7.1.2, we can finally write the entangled state resulting from by two-photon detection:

$$\boxed{\frac{\lambda^2 r^2}{\sqrt{2}}|cat_+\rangle_a|2\rangle_d - e^{i\Delta\varphi}\theta\lambda tr\hat{a}|cat_+\rangle_a|1\rangle_d + e^{i2\Delta\varphi}\frac{\theta^2 t^2}{2}\hat{a}^2|cat_+\rangle_a|0\rangle_d} \ , \tag{7.25}$$

In our experiment, the even cat state is emulated with a squeezed vacuum, thus leading to

$$\hat{S}(\zeta)\left(\mu^2|0\rangle_a|2\rangle_d + \sqrt{2}\mu|1\rangle_a|1\rangle_d + |2\rangle_a|0\rangle_d - \frac{1}{\sqrt{2}\tanh\zeta}|0\rangle_a|0\rangle_d\right) \ , \tag{7.26}$$

where we use the following relations

$$\begin{aligned} \hat{a}\hat{S}(\zeta)|0\rangle &= -\sinh\zeta\hat{S}(\zeta)|1\rangle \\ \hat{a}^2\hat{S}(\zeta)|0\rangle &= -\cosh\zeta\sinh\zeta\hat{S}(\zeta)|0\rangle + \sqrt{2}\sinh^2\zeta\hat{S}(\zeta)|2\rangle \ . \end{aligned} \tag{7.27}$$

■ Density matrix

The local squeezing shown in equation (7.26) will be neglected in the following discussion since it doesn't change the main properties of interest (e.g. entanglement, or negativity of the Wigner function). In particular, we will focus on the state [6]:

$$|\Psi\rangle = \frac{1}{\sqrt{c^2 + (1+\mu^2)^2}}(\mu^2|2,0\rangle_{II,I} + \sqrt{2}\mu|1,1\rangle_{II,I} + |0,2\rangle_{II,I} - c|0,0\rangle_{II,I}) \ , \tag{7.28}$$

where

$$c = \frac{1}{\sqrt{2}\tanh\zeta} \ . \tag{7.29}$$

[6] Note that here we replace the subscripts a and d with I and II, respectively.

The corresponding density matrix is given by

$$\hat{\rho} = \frac{1}{c^2 + (1+\mu^2)^2} \times \left[\begin{array}{ccc|ccc|ccc} c^2 & 0 & -c & 0 & -\sqrt{2}c\mu & 0 & -c\mu^2 & 0 & 0 \\ 0 & 0 & 0 & 0 & 0 & 0 & 0 & 0 & 0 \\ -c & 0 & 1 & 0 & \sqrt{2}\mu & 0 & \mu^2 & 0 & 0 \\ \hline 0 & 0 & 0 & 0 & 0 & 0 & 0 & 0 & 0 \\ -\sqrt{2}c\mu & 0 & \sqrt{2}\mu & 0 & 2\mu^2 & 0 & \sqrt{2}\mu^3 & 0 & 0 \\ 0 & 0 & 0 & 0 & 0 & 0 & 0 & 0 & 0 \\ \hline -c\mu^2 & 0 & \mu^2 & 0 & \sqrt{2}\mu^3 & 0 & \mu^4 & 0 & 0 \\ 0 & 0 & 0 & 0 & 0 & 0 & 0 & 0 & 0 \\ 0 & 0 & 0 & 0 & 0 & 0 & 0 & 0 & 0 \end{array}\right] . \quad (7.30)$$

Figure 7.8 presents the theoretical hybrid qutrit entanglement in the condition of two-photon balancing $\mu^4 = 1 + c^2$. This condition maximizes the entanglement. Note that here we omit the local squeezing in mode I. In fact, the diagonal blocks $\langle 0|\hat{\rho}|0\rangle$, $\langle 1|\hat{\rho}|1\rangle$ and $\langle 2|\hat{\rho}|2\rangle$ correspond to the two-photon subtracted squeezed vacuum, the single-photon subtracted squeezed vacuum and the squeezed vacuum, respectively.

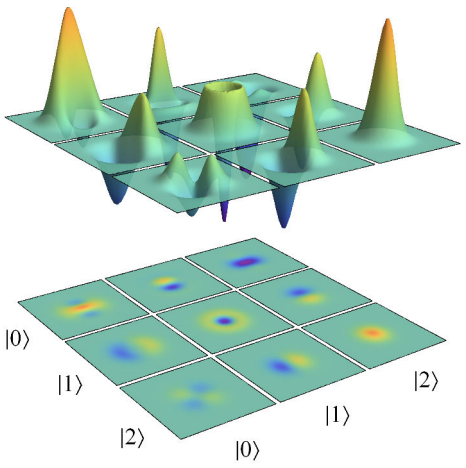

Figure 7.8: Hybrid representation of the two-photon heralded hybrid entangled state with $\mu^4 = 1 + c^2$ and 3 dB squeezing.

■ Negativity of entanglement

With equation (7.20), the negativity of entanglement can be calculated as [7]:

$$EN = \frac{\mu\left[\mu + \sqrt{1 + c^2 + \mu^4 - \sqrt{c^4 + 2c^2\left(\mu^4+1\right) + \left(\mu^4-1\right)^2}} + \sqrt{1 + c^2 + \mu^4 + \sqrt{\cdots}}\right]}{c^2 + \left(\mu^2+1\right)^2} . \quad (7.31)$$

It can be proven that the maximum negativity is achieved under the condition:

$$1 + c^2 = \mu^4 . \quad (7.32)$$

This condition corresponds to the two-photon balancing case where the two conditioning photons come from two modes with equal probabilities.

[7] Here "$\cdots$" denotes $c^4 + 2c^2\left(\mu^4+1\right) + \left(\mu^4-1\right)^2$ due to the limited space in one line.

The maximum negativity is thus given by

$$EN_{\max}(c) = \frac{\sqrt{2(1+c^2)}(\sqrt{\sqrt{1+c^2}-c}+\sqrt{\sqrt{1+c^2}+c})+\sqrt{1+c^2}}{2\left(1+c^2+\sqrt{1+c^2}\right)}\,, \tag{7.33}$$

which monotonously decreases with the parameter c (or increases with the local squeezing).

In the limit of infinite squeezing, the maximum negativity is given by

$$EN_{\max}|_{c=0} = \frac{1+2\sqrt{2}}{4} \approx 0.96. \tag{7.34}$$

The corresponding state can be obtained with $c = 0$ and $\mu = 1$, i.e. $|\Psi\rangle \propto |2,0\rangle_{II,I} + \sqrt{2}|1,1\rangle_{II,I} + |0,2\rangle_{II,I}$.

Note that for a maximally entangled qutrit, e.g. $|\Psi\rangle \propto |2,0\rangle_{II,I} + |1,1\rangle_{II,I} + |0,2\rangle_{II,I}$, the negativity of entanglement is 1.

Figure 7.9 presents the negativity of entanglement as a function of the balancing factor with different squeezing levels. We can see that larger negativity of entanglement can be obtained with a higher squeezing level.

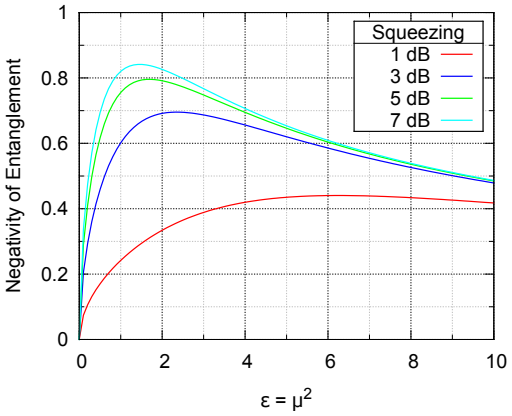

Figure 7.9: Negativity of entanglement as a function of the balancing factor with different squeezing levels.

Figure 7.10 plots the negativity of entanglement depending on the losses and balancing factor. Note that the plots are obtained by numerical calculations since there is no simple analytical expression for the negativity of entanglement in the presence of losses.

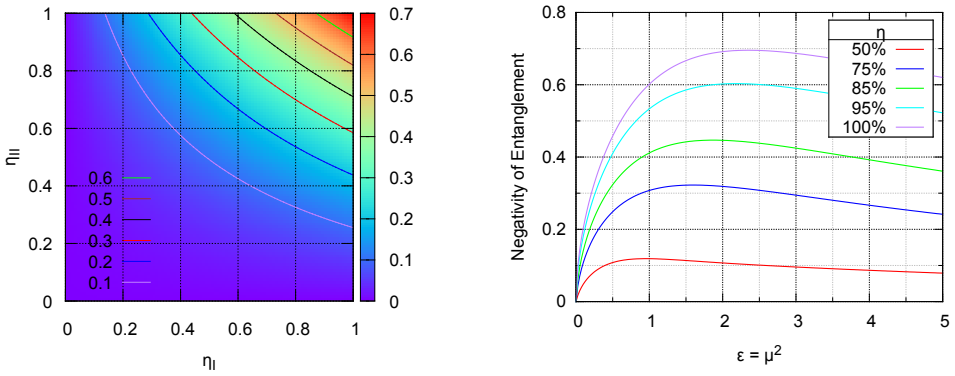

Figure 7.10: (Left) Negativity of entanglement as a function of the intensity transmittance of the two modes in the condition of two-photon balancing, $1+c^2 = \mu^4$. (Right) Negativity of entanglement as a function of the balancing factor with the assumption of symmetric losses in the two modes. 3-dB squeezing is used for the numerical simulation.

■ **Two-photon balancing**

Actually we can understand the condition (7.32) in another way. Let's denote $N_C^{I,II}$ the coincidence counts when two conditioning detectors fire at the same time. $N_{I,II}$ denote the single-photon counts for each detector. Interestingly, the coincident counts are linked with the single-photon counts by second-order correlation functions denoted as $g_2^{I,II}$:

$$\frac{N_C^I}{N_C^{II}} = \frac{g_2^I}{g_2^{II}} \times (\frac{N_I}{N_{II}})^2. \tag{7.35}$$

For two-photon balancing case we have $\frac{N_C^I}{N_C^{II}} = 1$, leading to

$$\frac{g_2^I}{g_2^{II}} = (\frac{N_{II}}{N_I})^2 = \mu^4, \tag{7.36}$$

where we use the definition in equation (7.13).

Since the mode I is in a thermal state, thus

$$g_2^I = 2 \ , \tag{7.37}$$

while the mode II is in a squeezed vacuum state, thus

$$g_2^{II} = 3 + \frac{1}{\sinh^2\zeta} \ . \tag{7.38}$$

Therefore equation (7.36) gives the condition as

$$\mu^4 = \frac{3}{2} + \frac{1}{2\sinh^2\zeta} \Leftrightarrow \mu^4 = 1 + c^2 \ , \tag{7.39}$$

where we use the hyperbolic function identity $\cosh^2\zeta - \sinh^2\zeta = 1$.

7.2.2 Experimental realization

The experimental setup for generating hybrid qutrit entanglement is almost the same as the one shown in figure 7.6. Now the conditioning detection is realized with a two-photon detection. As already demonstrated in the experiment of two-photon Fock state generation, a 50:50 fiber beam-splitter is used to spatially multiplex the conditioning photons towards two superconducting single-photon detectors (SSPDs). Given a coincidence event ($|t_1 - t_2| \leqslant 1.5$ ns), the heralded entangled state is characterized by two high-efficiency homodyne detections. After an accumulation of 100,000 quadrature measurements for each mode, the total data is then processed with a two-mode MaxLik algorithm to reconstruct the full two-mode density matrix.

According to equation (7.32), a two-photon balancing is required to obtain the maximal negativity of entanglement. In the experiment, this condition is achieved by balancing the acquisition time for accumulating a given number of coincident triggers [8] when either of the conditioning paths from type-I OPO and type-II OPO is blocked.

The reconstructed hybrid qutrit state is given in figure 7.11 after correcting 15% detection losses. Indeed the generated entangled state occupies a higher dimension of Hilbert space

[8] The oscilloscope (Teledyne LeCroy - WaveRunner 610 Zi) provides the possibility to read the timing of each trigger event.

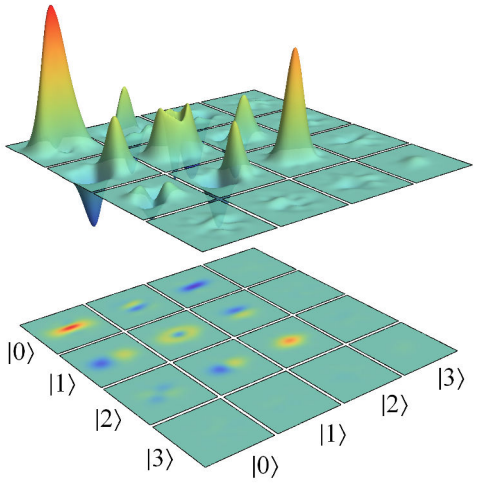

Figure 7.11: Experimental quantum state tomography of hybrid qutrit entanglement with correction of 15% detection losses. The state is prepared with two-photon balancing and 3-dB initial squeezing.

up to $|2\rangle$ for the discrete mode. The diagonal projections correspond to the two-photon subtracted squeezed vacuum ($\langle 0|\hat{\rho}|0\rangle$), the single-photon subtracted squeezed vacuum ($\langle 1|\hat{\rho}|1\rangle$), and the squeezed vacuum ($\langle 2|\hat{\rho}|2\rangle$). The negativity of entanglement is calculated to be 0.3 with the correction (0.2 without correction). This value is lower than the one we estimate theoretically (around 0.4) with the model built in Section 7.2.1. This discrepancy is still under investigation. We suspect that the degradation of entanglement may be due to the stability of the initial sources since the total acquisition time here lasts about three hours.

7.3 Additional subtraction for hybrid qubit entanglement

In this section we will further extend the experimental setup to implement a local single-photon subtraction in Bob's side (type-I OPO) to initially prepare an odd cat state. Consequently a hybrid qubit state $|1\rangle_A|cat_-\rangle_B + |0\rangle_A|cat_+\rangle_B$ is expected given a conditioning detection in the Router station. The prepared state can be regarded as the result of operating a π-phase gate on the previously demonstrated hybrid qubit state. In this newly prepared state, the even cat is approximated by a two-photon subtracted state instead of a squeezed vacuum. Consequently, we can expect a higher achievable fidelity with the target hybrid state. Here we will present in detail a theoretical model as well as the corresponding experimental realization.

7.3.1 Theoretical consideration

■ Principle

As shown in figure 7.12, n photons are first subtracted from the initial even cat state. Then the remaining part is mixed with one mode of the two-mode squeezed vacuum on a beam splitter, still in a indistinguishable fashion. The detection of single photon will herald the generation of the hybrid entanglement. Therefore, this scheme combines local and non-local photon detections.

In the following, we will consider the case of using a single-photon local subtraction. For

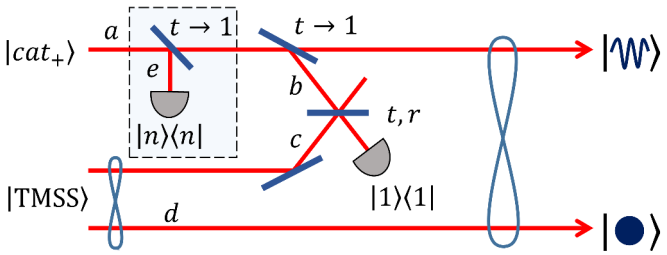

Figure 7.12: Scheme to generate hybrid entangled states with an additional local subtraction.

the type-I OPO side (initially preparing an even cat states), we have

$$\begin{aligned}\hat{B}_{ab}(\theta_0)\hat{B}_{ae}(\theta)|cat_+\rangle_a|0\rangle_b|0\rangle_e \\ \approx (1+\theta_0\hat{a}\hat{b}^\dagger)(1+\theta\hat{a}\hat{e}^\dagger)|cat_+\rangle_a|0\rangle_b|0\rangle_e\ ,\end{aligned} \tag{7.40}$$

where $\hat{B}(\theta)$ is the beam splitter operator with an amplitude reflectivity $\sin\theta \approx \theta \ll 1$.

For the type-II OPO side, the prepared two-mode squeezed vacuum state ($\lambda \ll 1$) can be approximated as

$$\begin{aligned}|\text{TMSS}\rangle &\approx |0\rangle_c|0\rangle_d + \lambda|1\rangle_c|1\rangle_d \\ &= (1+\lambda\hat{c}^\dagger\hat{d}^\dagger)|0\rangle_c|0\rangle_d\ .\end{aligned} \tag{7.41}$$

The modes b and c are then spatially combined by another beam splitter with an amplitude reflection r and a transmission t, which gives the transformation $\hat{b}^\dagger \to t\hat{b}^\dagger + r\hat{c}^\dagger$ and $\hat{c}^\dagger \to t\hat{c}^\dagger - r\hat{b}^\dagger$. Moreover, we can include the phase evolution during the propagation by simply doing the replacement $\hat{b}^\dagger \to e^{i\varphi_1}\hat{b}^\dagger$ and $\hat{c}^\dagger \to e^{i\varphi_2}\hat{c}^\dagger$, leading to

$$(1+e^{i\varphi_1}\theta r\hat{a}\hat{c}^\dagger + e^{i\varphi_1}\theta t\hat{a}\hat{b}^\dagger)(1+\theta_0\hat{a}\hat{e}^\dagger)(1+e^{i\varphi_2}\lambda t\hat{c}^\dagger\hat{d}^\dagger - e^{i\varphi_2}\lambda r\hat{b}^\dagger\hat{d}^\dagger)|cat_+\rangle_a|0\rangle_b|0\rangle_c|0\rangle_d|0\rangle_e\ . \tag{7.42}$$

We only keep the first-order terms in θ and λ, and the terms containing $\hat{b}^\dagger$ and $\hat{e}^\dagger$. This yields to

$$(e^{i\varphi_1}\theta t\hat{a}^2\hat{b}^\dagger\hat{e}^\dagger - e^{i\varphi_2}\lambda r\hat{a}\hat{b}^\dagger\hat{d}^\dagger\hat{e}^\dagger)|cat_+\rangle_a|0\rangle_b|0\rangle_c|0\rangle_d|0\rangle_e\ . \tag{7.43}$$

We detect one photon on mode b and one photon on mode e, and trace out the mode c, resulting in

$$e^{i\Delta\varphi}\theta t\hat{a}^2|cat_+\rangle_a|0\rangle_d - \lambda r\hat{a}|cat_+\rangle_a|1\rangle_d\ , \tag{7.44}$$

where $\Delta\varphi = \varphi_1 - \varphi_2$.

In our experiment, we use a squeezed vacuum $\hat{S}(\zeta)$ to approximate the initial even cat state. Therefore, the output state can be rewritten as [9]

$$\boxed{\sqrt{3+1/\sinh^2\zeta}|2\text{PS}\rangle_a|0\rangle_d + \mu|1\text{PS}\rangle_a|1\rangle_d}\ , \tag{7.45}$$

[9] where we use the following relations

$$\begin{aligned}\hat{a}\hat{S}(\zeta)|0\rangle &= -\sinh\zeta\hat{S}(\zeta)|1\rangle \\ \hat{a}^2\hat{S}(\zeta)|0\rangle &= -\cosh\zeta\sinh\zeta\hat{S}(\zeta)|0\rangle + \sqrt{2}\sinh^2\zeta\hat{S}(\zeta)|2\rangle\ ,\end{aligned}$$

and the definition of

$$\mu = \frac{\lambda r}{\theta t\sinh\zeta} = \sqrt{\frac{n_{II}}{n_I}} = \sqrt{\frac{N_{II}}{N_I}} = \sqrt{\varepsilon}\ .$$

where $|1\text{PS}\rangle$ and $|2\text{PS}\rangle$ are normalized single-photon and two-photon subtracted vacuum states, respectively.

■ Balancing

To balance the superposition weights, it requires

$$\boxed{\mu^2 = 3 + \frac{1}{\sinh^2\zeta}} \ . \tag{7.46}$$

There is another way to obtain the balancing condition from the point view of photon counting. Assume that N_0 is the count due to the local subtraction in the type-I OPO side; N_I (N_{II}) is the count in the conditional path when the photons are only from type-I OPO (type-II OPO). Then the coincidence counts needed to be balanced are given by

$$\begin{aligned} C_{0I} &= g_1 N_0 N_I \\ C_{0II} &= g_2 N_0 N_{II} \ , \end{aligned} \tag{7.47}$$

where $g_{1,2}$ is the degree of correlation for the coincident detections.

Since the counts N_0 and N_1 are from the same squeezed vacuum source, the auto-correlation function is thus given by

$$g_1 = 3 + \frac{1}{\sinh^2\zeta} \ . \tag{7.48}$$

The counts N_0 and N_2 are from two uncorrelated sources (one from type-I OPO and the other from type-II OPO), hence the cross-correlation function is simply given by

$$g_2 = 1 \ . \tag{7.49}$$

Finally the balancing of coincident counts between two modes requires

$$C_{01} = C_{02} \Rightarrow \frac{g_1}{g_2} = \frac{N_{II}}{N_I} \Rightarrow 3 + \frac{1}{\sinh^2\zeta} = \mu^2 \ , \tag{7.50}$$

which is the condition we got previously.

■ Density matrix

If we apply a local squeezing operation $\hat{S}(-\zeta)$ on mode a in equation (7.45), then the resulting state is simply represented by

$$|\Psi\rangle = \frac{1}{\sqrt{1 + c^2 + \mu^2/2}} (|0,2\rangle_{II,I} + \frac{\mu}{\sqrt{2}}|1,1\rangle_{II,I} - c|0,0\rangle_{II,I}) \ , \tag{7.51}$$

where

$$c = \frac{1}{\sqrt{2}\text{tanh}\zeta} \ . \tag{7.52}$$

The corresponding density matrix is thus given by

$$\hat{\rho} = \frac{1}{1 + c^2 + \mu^2/2} \times \left[\begin{array}{ccc|ccc} c^2 & 0 & -c & 0 & -\frac{c\mu}{\sqrt{2}} & 0 \\ 0 & 0 & 0 & 0 & 0 & 0 \\ -c & 0 & 1 & 0 & \frac{\mu}{\sqrt{2}} & 0 \\ \hline 0 & 0 & 0 & 0 & 0 & 0 \\ -\frac{c\mu}{\sqrt{2}} & 0 & \frac{\mu}{\sqrt{2}} & 0 & \frac{\mu^2}{2} & 0 \\ 0 & 0 & 0 & 0 & 0 & 0 \end{array}\right] \ . \tag{7.53}$$

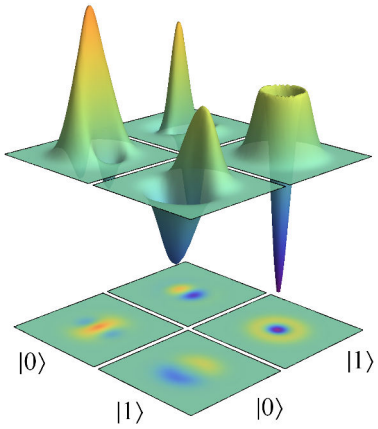

Figure 7.13: Hybrid representation of the single-photon heralded hybrid entangled state with a local subtraction.

Figure 7.13 shows the hybrid representation of the density matrix with a 3-dB initial squeezing from the type-I OPO. Note that here we omit the local squeezing in mode I. In fact, the diagonal blocks correspond to the single-photon-subtracted squeezed vacuum ($\langle 0|\hat{\rho}|0\rangle$) and the two-photon-subtracted squeezed vacuum ($\langle 1|\hat{\rho}|1\rangle$), which in principle live in an infinite Hilbert space.

■ Negativity of entanglement

The negativity of entanglement is thus computed to be

$$EN = \frac{\mu\sqrt{2+2c^2}}{2+2c^2+\mu^2}. \tag{7.54}$$

It is easy to prove that the maximum negativity (0.5) can be always obtained when the two-photon balancing condition is satisfied, namely,

$$\mu^2 = 2 + 2c^2 \ . \tag{7.55}$$

In this case, the generated state corresponds to a maximally entangled qubit state.

■ Fidelity

With an additional local subtraction, the even cat state in the generated hybrid state is approximated by a two-photon-subtracted squeezed vacuum (instead of a squeezed vacuum in the case of no local subtraction). Therefore we can expect a higher fidelity between the generated hybrid entangled qubit and the target hybrid state (for a cat size $|\alpha|^2 \simeq 1$).

To rigorously illustrate this point, we consider a maximally entangled hybrid qubit obtained with a local subtraction:

$$|\Phi_1\rangle = \frac{1}{\sqrt{2}}(|0\rangle|2\mathrm{PS}\rangle + |1\rangle|1\mathrm{PS}\rangle) \ , \tag{7.56}$$

where $|1\mathrm{PS}\rangle$ and $|2\mathrm{PS}\rangle$ are normalized single-photon and two-photon subtracted squeezed vacuum states, respectively.

And the target hybrid state is given by:

$$|\Psi_1\rangle = \frac{1}{\sqrt{2}}(|0\rangle|cat_+^\alpha\rangle + |1\rangle|cat_-^\alpha\rangle) \ . \tag{7.57}$$

The fidelity can be thus obtained by

$$\begin{aligned}\mathcal{F}_{n=1} &= |\langle\Psi_1|\Phi_1\rangle|^2 = \frac{1}{4}|\langle cat_+^\alpha|2\text{PS}\rangle + \langle cat_-^\alpha|1\text{PS}\rangle|^2 \\ &= \frac{1}{4}|\sqrt{\mathcal{F}_2} + \sqrt{\mathcal{F}_1}|^2 \ ,\end{aligned} \tag{7.58}$$

where $\mathcal{F}_1$ and $\mathcal{F}_2$ are given by equations (6.3) and (6.11), respectively.

As a comparison, we also consider a maximally entangled hybrid qubit obtained without local subtraction:

$$|\Phi_0\rangle = \frac{1}{\sqrt{2}}(|1\rangle|0\text{PS}\rangle + |0\rangle|1\text{PS}\rangle) \ , \tag{7.59}$$

where $|0\text{PS}\rangle$ is a squeezed vacuum state.

Compared to the target hybrid state

$$|\Psi_0\rangle = \frac{1}{\sqrt{2}}(|1\rangle|cat_+^\alpha\rangle + |0\rangle|cat_-^\alpha\rangle) \ , \tag{7.60}$$

the corresponding fidelity is thus calculated by

$$\begin{aligned}\mathcal{F}_{n=0} &= |\langle\Psi_0|\Phi_0\rangle|^2 = \frac{1}{4}|\langle cat_+^\alpha|0\text{PS}\rangle + \langle cat_-^\alpha|1\text{PS}\rangle|^2 \\ &= \frac{1}{4}|\sqrt{\mathcal{F}_0} + \sqrt{\mathcal{F}_1}|^2 \ ,\end{aligned} \tag{7.61}$$

where $\mathcal{F}_0$ is given by equation (6.8).

These fidelities are plotted in figure 7.14 as a function of cat size $|\alpha|^2$ for different values of squeezing. We can see that the fidelity with the targeted hybrid state can indeed be improved by the additional local subtraction for a cat size $|\alpha|^2 \gtrsim 1$. Specifically, in the case of 3 dB squeezing, we have $\mathcal{F}_{n=0} \approx 92\%$ and $\mathcal{F}_{n=1} \approx 99\%$ for $|\alpha|^2 = 1$.

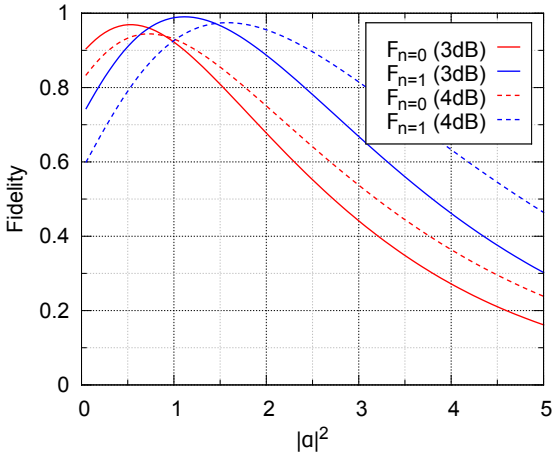

Figure 7.14: Fidelity $\mathcal{F}_{n=0}$ and $\mathcal{F}_{n=1}$ as a function of cat size $|\alpha|^2$ for different squeezing levels.

7.3.2 Experimental realization

The experimental setup is shown in figure 7.15, which is the same as the one shown in figure 7.6 except for the additional implementation of a local single-photon subtraction in Bob's side. In Alice node, a weak two-mode squeezed vacuum state is prepared with a type-II OPO. Then the orthogonally-polarized signal and idler modes are spatially separated by a polarization beam-splitter. In Bob's node, a pure 3 dB squeezed vacuum is produced by

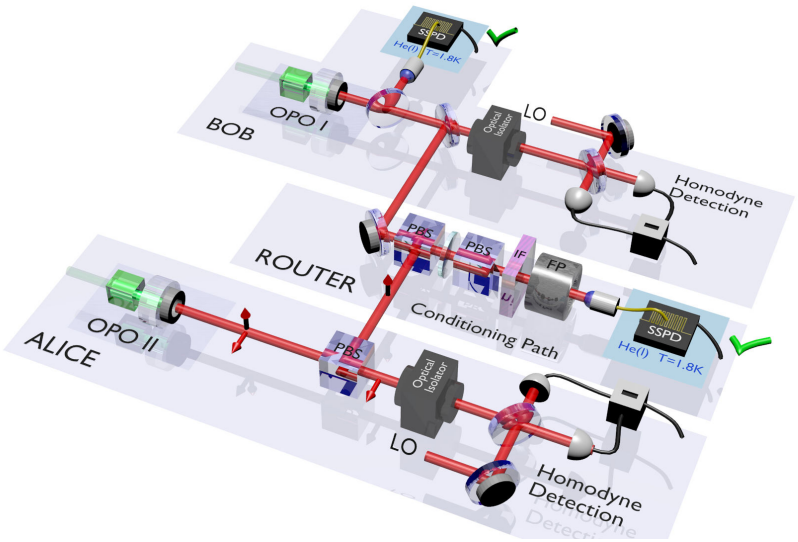

Figure 7.15: Experimental setup for generating hybrid entanglement with a local subtraction in Bob's node.

a type-I OPO. A highly-transmitted beam-splitter (R = 10%) is used to implement the local photon subtraction together with a SSPD for the conditional detection. Hence Bob locally prepares an odd cat state (single-photon-subtracted squeezed vacuum) as the initial resource.

Then another beam-splitter is used to tap off a small fraction (R = 10%) from the odd cat state, which is directed to the central station and mixed with the idler mode from Alice's side. The combined beams are then sent through a frequency filtering stage to remove the non-degenerate modes. The filtered light is then detected with another SSPD. Given a coincident detection of the two SSPDs, the heralded entangled hybrid state is characterized by two homodyne detections. After accumulating 100,000 quadrature measurements for each mode, the recorded the homodyne data is then processed with the two-mode MaxLik algorithm to reconstruct the density matrix.

To generate a maximally entangled state, the superposition weights are required to be equal. This condition can be realized by adjusting the beam-splitter ratio in the central station. Practically, we can balance the coincident counts between the local detection and non-local detections either from the type-I OPO or the type-II OPO.

Figure 7.16 shows the reconstructed hybrid entangled state with correction for 20% detection losses. In this hybrid representation, the diagonal Wigner functions correspond to the two-photon subtracted squeezed vacuum ($\langle 0|\hat{\rho}|0\rangle$) and the single-photon subtracted squeezed vacuum ($\langle 1|\hat{\rho}|1\rangle$) as expected. The presence of the off-diagonal terms indicate the coherence terms of the superposition state. The demonstrated state has a fidelity of 73.5% compared to the targeted state $|0\rangle_A|cat_+^{\alpha=1}\rangle_B - |1\rangle_A|cat_-^{\alpha=1}\rangle_B$ (60.3% without correction). The corresponding negativity of entanglement is 0.31 (0.18 without correction).

There are at least two factors limiting the state fidelity. First, to collect sufficient heralding events (typically 100,000 quadratures for each mode) for the two-mode quantum state tomography in a reasonable time (typically 3 hours), the tapping ratios of two beam-splitters in Bob's side are both set to be 10%, leading to effective losses on the prepared state. Second, it is hard to passively maintain the quality of the prepared states from the two OPOs. Specifically, the purity of the produced squeezing from type-I OPO needs to be optimized by adjusting the crystal temperature about every 30 minutes. The triple resonance of the

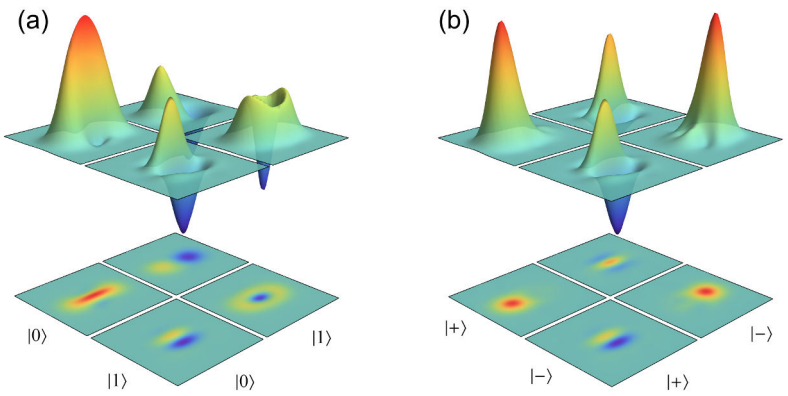

Figure 7.16: (a) Experimental quantum state tomography of hybrid entangled quibit state after correction of 20% detection losses. (b) Hybrid representation in the rotated basis of the discrete mode. Wigner functions are associated with the reduced density matrices $\langle k|\hat{\rho}|l\rangle$ with $k, l \in \{+, -\}$.

type-II OPO cavity also requires optimization.

The obtained state can also be expressed in the rotated basis of the discrete mode, e.g. $|\pm\rangle = (|0\rangle \pm |1\rangle)/\sqrt{2}$. As can be seen, the Wigner functions of the diagonal elements are positive and almost round. Indeed they exhibit a higher fidelity to coherent states compared to the previously obtained state without this additional local subtraction (cf. figure 7.7).

Moreover, by playing with the initial squeezing in Bob's node, the displacement of two coherent states can be increased, as further investigated in the following.

7.4 Squeezing-induced micro-macro states

In this section, we will investigate the optical hybrid entanglement generated here in the framework of the recent micro-macro description. With the additional subtraction in the Bob's side, we already observed that the diagonal elements in the rotation basis corresponded to two coherent states and they were well separated in phase space. The "macroscopicity" of these two states can be characterized by the mean distance in phase space, which can be discriminated with homodyne detection with a large success probability [137]. Moreover the separation can be further enlarged by increasing the squeezing level and the number of locally subtracted photons, in contrast to recently reported results based on displaced single-photon entanglement [138, 139]. In the following we will dedicate a theoretical investigation about the so-called *squeezing-induced micro-macro states*.

7.4.1 Basic principles

Let us start to examine the following maximally hybrid entangled state

$$|\Psi\rangle = \frac{1}{\sqrt{2}}(|0\rangle_A|cat_-\rangle_B + |1\rangle_A|cat_+\rangle_B) \ , \tag{7.62}$$

which can be rewritten in the rotated qubit basis [10], e.g. $|\pm\rangle = (|0\rangle \pm |1\rangle)/\sqrt{2}$:

$$|\Psi\rangle = \frac{1}{\sqrt{2}}(|+\rangle_A|\alpha\rangle_B - |-\rangle_A|-\alpha\rangle_B) \ . \tag{7.63}$$

[10] The reformulation is valid for not too small amplitudes, such as $\alpha \gtrsim 1$.

The states $|\pm\rangle$ (discrete variables) can be regarded as microscopic states while $|\pm\alpha\rangle$ (continuous variables) can be macroscopically distinguished in phase space for an amplitude $\alpha \gtrsim 1$. Actually the micro-macro state corresponds to the initial spirit of the Schrödinger cat state gedanken experiment.

Here the macroscopicity of the states is interpreted through their amplitude quadratures. Specifically one can define the mean distance between the two superposed macroscopic states $|\Phi_\pm\rangle$ in phase space [137]:

$$D = \frac{1}{\sigma_0}|\langle\Phi_+|\hat{x}|\Phi_+\rangle - \langle\Phi_-|\hat{x}|\Phi_-\rangle| \ , \tag{7.64}$$

where $\hat{x} = \sigma_0(\hat{a} + \hat{a}^\dagger)$ is the amplitude quadrature operator. The introduction of factor σ_0 will normalize the parameter D in the unit of short noise σ_0^2.

Additionally the success probability for discriminating the two states by a homodyne detector is define as

$$P = \frac{1}{2}(\langle\Phi_+|\hat{\Pi}_+|\Phi_+\rangle + \langle\Phi_-|\hat{\Pi}_-|\Phi_-\rangle) \ , \tag{7.65}$$

where the measurement projectors are given by $\hat{\Pi}_+ = \int_0^\infty |x\rangle\langle x|dx$ and $\hat{\Pi}_- = \int_{-\infty}^0 |x\rangle\langle x|dx$.

Using these witness parameters, the two coherent states shown in equation (7.63) has a mean phase-space separation $D = 4\alpha$ and a discrimination success probability $P = (1 + \mathrm{erf}(\sqrt{2}\alpha))/2$ [140]. Apparently, with an increase of the amplitude α, the macroscopicity will become more pronounced with a success probability close to unit.

In our experiment, we use photon-subtracted states to emulate the cat states. The state shown in equation (7.62) is thus generally given by

$$|\Psi\rangle = \frac{1}{\sqrt{2}}(|0\rangle_A|\phi_-\rangle_B + |1\rangle_A|\phi_+\rangle_B) \ , \tag{7.66}$$

where $|\phi_\pm\rangle$ denotes the even- and odd-photon-number subtracted squeezed states, which are orthogonal.

Similarly the state can also expressed in the rotated basis

$$|\Psi\rangle = \frac{1}{\sqrt{2}}(|+\rangle_A|\Phi_+\rangle_B - |-\rangle_A|\Phi_-\rangle_B) \ . \tag{7.67}$$

where $|\Phi_\pm\rangle = (|\phi_+\rangle \pm |\phi_-\rangle)/\sqrt{2}$.

It is well known that using higher photon-number subtraction together with higher initial squeezing can approximate larger cat states [114]. In the following we will investigate the macroscopicity of the states $|\Phi_\pm\rangle$ using the two introduced parameters.

For the case with no local subtraction in the Bob's node (cf. scheme in figure 7.12), we have

$$|\phi_+\rangle = \hat{S}|0\rangle \ , \qquad |\phi_-\rangle = \mathcal{N}[\hat{a}\hat{S}|0\rangle] = \hat{S}|1\rangle \ ,$$

which results in

$$|\Phi_\pm\rangle = \frac{1}{\sqrt{2}}\hat{S}(|0\rangle \pm |1\rangle) = \hat{S}|\pm\rangle \ . \tag{7.68}$$

The marginal distribution along the amplitude quadrature of state $|\Phi_+\rangle$ is given by [11]

$$\mathcal{P}(x) = \frac{\sqrt{s}\left(\sqrt{s}xe^{-sx^2/4} + e^{-sx^2/4}\right)^2}{2\sqrt{2\pi}} \ , \tag{7.69}$$

[11] The marginal distribution of state $|\Phi_-\rangle$ is simply given by $\mathcal{P}(-x)$. In the calculation of the marginal distribution for squeezed photon-number superposition, we use the relation:

$$\mathcal{P}_{\hat{S}\hat{\rho}\hat{S}^\dagger}(x) = e^{-\zeta}\mathcal{P}_{\hat{\rho}}(xe^{-\zeta}) \ .$$

with the squeezing factor $s = e^{-2\zeta}$.

Therefore the two parameters for measuring the macroscopicity are given by [12]

$$\begin{aligned} D &= 2\int_{-\infty}^{\infty} x\mathcal{P}(x)dx = \frac{2}{\sqrt{s}} = 2e^{\zeta} \ , \\ P &= \int_{0}^{\infty} \mathcal{P}(x)dx = \frac{1}{2} + \frac{1}{\sqrt{2\pi}} \approx 0.9 \ . \end{aligned} \tag{7.70}$$

For the case with a local single-photon subtraction, we have

$$\begin{aligned} |\phi_+\rangle &= \mathcal{N}[\hat{a}^2\hat{S}|0\rangle] = \frac{1}{\sqrt{2\lambda^2+1}}\hat{S}(\sqrt{2}\lambda|2\rangle + |0\rangle) \\ |\phi_-\rangle &= \mathcal{N}[\hat{a}\hat{S}|0\rangle] = \hat{S}|1\rangle \ , \end{aligned}$$

leading to

$$|\Phi_\pm\rangle = \frac{1}{\sqrt{2(2\lambda^2+1)}}\hat{S}(\sqrt{2}\lambda|2\rangle + |0\rangle \pm \sqrt{2\lambda^2+1}|1\rangle) \ . \tag{7.71}$$

The marginal distribution along the amplitude quadrature of state $|\Phi_+\rangle$ is given by

$$\mathcal{P}(x) = \frac{\sqrt{s}e^{-sx^2/2}\left(\lambda\left(sx^2-1\right) + \sqrt{2\lambda^2+1}\sqrt{s}x + 1\right)^2}{2\sqrt{2\pi}\left(2\lambda^2+1\right)} \ , \tag{7.72}$$

where $\lambda = \tanh\zeta$.

Therefore the two parameters are given by

$$\begin{aligned} D &= \frac{2+4\lambda}{\sqrt{s(1+2\lambda^2)}} \ , \\ P &= \frac{1}{2} + \frac{1+\lambda}{\sqrt{2\pi(1+2\lambda^2)}} \ . \end{aligned} \tag{7.73}$$

Figure 7.17 shows such entangled hybrid states for different photon-number subtractions and squeezing levels. We can clearly observe that the separation between the two micro-macro states $|\Phi_\pm\rangle$ is enlarged in phase space as the increase of the squeezing level. Moreover, the separation can be further enhanced by applying a local subtraction, as presented in the corresponding marginal distributions.

To quantitatively describe such squeezing-induced macroscopicity, we plot the mean phase-space distance D and success probability P in figure 7.18. In the case without local subtraction ($n = 0$), the probability of successful discrimination by a dichotomic homodyne detector is constant (≈ 0.9) independent from the squeezing level in spite of a larger phase-space separation. Only a single-photon subtraction ($n = 1$) can break this limit, leading to a discrimination probability close to unit even for a modest squeezing (~ 3 dB). Particularly, for a 5-dB squeezing, a distance $D \approx 6$, corresponding to six shot noise units, is obtained with a success probability $P \approx 99\%$.

Note that for the states based on displaced single-photon entanglement [138, 139], e.g. $|\Psi\rangle = \frac{1}{\sqrt{2}}(|0\rangle_A\hat{D}(\alpha)|1\rangle_B + |1\rangle_A\hat{D}(\alpha)|0\rangle_B)$, the states in the rotated basis are given by:

$$|\Phi_\pm\rangle = \frac{1}{\sqrt{2}}\hat{D}(\alpha)(|0\rangle \pm |1\rangle) = \hat{D}(\alpha)|\pm\rangle \ . \tag{7.74}$$

[12] Here we use the convention $\sigma_0^2 = 1$.

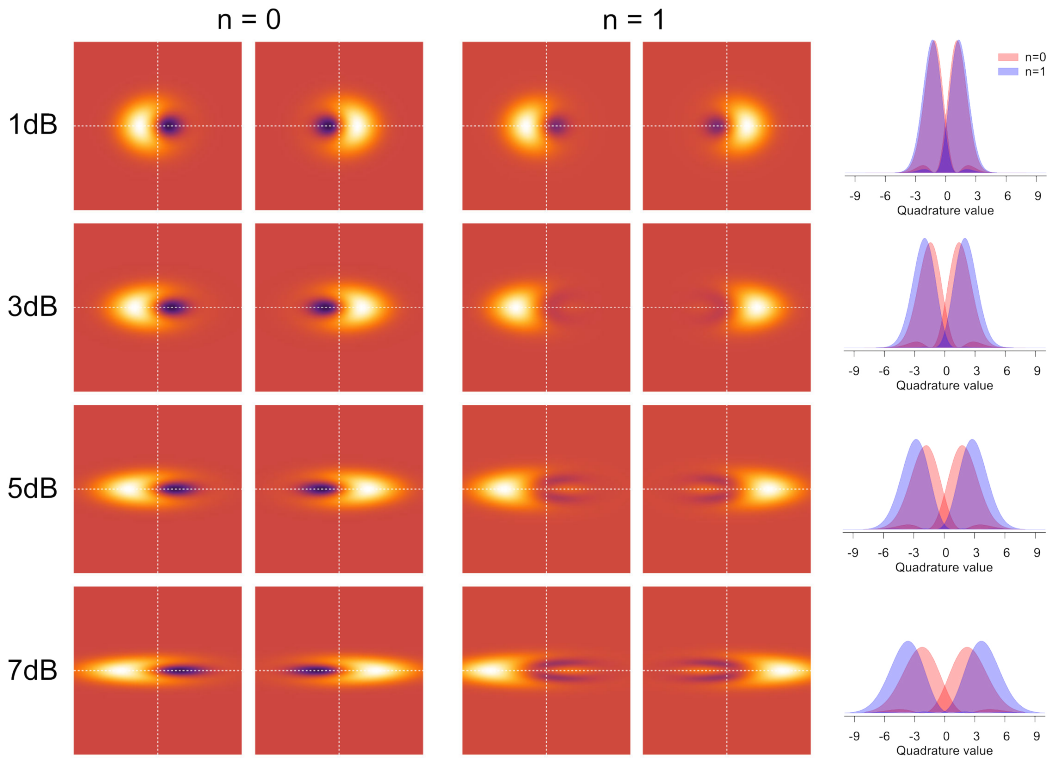

Figure 7.17: Squeezing induced micro-macro states. The contour plots give the Wigner functions of the two macroscopic states $|\Phi_{\pm}\rangle$ for a given photon-number subtraction and squeezing level. The corresponding marginal distributions along the amplitude quadrature are given in the right column.

Since they are just translated in phase space, the effective parameters D and P can be obtained by shifting them back to the origin. According to equation (7.73) we can obtain

$$\begin{aligned} D|_{\lambda=0} &= 2 \ , \\ P|_{\lambda=0} &= \frac{1}{2} + \frac{1}{\sqrt{2\pi}} \approx 0.9 \ . \end{aligned} \tag{7.75}$$

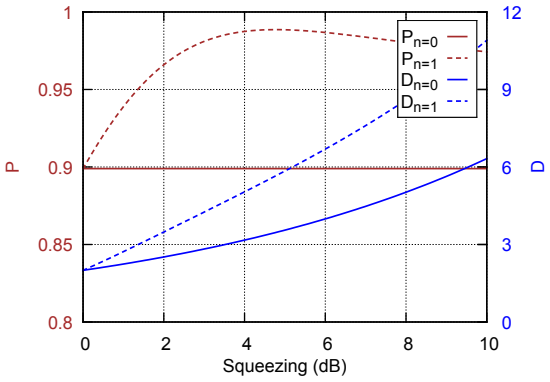

Figure 7.18: Mean phase-space distance D (blue lines) of two macroscopic states and success probability of discrimination P (brown lines) by dichotomic homodyne detection as a function of the squeezing levels for different photon number local subtractions.

7.4.2 Experimental realization and discussion

Experimental realization of the squeezing induced micro-macro states can be realized using the setup shown in figure 7.15. The different squeezing levels can be obtained by changing the pump power in the single-mode squeezer (type-I OPO). Thanks to the high escape efficiency ($\approx 95\%$) and low intra-cavity losses ($\approx 0.5\%$), the single-mode squeezer can in principle provide a squeezing of 16.5 dB (corrected for detection losses) with a pump power close to threshold (cf. Section 2.2.3). To maintain the purity of squeezing, usually the pump power is set to be much below the threshold. In this experiment, the pump power is chosen to be (5 mW, 10 mW, 15 mW, 20 mW, 30 mW), corresponding to measured squeezing/anti-squeezing of (-3 dB/3.5 dB, -3.5 dB/5.0 dB, -4.0 dB/6.0 dB, -5.0 dB/8.0 dB, -5.5 dB/10.0 dB).

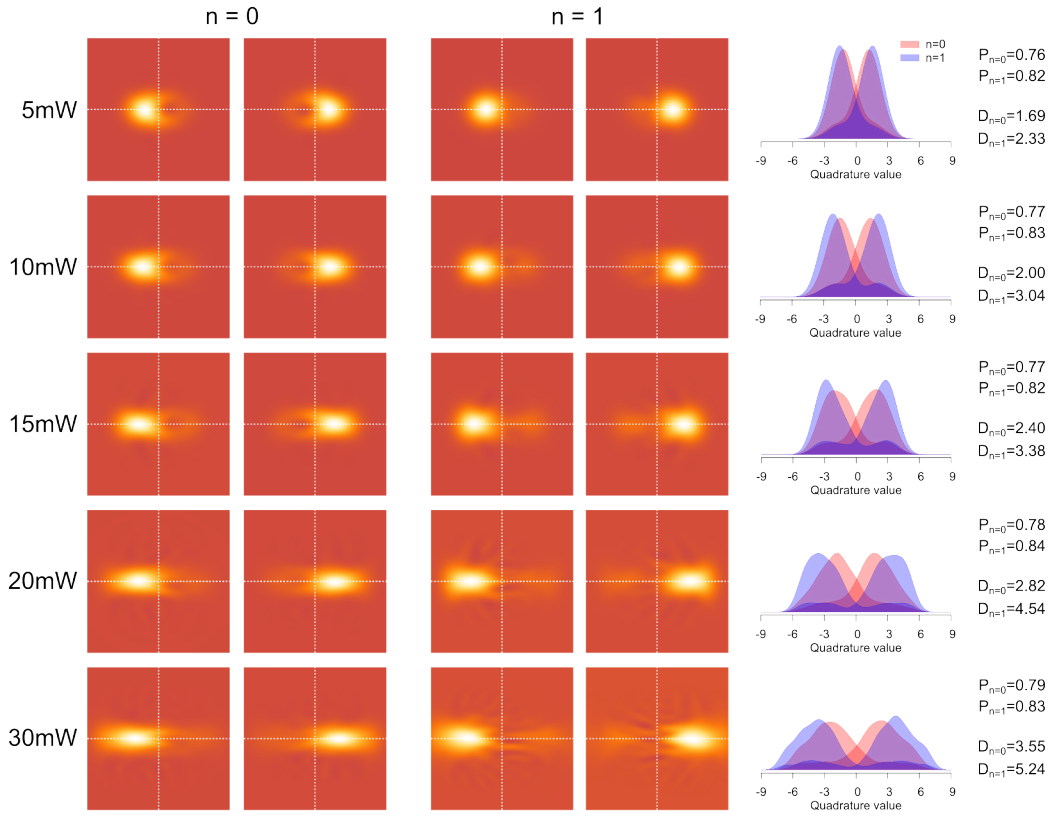

Figure 7.19: Experimental demonstration of squeezing induced micro-macro states for different photon-number local subtractions and various pump power for squeezing generation. The contour plots in left columns present the Wigner functions of two macroscopic states $\langle\pm|\hat{\rho}|\pm\rangle$. The corresponding marginal distributions along the amplitude quadrature are also given in the right column as well as the parameters D and P for quantitatively measuring the macroscopicity. These results are obtained without any loss correction.

For a given degree of squeezing, two hybrid maximally entangled states are obtained respectively with and without a local single-photon subtraction in the Bob's side. Then the hybrid entangled states are rewritten in the rotated basis of the discrete modes, e.g. $|\pm\rangle = (|0\rangle \pm |1\rangle)/\sqrt{2}$. As pointed out in the previous section, the diagonal elements $\langle\pm|\hat{\rho}|\pm\rangle$ exhibit the macroscopic feature in phase space by increasing the local squeezing and applying

the local photon-subtraction, which is verified by the experimental results as shown in figure 7.19. The contour plots in the left columns correspond to the Wigner functions of the two macroscopic states $\langle\pm|\hat{\rho}|\pm\rangle$. It can be seen that as the increase of the power pump (leading to higher squeezing) the two states are further away from each other in phase space.

In order to quantitatively investigate the squeezing-induced macroscopicity, the values of phase-space separation D and successful discrimination probability P are computed from the corresponding marginal distributions along the amplitude quadrature. With a single-photon local subtraction ($n = 1$), both parameter values are higher than the ones obtained without local subtraction ($n = 0$). In particular, at the pump of 30 mW, the distance is $D = 5.24$ corresponding to more than five short noise units, while the discrimination probability P reaches 83.4%. Note that all these values are obtained without any loss correction. After correcting 20% detection losses, these values increases to $D = 6.52$ and $P = 87.4\%$. In principle, larger phase-space separations between the two macroscopic states are achievable by implementing higher photon-number subtraction [137], resulting in more pronounced creation of macroscopicity.

The experimental implementation here for generating micro-macro states has two distinct features. First, the hybrid entangled state is heralded and is thus generated *a priori*, in contrast to the proposal [141]. Additionally the entangled state is generated remotely. The losses in the conditioning channel has no effect on the state, only reducing the heralding rate [76]. Second, the generated states here can demonstrate the macroscopic property lying in the phase-space separation induced by squeezing [142], which is not the case for the experimental realizations based on displaced single-photon entanglement [138, 139]. Such displacement merely adds a classical amplitude to the state without increasing the *quantum* macroscopicity [143].

7.5 Conclusion

In summary, we have experimentally generated the hybrid qubit entanglement between two remote nodes using two different information encodings. Such resource allows the mapping between particle qubits $|0\rangle, |1\rangle$ and coherent state wave quibits $|\alpha\rangle, |-\alpha\rangle$. Additionally, the hybrid qutrit entanglement has also been experimentally demonstrated by the two-photon conditioning detection. Furthermore, using an additional local photon-subtraction, we have investigated the squeezing-induced micro-macro entanglement. The diagonal states in the rotated basis representation indeed exhibited the increasing phase-space separation with the larger squeezing and the higher-photon-number local subtraction.

In future work, the obtained hybrid entangled states will be used to carry out a quantum state teleportation between different degrees of freedom of light based on discrete and continuous variables (cf. the hybrid converter detailed in Section 7.1.1).

Part III

Frequency Up-conversion

8 | Coincident Frequency Up-conversion System

Infrared single-photon detection with high efficiency and low dark noise played a crucial role of the conditioning measurement in the previously reported experiments. The infrared photon detection (specifically at 1064 nm in our experiments) was achieved with superconducting nanowire single-photon detectors (Appendix F). Although the SSPDs already demonstrate an excellent performance, yet the requirement of cryogenic operation inevitably increases the complication of the detection system. Parallel to the development of efficient infrared photon detectors, a large effort is therefore dedicated to the so-called *single-photon frequency up-conversion detectors*[144, 145, 146]. Such up-conversion detectors convert the infrared photons to the visible regime where Silicon avalanche photodiodes (Si-APDs) can be harnessed [147]. Compared to SSPDs, Si-APDs have distinct advantages: they are more compact, relatively inexpensive and operate at room temperature [148].

In this chapter, we will first give a general introduction of the single-photon frequency up-conversion detection. Next we will detail the experimental realization of a frequency up-conversion system based on synchronously pulsed pumping. The single-photon detection performance will then be evaluated in terms of the detection efficiency and dark noise. Finally the photon-number correlation during the up-conversion process will also be investigated.

8.1 Introduction

8.1.1 Motivation

Single-photon frequency up-conversion is a nonlinear process where the incident single photon is spectrally converted to one with higher frequency while keeping all the coherence properties (cf. Section 2.3), such as photon correlation [43], entanglement [149], and photon statistics [150]. Generally speaking, the coherent up-conversion process can mainly benefit to three purposes.

- **Efficient photon detection:** One promising application of the single-photon frequency up-conversion is to convert infrared photons to the desired spectral regime (usually visible regime) where high-performance detectors (usually Si-APDs) are available [145, 147, 151, 152, 153]. Compared to conventional detectors, the up-conversion detectors have some unique features owing to the phase-matching condition in the frequency up-conversion process, for instance narrow-band wavelength acceptance [154] and polarization selectivity [155]. The efficient detection of infrared photons by up-conversion detector has been successfully demonstrated in various applications, such as infrared imaging [156, 157, 158] and infrared ultra-sensitive spectroscopy [159, 160, 161]. Additionally, such up-conversion detectors also play an important role in optical quantum computation and communication which stringently require efficient photon detection, like quantum key distribution [162].
- **Photonic quantum interface:** Coherent frequency up-conversion can preserve the quantum characteristics of the "flying" qubits where the information is encoded with photons. This feature enables the frequency up-convertor to be a photonic quantum information interface between the transferring channel (e.g. optical fiber) and the processing node (e.g. alkaline memory) in quantum information networks [40, 163].
- **Spectro-temporal manipulation of quantum states:** As a nonlinear process, efficient frequency up-conversion requires energy and momentum conservation. Therefore, one can engineer the spectral and temporal properties of the pump field to manipulate the pulsed quantum states [164]. For instance, the frequency up-conversion has recently been demonstrated to compress a quantum light pulse by using a chirped classical pump [44, 165, 166]. Additionally a dispersion-tailored frequency conversion can lead to the realization of a quantum pulse gate that can be used to select time-frequency Schmidt modes of ultrafast quantum states [41, 167].

8.1.2 Classical description

The quantum description of coherent frequency up-conversion has already been detailed in Section 2.3. Here we will present its complementary description in the perspective of classical nonlinear optics.

Indeed the frequency up-conversion is basically a sum frequency generation (SFG) process. With the approximation of ideal plane waves and lossless nonlinear media, the coupling equations for the three involved fields are

$$\begin{aligned}
\frac{dE_s}{dz} &= i\frac{\omega_s d_{\text{eff}}}{n_s c} E_{up} E_p^* \exp(i\Delta k z) \\
\frac{dE_p}{dz} &= i\frac{\omega_p d_{\text{eff}}}{n_p c} E_{up} E_s^* \exp(i\Delta k z) \\
\frac{dE_{\text{up}}}{dz} &= i\frac{\omega_{up} d_{\text{eff}}}{n_o c} E_s E_{\text{p}} \exp(i\Delta k z) \ ,
\end{aligned} \tag{8.1}$$

where E_s, E_p, and E_{up} are the electric field amplitudes of the signal, pump and up-converted light, respectively; n_s, n_p and n_{up} are the indices of refraction at the three wavelengths; d_{eff} is the effective nonlinear coefficient of the crystal; c is the speed of light, and z is the longitudinal position along the propagation direction of the output light within the crystal. Δk represents the phase mismatch, which is defined by:

$$\Delta k = 2\pi\left(\frac{n_{up}}{\lambda_{up}} - \frac{n_p}{\lambda_p} - \frac{n_s}{\lambda_s}\right) . \tag{8.2}$$

By solving the wave equations [32], the conversion efficiency can be derived as

$$\begin{aligned}
\eta &= \frac{P_{up}}{P_s} = \frac{\lambda_s}{\lambda_{up}} \frac{(1+\gamma_0^{-2})}{2} p_- \mathrm{sn}^2[\sqrt{\tfrac{1}{2}(1+\gamma_0^2)p_+}(L/L_{\text{NL}}), \gamma] \ , \\
\gamma^2 &= \frac{p_-}{p_+} \ , \quad \gamma_0^2 = \frac{\lambda_s P_s(0)}{\lambda_p P_p(0)} \ , \\
L_{\text{NL}} &= \frac{1}{4\pi d_{\text{eff}}} \sqrt{\frac{2\varepsilon_0 n_p n_s n_{up} c \lambda_s \lambda_{up}}{I_p(0)}} \ , \\
p_\pm &= 1 + \frac{(\Delta k L/2)^2 (L_{\text{NL}}/L)^2}{1+\gamma_0^2} \pm \sqrt{\left[1 + \frac{(\Delta k L/2)^2 (L_{\text{NL}}/L)^2}{1+\gamma_0^2}\right]^2 - \left(\frac{2\gamma_0}{1+\gamma_0^2}\right)^2} \ ,
\end{aligned} \tag{8.3}$$

where $\mathrm{sn}(x, \gamma)$ is the Jacobi elliptic sine function depending on the parameter γ [1], known as the modulus; $P_{s,p}(0)$ is the input power of the signal or the pump; $I_p(0)$ is the input intensity of the signal; L_{NL} is the characteristic length of the nonlinear interaction.

For an up-conversion process where the power of the signal is much lower than the one of the pump, $\gamma_0 \to 0$. Consequently, the conversion efficiency is simplified as

$$\eta = \frac{\lambda_s}{\lambda_{up}} \frac{1}{1 + \left(\frac{\Delta k L_{\text{NL}}}{2}\right)^2} \sin^2 \sqrt{\left(\frac{L}{L_{\text{NL}}}\right)^2 + \left(\frac{\Delta k L}{2}\right)^2} \ . \tag{8.4}$$

Usually the conversion efficiency is also defined as the ratio of the photon fluxes between the up-converted field and input signal field:

$$\boxed{\eta = \left(\frac{L}{L_{NL}}\right)^2 \mathrm{sinc}^2 \sqrt{\left(\frac{L}{L_{NL}}\right)^2 \left[1 + \left(\frac{\Delta k L_{NL}}{2}\right)^2\right]}} \ , \tag{8.5}$$

where the $\mathrm{sinc}(x)$ function is defined as $\sin(x)/x$.

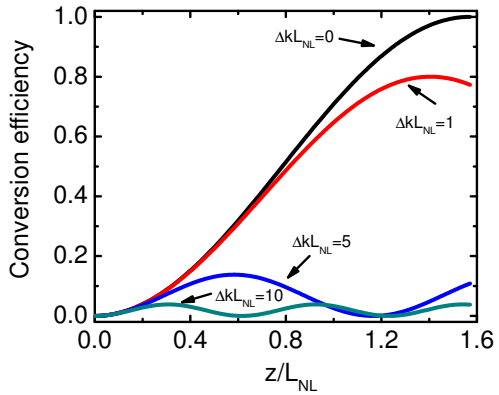

Figure 8.1: SFG conversion efficiency as a function of position in nonlinear medium including the effect of phase mismatch.

[1] For $\gamma \to 1, \mathrm{sn}(x, \gamma) \to \tanh(x)$; for $\gamma \to 0, \mathrm{sn}(x, \gamma) \to \sin(x)$.

Figure 8.1 gives the SFG conversion efficiency as a function of position in the nonlinear medium under different phase mismatch conditions. We can seen that a unit conversion efficiency can only be obtained in the case of perfect phase matching ($\Delta k = 0$). Therefore, momentum conservation on the phase velocities of the three beams should be satisfied to obtain efficient frequency conversion.

With perfect phase-matching condition, the conversion efficiency can be simplified as

$$\eta = \sin^2\left(\frac{L}{L_{NL}}\right) . \tag{8.6}$$

For a given nonlinear crystal, the interaction length is fixed. The conversion efficiency usually varies with the pump power. Therefore, we can finally rewrite the above equation as:

$$\boxed{\begin{aligned} \eta &= \sin^2\left(\frac{\pi}{2}\sqrt{\frac{P}{P_m}}\right) , \\ P_m &= \frac{\varepsilon_0 n_p n_s n_{up} c \lambda_s \lambda_{up} A_{\text{eff}}}{32 d_{\text{eff}}^2 L^2} , \end{aligned}} \tag{8.7}$$

where P_m is the required pump power for complete conversion and A_{eff} is the effective area of the pump beam. The obtained expression for the conversion efficiency is consistent with the one obtained previously within the frame of quantum description (cf. Section 2.3). Through the above discussion, we can see that unit conversion efficiency can only be obtained under the conditions of perfect phase matching and sufficiently strong pump field.

With realistic experimental parameters [2], the pump power required to achieve unity conversion efficiency is typically around 20 W. Such intense pump power can be achieved by using cavity enhancement, waveguide confinement or pulsed excitation. In the next section, we will introduce these methods and give a general comparison.

8.1.3 Comparison of pumping schemes

In order to realize a quantum up-converter, it requires a perfect phase matching and sufficiently intense pump field. Phase-matching condition can be usually obtained by optimizing the interacting wavelengths, crystal alignment, and operating temperature. Moreover, use of a QPM nonlinear crystal can even make it easier to obtain phase matching via choosing an appropriate poling period.

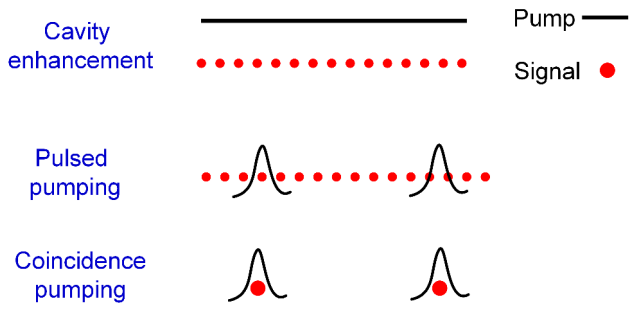

Figure 8.2: Three typical schemes for frequency up-conversion.

To achieve strong pump intensity, there are three methods: cavity enhancement, waveguide confinement, and pulsed pumping. Cavity enhancement is suitable for continuous-wave

[2] $\lambda_p = 1550$ nm, $\lambda_s = 1064$ nm, $L = 50$ mm, $A_{\text{eff}} \approx \pi \times 50^2$ μm^2, and $d_{\text{eff}} \approx 17$ pm/V.

regime, yet the strong average power would inevitably bring severe background noise due to parasitic nonlinear interactions [147, 151]. Use of a waveguide medium can reduce the required average power due to the strong spatial confinement, but the coupling loss is not satisfying [163]. Frequency conversion with pulsed pumping can be another option to decrease the background noise, as the pulse energy is concentrated within a very narrow time window to produce a high peak power [168]. However, as shown in figure 8.2, pulsed pumping for a continuous stream of signal photons will result in a very low overall detection efficiency due to the extremely low duty cycle ratio of the escorting pump. Hence, coincident pumping up-conversion, where the signal and pump sources are temporally synchronized, enables to make sure that every signal photon can be converted with the pulsed pump field.

To realize the temporal synchronization between the pump and the signal sources, one can use electrooptics intensity modulator to obtain a stream of pulses synchronized with an external lock [152]. Another way is to use an optical parametric oscillator that can produce dual-color beams by parametric down-conversion [169]. In our experiment, an alternative solution is used based on two temporally synchronized mode-locked fiber lasers [145, 144]. This technique can benefit from recent advances in dispersion management of fiber laser cavity, enabling us to control the temporal and spectral properties of pulses. We will detail the implementation of such synchronized fiber lasers in the next section.

8.2 Synchronized fiber lasers

8.2.1 Overall configuration

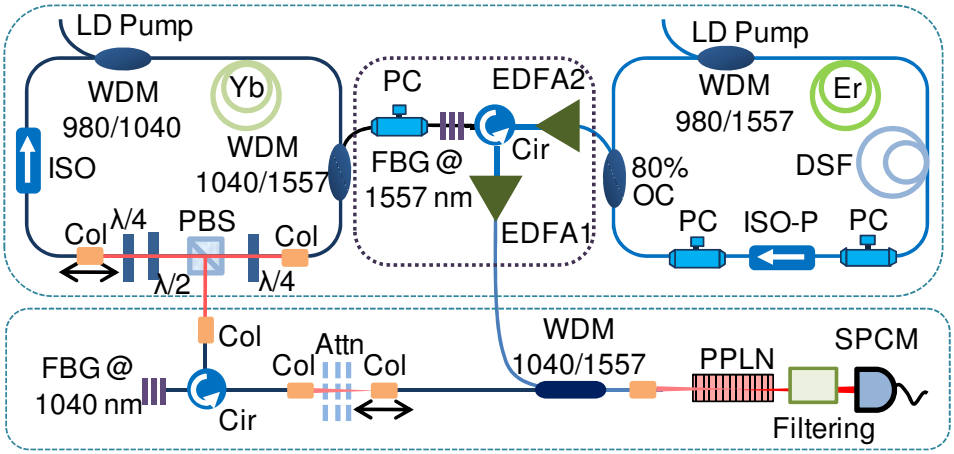

Figure 8.3: Experimental setup of the synchronization pumping system. LD, laser diode; Cir, circulator; Col, collimator; PC, polarization controller; DSF dispersion-shifted fiber; OC, output coupler; ISO, optical isolator; ISO-P, polarization-dependent isolator; PBS, polarization beam splitter; Attn, attenuator; SPCM, single-photon counting module.

As depicted in figure 8.3, the frequency up-conversion system mainly consists of two parts: a passive master-slave synchronization fiber-laser system and a single-photon frequency up-conversion counting system.

In the fiber-laser synchronization system, the master laser is an Er-doped fiber laser (EDFL) while the slave laser is an Yb-doped fiber laser (YDFL) with a mixed fiber-space configuration. The gain media are pumped by laser diodes emitting at 980 nm through

wavelength-division multiplexers. Both two fiber lasers are passively mode-locked by the nonlinear polarization rotation in the fiber cavity, operating at a repetition rate of 17.6 MHz to enable a high-speed detection. The initialization of the mode-locking is realized by adjusting the angles of the polarization controller (in EDFL) or wave plates (in YDFL). The two fiber lasers are then used to provide signal and pump sources in the sum frequency generation after appropriate engineering and control.

Frequency conversion as a nonlinear process is only significant for a sufficiently intense pump excitation. In our experiment, the pulsed pump is used to provide a high peak power since the energy is concentrated within an extremely short temporal window. Additionally, in order to reduce the required pump power for the complete conversion, a nonlinear crystal with a large effective nonlinear coefficient and a long interaction length will be preferable (cf. equation (8.7)). Thanks to the quasi-phase-matching (QPM) technique, a periodically poled lithium niobate (PPLN) crystal is utilized in our experiment. However, a long crystal length length (50 mm) leads to a quite narrow acceptance bandwidth ($\approx$ 0.3 nm) [3], which cannot be matched by typical mode-locked fiber lasers with a relatively broad bandwidth of a few nm. To realize an efficient frequency conversion, specific control of the pulses in the spectrum domain is therefore required to satisfy the requisite QPM.

8.2.2 Spectro-temporal engineering

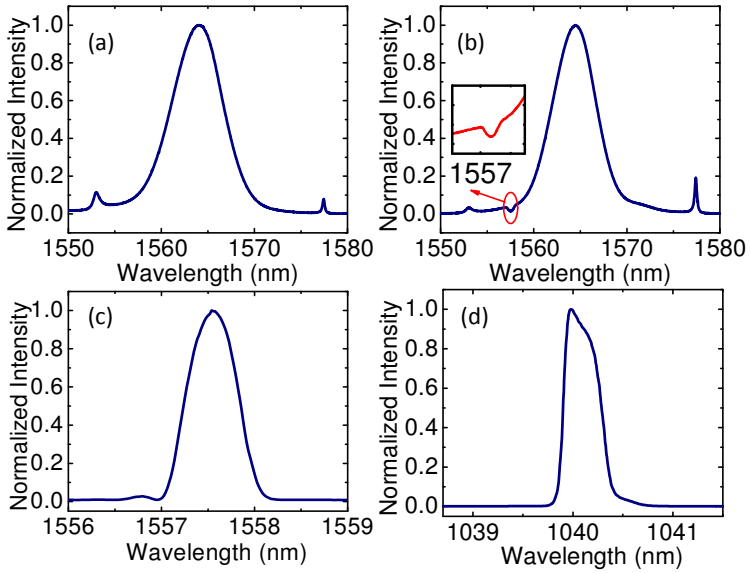

Figure 8.4: (a) The Er-doped fiber laser spectrum. (b) Spectrum of the FBG transmission. Inset: zoomed spectrum around 1557 nm. (c) Spectrum of the FBG reflection. (d) Spectrum of the signal source from the Yb-doped fiber laser.

As shown in figure 8.3, the EDFL includes a section of dispersion-shifted fiber (DSF) for the dispersion management in the ring cavity, which not only facilitates the mode-locking, but also tailors the output spectrum. Figure 8.4(a) shows the corresponding spectrum

[3] The acceptance bandwidth of the crystal can be estimated by

$$\Delta\lambda = \frac{2\lambda\Lambda}{\pi L} ,$$

where L is the crystal length and Λ is the grating period.

centered at 1563.8 nm with a full width at half maximum (FWHM) of 6.2 nm. The EDFL output is then spectrally filtered by a fiber Bragg grating (FBG) to approach the QPM bandwidth of the PPLN crystal. As a result, a narrow spectral portion of the EDFL is filtered out by the FBG reflection as shown in figure 8.4(b). The FBG reflection is further amplified by an Er-doped fiber amplifier (EDFA) as the pump source for the frequency conversion. The maximum average power after amplification reaches about 60 mW. The corresponding spectrum is centered at 1557.6 nm with a 0.56-nm FWHM bandwidth as shown in figure 8.4(c).

The FBG transmission is then injected into the slave laser cavity (YDFL) through a fiber wavelength-division multiplexer. The light injection is used to trigger the mode-locking of YDFL that will be synchronized with the master laser. Similarly, another FBG is used at the output of YDFL to realize spectral matching of the signal pulse. The filtered spectrum is centered at 1040.0 nm with a FWHM bandwidth about 0.35 nm as shown in figure 8.4(d).

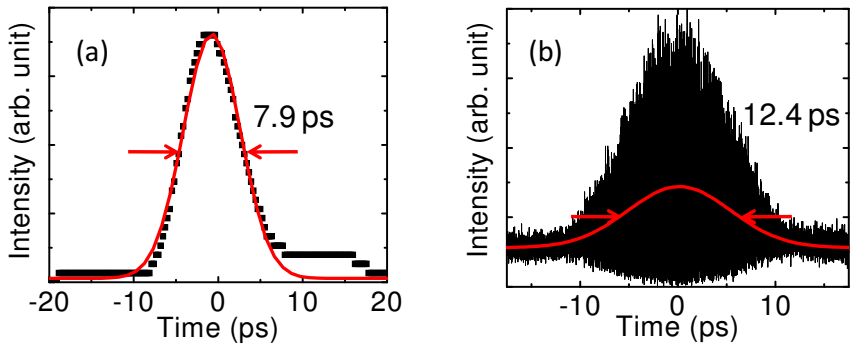

Figure 8.5: Autocorrelation pulse profiles of the signal source (a) and the pump source (b), respectively. Solid symbols in black are the experimental data and solid curves in red are the Gaussian fits to the data.

The pulse duration of the signal pulse is measured by an autocorrelator. Figure 8.5(a) gives an autocorrelation trace with a FWHM bandwidth of 7.9 ps, which corresponds to the actual pulse duration of 5.6 ps by assuming a Gaussian temporal profile (with a scaling factor of $\sqrt{2}$). In order to optimize the up-conversion efficiency, the pump pulse duration relative to the signal pulse needs to be carefully adjusted. The total conversion efficiency is indeed dependent on the pulse overlap as given by

$$P_{overlap} = \int_{-\infty}^{+\infty} P_0(I_p(t))I_s(t)dt \ , \tag{8.8}$$

where P_0 is the conversion efficiency dependent on the temporal distribution of the pump intensity I_P as $\sin^2(\sqrt{I_p(t)})$, and $I_s(t)$ is the normalized input pulse profile $\int I_s(t)dt = 1$.

Figure 8.6 gives the simulated conversion efficiency as a function of the pump pulse duration for the 5.6-ps signal pulse duration. When the pulse duration of the pump is much shorter than the one of the signal, the conversion efficiency is very low as expected since the signal photons have large probability to appear outside of the temporal window of pump pulses. Hence the increase of the pump pulse duration can lead to a higher conversion efficiency. However, the conversion efficiency will finally saturate when the pump pulse duration is about twice as the signal one. Practically, too long pump pulse duration will not favor the experiment due to the reduction of the peak energy and an increase of background counts.

Thanks to the spectral filtering by the FBGs in the experiment, the pulse durations of the

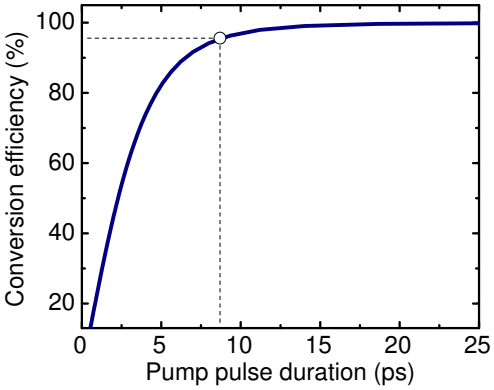

Figure 8.6: Simulated conversion efficiency as a function of the pump pulse duration by assuming a signal pulse with a FWHM of 5.6 ps. The circle shows the experimental situation.

master and slave lasers are almost stretched according to the time-frequency Fourier transform. Via cavity dispersion management in the master laser cavity, the spectro-temporal property of the output pulses can be precisely optimized. Consequently, a 8.8-ps pump pulse duration is inferred from the autocorrelation trace with a 12.4-ps bandwidth as shown in figure 8.5(b). Theoretically the conversion efficiency can reach 95.6% as shown by the circle in figure 8.6. The pump pulse duration (8.8 ps) is chosen to be slightly longer than the signal pulse duration (5.6 ps), which not only permits an efficient frequency up-conversion, but also mitigate the background noise indued by the intense pump field.

8.2.3 Passive injection locking

To implement a coincident pumping up-conversion, the signal pulses have to be synchronized with the pump pulses. In other words, the two fiber lasers (YDFL and EDFL) used as pump and signal sources need temporal synchronization. To this end, the two independently lasers should be mode-locked at exactly the same repetition rate. This generally requires a feed-back locking system to compensate the unavoidable laser cavity variation [4]. In our experiment, a passive synchronization is used due to its simplicity without the need of any electronic phase-loop devices [170].

The passive synchronization is realized via light injection in a master-slave configuration [171, 172]. Specifically, the master pulses (from EDFL) are injected into the slave cavity (YDFL), initiating a nonlinear interaction due to the cross-phase modulation. Consequently the pulse generation in the slave cavity is affected by the co-propagating injected pulses. This nonlinear coupling finally leads to the generation of synchronized pulses [173]. The master-slave injection configuration is well-suited for the fiber-laser synchronization because the cross-phase modulation effect is largely enhanced by the tight confinement of light in a single mode fiber. Additionally, the two synchronized lasers are independent from each other, thus eliminating the mutual perturbation.

In the experiment, when the two fiber lasers operate in free-running mode, their repetition rates are manually tuned to be roughly the same ($\Delta f_r \lesssim 5$ Hz) by precisely moving the fiber collimator on a translational stage (YDFL in figure 8.3). Then, in the presence of light injection, the slave laser can be mode-locked by carefully aligning the quarter- and half-wave plates in the laser cavity thanks to the nonlinear polarization evolution. Eventually, synchronized pulse trains are obtained as shown in figure 8.7. Practically the stability of the synchronization can be improved by optimizing the polarization of the master injection light. As a result, a cavity mismatch tolerance of 25 μm is obtained, which corresponds to

[4] Note that the repetition rate f_r is inversely proportional to the effective cavity length L_{eff} as $f_r = c/L_{\text{eff}}$, where c is the speed of light in vacuum.

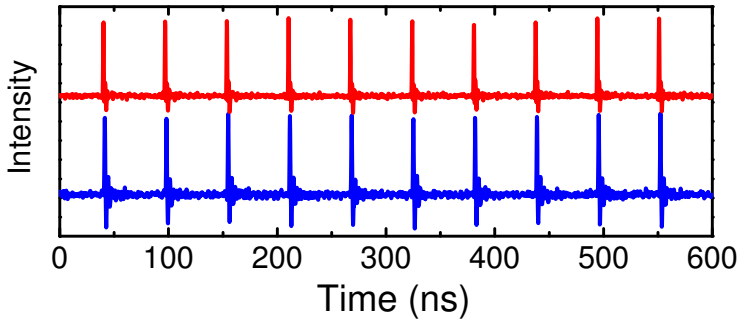

Figure 8.7: Pulse trains from the synchronized fiber lasers with a repetition rate of 17.6 MHz.

a repetition frequency tuning of 40 Hz. Such a large mismatch tolerance enables the stable synchronization of two fiber lasers for several hours.

8.2.4 Timing jitter

To quantitatively evaluate the synchronization precision, the concept of *timing jitter* is used. This quantity describes the temporal fluctuation between the two synchronous optical pulses. The measurement of timing jitter is carried out with a widely-used method so-called *optical cross-correlation technique* [174]. This technique is based on sum frequency generation between the synchronous pulses. By scanning the relative time delay, a cross-correlation trace is obtained as shown in figure 8.8(b). For the jitter measurement, the temporal delay is adjusted to the point where the SFG intensity is at its half maximum. In this situation, the intensity fluctuation has a linear relationship with the relative timing delay. Then the SFG signal is recorded by a spectrum analyzer (SRS, SR760), which can be translated into the time fluctuation (timing jitter).

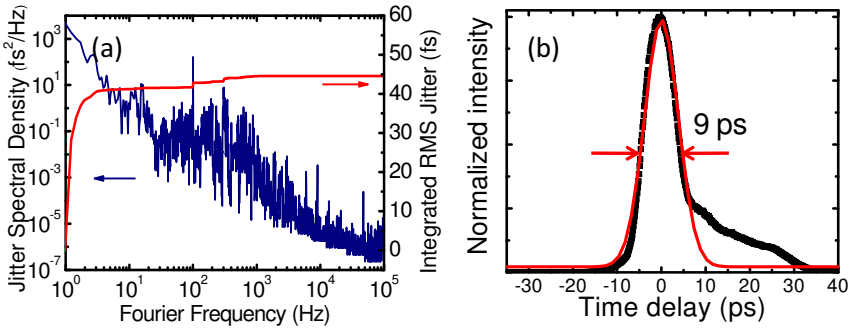

Figure 8.8: (a) Timing jitter power spectral density and the integrated timing jitter in Fourier domain. (b) Cross-correlation trace of the synchronized lasers.

Specifically the RMS (Root Mean Square) timing jitter σ_{RMS} is given by [174]:

$$\sigma_{\mathrm{RMS}} = \sqrt{\int_{f_1}^{f^2} [\frac{S(f)}{2\pi f_0 A_0}]^2 df} \ , \tag{8.9}$$

where $S(f)$ is the measured jitter spectral density, f_0 is the cavity repetition rate and A_0 is the amplitude of the correlation trace.

Figure 8.8(a) gives the power spectral density over the Fourier frequency from 1 Hz to the Nyquist frequency of 100 kHz. It can be seen that the phase noise is mostly concentrated at low frequency (below 100 Hz) due to the mechanical disturbance and thermal expansion. The integrated timing jitter is inferred to be as low as 45 fs, which is negligible compared to the pulse duration. Thus the timing jitter has no influence on the temporal distribution of the signal photons within the pump pulse window.

Besides, the FWHM bandwidth of the cross-correlation trace τ_c is related with the timing jitter τ_j as:

$$\tau_c = \sqrt{\tau_s^2 + \tau_p^2 + \tau_j^2} \ . \tag{8.10}$$

Inserting τ_s = 5.6 ps, τ_p= 8.8 ps and τ_j=45 fs into the above equation, we can obtain τ_c=10.4 ps. As shown in figure 8.8(b) the measured cross-correlation bandwidth is 9 ps in agreement with the calculated value.

8.3 Up-conversion system

As shown in figure 8.3, the synchronized pulses from the two fiber lasers are spatially mixed into a single-mode fiber using a 1064/1557-nm wavelength division multiplexer in order to achieve a good spatial overlap and beam quality. The combined beam is collimated to the free space via a fiber collimator, and then focused into a 50 mm long bulk PPLN in the up-conversion system. To improve the conversion efficiency, the quasi-phase matching needs to be fulfilled. Additionally, the spectral filtering in the up-conversion counting system should be concerned to reduce the background noise of the frequency up-convertor.

8.3.1 Phase matching

Various phase-matching techniques have been developed heretofore, such as angle tuning, temperature tuning, and quasi-phase matching (QPM). Contrast to the others, QPM fulfills the required momentum conservation by introducing a periodic modulation of nonlinear medium properties instead of matching the phase velocities in the birefringent medium [175]. Therefore, QPM has some strong advantages that explain its now widespread use. For instance QPM has no constraints on finding wavelengths and beam orientation angles to satisfy the phase matching, thus allowing to access the highest nonlinear coefficient. Additionally QPM permits a long interaction distance without suffering from the spatial walk-off.

QPM technique is also used in our experiment. The PPLN crystal is based on multiple grating domains varying from 11.0 to 12.0 μm with a step of 0.2 μm. The ends of the PPLN crystal are anti-reflection coated ($R < 1\%$) for the three wavelengths involved in the sum frequency generation process. To stabilize the operating temperature, the nonlinear crystal is housed in an oven with a Peltier temperature controller. The temperature fluctuation is less than 0.1 °C. In particular, the sum-frequency mixing of the input signal at 1040 nm with the pump at 1557 nm is performed with a grating period of 11.0 μm at a temperature of 130.4 °C.

8.3.2 Spectral filtering

An issue plaguing most implementations of single-photon up-conversion detectors is detrimental dark noise induced by the strong pump. The scattered pump photons within the bandwidth of the phase-matching acceptance can be efficiently up-converted leading to the "false" counts. In our experiment, the pump power for maximum conversion is about 50 mW, which corresponds to about 10^{18} photons per second. Hence even extremely weak

scattering will induce noise count rates that can be prohibitively high for applications in quantum state engineering or quantum communication.

There are two primary sources for these noises: spontaneous parametric down-conversion (SPDC) and spontaneous Raman scattering (SRS) [176]. Specifically SPDC only produces noise photons with energy lower than the pump while SRS produces both red- and blue-shifted scattered photons as Stokes or anti-Stokes sidebands. The anti-Stokes shifted scattering is weaker than the Stokes scattering by a ratio given by the Boltzmann factor $e^{-h\Delta\nu/kT}$ owing to the thermal occupation of phonons [177]. Therefore choosing a longer pump wavelength can effectively reduce the noise photons for an up-conversion detector [168].

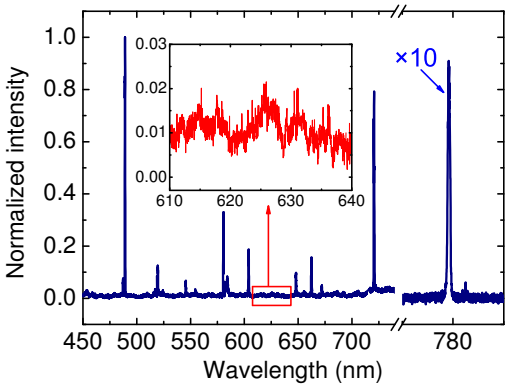

Figure 8.9: Background spectrum in the visible region without the signal injection. Inset: the detailed background spectrum around the SFG-photon wavelength.

For this reason, a long-wavelength-pumped technique is used in our experiment, where the pump wavelength is 1557 nm and the signal wavelength is 1040 nm. Figure 8.9 presents the pump-induced noise spectrum without the injection of signal light. Thanks to the long-wavelength pumping, there is no observable peaks near the targeted SFG wavelength ($\sim$ 623 nm) as shown in the inset of figure 8.9. The pronounced peak at 780 nm is due to the frequency doubling of the pump. The pump-induced parametric fluorescence is then filtered out via a spectral filtering system based on a dispersive prism, a spatial filter system, and a bandpass filter. The filtered beam is finally recorded by a Si-APD single-photon counting module (SPCM, PerkinElmer) as shown in figure 8.3

8.4 Results and discussion

8.4.1 System efficiency and background noise

To emulate single-photon souce, the signal at 1040 nm is attenuated to single-photon level about 0.4 ± 0.1 photons per pulse for the up-conversion. The temporal overlap between the signal photons and the pump pulses is optimized by finely tuning the time delay (cf. figure 8.3). Eventually a maximum photon counting of 1.86 MHz is achieved at the pump power of 59 mW as shown in figure 8.10, which indicates a photon detection efficiency (PDE) of 31%. Accordingly, the up-conversion efficiency is inferred to be 92% after taking into account the transmittance of the filtering system (49%) and the quantum efficiency (70%) of the Si-APD SPCM. The conversion efficiency is slightly smaller than the theoretical value (96%). This slight discrepancy may be due to the spatial mode mismatching of the focused pump and signal beams in the PPLN crystal. Thanks to the long-wavelength pumping, the corresponding background counts are reduced to 2.8 kHz. Taking into account the repetition rate of 17.6 MHz, the noise probability per pulse is about 1.6×10^{-4}.

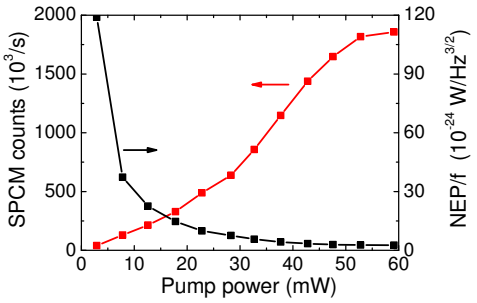

Figure 8.10: Signal counts recorded by the Si-APD SPCM and noise equivalent power (NEP) divided by the repetition rate f as a function of the pump power.

The performance of an optical detector can be generally described by a figure of merit so-called *noise equivalent power* (NEP) defined as:

$$\mathrm{NEP} = h\nu\sqrt{2R_{\mathrm{BC}}}/\eta \ , \tag{8.11}$$

where $h\nu$, R_{BC} and η are the energy of the signal photon, the dark noise rate and the detection efficiency, respectively. At the peak detection efficiency, the NEP is as low as 4.6×10^{-17} W/Hz$^{1/2}$, corresponding to -133 dBm (power in a 1-Hz bandwidth). In quantum cryptography, the sensitivity of the detection system for a single pulse is more significant since the information is encoded into the individual photon pulse. The parameter NEP$/f_r$ is thus used to evaluate the performance of the photon-counting systems by taking into account the operation rate f_r [177]. For our up-conversion detector, a NEP$/f_r$ of 2.6×10^{-24} W/Hz$^{3/2}$ is obtained.

The compact fiber-laser synchronization system is not only suitable for the efficient infrared single-photon detection, but can also benefit to applications such as infrared photon-number-resolving detection and ultra-sensitive infrared imaging (both will be detailed in Chapter 9).

8.4.2 Photon correlation

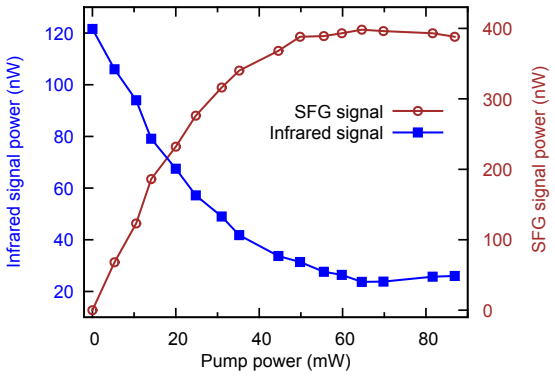

Figure 8.11: SFG signal and the unconverted infrared signal intensity as a function of the pump power.

In addition to the demonstration of efficient single-photon detection, we also investigate the intensity cross-correlation between the unconverted photons and up-converted photons. In order to separate the unconverted infrared light at 1064 nm and visible SFG photons at 622 nm, a dispersive prism is used at the output of the PPLN crystal. Then the spatially separated beams are recorded by two power-meters for an input infrared signal set at few μW. Figure 8.11 shows the SFG light power and the unconverted infrared signal power as

a function of the pump power. An anti-correlation between the two channels can be clearly seen. When the pump power is about 70 mW, the SFG signal power increases to the peak point while the infrared unconverted signal power accordingly drops to the valley position. The corresponding maximum conversion efficiency can be inferred from the depletion of the infrared signal, giving a value of 80.5%.

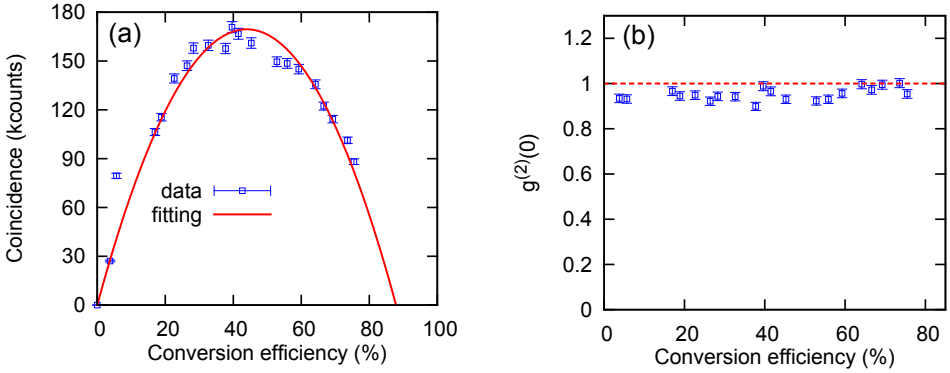

Figure 8.12: (a) Coincidence measurement between the SFG photons and the unconverted infrared photons as a function of the conversion efficiency. (b) Intensity cross-correlation of the SFG photons and unconverted infrared photons at different conversion efficiencies.

To measure the photon-number correlation during the sum frequency generation, the incident infrared signal is attenuated to few-photon level ($\sim$ 10 photons/pulse). The power-meters are then replaced by two single-photon detectors with quantum efficiencies of 6% and 70% at 1040 nm and 622 nm, respectively. The outputs of detectors are connected to a coincidence counters. The coincident window is set to be 2 ns, which is large enough to include all the effective photon counts within the pump pulse envelope. The recorded coincidence counts are shown in figure 8.12(a) as a function of the conversion efficiency. The maximum coincidence counts is found at a conversion efficiency of 43%, i.e. around half of the maximum conversion efficiency $\eta_{\max}$. The fitted line is given by equation (2.25):

$$C \propto \eta(\eta_{\max} - \eta) \ , \tag{8.12}$$

with the fitting variable $0 \leqslant \eta \leqslant \eta_{\max}$.

Additionally the coincidence rate N_c can be used to calculate the intensity cross-correlation function $g^{(2)}(0)$ after a proper normalization [178] given by:

$$g^{(2)}(0) = \frac{N_c}{N_1 N_3 RT} \ , \tag{8.13}$$

where $N_{1,3}$ are the counting rates on each detector, R is the repetition period and T is the acquisition time. According to the equation (2.26), $g^{(2)}(0)$ is equal to 1 independent of conversion efficiency when the input signal is a coherent state. This prediction is well verified from the experimental result as shown in figure 8.12(b).

The result can be understood in the following way. As discussed in Chapter 2, the up-conversion process can be regarded as a special beam-splitter (one-color input and two-color output) with a transmittance depending on the conversion efficiency [41]. Therefore, the cross-correlation intensity measurement for the two outputs can be treated as the Hanbury Brown and Twiss (HBT) measurement with a variable beam-splitter. It is well known that such $g^{(2)}(0)$ measurement is independent of the losses and beam-splitting ratio (cf. Appendix

B). As a result, what we measure in the experiment is actually $g^{(2)}(0)$ of the input coherent state, which equals to 1.

The beam-splitter feature of the up-conversion process indicates that there is no noisy photon introduced, thus maintaining the second-order intensity correlation. It is this feature that makes the up-convertor potentially useful as a quantum interface in a quantum communication networks [40].

8.5 Conclusion

In this Chapter, we have demonstrated the implementation of a coincident frequency up-conversion system with a synchronous pumping. A peak conversion efficiency of 92% has been achieved via spectro-temporal engineering of the signal and pump pulses. Due to the pulsed excitation together with the long-wave-pump technique, the dark noise probability per pulse of the up-conversion system was reduced to 1.6×10^{-4}. Based on the coincidence frequency conversion system, the extension to infrared photon-number-resolving detection and ultra-sensitive infrared imaging will be discussed in the next chapter.

9 | Applications of Frequency Conversion System

Besides of the single-photon infrared detection presented in Chapter 8, the developed coincidence frequency up-conversion system can be easily adapted to other applications. For instance, infrared photon-number-resolving detection is readily implemented by replacing the Si-APD with a silicon multipixel photon counter (Si-MPPC) in the up-conversion system. With a silicon electron multiplying charged coupled devices (EMCCD), single-photon-level infrared up-conversion imaging can also be realized. Finally, a coincidence frequency down-conversion system can be similarly constructed based on the synchronized fiber lasers. All the details about these three applications will be given in this chapter.

9.1 Infrared photon-number-resolving detection

9.1.1 Introduction

Photon-number-resolving (PNR) detectors play an important role in many applications, including low-light-level detection, measurement of nonclassical photon statistics [179] and quantum states engineering with multi-photon subtraction [112]. Additionally, the photon-number-resolving functionality is critical for many protocols in quantum information processing and quantum computation, such as the implementation of quantum repeaters [180] and linear-optics quantum computing [28].

PNR detectors working in the infrared can be efficiently realized with transistor edge sensors (TES) and superconducting parallel nanowires detectors [57]. However the requirement of cryogenic cooling makes them expensive and prevents them from working as plug-and-play systems. Compared to those detectors, a silicon multipixel photon counter (Si-MPPC) can operate at temperatures achievable by thermoelectric cooling and also demonstrate a high efficiency and low dark noise [181]. Therefore, it is interesting to develop a system based on Si-MPPC for infrared PNR detection. This idea can be realized via the frequency convertor to bridge the gap between the operating wavelength of Si-MPPC (visible light) and the wavelength of interest (infrared light).

In this section, we will modify the frequency up-conversion system presented in the previous chapter to implement a frequency up-conversion PNR detector targeting at wavelengths around 1 μm [150].

9.1.2 Experimental setup

The up-conversion system implemented in Chapter 8 can be modified for infrared PNR detection by replacing the Si-APD detector with a Si-MPPC. For the sake of simplicity, here we only give details about the modified part.

■ Synchronized fiber laser system

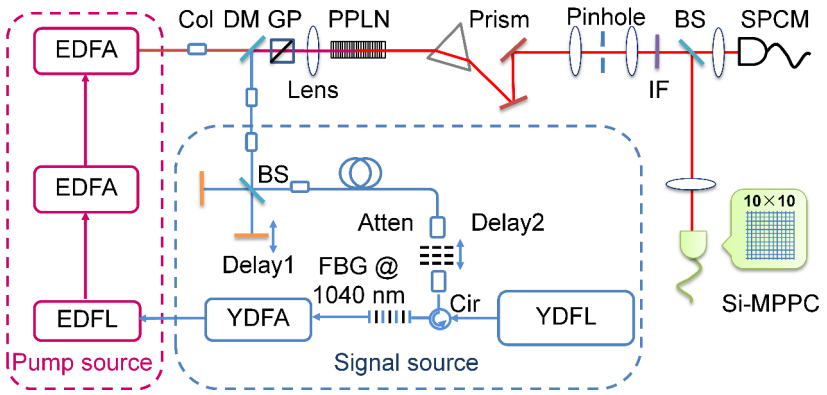

Figure 9.1: Experimental setup for the photon-number-resolved detection at 1.04 μm. Cir, circulator; Col, collimator; BS, beam slitter; DM, dichroic mirror; IF, interference filter; GP, Glan prism; Atten, attenuator; Si-MPPC, silicon multipixel photon counter; SPCM, single-photon counting module.

Figure 9.1 gives the corresponding experimental configuration. Limited by the reset time

of Si-MPPC (8 MHz), the repetition frequency of the synchronized fiber lasers is set to be 3.6 MHz in this experiment. To meet the requirement of the phase-matching bandwidth of the nonlinear crystal, the output of the YDFL is filtered by a FBG with a bandwidth (FWHM) of 0.3 nm, which is then used as the signal source. The pulse duration is estimated to be about 6 ps from the auto-correlation measurement. Instead of using a FBG, the spectro-temporal control of the pump source is realized by inserting a 3-nm fiber band-pass filter into the ring cavity of a EDFL. The resulting bandwidth of the output spectrum is about 0.2 nm with a pulse duration of 23 ps.

■ Up-conversion PNR detection

The signal and pump beams are then combined via a dichroic mirror before being injected into the crystal. The quasi-phase-matching condition for the involved optical fields is satisfied by choosing a 11-μm grating period of PPLN crystal and stabilizing the operation temperature at 100.4 °C.

The up-converted light is steered through spectral filtering with a transmittance $\eta_F = 48\%$. To compare the detection performances of the PNR detector and the on/off detector, the filtered light is spatially split by a beam-splitter with a reflectance $\eta_{BS} = 35\%$. The transmitted portion is detected by a conventional Si-APD-based single-photon counting module (SPCM) while the reflected part is recorded by a Si-MPPC pigtailed with a multimode fiber. The Si-MPPC (Hamamatsu Photonics S10362-11-100U) is made of 10×10 APD pixels on an effective area of 1 mm^2 with a detection efficiency $\eta_D = 16\%$ at 622 nm. When the light illuminates the different APD pixels, the Si-MPPC will output a summation voltage of all the pixels. The amplitude of the summed voltage is proportional to the incident photon number [182]. To reduce the effect of thermal noise, the detector is Peltier cooled to -35 °C.

9.1.3 Results and discussion

■ Photon-number resolving

The waveforms of the output voltage from Si-MPPC are accumulated to give the histogram of the corresponding voltage amplitudes. Figure 9.2 presents the typical histogram of peak voltage, which is fitted by the sum of a series of Gaussian functions. The integration of each Gaussian function is proportional to the event number for different photon-number detection. Hence the area under each Gaussian peak normalized with the total area gives corresponding photon-number distribution of the incident light as shown in the inset of figure 9.2. Since the input light is a coherent state, the up-converted photon statistics should follow the Poissonian distribution. The likelihood between the experimental data and expected Poissonian statistics is optimized to give a detected photon number per pulse of 3.19 ± 0.01. Due to the pulsed pumping and long-wavelength pump scheme, a low noise probability per pulse of 2×10^{-4} is obtained in the experiment, which is close to the intrinsic dark noise of the detector itself.

■ Dynamic detection range

Figure 9.2(b) gives the detected photon number as a function of the incident photon number for SPCM and Si-MPPC, respectively. Since SPCM cannot discriminate more than one photon per shot, a saturation in the case of large incident photon numbers is observed due to the increase of multi-photon components. In contrast, the Si-MPPC exhibits a linear dependance with the incident photon numbers owing to the PNR ability. The total detection efficiency η_A is inferred to be 1.3% from the slope of the fitted straight line. After correcting the reflectance of the beam-splitter, the actual detection efficiency of the up-conversion PND detector is 3.7%. Consequently, the conversion efficiency η_C is estimated to be 47.9%. The

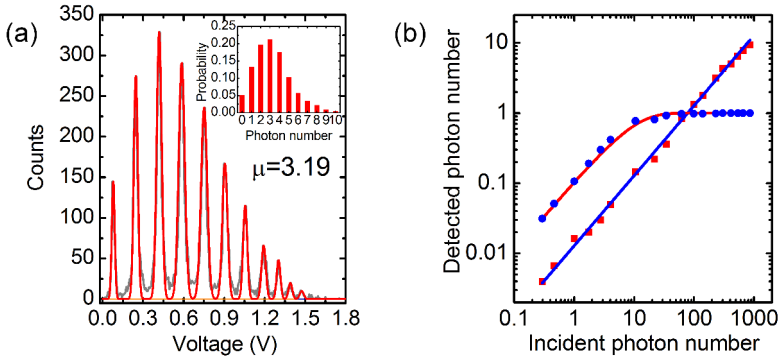

Figure 9.2: (a) Output voltage amplitude histogram for the up-converted photons. The photon number distribution is shown in the inset. (b) Detected photon numbers by SPCM (dots) and Si-MPPC (squares) as a function of incident photon numbers. Solid curves are the fits to the data.

limiting factor of the conversion efficiency may be the temporal mismatching due to the deformed profile of signal pulses from a all-normal-dispersion YDFL operating at a low repetition rate [183].

■ An example

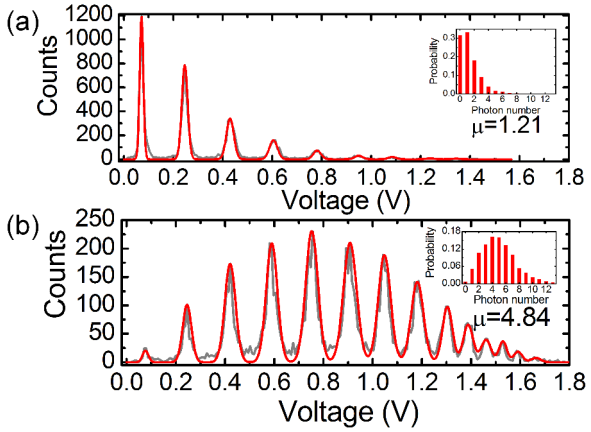

Figure 9.3: Output voltage amplitude histograms of frequency up-conversion PNRD with one arm of the interferometer blocked (a) and with constructive interference (b). The corresponding photon number distributions are shown in the insets.

As shown in figure 9.1 a Michelson interferometer is inserted after the signal source for modulating the signal intensity. In the case of one arm blocked the photon number is measured to be 1.21 as shown in figure 9.3(a) while in the case of constructive interference, a photon number of 4.84 is obtained. The ratio of the photon numbers is found to be 1/4 in agreement with the theoretical expectation. The example here indicates the competence

of such up-conversion PNR detector for correctly identifying the photon numbers.

We now turn to another application of the frequency up-conversion system.

9.2 Few-photon-level infrared imaging

9.2.1 Introduction

Ultra-sensitive infrared imaging is of great importance in various applications such as astronomy, biology, medical diagnosis and two-dimensional (2D) infrared spectroscopy [160, 184]. The integration of InGaAs avalanche photodiode (APD) detectors with CMOS technology makes it possible to realize a massively parallel photon counting image sensor [185]. However, the sensitivity of such imaging detector is largely limited by its severe dark current, preventing its use for wider applications [186]. Compared to infrared imaging detectors, silicon charged coupled devices (CCDs) operating in the visible regime exhibit a superior performance for high-efficiency and low-noise imaging. The current fabrication technology enables to integrate active pixels as many as 1024×1024, making it suitable for full 2D imaging. Moreover, single-photon-level imaging has seen important developments, particularly the introduction of the electron multiplying CCDs (EMCCDs). Therefore, it would be desirable if we can use the multiplexing capability and high sensitivity of EMCCDs for ultra-sensitive infrared imaging. For this end, frequency transduction from the infrared light to visible regime is required to bridge the spectral gap. Thanks to the frequency up-conversion technique, spectral translation in single-photon level has been accomplished with high efficiency and low noise [147, 168], which provides an effective solution for the achievement of ultra-sensitive infrared imaging [156, 157, 158, 187].

9.2.2 Theoretical model

■ Simple consideration

The conceptual scheme for the infrared frequency up-conversion imaging is depicted in figure 9.4. The experimental configuration is based on a 4-f imaging system consisting of an object plane, a Fourier plane, an image plane and two lenses (with focal lengths f_1 and f_2, respectively). In the following, we will present a simple description about an ideal imaging conversion.

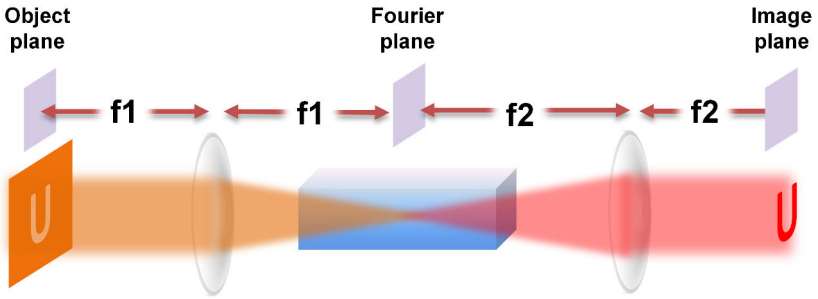

Figure 9.4: 4-f system configuration for infrared imaging by frequency up-conversion. The Fourier plane is centered in a nonlinear crystal where it interacts with a strong pump field. Due to the sum frequency generation, an up-converted field is generated at the image plane.

First, let us assume that the optical field of the image in the image plane is given by $E_1(x, y)$ where x,y represent two-dimensional coordinates. After passing through the first

lens in the 4-f imaging system, the diffracted image at the Fourier plane is simply defined by the Fourier transformation of the object image:

$$E_T(\xi,\eta) \propto \iint E_1(x,y)\exp(-ik_1\frac{x\xi+y\eta}{f_1})dxdy \ , \tag{9.1}$$

where $k_1 = 2\pi/\lambda_1$ denotes the wave number of the input field.

Then the generated diffracted image at the Fourier plane is transformed by the second lens, resulting in an image at the image plane as

$$E_2(x',y') \propto \iint E_T(\xi,\eta)\exp(-ik_2\frac{x'\xi+y'\eta}{f_2})d\xi d\eta \ , \tag{9.2}$$

where $k_2 = 2\pi/\lambda_2$ denotes the wave number of the converted field.

With equation (9.1), the input image can be expressed as

$$E_1(x,y) \propto \iint E_T(\xi,\eta)\exp(ik_1\frac{x\xi+y\eta}{f_1})d\xi d\eta \ . \tag{9.3}$$

Comparing equations (9.2) and (9.3), we can obtain the following relationship between the input field and the up-converted field:

$$E_2(x,y) \propto E_1(-\frac{\lambda_1 f_1}{\lambda_2 f_2}x, -\frac{\lambda_1 f_1}{\lambda_2 f_2}y) \ . \tag{9.4}$$

It indicates that the up-converted image is conjugate to the input one with a scaling factor $-\frac{\lambda_2 f_2}{\lambda_1 f_1}$

■ Filtering effect

Till so far, we only consider a perfect frequency conversion without taking into account the spatial modulation due to the Gaussian pump field. According to equation (8.7), the conversion efficiency is dependent on the spatial distribution of the pump intensity

$$\eta(x,y) = \sin^2(\frac{\pi}{2}\sqrt{P}) \ , \tag{9.5}$$

where P is the spatial intensity distribution given by

$$P = e^{-2\frac{x^2+y^2}{w^2}} \ . \tag{9.6}$$

Therefore the up-converted field can be rewritten with a convolution product [156]

$$E_2(x,y) \propto E_1(-\frac{\lambda_1 f_1}{\lambda_2 f_2}x, -\frac{\lambda_1 f_1}{\lambda_2 f_2}y) \otimes (\frac{\pi w^2}{\lambda_2^2 f_2^2}e^{-\frac{x^2+y^2}{(\frac{\lambda_2 f_2}{\pi w})^2}}) \ , \tag{9.7}$$

demonstrating a spatial filtering due to the Gaussian pump field. In the limit of infinitely large beam waist w, the normalized convolution function is approaching to a delta-function. The effective transformation is then reduced to a perfect up-converted replica of the input image with a scaling factor of $-\frac{\lambda_2 f_2}{\lambda_1 f_1}$ as shown in (9.4).

In the analysis of optical imaging, the point spread function $P(x,y,x_0,y_0)$ is frequently used to describe the impulsed response of an optical system to a delta function input located at the coordinates (x_0, y_0). The point spread function of the up-conversion imaging system is thus given by

$$P(x,y,x_0,y_0) \propto e^{-\frac{(x-x_0)^2+(y-y_0)^2}{(\frac{\lambda_2 f_2}{\pi w})^2}} \ . \tag{9.8}$$

It can be seen that the waist size of the pump beam determines the shape of the point spread function, thus defining the resolution of the imaging process. Increasing the size of Gaussian pump beam can effectively improve the imaging resolution. However it will lead to the reduction of the pump intensity, thus decreasing the conversion efficiency accordingly.

Note that the limited size of the nonlinear crystal (in our case the thickness is 0.5 mm) acts as an iris, which will also impose a filtering effect.

9.2.3 Experimental realization

■ Synchronized fiber lasers

The experimental setup mainly consists of two parts: a synchronized fiber laser system and an up-conversion imaging system as shown in figure 9.5. In the synchronized laser system, two independent fibers are arranged in a master-slave configuration. The master is a mode-locked ytterbium-doped fiber laser (YDFL) with a repetition frequency of 19.1 MHz. The output from YDFL is spectrally filtered by a 0.3-nm bandwidth fiber Bragg grating (FBG) to approach the acceptance bandwidth of the PPLN crystal. The corresponding pulse duration is inferred to be 6 ps from the auto-correlation measurement. The transmitted portion from the FBG is then injected into an erbium-doped fiber laser (EDFL), which leads to the realization of passive synchronization between the two fiber lasers.

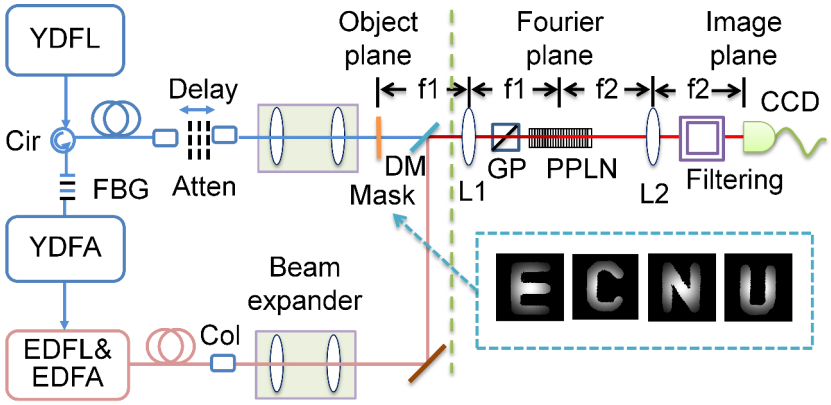

Figure 9.5: Experimental setup for infrared imaging by coincidence frequency upconversion. YDFL, ytterbium-doped fiber laser; YDFA, ytterbium-doped fiber amplifier; EDFL, erbium-doped fiber laser; EDFA, erbium-doped fiber amplifier; Cir, circulator; Col, collimator; Atten, attenuator; DM, dichroic mirror; GP, Glan prism; PPLN, periodically poled lithium niobate crystal; CCD, charged coupled device. Transmission masks were shown in the bottom-right corner.

Besides of the temporal synchronization, efficient frequency conversion also requires an appropriate control of the spectro-temporal property of the pulses. In the laser cavity of the EDFL, a 3-nm bandwidth band-pass filter is inserted to obtain a narrow output spectrum. The output of the EDFL is then amplified by an EDFA as the pump source, which has a maximum power of 40.0 mW. The corresponding spectrum is centered at 1549 nm with a bandwidth of 0.7 nm. The pulse duration is measured to be 16 ps, which is longer than that of the signal source. Therefore the signal photons are tightly enwrapped within the envelope of the pump field.

The synchronized pump and signal beams are then spatially expanded into free space after fiber collimators. The (e^{-2} intensity) beam radii of the signal and pump are measured to be 1.7 and 1.0 mm. The larger beam waist of the signal source leads to a tighter focus

after a lens so that the image at the Fourier plane can be covered by the focused pump beam.

■ Up-conversion imaging system

The signal beam then illuminates a transmission mask carved with letters "E', "C", "N", and "U" to form the object images, which are presented in the bottom-right corner in figure 9.5. Via a dichroic mirror the object image and pump beam are spatially combined, and then sent into the up-conversion imaging system. The imaging system is arranged in a 4-f imaging configuration using lens L1 (f1 = 250 mm) and L2 (f2 = 300 mm). The mask is placed at the object plane while a CCD detector is located at the image plane. The center of the PPLN crystal is aligned with the Fourier plane.

To facilitate the type-I quasi-phase matching, a Glan prism is inserted after lens L1 to enforce the proper polarization. A grating period of 11.0 μm is chosen to perform the nonlinear mixing between the object beam at 1040 nm and pump beam at 1549 nm. The operation temperature of the PPLN crystal is stabilized at 104.3 °C. As a result, an up-converted image is generated at 622 nm, and recorded by a CCD camera. To reduce the background noise, a set of filtering is used, including a dispersion prism and a band-pass interferential filter.

9.2.4 Results and discussion

■ Conversion efficiency

To evaluate the conversion efficiency of the up-conversion imaging system, it is more convenient to use a strong signal light that can been precisely measured with a power-meter. The power detection efficiencies are measured to 41%, 36%, 45%, and 41% for the character "E", "C", "N", and "U", respectively. After correction of 20% propagation loss due to the filtering system, the conversion efficiencies for the corresponding character are inferred to be 31%, 27%, 34%, and 31%, respectively. The variation of the conversion efficiency in the up-conversion imaging process is due to the different Fraunhofer diffraction patterns at the Fourier plane as shown in figures 9.7(a)-(d). Only the low spatial frequency components at the center of the focused pump can be efficiently up-converted. Indeed the focused pump beam acts as a Gaussian spatial filter, which results in filtered Fourier transformation patterns as shown in figures 9.7(e)-(h). Without the mask, the conversion efficiency could reach 57% because the signal beam with a Gaussian profile is more focused at the center of the Fourier plane. Figure 9.6 gives the conversion efficiency as a function of the pump power.

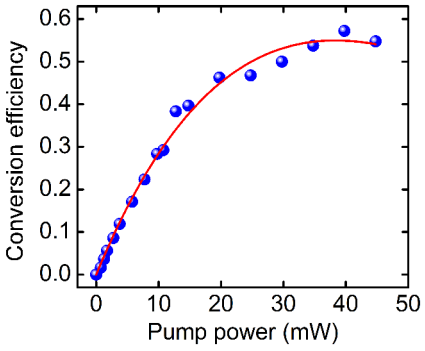

Figure 9.6: Conversion efficiency as a function of the pump power without inserting the mask.

■ Up-converted images

Figures 9.7(m)-(p) show the up-converted images from which the four characters can be

recognized in spite of blurred edges. As discussed in the theoretical section, the deformation of the image is due to the intrinsic point spread function (PSF). For the coherent imaging in our experiment, the up-converted field at the image plane can be expressed as a convolution between a scaled copy of the object field, and the PSF of the imaging system. The main part of PSF is given by

$$\mathrm{PSF} \propto e^{-\frac{x^2+y^2}{(\frac{\lambda_2 f_2}{\pi w})^2}}, \tag{9.9}$$

where λ_2 is the wavelength of the up-converted field, and w is the radius of the pump beam at the Fourier plane.

The theoretically simulated up-converted images are presented in figures 9.7(i)-(l) using the realistic parameters in the experiment. The smearing of the images due to the effect of PSF is indeed observed, in agreement with the experimental results.

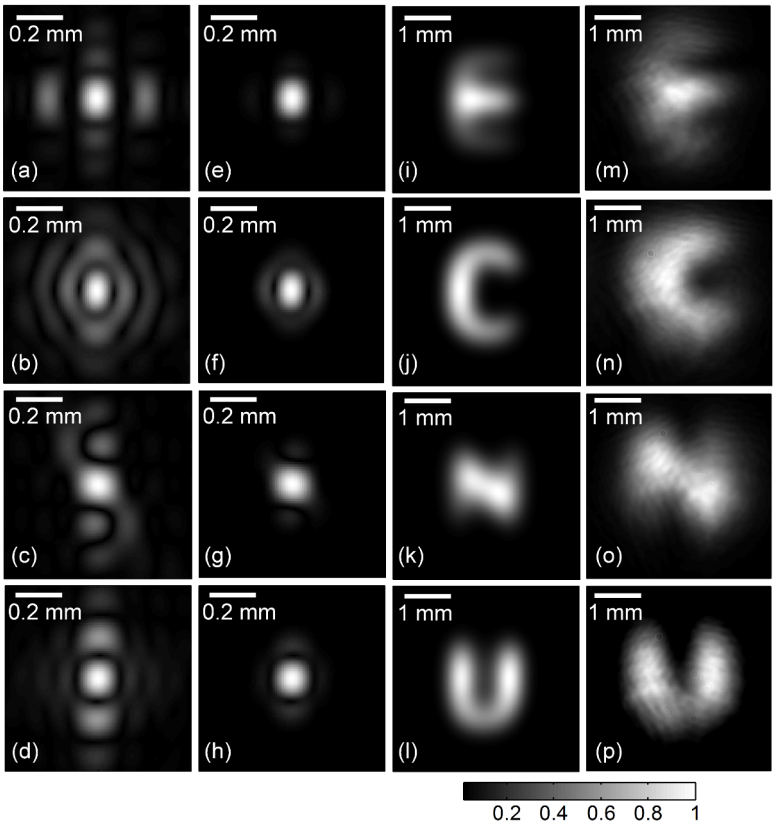

Figure 9.7: Distribution of electric field of the signal beams at the Fourier plane with (a-d) and without (e-h) the filtering effect due to the Gaussian pump beam. Theoretical simulation of upconverted images (i-l) and experimental results (m-p).

■ Few-photon-level imaging

In our coincidence frequency up-conversion system, the background noise due to the parametric florescence is effectively reduced thanks to the pulsed excitation of the pump. Additionally, the long-wave-pump technique helps to further reduce the dark noise to 1.5 kHz, indicating a noise probability per pulse of 8×10^{-5}. Such a low noise enables to realize an ultra-sensitive imaging without suffering from the smearing effect due to background counts.

To investigate the sensitivity limit of the up-conversion imaging system, the object beam is attenuated to the few-photon level. Specifically, the average photon numbers per pulse for "E", "C", "N", and "U" are estimated to be 1.9, 2.0, 2.4, and 2.6, respectively. These photon numbers are optimized according to the resolution of the corresponding up-converted images. To capture the visible up-converted images, we use an EMCCD (Andor iXon3 897) capable for single-photon imaging. The EMCCD is operated at -85 °C via a thermal-electrical cooling in order to lower the dark noise. The EMCCD is a silicon-based semiconductor chip containing 512×512 pixels. Each pixel has a size of 16 $\mu m \times 16$ μm, which is suitable for the high spatial resolution imaging.

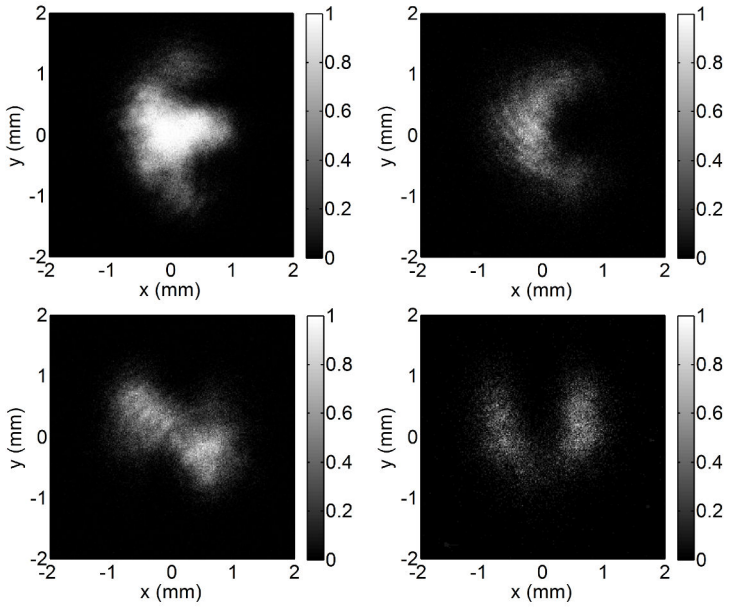

Figure 9.8: Measured upconverted images with few-photon-level object beam light.

To recover the up-converted images at the single-photon level, it is necessary to accumulate enough photons. For object beams "E", "C", "N", "U" we set the integration time to be 30 s, 30 s, 35 s, 30 s, and the accumulation number of 50, 50, 50, 30, respectively. The obtained images are shown in figure 9.8, which are similar to the ones obtained with strong signal light illumination.

The formation of the up-converted image can be regarded as an imaging process through a small soft aperture with an effective size defined by the the pump profile according to equation (9.9). The enhancement of the imaging resolution requires the efficient conversion of spatial components at the Fourier plane as much as possible. Indeed the loss of the high-frequency components will result in the blurring of the converted image. To this end, we can use either a larger pump size at the beam waist or a tighter focusing of the infrared object image. However the increasing of the pump beam size will lead to the reduction of the intensity (assuming a constant power), thus lowering the conversion efficiency. Additionally, the focusing of the object image is ultimately limited by the angular acceptance of the nonlinear crystal. The problem can be solved either by boosting the pump power or resorting to nonlinear crystals with a larger nonlinear coefficient and a wider acceptance angle. In addition to the improvement of the up-conversion imaging system, post-processing of the up-

converted images may provide another solution for obtaining a sharper image. For instance, one can choose a suitable PSF to deconvolve the up-converted image since the PSF is fixed for a given up-conversion system.

Now we turn to another possible application in the next section.

9.3 Generation of mid-infrared light

9.3.1 Introduction

■ Motivation

Mid-infrared light plays an important role in many applications such as biomolecular sensing, trace-gas detection, pollution monitoring, and mid-infrared spectroscopy. Typically, coherent radiation in the mid-infrared regime can be generated using quantum cascade lasers [188] or optical parametric oscillators [189]. Recently nonclassical lights, e.g. squeezed states and entangled states in the mid-infrared spectral region, are increasingly demanded due to their great potential in quantum-enhanced metrology and free-space quantum communication. However squeezed states are currently generated in the near-infrared spectral regime [36, 190, 191]. Via the coherent up-conversion technique, Ref. [192] demonstrated a quantum spectral translation of squeezed vacuum states from 1550 nm to 532 nm. Following the same idea, one can obtain the squeezed vacuum in the longer wavelength with the recently proposed coherent down-conversion [45, 46].

Quantum frequency translation can be efficiently realized by two optical nonlinear processes. The first one is based on the four-wave mixing effect via Bragg scattering in photonic crystal fibers [51]. In this case, the amount of frequency shift is limited by the low-energy phonon level transition (e.g within the visible regime). In contrast, the second way based on difference frequency generation (DFG) can provide a much wider shift band (e.g from visible to telecom wavelengths) [50, 47, 49]. The DFG-based frequency down-conversion is thus used in our experiment.

■ Basic theory

Although the coherent up-conversion was proposed [39] and implemented [147] long time ago, its counterpart, i.e. coherent down-conversion, was brought up very recently [45, 46] because of the common belief that the spontaneous down-conversion would inevitably introduce noisy photons. Actually, noise-free down-conversion can be realized in the gain saturation regime where the pump field is provided by the optical mode with lower photon energy. For details about the theoretical description of the coherent down-conversion, readers can refer to Chapter 2. Here we only give some important results used for explaining the experimental results presented afterwards.

Let us consider the simplest case where all the involved fields are single-mode, e.g. input pump and signal fields are at frequencies ω_p and ω_s, respectively. The DFG interaction in a nonlinear $\chi^{(2)}$ crystal will result in a converted field at frequency ω_c, fulfilling the energy conservation condition: $\omega_s{=}\omega_p{+}\omega_c$. For perfect phase-matching and non-depleted pump, the corresponding interaction Hamiltonian reads:

$$\hat{H} = i\hbar g E_p(\hat{a}_s\hat{a}_c^\dagger - h.c.) \ , \tag{9.10}$$

where $\hat{a}$ and $\hat{a}^\dagger$ denote the annihilation and creation operators; g is the nonlinear coupling constant; E_p is the pump electric filed. After a given interaction length L, the down-converted mode is given by:

$$\hat{a}_c(L) = \sin(|gE_p|L)\hat{a}_s(0) + \cos(|gE_p|L)\hat{a}_c(0) \ . \tag{9.11}$$

From the above equation, we can see that a complete frequency conversion indeed occurs when $|gE_p|L = \pi/2$. Thanks to the operation in the gain saturation regime where the pump field at ω_p is much stronger than the signal field at ω_s ($\omega_s > \omega_p$), the noise photons from the spontaneous parametric down-conversion are effectively suppressed [45, 46].

9.3.2 Experimental setup

The experimental setup is illustrated in figure 9.9. It is based on three parts: synchronized fiber lasers, frequency down-conversion and mid-infrared detection. The output of an ytterbium-doped fiber (YDFL) is used as the signal source at 1.04 μm with a spectral bandwidth of 0.3 nm and a pulse duration of 6 ps. The pump source at 1.55 μm is provided by an erbium-doped fiber laser (EDFL) with a spectral bandwidth of 0.5 nm and a pulse duration of 39.5 ps. Both two fiber lasers operate at 19.1 MHz, which are then passively synchronized in a master-slave configuration. For details about the synchronous laser system, readers can refer to Chapter 8.

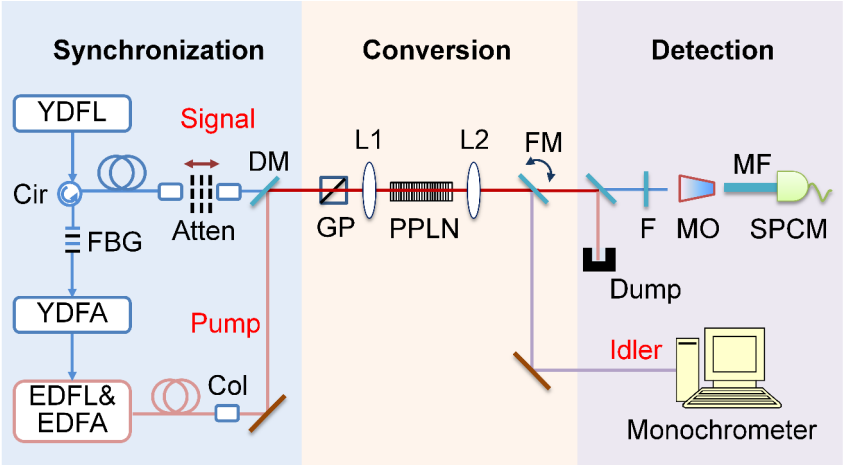

Figure 9.9: Experimental setup for generating mid-infrared photon source by coincidence frequency downconversion. FBG, fiber Bragg grating; Cir, circulator; Col, collimator; Atten, attenuator; L1,2, lens; DM, dichroic mirror; GP, Glan prism; PPLN, periodically poled lithium niobate crystal; FM, flipping mirror; MO, microscope objective; MF, multimode fiber; F, filter; SPCM, single photon counting module.

The pump and signal beams are spatially overlapped by a dichroic mirror. The mixed beams then pass through a Glan prism to obtain a proper linear polarization. After an achromatic doublet lens (f = 200 mm), the mixed beams are focused at the center of a 50-mm MgO:PPLN crystal. The ends of the PPLN crystal are fabricated with an anti-reflection coating at all three involved wavelengths. To satisfy the phase matching between the involved optical fields, the grating period of the nonlinear crystal is chosen to be 30.49 μm with an optimal operation temperature of 23.5 °C.

To calibrate the conversion efficiency during the down-conversion process, we measure the depletion of the infrared signal at 1.04 μm by a Si-APD or a power-meter. This trick is necessary especially in the single-photon level due the absence of efficient single-photon detectors in the mid-infrared regime. Moreover, the indirect calibration of conversion efficiency has a unique advantage that it does not require a loss calibration. Experimentally, the beams out of the PPLN crystal are sent through a dichroic mirror for removing the

pump light. To suppress the parametric fluorescence, a long-pass filter cutting at 1 μm is inserted before the signal light being coupled into a multimode fiber. Then the unconverted signal at 1.04 μm is detected by a silicon single-photon counting module (Si-SPCM). Note that no effort is dedicated to filter out the mid-infrared light, since the Si-SPCM is almost blind in this spectral regime.

9.3.3 Results and discussion

■ Conversion efficiency

The signal source at 1.04 μm is attenuated to the single-photon level. In this case, the power of the signal field is much smaller than that of the pump field, thus satisfying the condition for the coherent down-conversion. The down-conversion process can be confirmed by the decrease of the unconverted signal photons recorded with the Si-SPCM.

Table 9.1 shows a list of notations for the count rates in the presence or absence of signal and pump pulses.

Table 9.1: List of notations for the count rates in the presence (✓) or absence (✗) of signal and pump pulses.

	N_1	N_2	N_3	N_4
Pump	✓	✗	✓	✗
Signal	✗	✓	✓	✗

N_1 is the background noise of the down-converter including the pump-induced noise, ambient noise and detector dark noise while N_4 only corresponds to the last two terms. Therefore, the down-conversion efficiency η is given by

$$\eta = 1 - \frac{N_3 - N_1}{N_2 - N_4} \ . \tag{9.12}$$

Note that the conversion efficiency can be precisely inferred without the need to correct the losses due to the filtering system and the SPCM.

Figure 9.10 shows the down-conversion efficiency as a function of the pump power. The fitting to the experimental data is given by the function

$$\eta = \eta_m \sin^2\left(\frac{\pi}{2}\sqrt{\frac{P}{P_m}}\right) ,$$

where η_m is the expected maximum conversion efficiency and P_m is the required pump power. In the experiment, a maximum conversion efficiency of 65% is obtained at 80 mW, which can be further increased by boosting the pump power, as indicated by the solid fitted line.

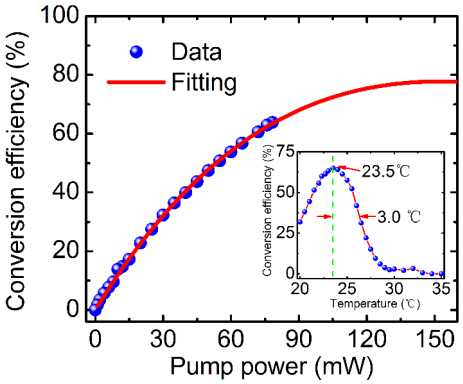

Figure 9.10: Conversion efficiency as a function of the pump power. Inset: conversion efficiency dependent on the working temperature of the MgO:PPLN.

■ **Mid-infrared spectrum**

To directly witness the generation of the mid-infrared light, the down-converted idler light is reflected by a flipping mirror (cf. figure 9.9) into a monochromator (iHR550, HORIBA Jobin Yvon) to record its spectrum. The measured spectrum is centered at 3.16 μm as expected with a FWHM bandwidth of 3.7 nm. Without the signal light, there is no observable peaks around the target DFG wavelength in the background spectrum. Indeed the spectral separation between the pump and target DFG wavelength is about 3300 cm^{-1}, which is much larger than the Stokes Raman band of the MgO:PPLN crystal($\approx$ 1000 cm^{-1}) [193].

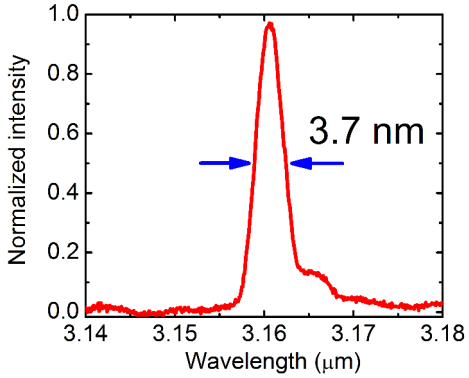

Figure 9.11: Spectrum of mid-infrared photon source with background correction.

Since the signal pulse duration (6 ps) is much smaller than the one of the pump source (39.5 ps), the pulse duration of the generated mid-infrared light is estimated to be around 6 ps. The product of the temporal and spectral bandwidth is thus calculated to be 0.67, which is slightly larger than the Fourier transform limit of 0.44 in the assumption of a Gaussian profile. Therefore, the mid-infrared pulse is inferred to be chirped, which may be due to the phase superposition by the chirped pump pulse during the nonlinear mixing process.

9.4 Conclusion

In this chapter we have demonstrated three applications based on the coincidence frequency conversion system. The first one was infrared PNR detection. The infrared light was spectrally converted into the visible regime where a high-performance Si-MPPC was used. The detection efficiency of the up-conversion PNR detector was measured to 3.7% with a noise probability as low as 2×10^{-5}. The second application was ultra-sensitive infrared imaging. Accordingly a Si-EMCCD was utilized for the single-photon-level imaging for the up-converted visible fields. Such imaging system performed a full 2D image without the need of time-consuming scanning devices, thus gaining simplicity and speed. The last application was a proof-of-principle demonstration of coherent down-converter. The near infrared signal at 1.04 μm was coherently converted to the mid-infrared regime with a peak conversion efficiency of 65%.

It is worth noting that both the up-converter and down-converter can maintain the quantum properties of the input states. Therefore, the demonstrated up-conversion PNR detection and imaging can be used to directly demonstrate the nonclassicality [194] or intensity correlation [195]. Additionally the coherent frequency conversion of quantum states provides a bridge between different wavelengths within a sequence of downstream applications and also allows to prepare quantum states at currently inaccessible wavelengths [192]. Moreover the combination of the coherent up-converter and down-converter paves the way to build a quantum frequency translator as mentioned in Section 2.3.4, which enables the fine tuning of the central frequency of the input quantum state.

Conclusion and outlook

The works demonstrated in this thesis focused on quantum state engineering and state manipulation. They aimed at developing some useful resources and tools in the emerging optical hybrid approach of quantum information processing. The presented results relied on two essential nonlinear processes: frequency down-conversion and frequency up-conversion.

The frequency down-conversion was experimentally implemented with optical parametric oscillators (OPOs) in the continuous-wave regime. They provided an efficient way to prepare non-classical light, for instance single-mode or two-mode squeezed vacuum states depending on the phase-matching condition of the nonlinear crystal [74]. Thanks to the OPO cavity, a well-defined and controllable spatio-temporal mode was obtained for the traveling optical field. This feature not only facilitates the mode matching with local oscillator in homodyne detection for state characterization, but also permits the generated states to be subsequently used in protocols.

Specifically, we have generated with high fidelity a single-photon state and an odd Schrödinger cat state based on the type-II and type-I OPOs, respectively. In contrast to the initial squeezed state, which was a Gaussian state, these prepared states exhibited strongly negative Wigner functions [38, 74]. It is worth mentioning that direct observation of non-Gaussian states with negative Wigner functions is practically challenging, and typically requires a high efficiency throughout the system including preparation, propagation and measurement. A directly measured negativity of the Wigner function can thus be regarded as the signature of the high "quality" of the prepared states. This quantum feature not only constitutes the requisite resource to perform certain quantum computation tasks, but can also benefit other fields like quantum communication and metrology.

The transformation from Gaussian states to non-Gaussian states requires over-quadratic nonlinearity, and it cannot be accomplished only with Gaussian operations. In our case, the nonlinearity was induced by photon-counting-based measurements. Such conditional preparation technique has been used in all the experiments for quantum state engineering. Specifically, the photon counting was carried out by superconducting nanowire single-photon detectors (SNSPDs), which demonstrated high performances at 1064 nm, with a high detection efficiency ($> 80\%$) and a very low dark count rate (< 10 Hz). Based on the type-II OPO, the remarkable detection capability enabled to prepare heralded single-photon state with an unprecedented rate above MHz and a very high fidelity about 76% (without correction). The single-photon source would benefit many down-stream applications in quantum communication, such as quantum key distribution or heralded noiseless amplification of quantum states.

The high-performance SNSPDs have also led to generating the heralded two-photon Fock state with a preparation rate as high as 150 Hz. The achieved fidelity reached 58% (without correction), which is the highest value to date. Furthermore, a two-photon state engineering has been presented based on the mode mixing between the down-converted orthogonally-polarized modes, allowing to access an arbitrary superposition of the form $c_0|0\rangle + c_2|2\rangle$. With the synthesis of the coefficients, a squeezed even cat state of a large size $|\alpha|^2 = 3$ has been obtained with a fidelity of 67% (after 15% loss correction). To the best of our knowledge, the state demonstrated here already represents the largest cat state and highest fidelity reported so far. Additionally, we have also investigated how the generated states were affected by the time separation of the conditional detections, leading to a deeper understanding of the temporal modes in which the states are generated.

For the type-I OPO side, a π-phase gate was applied on the previously obtained odd cat state to flip the superposition sign between two coherent states, resulting in the even cat state of a size $|\alpha|^2 = 1$ with a fidelity as high as 80% (without correction). Moreover, the cat size was further enlarged via a time-separated two-photon subtraction from the continuous-wave squeezed light. As a result, a large-size cat state ($|\alpha|^2 = 2.0$) was obtained with a fidelity of 60% (without correction).

The prepared Fock states and Schrödinger cat states were then combined to generate for the first time hybrid entanglement between particle-like and wave-like optical qubits [76]. This novel resource would permit via teleportation the mapping between two remote quantum processors based on different encodings. Interestingly, we have also demonstrated hybrid qutrit entanglement with two-photon conditioning, enabling to extend the hybrid quantum information processing to higher dimensions. Furthermore, squeezing-induced micro-macro entangled states have been investigated by implementing additional local subtractions. Specifically, with a larger squeezing and higher-photon-number local subtraction, the diagonal states represented in the rotated basis exhibited an increasing phase-space distance, thus indicating the growth of the macroscopicity in phase space.

All the experiments summarized so far were performed with OPOs exploiting down-conversion. In this thesis, its complementary process, quantum frequency up-conversion, has also been investigated theoretically and experimentally. The coherent frequency up-converter in principle maintains the quantum properties of the input state. Therefore, it can be used to broaden the accessible spectra of quantum states, enabling to bridge the spectral discrepancy within a sequence of downstream applications in quantum information science. Besides of the coherent manipulation of quantum states, frequency up-conversion is also useful to implement an up-conversion detector, particularly in the infrared regime. The efficient photon counting would constitute an essential tool in the hybrid architecture as conditioning measurement. It would benefit our previously demonstrated experiments.

Experimentally, we have implemented a coincidence frequency conversion system based on two synchronized fiber lasers, which exhibited a detection efficiency as high as 30%. Thanks to the long-wavelength-pump technique, the dark noise probability per pulse was reduced to 1.6×10^{-4} [144]. Then the conversion system has been adapted to demonstrate infrared photon-number-resolving detection and few-photon-level infrared imaging [150, 158]. These capabilities would provide effective tools to directly demonstrate the nonclassicality of infrared optical quantum states.

Outlook

As mentioned before, the frequency conversion may find useful applications for quantum state engineering and manipulation. First, one can use the capability for efficient infrared photon detection. Particularly, photon-number-resolving detection can be used to perform various protocols based on multi-photon subtraction, for instance the generation of large-size cat states or higher-photon-number Fock states. Additionally, Such photon-number counter can also be used to directly verify the non-Gaussianity of quantum states from the measured photon-number distributions [196]. To this end, quantum tomography of the up-conversion detector should be performed in advance. Second, one can exploit the feature of quantum frequency translation during the conversion process, which allows to extend the spectra of quantum states to the wavelengths difficult to access [192]. Such coherent spectral manipulation of quantum states has great potential in quantum communication and quantum metrology applications.

Quantum computing requires the ability to prepare qubits in a given state and to make

them evolve and interact in a controlled way thanks to quantum gates. The high-fidelity non-Gaussian states presented in this thesis addressed the first requirement, i.e. the preparation of the qubits based on superposed coherent states. The second step is to manipulate the qubits. A challenge is to implement elementary quantum gates in this regime. Note that only a few probabilistic gates have been realized [119, 123] heretofore. The ongoing work will demonstrate some quantum gates and test the principles of quantum information processing with superposed coherent states [120]. Meanwhile, based on the generated hybrid entangled state, we are developing a teleportation experiment to map a discrete-variable qubit into a continuous-variable one [76, 137], a first application of this novel kind of optical entanglement.

Appendix

A | Mathematical formula

A.1 Gauss integrals

$$\int_{\mathbb{R}} e^{-ax^2+bx+c}dx = \sqrt{\frac{\pi}{a}}e^{\frac{b^2}{4a}+c} \tag{A.1}$$

$$\int_{\mathbb{R}} x^2 e^{-ax^2+bx}dx = \left(\frac{1}{2a}+\frac{b^2}{4a^2}\right)\int_{\mathbb{R}} e^{-ax^2+bx}dx \tag{A.2}$$

$$\int_{\mathbb{R}} x^{2n} e^{-ax^2}dx = \sqrt{\frac{\pi}{a}}\frac{(2n-1)!!}{(2a)^n} \tag{A.3}$$

A.2 Laguerre polynomials

The Laguerre polynomials satisfy the recurrence relation:

$$L_n(x) = \frac{2n-1-x}{n}L_{n-1}(x) - \frac{n-1}{n}L_{n-2}(x)\ , \tag{A.4}$$

with $L_0(x) = 1$, $L_1(x) = -x+1$, $L_2(x) = \frac{1}{2}(x^2-4x+2)$.

Actually, they are the specific case of associated Laguerre polynomials L_n^α ($\alpha \in \mathbb{R}$) with $\alpha = 0$. The associated Laguerre polynomials generally satisfy the following recurrence relations:

$$L_n^\alpha(x) = \frac{2n-1+\alpha-x}{n}L_{n-1}^\alpha(x) - \frac{n-1+\alpha}{n}L_{n-2}^\alpha(x)\ , \tag{A.5}$$

with $L_0^\alpha(x) = 1$, $L_1^\alpha(x) = -x+1+\alpha$.

$$L_l^{k-l}(x) = \frac{k-l+1-x}{l}L_{l-1}^{k-(l-1)} - \frac{x}{l}L_{l-2}^{k-(l-2)}(x)\ , \tag{A.6}$$

with $L_0^k = 1$, $L_1^{k-1} = -x+k$.

A.3 Hermite polynomials *(physicists' version)*

This is the definition used in the whole manuscript

$$H_{n+1}(x) = 2xH_n(x) - 2nH_{n-1}(x)\ , \tag{A.7}$$

with $H_0(x) = 1$, $H_1(x) = 2x$, $H_2(x) = 4x^2-2$.

B | $g^{(2)}(0)$ invariance to loss

Here we calculate the second-order correlation function at zero delay $g^{(2)}(0)$ for a general Gaussian state. The technique is based on the Wigner function representation. Note that sometimes using the density matrix in the Fock state basis may be a better choice. Here we want to underline a link between the Wigner function and $g^{(2)}(0)$.

B.1 Expectation value for symmetric ordered operator

For an operator function $\mathrm{F}(\hat{x},\hat{p})$ that is symmetrically ordered with respect to $\hat{x}$ and $\hat{p}$, the quantum mechanical expectation value agrees with the corresponding "classical" average, where the Wigner function $W(x,p)$ plays the role of the weight function:

$$\langle \mathrm{F}(\hat{x},\hat{p})\rangle = \iint W(x,p)f(x,p)dxdp \ . \tag{B.1}$$

Here, the classical function $f(x,p)$ is obtained from the operator function $\mathrm{F}(\hat{x},\hat{p})$ by replacing $\hat{x}$ by x and $\hat{p}$ by p.

The relationship can be generalized to the operator function based on the symmetrically ordered photon creation and annihilation operators, $\hat{a}^\dagger$ and $\hat{a}$:

$$\langle F(\hat{a}^\dagger,\hat{a})\rangle = \int W(x,p)f(x,p)dxdp \ . \tag{B.2}$$

The classical function $f(x,p)$ is simply obtained with the flowing substitutes:

$$\begin{aligned} \hat{a}^\dagger &\to \frac{x+ip}{2\sigma_0} \ , \\ \hat{a} &\to \frac{x-ip}{2\sigma_0} \ . \end{aligned} \tag{B.3}$$

σ_0 is associated with the standard deviation of the vacuum fluctuation:

$$\langle 0|\hat{x}|0\rangle = \sigma_0^2 \ . \tag{B.4}$$

This also leads to the commutator for the quadrature operators:

$$[\hat{x},\hat{p}] = i2\sigma_0^2 \ . \tag{B.5}$$

B.2 Symmetric ordering of field operator

First we construct the following operators:

$$\hat{n}_W = \{\hat{a}^\dagger,\hat{a}\}_{sym} = \frac{1}{2}(\hat{a}^\dagger\hat{a}+\hat{a}\hat{a}^\dagger) = \hat{n}+\frac{1}{2} \ , \tag{B.6}$$

and

$$\begin{aligned} \hat{n}_W^2 &= \{\hat{a}^{\dagger 2},\hat{a}^2\}_{sym} \\ &= \frac{1}{6}(\hat{a}^\dagger\hat{a}^\dagger\hat{a}\hat{a}+\hat{a}\hat{a}\hat{a}^\dagger\hat{a}^\dagger+\hat{a}\hat{a}^\dagger\hat{a}\hat{a}^\dagger+\hat{a}^\dagger\hat{a}\hat{a}^\dagger\hat{a}+\hat{a}^\dagger\hat{a}\hat{a}\hat{a}^\dagger+\hat{a}\hat{a}^\dagger\hat{a}^\dagger\hat{a}) \\ &= \hat{a}^\dagger\hat{a}^\dagger\hat{a}\hat{a}+2\hat{a}^\dagger\hat{a}+\frac{1}{2} \\ &= \hat{n}^2+\hat{n}+\frac{1}{2} \ . \end{aligned} \tag{B.7}$$

Therefore, the $g^{(2)}(0)$ is given by:

$$g^{(2)}(0) = \frac{\langle \hat{a}^\dagger \hat{a}^\dagger \hat{a}\hat{a} \rangle}{\langle \hat{a}^\dagger \hat{a} \rangle^2} = \frac{\langle \hat{n}^2 \rangle - \langle \hat{n} \rangle}{\langle \hat{n} \rangle^2} = \frac{\langle \hat{n}_W^2 \rangle - 2\langle \hat{n}_W \rangle + \frac{1}{2}}{\left(\langle \hat{n}_W \rangle - \frac{1}{2}\right)^2} \ . \tag{B.8}$$

B.3 Single-mode Gaussian state

The Wigner function of a single-mode Gaussian state is generally given by

$$W_G(x,p) = \frac{1}{2\pi\sigma_x\sigma_p} e^{-\frac{(x-x_0)^2}{2\sigma_x^2} - \frac{(p-p_0)^2}{2\sigma_p^2}} \ . \tag{B.9}$$

Therefore we have

$$\begin{aligned} \langle \hat{n}_W \rangle &= \frac{1}{4\sigma_0^2} \int (x^2 + p^2) W_G(x,p) dx dp \\ &= \frac{1}{4\sigma_0^2} (\langle x^2 \rangle + \langle p^2 \rangle) \ , \end{aligned} \tag{B.10}$$

and

$$\begin{aligned} \langle \hat{n}_W^2 \rangle &= \frac{1}{16\sigma_0^4} \int (x^4 + 2x^2p^2 + p^4) W_G(x,p) dx dp \\ &= \frac{1}{16\sigma_0^4} \int (x^4 + 2x^2p^2 + p^4) W_G(x,p) dx dp \\ &= \frac{1}{16\sigma_0^4} (\langle x^4 \rangle + 2\langle x^2 \rangle \langle p^2 \rangle + \langle p^4 \rangle) \ . \end{aligned} \tag{B.11}$$

For multivariate normal distribution, by using the Isserlis' theorem:

$$\langle x^n \rangle = (n-1)\langle x^2 \rangle \langle x^{n-2} \rangle \ , \tag{B.12}$$

we can obtain

$$\langle x^{2n} \rangle = \frac{(2n-1)!}{2^{n-1}(n-1)!} \langle x^2 \rangle^n \ . \tag{B.13}$$

Hence equation (B.11) can be rewritten as

$$\langle \hat{n}_W^2 \rangle = \frac{1}{16\sigma_0^4} (3\langle x^2 \rangle^2 + 2\langle x^2 \rangle \langle p^2 \rangle + 3\langle p^2 \rangle^2) \ . \tag{B.14}$$

As a result, we just need to calculate the second moment of x and p, which are trivially obtained by:

$$\begin{aligned} \langle x^2 \rangle &= \sigma_x^2 + x_0^2 \ , \\ \langle p^2 \rangle &= \sigma_p^2 + p_0^2 \ . \end{aligned} \tag{B.15}$$

Finally, the $g^{(2)}(0)$ is given by

$$g^{(2)}(0) = \frac{\frac{2(\sigma_p^2+p_0^2)(\sigma_x^2+x_0^2)+3(\sigma_x^2+x_0^2)^2+3(\sigma_p^2+p_0^2)^2}{16\sigma_0^4} - \frac{\sigma_x^2+x_0^2+\sigma_p^2+p_0^2}{2\sigma_0^2} + \frac{1}{2}}{\left(\frac{\sigma_x^2+x_0^2+\sigma_p^2+p_0^2}{4\sigma_0^2} - \frac{1}{2}\right)^2} \ . \tag{B.16}$$

If we consider a Gaussian state with zero offset, then we can have the following concise form:

$$\boxed{\begin{aligned} g^{(2)}(0) &= (\frac{\sigma_x^2 - \sigma_p^2}{\sigma_x^2 - 2\sigma_0^2 + \sigma_p^2})^2 + 2 \\ &= (\frac{s_x - s_p}{s_x + s_p - 2})^2 + 2 \ , \end{aligned}} \tag{B.17}$$

where s_x and s_p are normalized variance to the vacuum fluctuation.

Now we can apply this expression to some usual Gaussian states to justify the result we obtained.

B.3.1 Thermal state

For a thermal state, we have $\sigma_x^2 = \sigma_p^2$, leading to $g^{(2)}(0) = 2$.

B.3.2 Squeezed state

For a single-mode pure squeezed state (with a squeezing parameter ζ), we have

$$\begin{aligned} s_x &= e^{-2\zeta} \\ s_p &= e^{2\zeta} \ , \end{aligned}$$

resulting in

$$g^{(2)}(0) = 3 + \frac{1}{\sinh^2 r} \ . \tag{B.18}$$

B.4 Loss on single-mode Gaussian state

For simplicity, we consider a Gaussian state with zero offset:

$$W_G(x,p) = \frac{1}{2\pi\sigma_x\sigma_p} e^{-\frac{x^2}{2\sigma_x^2} - \frac{\mathrm{p}^2}{2\sigma_p^2}} \ . \tag{B.19}$$

A fictitious beam splitter is used to model the loss, thus the state after tracing out the unused mode is given by:

$$W_{Loss}(x,p) = \frac{1}{2\pi\sqrt{(r^2\sigma_0^2 + t^2\sigma_x^2)(r^2\sigma_0^2 + t^2\sigma_p^2)}} e^{-\frac{x^2}{2(r^2\sigma_0^2 + t^2\sigma_x^2)} - \frac{\mathrm{p}^2}{2(r^2\sigma_0^2 + t^2\sigma_p^2)}} \ , \tag{B.20}$$

where t and r are the amplitude transmittance and reflectance of beam splitter, respectively.

We can see that the resulting state is still a Gaussian state with new variances for x and p quadratures:

$$\begin{aligned} \sigma'^2_x &= r^2\sigma_0^2 + t^2\sigma_x^2 \ , \\ \sigma'^2_p &= r^2\sigma_0^2 + t^2\sigma_p^2 \ . \end{aligned} \tag{B.21}$$

Inserting the above equations into equation (B.17), we can get the same value of $g^{(2)}(0)$ with the one for the initial state. More generally, it can be shown that ***for any state (pure or mixed),*** $\mathbf{g^{(2)}(0)}$ ***is invariant to the loss.***

B.5 $g^{(2)}(0)$ invariant to loss

In this section, we will prove that $g^2(0)$ is invariant to the loss. Let us recall the definition of $g^2(0)$:

$$\begin{aligned} g^{(2)}(0) &= \frac{\langle \hat{a}^{\dagger 2}\hat{a}^2\rangle}{\langle \hat{a}^\dagger \hat{a}\rangle^2} \\ &= \frac{\langle \hat{n}^2\rangle - \langle \hat{n}\rangle}{\langle \hat{n}\rangle^2} \ . \end{aligned} \tag{B.22}$$

We consider an initial state $\hat{\rho}$, and model the loss by a beam splitter. Then the first- and second-order momentums of the photon number operator are calculated by:

$$\begin{aligned} \langle \hat{n}\rangle &= \mathrm{Tr}_a[\mathrm{Tr}_b(\hat{B}_{ab}\hat{\rho}_a\hat{B}^\dagger_{ab})\hat{n}_a] \\ &= \mathrm{Tr}(\hat{\rho}_a\hat{B}^\dagger_{ab}\hat{n}_a\hat{B}_{ab}) \\ &= \mathrm{Tr}[\hat{\rho}_a(t\hat{a}^\dagger + r\hat{b}^\dagger)(t\hat{a}+r\hat{b})] \\ &= t^2\,\mathrm{Tr}(\hat{\rho}_a\hat{a}^\dagger\hat{a}) \\ &= t^2\langle \hat{n}\rangle_0 \ , \end{aligned} \tag{B.23}$$

$$\begin{aligned} \langle \hat{n}^2\rangle &= \mathrm{Tr}_a[\mathrm{Tr}_b(\hat{B}_{ab}\hat{\rho}_a\hat{B}^\dagger_{ab})\hat{n}_a^2] \\ &= \mathrm{Tr}(\hat{\rho}_a\hat{B}^\dagger_{ab}(\hat{a}^{\dagger 2}\hat{a}^2 + \hat{a}^\dagger\hat{a})\hat{B}_{ab}) \\ &= \mathrm{Tr}[\hat{\rho}_a(t\hat{a}^\dagger + r\hat{b}^\dagger)^2(t\hat{a}+r\hat{b})^2] + \mathrm{Tr}[\hat{\rho}_a(t\hat{a}^\dagger + r\hat{b}^\dagger)(t\hat{a}+r\hat{b})] \\ &= t^4\langle \hat{a}^{\dagger 2}\hat{a}^2\rangle_0 + t^2\langle \hat{n}\rangle_0 \ . \end{aligned} \tag{B.24}$$

Therefore, it can be seen that the $g^2(0)$ is independent from the loss:

$$g^{(2)}(0) = \frac{\langle \hat{a}^{\dagger 2}\hat{a}^2\rangle_0}{\langle \hat{a}^\dagger\hat{a}\rangle_0^2} = {g_0}^{(2)}(0) \ . \tag{B.25}$$

C | Homodyne data simulation

Numerical simulation of quadrature values for a given quantum state not only enables to test data-processing programs, but also provides a way to evaluate the accuracy of reconstruction algorithms. Moreover, one can easily investigate the quantum state properties with the simulated data by controlling certain parameters.

C.1 Intuitive method

Ref. [20] has demonstrated a nice way for the homodyne data simulation. Here we present an alternative method that is simpler and more intuitive. Specifically, the idea is realized with the following steps:

1. Discretization of the phase-quadrature space into grids with bin sizes of $\delta\theta$ and δx as shown in figure C.1.

2. For a given coordinate (θ_i, x_j), the expected probability density is given by $\mathcal{P}(\theta_i, x_j) = \mathrm{Tr}(|\theta_i, x_j\rangle\langle\theta_i, x_j|\hat{\rho})$, which can be easily obtained with a numerical calculation based on the truncated density matrix.

3. The number of data contained within the square as shown in the figure is thus given by $N \times \mathcal{P} \times \delta x$, where N is a user-defined integer. The coordinate values (θ', x') of the data points (shown with blue dots) are random numbers evenly distributed in the ranges of $[\theta_i - \delta\theta/2, \theta_i + \delta\theta/2]$ and $[x_i - \delta x/2, x_i + \delta x/2]$. These random numbers, which can be rescaled to the interval $[0, 1]$, are readily available in most programming languages. Note that N should be large enough to avoid the truncation error of the integer number format.

4. Repeat the steps 2 and step 3 till fulfilling the defined phase-quadrature space. Finally we can obtain a set of simulated quadrature values corresponding to the state under investigation.

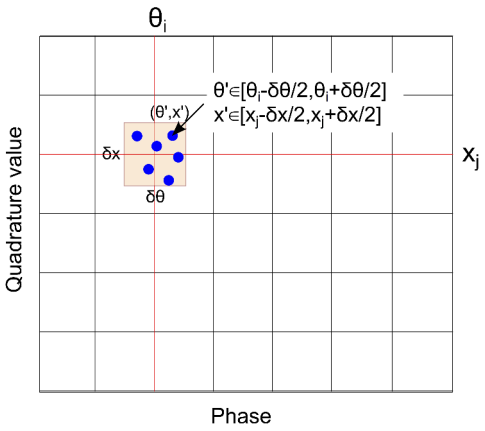

Figure C.1: Intuitive method for numerically simulating quadrature values for a given quantum state.

C.2 Homodyne signal simulation

The method proposed here have three advantages. First it doesn't require the effort to obtain random numbers following a specific distribution. The quadrature probability is numerically calculated from the given density matrix without needing the analytical expression of the marginal distribution. Second, the flatness of phase distribution is intrinsically guaranteed due to the algorithm. Third the intuitive and simple method can be easily extended to multi-mode states using $\mathcal{P}(x_a, \theta_a, x_b, \theta_b) = \mathrm{Tr}[(|\theta_a, x_a\rangle\langle\theta_a, x_a| \otimes |\theta_b, x_b\rangle\langle\theta_b, x_b|)\hat{\rho}_{ab}]$.

Figure C.2 gives the simulated homodyne signal for an odd cats state $|cat_-^{|\alpha|^2=3}\rangle$.

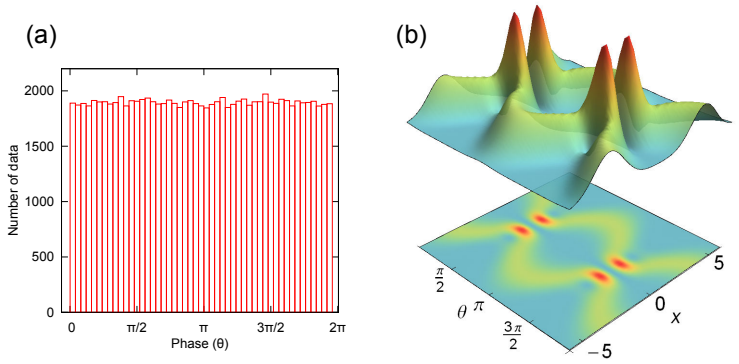

Figure C.2: Example of generating 100,000 quadrature values for an odd cat state $|cat_-^{|\alpha|^2=3}\rangle$. (a) Histogram of the phase distribution. (b) Marginal distribution along the phase.

C.3 Quantum state reconstruction

The simulated data is then processed with a MaxLik algorithm for the quantum state tomography. The results of the reconstructed state are given in figure C.3, which corresponds to the odd cat states as expected.

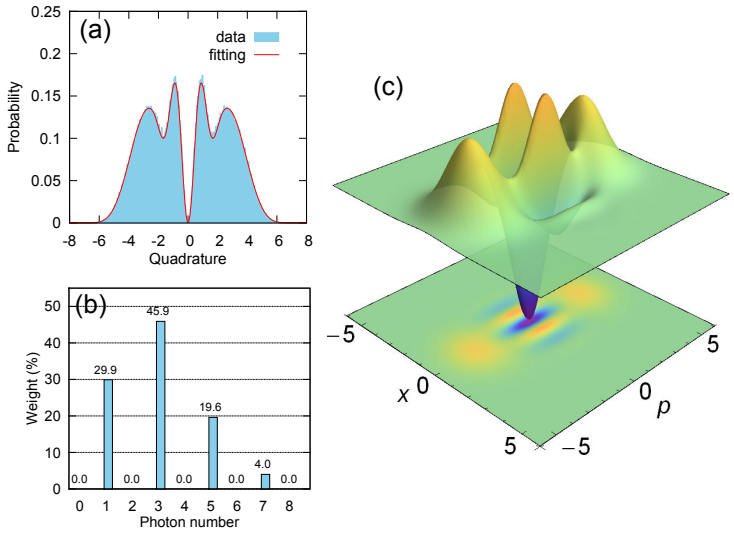

Figure C.3: Reconstructed state from the simulated quadrature values. (a) Marginal distribution from 100,000 quadrature values. (b) Photon-number distribution of the reconstructed state. (c) Corresponding Wigner function.

D | Qmixer

Here we give some examples of modeling quantum state engineering based on the "Qmixer" software.

D.1 Fock states generation

■ Generating Fock states with a two-mode squeezed vacuum state [92, 86]:

$$|\psi\rangle \propto \mathrm{Tr}_b[\hat{B}(\frac{\pi}{4})|\phi\rangle_{ab}\langle\phi|\hat{B}^\dagger(\frac{\pi}{4})|n\rangle_b\langle n|] \ ,$$

where $|\phi\rangle_{ab} = \hat{S}_a(\zeta)|0\rangle \otimes \hat{S}_b(-\zeta)|0\rangle$ is the input state.

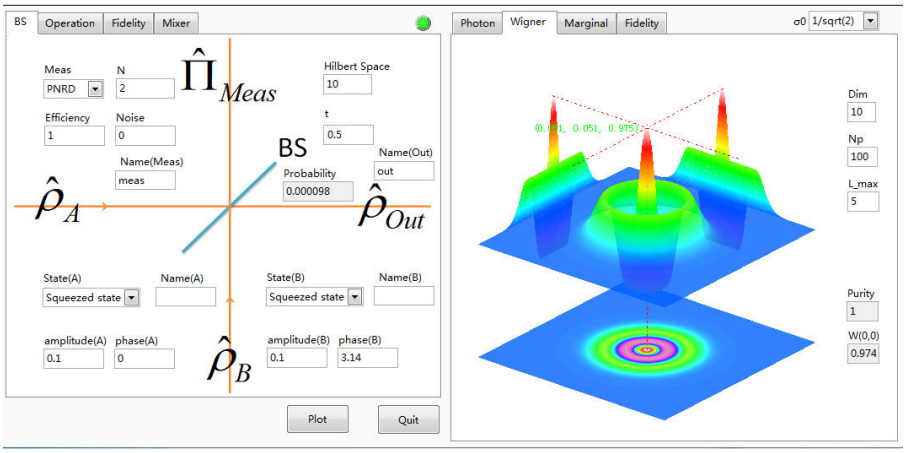

Figure D.1: Generation of Fock states. Two squeezed vacua are mixed on a 50:50 beam splitter. The measurement in the conditional path is performed with a photon-number-resolving detector. Detection of n photons heralds the generation of n-photon Fock state. The generated state here is a two-photon Fock state.

D.2 Superposition of $|0\rangle$ and $|2\rangle$

■ Generating $\alpha|0\rangle + \beta|2\rangle$ with a two-mode squeezed vacuum state:

$$|\psi\rangle \propto \mathrm{Tr}_b[\hat{B}(\theta)|\phi\rangle_{ab}\langle\phi|\hat{B}^\dagger(\theta)|2\rangle_b\langle 2|] \ ,$$

where $|\phi\rangle_{ab} = \hat{S}_a(\zeta)|0\rangle \otimes \hat{S}_b(-\zeta)|0\rangle$ is the input state.

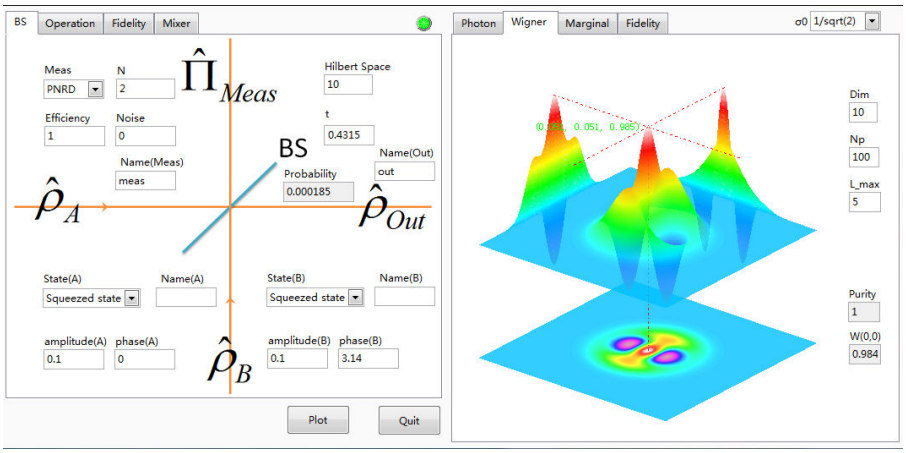

Figure D.2: Generation of $\alpha|0\rangle + \beta|2\rangle$. Two squeezed vacua are mixed on a slightly asymmetric beam splitter. The measurement in the conditional path is performed with a PNR detector. Detection of 2 photons heralds the generation of $\alpha|0\rangle + \beta|2\rangle$. The generated state here is $|0\rangle + |2\rangle$.

D.3 Photon-subtracted squeezed vacuum states

■ Photon-subtracted squeezed vacuum state $\hat{a}^n \hat{S}(\zeta)|0\rangle$ is usually used to approximate a Schrödinger cat state [109, 111]:

$$|\psi\rangle \propto \mathrm{Tr}_b[\hat{B}(\theta \to 0)|\phi\rangle_{ab}\langle\phi|\hat{B}^\dagger(\theta \to 0)|n\rangle_b\langle n|] \ ,$$

where $|\phi\rangle_{ab} = \hat{S}_a(\zeta)|0\rangle$ is the input state.

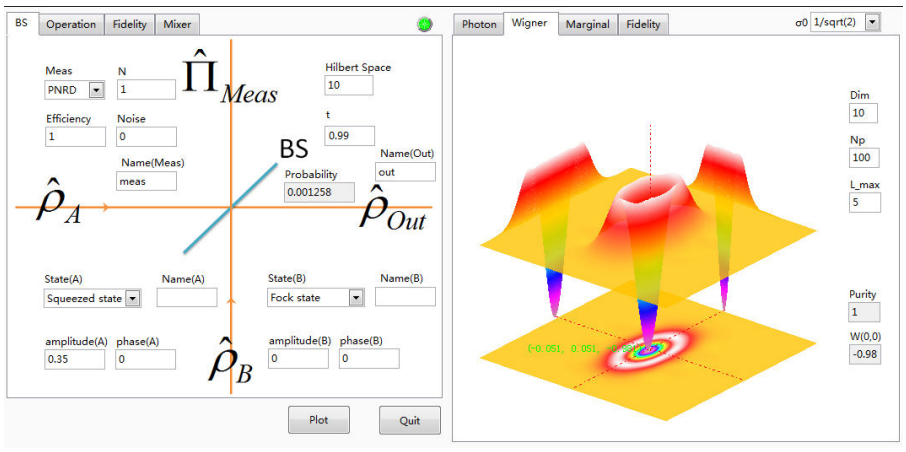

Figure D.3: Generation of photon-subtracted squeezed vacuum states. A beam splitter is used to tap a small fraction from the squeezed vacuum. The tapped part is then detected by a PNR detector. Detection of n photons heralds the generation of $\hat{a}^n \hat{S}(\zeta)|0\rangle$. The generated state here is $\hat{a}\hat{S}(\zeta)|0\rangle \propto \hat{S}(\zeta)|1\rangle$.

D.4 Squeezed cat states from $|n\rangle$

■ Squeezed Schrödinger cat state can be generated from a Fock state conditioned with homodyne detection given a small acceptance window for the quadrature values [79]:

$$|\psi\rangle \propto \mathrm{Tr}_b[\hat{B}(\frac{\pi}{4})|\phi\rangle_{ab}\langle\phi|\hat{B}^\dagger(\frac{\pi}{4})|\varepsilon\to 0\rangle_b\langle\varepsilon\to 0|] \ , \quad \text{where} \quad |\phi\rangle_{ab} = |n\rangle_a \ .$$

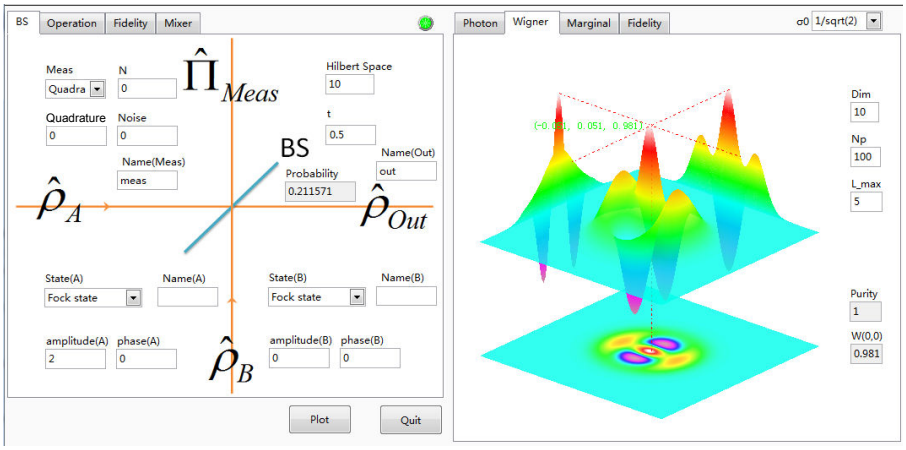

Figure D.4: Generation of squeezed Schrödinger cat states from Fock states. A Fock state $|n\rangle$ impinges on a 50:50 beam splitter. The measurement in the conditional path is performed by a homodyne detection. Detection of small quadrature values within an acceptance window heralds the generation of squeezed cat states. The generated state here is $\sqrt{2/3}|2\rangle - \sqrt{1/3}|0\rangle$.

D.5 Quantum-optical catalysis

■ The so-called quantum catalysis can be obtained by the heralded interference between a Fock state $|n\rangle$ and a coherent state $|\alpha\rangle$, which is useful for engineering exotic nonclassical states [197, 78]. For instance, a single photon state interferes with a week coherent state on a highly asymmetric beam-splitter: $\alpha \sim t \ll 1$. The coherent state is thus approximated by $|\alpha\rangle \approx |0\rangle + \alpha|1\rangle$. The detection of a single photon in one output of the beam-splitter will result in a superposition state:

$$\psi \approx t|0\rangle + \alpha|1\rangle \ .$$

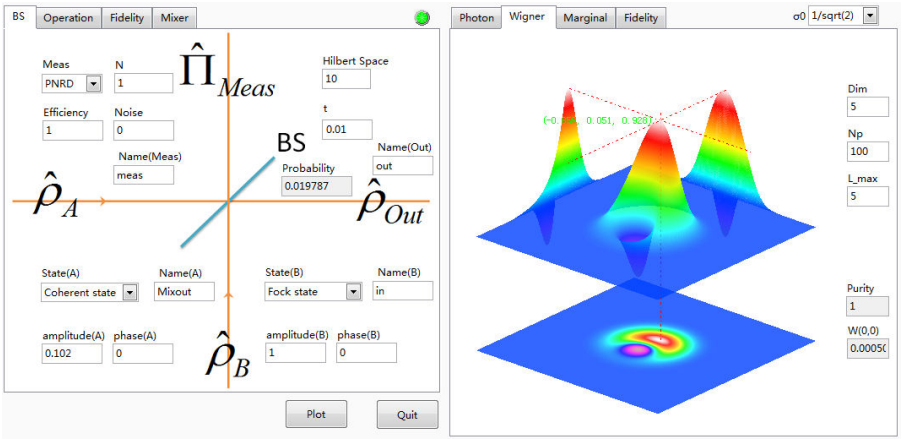

Figure D.5: Generation of nonclassical states based on quantum catalysis. The Fock state plays the role of "catalysis". The generated state here is a qubit state, $|0\rangle + |1\rangle$.

D.6 Amplification of cat states

■ Amplification of small cat states can be realized by mixing them in a beam-splitter [117, 118]:

$$|cat^{\alpha}_{\pm}\rangle_a \otimes |cat^{\alpha}_{\pm}\rangle_b \rightarrow |cat^{\sqrt{2}\alpha}_{+}\rangle_a \otimes |0\rangle_b \pm |0\rangle_a \otimes |cat^{\sqrt{2}\alpha}_{+}\rangle_b \ .$$

When α is large enough, the overlap $\langle 0|cat^{\sqrt{2}\alpha}_{+}\rangle$ is negligible. Therefore we can use a homodyne measurement of quadrature $x = 0$ to discriminate them.

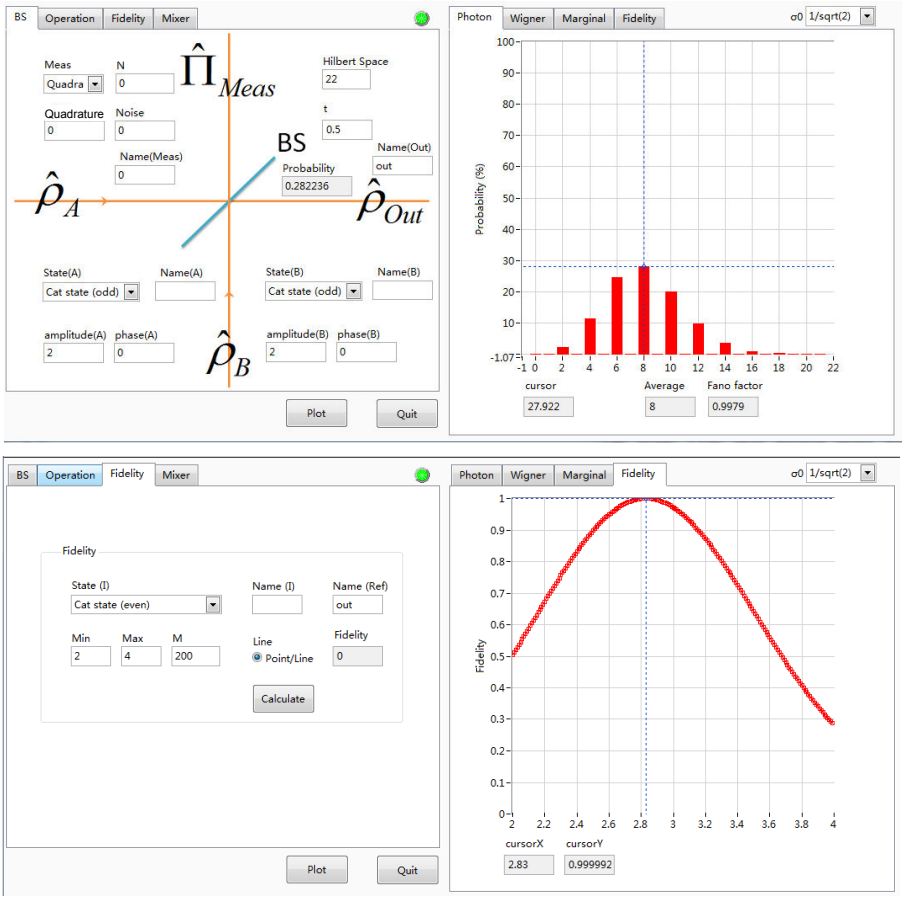

Figure D.6: Amplification of Schrödinger cat states by homodyne heralding. Two small cat states with amplitudes of α interfere on a 50:50 beam-splitter. The measurement in the conditional path is performed with a homodyne detection. Detection of a small quadrature value ($x \rightarrow 0$) heralds the generation of a cat state with a larger amplitude of $\sqrt{2}\alpha$. Here we obtain an amplified even cat state with an amplitude of $2\sqrt{2}$, which is verified by the fidelity compared to an ideal even cat state as shown in the "Fidelity" sub-panel.

E | MCU locking

E.1 Pseudo code for multi-locking

A single evaluation board can be used to lock two cavities with a proper programming. Specifically, we use a main loop in the program, and break every event loop (e.g long sweep, short sweep, lock) into pieces. The following gives a possible pseudo-code:

```
#define EVENT1  1
#define EVENT2  2

int main (void)
{
        int     Flag_locking1, Flag_locking2,
                Locking1_delay_event1, Locking1_delay_event2,
                Locking1_timer_event1, Locking1_timer_event2,
                Locking2_delay_event1, Locking2_delay_event1,
                Locking2_timer_event1, Locking2_timer_event2;

        while(1){
                // Cavity I
                Switch (Flag_locking1){
                case EVENT1:
                        if(Locking1_timer_event1==Locking1_delay_event1){
                                codes;
                                Locking1_timer_event1=0;
                        }
                        Locking1_timer_event1++;
                        break;

                case EVENT2:
                        if(lockingL_timer_event2==Locking_delay_event2){
                                codes;
                                Locking1_timer_event2=0;
                        }
                        Locking1_timer_event2++;
                        break;
                }
                // Cavity II
                Switch (Flag_locking2){
                case EVENT1:
                        if(Locking2_timer_event1==Locking2_delay_event1){
                                codes;
                                Locking2_timer_event1=0;
                        }
                        Locking2_timer_event1++;
                        break;

                case EVENT2:
                        if(Locking2_timer_event2==Locking2_delay_event2){
                                codes;
                                Locking2_timer_event2=0;
                        }
                        Locking2_timer_event2++;
                        break;
                }
        }
}
```

The "delay_event" defines the time delay of each step executed in the event. It enables to control the execution time for each event, for example how fast the long sweep will be, how much time each step will take for the locking. These delays should be adapted with the specific locking system.

E.2 Configuration of integration box

E.2.1 Locking of OPO & Gain

We integrate the lockings of OPO and Gain [1] into one box. The corresponding configuration is illustrated in figure E.1.

[1] Here the locking of Gain refers to the locking of the relative phase between the seeded signal and the pump light.

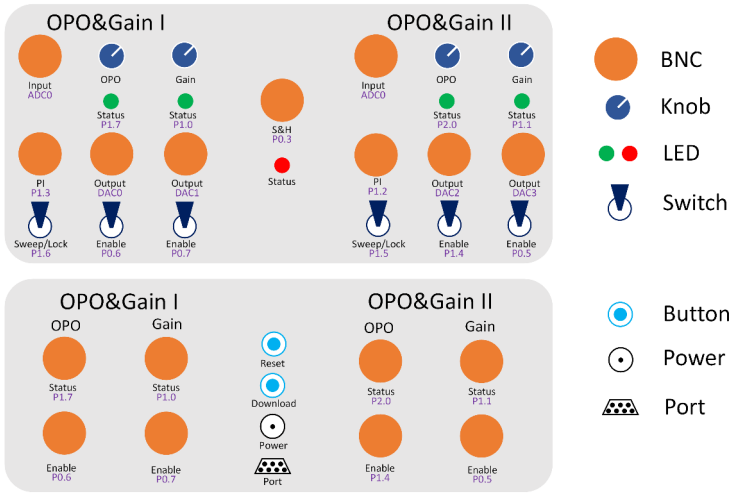

Figure E.1: Integration box for OPO & Gain locking. Front panel (up) and back panel (bottom) of the box.

E.2.2 Locking of μCavities

We integrate two μCavities lockings in one box. The corresponding configuration is illustrated in figure E.2.

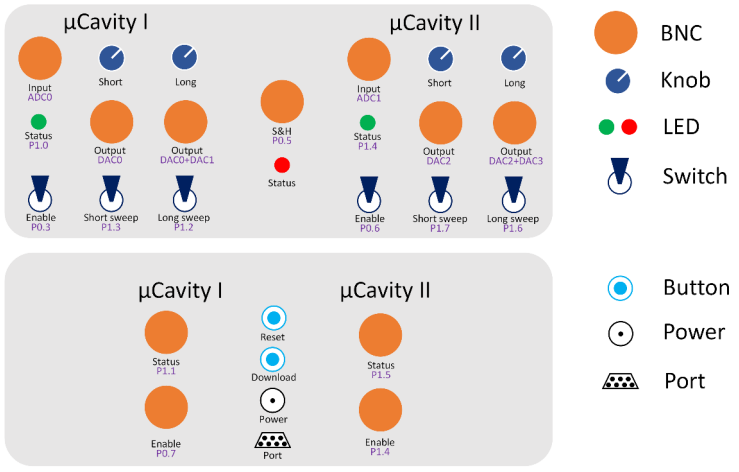

Figure E.2: Integration box for locking two μCavities. Front panel (up) and back panel (bottom) of the box.

F | SSPD

Photon detectors play a crucial role in our experiment to efficiently and correctly herald the generation of the desirable states, such as Fock states (Chapter 5), Schrödinger cat stats (Chapter 6) and hybrid entangled states (Chapter 7). In general, the generation of high-quality states requires high-performance detectors in terms of three aspects: high detection efficiency, low dark noise, and small timing jitter. Remarkably, superconducting nanowire single-photon detectors (SNSPDs or SSPDs) satisfy all these requirements at our working wavelength of 1064 nm.

F.1 Structure

The SSPDs used in our experiments is fabricated and provided by NIST and JPL [1] in the framework of a collaboration. The configuration of the detector is illustrated in figure F.1. The material used for the SSPD is tungsten silicide (WSi), different from the conventional fabrication using niobium nitride (NbN). Because the crystal structure of WSi is homogeneously disordered, this property enables to fabricate a detector meander with a large area about 20×20 μm^2 [198]. Thus it is very easy to bring the light onto the detector by a fiber (typically with a core diameter < 10 μm) without the need of precise alignment.

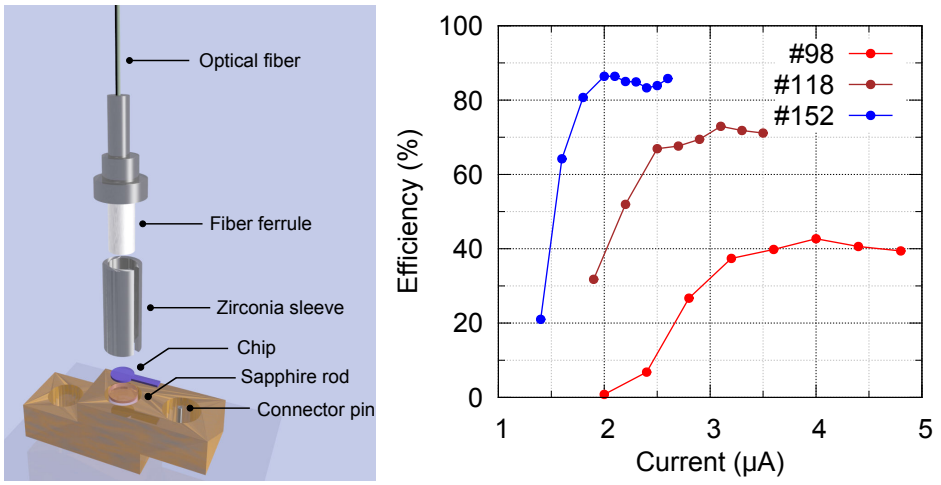

Figure F.1: (Left) Configuration of a superconducting nanowire single-photon detector. The detection area is about 20×20 μm^2. (Right) Detection efficiency as a function of the bias DC current for different tested SSPDs. Number 98 and 118 are the detectors used in this thesis. Number 152 is one of the optimized detector for 1064 nm, which will boost the experiments in the future.

[1] NIST: National Institute of Standards and Technology; JPL: Jet Propulsion Laboratory.

F.2 Performance

The nanowire is cooled down to about 2K with liquid helium, well below its superconducting critical temperature. Then the nanowire is biased with a DC current that is close but less than the superconducting critical current. The impinging photons on the nanowire will form a localized hotspot which has a electrical resistance larger than the 50 Ω input impedance of the readout amplifier. Consequently the bias current is shunted to the amplifier resulting in a measurable voltage pulse.

Figure F.1 shows the behavior of detection efficiency as a function of the bias DC current. Generally speaking, larger bias current leads to higher efficiency, but the bias current too close to the critical current of the nanowire will produce severe dark counts. Practically, the operation current is chosen to be near the beginning of the plateau, which gives maximum efficiency and reasonable dark noise (typically below 10 Hz).

Additionally, we find that the WSi SSPD has a slight polarization dependency, at most 10%. Usually, it is not a problem for the single-click experiments since detection efficiency only affects the heralding probability instead of the conditioned state. As for the two-click experiments needing the balance of photon counting, fixing the fibers can help to achieve a stable count rate for hours [2].

F.3 Optimization

WSi SSPDs have great potential for the efficient photon detection within a broad spectral range from visible to mid-infrared light [199]. The detection performance at a specific wavelength can be optimized by engineering the structure of nanowires, such as thickness, width and pitch. As shown in figure F.1, the detection efficiency has been recently improved up to 90% at 1064 nm. Note that the SSPDs used during this thesis were not yet fully optimized, with a detection efficiency about 50%.

[2]Fortunately, the balancing condition of the two-click experiments (e.g. two-click hybrid entanglement generation) presented in this thesis are independent from the variation of the detection efficiency.

Bibliography

[1] M.A. Nielsen and I.L. Chuang. *Quantum computation and quantum information*. Cambridge university press, 2010.

[2] P. Kok and B.W. Lovett. *Introduction to optical quantum information processing*. Cambridge university press, 2010.

[3] N. Gisin and R. Thew. Quantum communication. *Nat. Photon.*, 1(3):165–171, 2007.

[4] T.D. Ladd, F. Jelezko, R. Laflamme, Y. Nakamura, C. Monroe, and J.L. O'Brien. Quantum computers. *Nature*, 464(7285):45–53, 2010.

[5] V. Giovannetti, S. Lloyd, and L. Maccone. Quantum-enhanced measurements: beating the standard quantum limit. *Science*, 306(5700):1330–1336, 2004.

[6] C.H. Bennett, G. Brassard, C. Crépeau, R. Jozsa, A. Peres, and W.K. Wootters. Teleporting an unknown quantum state via dual classical and Einstein-Podolsky-Rosen channels. *Phys. Rev. Lett.*, 70:1895–1899, Mar 1993.

[7] C.H. Bennett and S.J. Wiesner. Communication via one- and two-particle operators on Einstein-Podolsky-Rosen states. *Phys. Rev. Lett.*, 69:2881–2884, Nov 1992.

[8] P. Kok, W.J. Munro, K. Nemoto, T.C. Ralph, J.P. Dowling, and G.J. Milburn. Linear optical quantum computing with photonic qubits. *Rev. Mod. Phys.*, 79(1):135, 2007.

[9] S.L. Braunstein and P. van Loock. Quantum information with continuous variables. *Rev. Mod. Phys.*, 77:513–577, Jun 2005.

[10] P. van Loock. Optical hybrid approaches to quantum information. *Laser & Photon. Rev.*, 5(2):167–200, 2011.

[11] S. Takeda and A. Furusawa. Optical hybrid quantum information processing. arXiv:1404.2349, 2014.

[12] U.L. Andersen, J.S. Neergaard-Nielsen, P. van Loock, and A. Furusawa. Hybrid quantum information processing. arXiv:1409.3719, 2014.

[13] P. van Loock, W.J. Munro, K. Nemoto, T.P. Spiller, T.D. Ladd, S.L. Braunstein, and G.J. Milburn. Hybrid quantum computation in quantum optics. *Phys. Rev. A*, 78:022303, Aug 2008.

[14] K. Kreis and P. van Loock. Classifying, quantifying, and witnessing qudit-qumode hybrid entanglement. *Phys. Rev. A*, 85:032307, Mar 2012.

[15] G. Grynberg, A. Aspect, and C. Fabre. *Introduction to quantum optics: from the semi-classical approach to quantized light*. Cambridge University Press, 2010.

[16] S.M. Barnett and P.M. Radmore. *Methods in theoretical quantum optics*. Oxford University Press, 1997.

[17] R. Loudon. *The quantum theory of light*. Oxford University Press, 2000.

[18] S. Haroche and J. Raimond. *Exploring the quantum: atoms, cavities, and photons*. Oxford University Press, 2006.

[19] U. Leonhardt. *Measuring the quantum state of light*. Cambridge University Press, 1997.

[20] O. Morin. *Non-Gaussian states and measurements for quantum information*. PhD thesis, University Paris VI, 2013.

[21] J.A. Miszczak, Z. Puchala, P. Horodecki, A. Uhlmann, and K. Zyczkowski. Sub- and super-fidelity as bounds for quantum fidelity. *Quantum Inf. & Comput.*, 9(1&2):0103–0130, 2009.

[22] A. Ferraro, S. Olivares, and M.G.A. Paris. *Gaussian states in continuous variable quantum information*. Bibliopolis, 2005.

[23] C. Weedbrook, S. Pirandola, R. Garcia-Patron, N.J. Cerf, T.C. Ralph, J.H. Shapiro, and S. Lloyd. Gaussian quantum information. *Rev. Mod. Phys.*, 84:621–669, May 2012.

[24] R.L. Hudson. When is the Wigner quasi-probability density non-negative? *Report on Mathematical Physics*, 6:249, Jun 1974.

[25] A. Mandilara, E. Karpov, and N.J. Cerf. Extending Hudson's theorem to mixed quantum states. *Phys. Rev. A*, 79:062302, Jun 2009.

[26] M.G. Genoni, M.L. Palma, T. Tufarelli, S. Olivares, M.S. Kim, and M.G.A. Paris. Detecting quantum non-Gaussianity via the Wigner function. *Phys. Rev. A*, 87:062104, Jun 2013.

[27] M.S. Kim, W. Son, V. Bužek, and P.L. Knight. Entanglement by a beam splitter: nonclassicality as a prerequisite for entanglement. *Phys. Rev. A*, 65:032323, Feb 2002.

[28] E. Knill, R. Laflamme, and G.J Milburn. A scheme for efficient quantum computation with linear optics. *nature*, 409(6816):46–52, 2001.

[29] J. Eisert, S. Scheel, and M. Plenio. Distilling Gaussian states with Gaussian operations is impossible. *Phys. Rev. Lett.*, 89:137903, Sep 2002.

[30] M. Ježek, I. Straka, M. Mičuda, M. Dušek, J. Fiurášek, and R. Filip. Experimental test of the quantum non-Gaussian character of a heralded single-photon state. *Phys. Rev. Lett.*, 107:213602, Nov 2011.

[31] R.W. Boyd. *Nonlinear optics*. Academic Press, 2008.

[32] R.L. Sutherland. *Handbook of nonlinear optics*. Taylor & Francis, 1996.

[33] J. Laurat. *Non-classical states generation and continuous variable entanglement with an optical parametric oscillator*. PhD thesis, University Paris VI, 2004.

[34] A. G. White. *Classical and quantum dynamics of optical frequency conversion*. PhD thesis, Australian National University, 1997.

[35] A. Einstein, B. Podolsky, and N. Rosen. Can quantum-mechanical description of physical reality be considered complete? *Phys. Rev.*, 47:777–780, May 1935.

[36] Y. Takeno, M. Yukawa, H. Yonezawa, and A. Furusawa. Observation of -9 dB quadrature squeezing with improvement of phasestability in homodyne measurement. *Opt. Express*, 15(7):4321–4327, Apr 2007.

[37] M. Mehmet, H. Vahlbruch, N. Lastzka, K. Danzmann, and R. Schnabel. Observation of squeezed states with strong photon-number oscillations. *Phys. Rev. A*, 81:013814, Jan 2010.

[38] O. Morin, V. D'Auria, C. Fabre, and J. Laurat. High-fidelity single-photon source based on a Type II optical parametric oscillator. *Opt. Lett*, 37:3738–3740, Sep 2012.

[39] J. Huang and P. Kumar. Observation of quantum frequency conversion. *Phys. Rev. Lett.*, 68:2153–2156, Apr 1992.

[40] S. Tanzilli, W. Tittel, M. Halder, O. Alibart, P. Baldi, N. Gisin, and H. Zbinden. A photonic quantum information interface. *Nature*, 437(7055):116–20, 2005.

[41] A. Eckstein, B. Brecht, and C. Silberhorn. A quantum pulse gate based on spectrally engineered sum frequency generation. *Opt. Express*, 19(15):13770–13778, Jul 2011.

[42] H. Pan, E Wu, H. Dong, and H. Zeng. Single-photon frequency up-conversion with multimode pumping. *Phys. Rev. A*, 77:033815, Mar 2008.

[43] X. Gu, K. Huang, H. Pan, E Wu, and H. Zeng. Photon correlation in single-photon frequency upconversion. *Opt. Express*, 20(3):2399–2407, Jan 2012.

[44] J. Lavoie, J.M. Donohue, L.G. Wright, A. Fedrizzi, and K.J. Resch. Spectral compression of single photons. *Nat. Photon.*, 7(5):363–366, 2013.

[45] Y. Ding and Z.Y. Ou. Frequency downconversion for a quantum network. *Opt. Lett.*, 35:2591–2593, Aug 2010.

[46] H. Takesue. Single-photon frequency down-conversion experiment. *Phys. Rev. A*, 82:013833, Jul 2010.

[47] S. Zaske *et al.* Visible-to-telecom quantum frequency conversion of light from a single quantum emitter. *Phys. Rev. Lett.*, 109:147404, Oct 2012.

[48] R. Ikuta, Y. Kusaka, T. Kitano, H. Kato, T. Yamamoto, M. Koashi, and N. Imoto. Wide-band quantum interface for visible-to-telecommunication wavelength conversion. *Nat. Comm.*, 2:537, 2011.

[49] B. Albrecht, P. Farrera, X. Fernandez-Gonzalvo, M. Cristiani, and H. de Riedmatten. A waveguide frequency converter connecting rubidium-based quantum memories to the telecom C-band. *Nat. Comm.*, 5:3376, Feb 2014.

[50] K. De Greve *et al.* Quantum-dot spin-photon entanglement via frequency downconversion to telecom wavelength. *Nature*, 491(7424):421–425, 2012.

[51] H.J. McGuinness, M.G. Raymer, C.J. McKinstrie, and S. Radic. Quantum frequency translation of single-photon states in a photonic crystal fiber. *Phys. Rev. Lett.*, 105:093604, Aug 2010.

[52] M.G. Genoni, F.A. Beduini, A. Allevi, M. Bondani, S. Olivares, and M.G.A. Paris. Non-Gaussian states by conditional measurements. *Physica Scripta*, T140:014007, 2010.

[53] S.M. Barnett. *Quantum information*. Oxford University Press, 2009.

[54] V. D'Auria, O. Morin, C. Fabre, and J. Laurat. Effect of the heralding detector properties on the conditional generation of single-photon states. *Eur. Phys. J. D*, 66(10):249, 2012.

[55] J.S. Lundeen, A. Feito, H. Coldenstrodt-Ronge, K.L. Pregnell, C. Silberhorn, T.C. Ralph, J. Eisert, M.B. Plenio, and I.A. Walmsley. Tomography of quantum detectors. *Nat. Phys.*, 5(1):27–30, 2009.

[56] V. D'Auria, N. Lee, T. Amri, C. Fabre, and J. Laurat. Quantum decoherence of single-photon counters. *Phys. Rev. Lett.*, 107:050504, Jul 2011.

[57] A. Divochiy *et al.* Superconducting nanowire photon-number-resolving detector at telecommunication wavelengths. *Nat. Photon.*, 2(5):302–306, 2008.

[58] D. Achilles, C. Silberhorn, C. Śliwa, K. Banaszek, and I.A. Walmsley. Fiber-assisted detection with photon number resolution. *Opt. Lett.*, 28(23):2387–2389, Dec 2003.

[59] A.I. Lvovsky and M.G. Raymer. Continuous-variable optical quantum-state tomography. *Rev. Mod. Phys.*, 81(1):299, 2009.

[60] J. Clausen, M. Dakna, L. Knöll, and D.-G. Welsch. Conditional quantum-state transformation at a beam splitter. *J. Opt. B: Quantum Semiclass. Opt.*, 1:332–338, 1999.

[61] M. Dakna, L. Knöll, and D.-G. Welsch. Quantum state engineering using conditional measurement on a beam splitter. *Eur. Phys. J. D*, 3(3):295–308, 1998.

[62] A.I. Lvovsky. Iterative maximum-likelihood reconstruction in quantum homodyne tomography. *J. Opt. B: Quantum Semiclass. Opt.*, 6(6):S556, 2004.

[63] K. Huang, H. Le Jeannic, J. Ruaudel, O. Morin, and J. Laurat. Microcontroller-based locking in optics experiments. *Rev. Sci. Instrum.*, 85(12):123112, 2014.

[64] A. Rossi, V. Biancalana, B. Mai, and L. Tomassetti. Long-term drift laser frequency stabilization using purely optical reference. *Rev. Sci. Instrum.*, 73(7):2544–2548, 2002.

[65] D.V. Pantelić, B.M. Panić, and A.G. Kovačević. Digital control of an iodine stabilized He-Ne laser by using a personal computer and a simple electronic system. *Rev. Sci. Instrum.*, 74(6):3155–3159, 2003.

[66] K. Matsubara, S. Uetake, H. Ito, Y. Li, K. Hayasaka, and M. Hosokawa. Precise frequency-drift measurement of extended-cavity diode laser stabilized with scanning transfer cavity. *Jpn. J. Appl. Phys.*, 44(1R):229, 2005.

[67] N. Seymour-Smith, P. Blythe, M. Keller, and W. Lange. Fast scanning cavity offset lock for laser frequency drift stabilization. *Rev. Sci. Instrum.*, 81(7):075109, 2010.

[68] T. Ahola, J. Hu, and E. Ikonen. A digital control system for the iodine stabilized He-Ne laser. *Rev. Sci. Instrum.*, 69(5):1934–1937, 1998.

[69] W.Z. Zhao, J.E. Simsarian, L.A. Orozco, and G.D. Sprouse. A computer-based digital feedback control of frequency drift of multiple lasers. *Rev. Sci. Instrum.*, 69(11):3737–3740, 1998.

[70] B. M. Sparkes, H. M. Chrzanowski, D. P. Parrain, B. C. Buchler, P. K. Lam, and T. Symul. A scalable, self-analyzing digital locking system for use on quantum optics experiments. *Rev. Sci. Instrum.*, 82(7):075113, 2011.

[71] M.R. Dietrich and B.B. Blinov. Use of a microcontroller for fast feedback control of a fiber laser. *arXiv*, 0905.2484, 2009.

[72] Analog Devices. ADuC70xx series: precision analog microcontroller, data sheet, Rev. F. 2013.

[73] T. Eberle, V. Händchen, and R. Schnabel. Stable control of 10 dB two-mode squeezed vacuum states of light. *Opt. Express*, 21(9):11546–11553, May 2013.

[74] O. Morin, J. Liu, K. Huang, F.A.S. Barbosa, C. Fabre, and J. Laurat. Quantum state engineering of light with continuous-wave optical parametric oscillators. *J. Visual. Exp.*, (87):e51224, 2014.

[75] R.W.P. Drever, J.L. Hall, F.V. Kowalski, J. Hough, G.M. Ford, A.J. Munley, and H. Ward. Laser phase and frequency stabilization using an optical resonator. *Appl. Phys. B*, 31(2):97–105, 1983.

[76] O. Morin, K. Huang, J. Liu, H. Le Jeannic, C. Fabre, and J. Laurat. Remote creation of hybrid entanglement between particle-like and wave-like optical qubits. *Nat. Photon.*, 8(7):570–574, 2014.

[77] T.C. Briles, D.C. Yost, A. Cingöz, J. Ye, and T.R. Schibli. Simple piezoelectric-actuated mirror with 180 kHz servo bandwidth. *Opt. Express*, 18(10):9739–9746, May 2010.

[78] T.J. Bartley, G. Donati, J.B. Spring, X.-M. Jin, M. Barbieri, A. Datta, B.J. Smith, and I.A. Walmsley. Multiphoton state engineering by heralded interference between single photons and coherent states. *Phys. Rev. A*, 86:043820, Oct 2012.

[79] A. Ourjoumtsev, H. Jeong, R. Tualle-Brouri, and P. Grangier. Generation of optical Schrödinger cats from photon number states. *Nature*, 448(7155):784–786, 2007.

[80] J. McKeever, A. Boca, A.D. Boozer, R. Miller, J.R. Buck, A. Kuzmich, and H.J. Kimble. Deterministic generation of single photons from one atom trapped in a cavity. *Science*, 303(5666):1992–1994, 2004.

[81] C. Kurtsiefer, S. Mayer, P. Zarda, and H. Weinfurter. Stable solid-state source of single photons. *Phys. Rev. Lett.*, 85:290–293, Jul 2000.

[82] C. Santori, M. Pelton, G. Solomon, Y. Dale, and Y. Yamamoto. Triggered single photons from a quantum dot. *Phys. Rev. Lett.*, 86:1502–1505, Feb 2001.

[83] C.K. Hong and L. Mandel. Experimental realization of a localized one-photon state. *Phys. Rev. Lett.*, 56:58–60, Jan 1986.

[84] A.I Lvovsky, H. Hansen, T. Aichele, O. Benson, J. Mlynek, and S. Schiller. Quantum state reconstruction of the single-photon Fock state. *Phys. Rev. Lett.*, 87(5):050402, 2001.

[85] A. Zavatta, S. Viciani, and M. Bellini. Tomographic reconstruction of the single-photon fock state by high-frequency homodyne detection. *Phys. Rev. A*, 70:053821, Nov 2004.

[86] A. Ourjoumtsev, R. Tualle-Brouri, and P. Grangier. Quantum homodyne tomography of a two-photon Fock state. *Phys. Rev. Lett.*, 96:213601, Jun 2006.

[87] A.E.B. Nielsen and K. Mølmer. Single-photon-state generation from a continuous-wave nondegenerate optical parametric oscillator. *Phys. Rev. A*, 75:023806, Feb 2007.

[88] K. Wakui, H. Takahashi, A. Furusawa, and M. Sasaki. Photon subtracted squeezed states generated with periodically poled KTiOPO4. *Opt. Express*, 15(6):3568–3574, Mar 2007.

[89] J.S. Neergaard-Nielsen, B.M. Nielsen, H. Takahashi, A.I. Vistnes, and E.S. Polzik. High purity bright single photon source. *Opt. Express*, 15(13):7940–7949, Jun 2007.

[90] R. Kumar, E. Barrios, A. MacRae, E. Cairns, E.H. Huntington, and A.I. Lvovsky. Versatile wideband balanced detector for quantum optical homodyne tomography. *Opt. Comm.*, 285(24):5259–5267, 2012.

[91] A.E.B. Nielsen and K. Mølmer. Photon number states generated from a continuous-wave light source. *Phys. Rev. A*, 75:043801, Apr 2007.

[92] E. Bimbard, N. Jain, A. MacRae, and A.I. Lvovsky. Quantum-optical state engineering up to the two-photon level. *Nat. Photon.*, 4(4):243–247, 2010.

[93] M. Yukawa, K. Miyata, H. Yonezawa, P. Marek, R. Filip, and A. Furusawa. Emulating quantum cubic nonlinearity. *Phys. Rev. A*, 88:053816, Nov 2013.

[94] Y. Miwa, J. Yoshikawa, N. Iwata, M. Endo, P. Marek, R. Filip, P. van Loock, and A. Furusawa. Exploring a new regime for processing optical qubits: squeezing and unsqueezing single photons. *Phys. Rev. Lett.*, 113:013601, Jul 2014.

[95] M. Yukawa, K. Miyata, T. Mizuta, H. Yonezawa, P. Marek, R. Filip, and A. Furusawa. Generating superposition of up-to three photons for continuous variable quantum information processing. *Opt. Express*, 21(5):5529–5535, Mar 2013.

[96] S.R. Huisman, N. Jain, S.A. Babichev, F. Vewinger, A.N. Zhang, S.H. Youn, and A.I. Lvovsky. Instant single-photon fock state tomography. *Opt. Lett.*, 34(18):2739–2741, Sep 2009.

[97] M. Takeoka, H. Takahashi, and M. Sasaki. Large-amplitude coherent-state superposition generated by a time-separated two-photon subtraction from a continuous-wave squeezed vacuum. *Phys. Rev. A*, 77:062315, Jun 2008.

[98] M. Sasaki, M. Takeoka, and H. Takahashi. Temporally multiplexed superposition states of continuous variables. *Phys. Rev. A*, 77:063840, Jun 2008.

[99] H. Takahashi, K. Wakui, S. Suzuki, M. Takeoka, K. Hayasaka, A. Furusawa, and M. Sasaki. Generation of large-amplitude coherent-state superposition via ancilla-assisted photon subtraction. *Phys. Rev. Lett.*, 101:233605, Dec 2008.

[100] T.C. Ralph, A. Gilchrist, G.J. Milburn, W.J. Munro, and S. Glancy. Quantum computation with optical coherent states. *Phys. Rev. A*, 68:042319, Oct 2003.

[101] H. Jeong and M. S. Kim. Efficient quantum computation using coherent states. *Phys. Rev. A*, 65:042305, Mar 2002.

[102] M. Kira, S.W. Koch, R.P. Smith, A.E. Hunter, and S.T. Cundiff. Quantum spectroscopy with Schrödinger-cat states. *Nat. Phys.*, 7(10):799–804, 2011.

[103] A. Gilchrist, K. Nemoto, W.J. Munro, T.C. Ralph, S. Glancy, S.L. Braunstein, and G.J. Milburn. Schrödinger cats and their power for quantum information processing. *J. Opt. B: Quantum Semiclass. Opt.*, 6(8):S828, 2004.

[104] C.C. Gerry. Generation of optical macroscopic quantum superposition states via state reduction with a Mach-Zehnder interferometer containing a Kerr medium. *Phys. Rev. A*, 59:4095–4098, May 1999.

[105] H. Jeong. Using weak nonlinearity under decoherence for macroscopic entanglement generation and quantum computation. *Phys. Rev. A*, 72:034305, Sep 2005.

[106] R. Filip, P. Marek, and U.L. Andersen. Measurement-induced continuous-variable quantum interactions. *Phys. Rev. A*, 71:042308, Apr 2005.

[107] S. Scheel, K. Nemoto, W.J. Munro, and P.L. Knight. Measurement-induced nonlinearity in linear optics. *Phys. Rev. A*, 68:032310, Sep 2003.

[108] M. Dakna, T. Anhut, T. Opatrný, L. Knöll, and D.-G. Welsch. Generating Schrödinger-cat-like states by means of conditional measurements on a beam splitter. *Phys. Rev. A*, 55:3184–3194, Apr 1997.

[109] J.S. Neergaard-Nielsen, B.M. Nielsen, C. Hettich, K. Mølmer, and E.S. Polzik. Generation of a superposition of odd photon number states for quantum information networks. *Phys. Rev. Lett.*, 97:083604, Aug 2006.

[110] A. Ourjoumtsev, R. Tualle-Brouri, J. Laurat, and P. Grangier. Generating optical Schrödinger kittens for quantum information processing. *Science*, 312(5770):83–86, 2006.

[111] T. Gerrits, S. Glancy, T.S. Clement, B. Calkins, A.E. Lita, A.J. Miller, A.L. Migdall, S.W Nam, R.P. Mirin, and E. Knill. Generation of optical coherent-state superpositions by number-resolved photon subtraction from the squeezed vacuum. *Phys. Rev. A*, 82:031802, Sep 2010.

[112] N. Namekata, Y. Takahashi, G. Fujii, D. Fukuda, S. Kurimura, and S. Inoue. Non-gaussian operation based on photon subtraction using a photon-number-resolving detector at a telecommunications wavelength. *Nat. Photon.*, 4(9):655–660, 2010.

[113] S. Glancy and H. Macedo de Vasconcelos. Methods for producing optical coherent state superpositions. *J. Opt. Soc. Am. B*, 25(5):712–733, May 2008.

[114] A.E.B. Nielsen and K. Mølmer. Transforming squeezed light into a large-amplitude coherent-state superposition. *Phys. Rev. A*, 76:043840, Oct 2007.

[115] A. Kenfack and K. Zyczkowski. Negativity of the Wigner function as an indicator of non-classicality. *J. Opt. B: Quantum Semiclass. Opt.*, 6(10):396, 2004.

[116] J. Fiurášek and M. Ježek. Witnessing negativity of Wigner function by estimating fidelities of catlike states from homodyne measurements. *Phys. Rev. A*, 87:062115, Jun 2013.

[117] A. P. Lund, H. Jeong, T. C. Ralph, and M. S. Kim. Conditional production of superpositions of coherent states with inefficient photon detection. *Phys. Rev. A*, 70:020101, Aug 2004.

[118] A. Laghaout, J.S. Neergaard-Nielsen, T. Rigas, C. Kragh, A. Tipsmark, and U.L. Andersen. Amplification of realistic Schrödinger-cat-state-like states by homodyne heralding. *Phys. Rev. A*, 87:043826, Apr 2013.

[119] R. Blandino, F. Ferreyrol, M. Barbieri, P. Grangier, and R. Tualle-Brouri. Characterization of a π-phase shift quantum gate for coherent-state qubits. *New J. Phys.*, 14(1):013017, 2012.

[120] P. Marek and J. Fiurášek. Elementary gates for quantum information with superposed coherent states. *Phys. Rev. A*, 82:014304, Jul 2010.

[121] S.-J. Ma and W.-W. Luo. Comparison of nonclassicality between photon-added and photon-subtracted squeezed vacuum states. *Chin. Phys. B*, 21(2):024203, 2012.

[122] S. Glancy, H.M. Vasconcelos, and T.C. Ralph. Transmission of optical coherent-state qubits. *Phys. Rev. A*, 70:022317, Aug 2004.

[123] A. Tipsmark, R. Dong, A. Laghaout, P. Marek, M. Ježek, and U. Andersen. Experimental demonstration of a Hadamard gate for coherent state qubits. *Phys. Rev. A*, 84:050301, Nov 2011.

[124] J.L. O'Brien, A. Furusawa, and J. Vučković. Photonic quantum technologies. *Nat. Photon.*, 3(12):687–695, 2009.

[125] A. Furusawa and P. Van Loock. *Quantum teleportation and entanglement.* Wiley-Vch, 2011.

[126] S.L. Braunstein and A.K. Pati. *Quantum information with continuous variables.* Springer, 2003.

[127] H. Jeong, A. Zavatta, M. Kang, S.-W. Lee, L.S. Costanzo, S. Grandi, T.C. Ralph, and M. Bellini. Generation of hybrid entanglement of light. *Nat. Photon.*, 8(7):564–569, 2014.

[128] J. Rigas, O. Gühne, and N. Lütkenhaus. Entanglement verification for quantum-key-distribution systems with an underlying bipartite qubit-mode structure. *Phys. Rev. A*, 73:012341, Jan 2006.

[129] S.-W. Lee and H. Jeong. Near-deterministic quantum teleportation and resource-efficient quantum computation using linear optics and hybrid qubits. *Phys. Rev. A*, 87:022326, Feb 2013.

[130] H. Kwon and H. Jeong. Violation of the Bell-Clauser-Horne-Shimony-Holt inequality using imperfect photodetectors with optical hybrid states. *Phys. Rev. A*, 88:052127, Nov 2013.

[131] K. Park, S.-W. Lee, and H. Jeong. Quantum teleportation between particlelike and fieldlike qubits using hybrid entanglement under decoherence effects. *Phys. Rev. A*, 86:062301, Dec 2012.

[132] H. Jeong, M. Kim, and J. Lee. Quantum-information processing for a coherent superposition state via a mixedentangled coherent channel. *Phys. Rev. A*, 64:052308, Oct 2001.

[133] J. Gea-Banacloche. Impossibility of large phase shifts via the giant Kerr effect with single-photon wave packets. *Phys. Rev. A*, 81:043823, Apr 2010.

[134] L.-M. Duan, M.D. Lukin, J. I. Cirac, and P. Zoller. Long-distance quantum communication with atomic ensembles and linear optics. *Nature*, 414(6862):413–418, 2001.

[135] A. Ourjoumtsev, F. Ferreyrol, R. Tualle-Brouri, and P. Grangier. Preparation of non-local superpositions of quasi-classical light states. *Nat. Phys.*, 5(3):189–192, 2009.

[136] G. Vidal and R.F. Werner. Computable measure of entanglement. *Phys. Rev. A*, 65:032314, Feb 2002.

[137] U.L Andersen and J.S Neergaard-Nielsen. Heralded generation of a micro-macro entangled state. *Phys. Rev. A*, 88(2):022337, 2013.

[138] N. Bruno, A. Martin, P. Sekatski, N. Sangouard, R.T. Thew, and N. Gisin. Displacement of entanglement back and forth between the micro and macro domains. *Nat. Phys.*, 9(9):545–548, 2013.

[139] A.I. Lvovsky, R. Ghobadi, A. Chandra, A.S. Prasad, and C. Simon. Observation of micro-macro entanglement of light. *Nat. Phys.*, 9(9):541–544, 2013.

[140] C. Wittmann, U. Andersen, M. Takeoka, D. Sych, and G. Leuchs. Demonstration of coherent-state discrimination using a displacement-controlled photon-number-resolving detector. *Phys. Rev. Lett.*, 104:100505, Mar 2010.

[141] F. De Martini, F. Sciarrino, and C. Vitelli. Entanglement test on a microscopic-macroscopic system. *Phys. Rev. Lett.*, 100:253601, Jun 2008.

[142] R. Ghobadi, A. Lvovsky, and C. Simon. Creating and detecting micro-macro photon-number entanglement by amplifying and deamplifying a single-photon entangled state. *Phys. Rev. Lett.*, 110:170406, Apr 2013.

[143] A. Laghaout, J.S. Neergaard-Nielsen, and U.L. Andersen. Assessments of macroscopicity for quantum optical states. *Opt. Comm.*, 337:96–101, 2015.

[144] K. Huang, X. Gu, H. Pan, E Wu, and H. Zeng. Synchronized fiber lasers for efficient coincidence single-photon frequency upconversion. *IEEE J. Sel. Top. Quant. Electron.*, 18(2):562–566, Mar 2012.

[145] X. Gu, Y. Li, H. Pan, E Wu, and H. Zeng. High-speed single-photon frequency upconversion with synchronous pump pulses. *IEEE J. Sel. Top. Quant. Electron.*, 15(6):1748–1752, Nov 2009.

[146] X. Gu, K. Huang, Y. Li, H. Pan, E Wu, and H. Zeng. Temporal and spectral control of single-photon frequency upconversion for pulsed radiation. *Appl. Phys. Lett.*, 96(13):131111, 2010.

[147] M.A. Albota and F.N.C. Wong. Efficient single-photon counting at 1.55 μm by means of frequency upconversion. *Opt. Lett.*, 29(13):1449–1451, Jul 2004.

[148] R.H. Hadfield. Single-photon detectors for optical quantum information applications. *Nat. Photon.*, 3(12):696–705, 2009.

[149] S. Ramelow, A. Fedrizzi, A. Poppe, N. K. Langford, and A. Zeilinger. Polarization-entanglement-conserving frequency conversion of photons. *Phys. Rev. A*, 85:013845, Jan 2012.

[150] K. Huang, X. Gu, M. Ren, Y. Jian, H. Pan, G. Wu, E Wu, and H. Zeng. Photon-number-resolving detection at 1.04μm via coincidence frequency upconversion. *Opt. Lett.*, 36(9):1722–1724, May 2011.

[151] H. Pan and H. Zeng. Efficient and stable single-photon counting at 1.55 μm by intracavity frequency upconversion. *Opt. Lett.*, 31(6):793–795, Mar 2006.

[152] A.P. VanDevender and P.G. Kwiat. Quantum transduction via frequency upconversion (Invited). *J. Opt. Soc. Am. B*, 24(2):295–299, Feb 2007.

[153] A.P. Vandevender and P.G. Kwiat. High efficiency single photon detection via frequency up-conversion. *J. Mod. Opt.*, 51:1433–1445, Sep 2004.

[154] M.M. Fejer, G.A. Magel, D.H. Jundt, and R.L. Byer. Quasi-phase-matched second harmonic generation: tuning and tolerances. *IEEE J. Quant. Electron.*, 28(11):2631–2654, Nov 1992.

[155] H. Takesue, E. Diamanti, C. Langrock, M.M. Fejer, and Y. Yamamoto. 1.5-μm single photon counting using polarization-independent up-conversion detector. *Opt. Express*, 14(26):13067–13072, Dec 2006.

[156] C. Pedersen, E. Karamehmedović, J.S. Dam, and P. Tidemand-Lichtenberg. Enhanced 2D-image upconversion using solid-state lasers. *Opt. Express*, 17(23):20885–20890, Nov 2009.

[157] J.S. Dam, P. Tidemand-Lichtenberg, and C. Pedersen. Room-temperature mid-infrared single-photon spectral imaging. *Nat. Photon.*, 6(11):788–793, 2012.

[158] K. Huang, X. Gu, H. Pan, E Wu, and H. Zeng. Few-photon-level two-dimensional infrared imaging by coincidence frequency upconversion. *Appl. Phys. Lett.*, 100(15):151102, 2012.

[159] Q. Zhang, C. Langrock, M.M. Fejer, and Y. Yamamoto. Waveguide-based single-pixel up-conversion infrared spectrometer. *Opt. Express*, 16(24):19557–19561, Nov 2008.

[160] L. Ma, O. Slattery, and X. Tang. Experimental study of high sensitivity infrared spectrometer with waveguide-based up-conversion detector. *Opt. Express*, 17(16):14395–14404, Aug 2009.

[161] G.-L. Shentu, J.S. Pelc, X.-D. Wang, Q.-C. Sun, M.-Y. Zheng, M.M. Fejer, Q. Zhang, and J.-W. Pan. Ultralow noise up-conversion detector and spectrometer for the telecom band. *Opt. Express*, 21(12):13986–13991, Jun 2013.

[162] H. Xu, L. Ma, A. Mink, B. Hershman, and X. Tang. 1310-nm quantum key distribution system with up-conversion pump wavelength at 1550 nm. *Opt. Express*, 15(12):7247–7260, Jun 2007.

[163] M.T. Rakher, L. Ma, O. Slattery, X. Tang, and K. Srinivasan. Quantum transduction of telecommunications-band single photons from a quantum dot by frequency upconversion. *Nat. Photon.*, 4(11):786–791, 2010.

[164] M.T. Rakher, L. Ma, M. Davanço, O. Slattery, X. Tang, and K. Srinivasan. Simultaneous wavelength translation and amplitude modulation of single photons from a quantum dot. *Phys. Rev. Lett.*, 107:083602, Aug 2011.

[165] D. Kielpinski, J. Corney, and H. Wiseman. Quantum optical waveform conversion. *Phys. Rev. Lett.*, 106:130501, Mar 2011.

[166] J.M. Donohue, J. Lavoie, and K.J. Resch. Ultrafast time-division demultiplexing of polarization-entangled photons. *Phys. Rev. Lett.*, 113:163602, Oct 2014.

[167] B. Brecht, A. Eckstein, R. Ricken, V. Quiring, H. Suche, L. Sansoni, and C. Silberhorn. Demonstration of coherent time-frequency schmidt mode selection using dispersion-engineered frequency conversion. *Phys. Rev. A*, 90:030302, Sep 2014.

[168] H. Dong, H. Pan, Y. Li, E Wu, and H. Zeng. Efficient single-photon frequency up-conversion at 1.06 μm with ultralow background counts. *Appl. Phys. Lett.*, 93:071101, 2008.

[169] O. Kuzucu, F.N.C. Wong, S. Kurimura, and S. Tovstonog. Time-resolved single-photon detection by femtosecond upconversion. *Opt. Lett.*, 33(19):2257–2259, Oct 2008.

[170] D.D. Hudson, S.M. Foreman, S.T. Cundiff, and J. Ye. Synchronization of mode-locked femtosecond lasers through a fiber link. *Opt. Lett.*, 31(13):1951–1953, Jul 2006.

[171] M. Rusu, R. Herda, and O. Okhotnikov. Passively synchronized two-color mode-locked fiber system based on master-slave lasers geometry. *Opt. Express*, 12(20):4719–4724, Oct 2004.

[172] D. Yoshitomi, Y. Kobayashi, M. Kakehata, H. Takada, K. Torizuka, T. Onuma, H. Yokoi, T. Sekiguchi, and S. Nakamura. Ultralow-jitter passive timing stabilization of a mode-locked Er-doped fiber laser by injection of an optical pulse train. *Opt. Lett.*, 31(22):3243–3245, Nov 2006.

[173] Y. Li, X. Gu, M. Yan, E Wu, and H. Zeng. Square nanosecond mode-locked er-fiber laser synchronized to a picosecond yb-fiber laser. *Opt. Express*, 17(6):4526–4532, Mar 2009.

[174] Y.-F. Chen, J. Jiang, and D.J. Jones. Remote distribution of a mode-locked pulse train with sub 40-as jitter. *Opt. Express*, 14(25):12134–12144, Dec 2006.

[175] D.S. Hum and M.M. Fejer. Quasi-phasematching. *Comptes Rendus Physique*, 8(2):180–198, 2007.

[176] J.S. Pelc, L. Ma, C.R. Phillips, Q. Zhang, C. Langrock, O. Slattery, X. Tang, and M.M. Fejer. Long-wavelength-pumped upconversion single-photon detector at 1550 nm: performance and noise analysis. *Opt. Express*, 19(22):21445–21456, Oct 2011.

[177] C. Langrock, E. Diamanti, R.V. Roussev, Y. Yamamoto, M.M. Fejer, and H. Takesue. Highly efficient single-photon detection at communication wavelengths by use of upconversion in reverse-proton-exchanged periodically poled LiNbO3 waveguides. *Opt. Lett.*, 30(13):1725–1727, Jul 2005.

[178] A. Beveratos, S. Kühn, R. Brouri, T. Gacoin, J.-P. Poizat, and P. Grangier. Room temperature stable single-photon source. *Eur. Phys. J. D*, 18(2):191–196, 2002.

[179] A. Allevi, M. Bondani, and A. Andreoni. Photon-number correlations by photon-number resolving detectors. *Opt. Lett.*, 35(10):1707–1709, May 2010.

[180] N. Sangouard, C. Simon, H. De Riedmatten, and N. Gisin. Quantum repeaters based on atomic ensembles and linear optics. *Rev. Mod. Phys.*, 83(1):33, 2011.

[181] I. Afek, A. Natan, O. Ambar, and Y. Silberberg. Quantum state measurements using multipixel photon detectors. *Phys. Rev. A*, 79:043830, Apr 2009.

[182] E. Pomarico, B. Sanguinetti, R. Thew, and H. Zbinden. Room temperature photon number resolving detector for infared wavelengths. *Opt. Express*, 18:10750–10759, May 2010.

[183] A. Chong, W.H. Renninger, and F.W. Wise. All-normal-dispersion femtosecond fiber laser with pulse energy above 20nJ. *Opt. Lett.*, 32(16):2408–2410, Aug 2007.

[184] M.J. Nee, R. McCanne, K.J. Kubarych, and M. Joffre. Two-dimensional infrared spectroscopy detected by chirped pulse upconversion. *Opt. Lett.*, 32(6):713–715, Mar 2007.

[185] J. Mata Pavia, M. Wolf, and E. Charbon. Single-photon avalanche diode imagers applied to near-infrared imaging. *IEEE J. Sel. Top. Quant. Electron.*, 20(6):291–298, Nov 2014.

[186] X. Chen, E Wu, G. Wu, and H. Zeng. Low-noise high-speed InGaAs/InP-based single-photon detector. *Opt. Express*, 18(7):7010–7018, Mar 2010.

[187] Q. Zhou, K. Huang, H. Pan, E Wu, and H. Zeng. Ultrasensitive mid-infrared up-conversion imaging at few-photon level. *Appl. Phys. Lett.*, 102(24):241110, 2013.

[188] J. Faist, F. Capasso, D.L. Sivco, C. Sirtori, A.L. Hutchinson, and A.Y. Cho. Quantum cascade laser. *Science*, 264(5158):553–556, 1994.

[189] J. Liu, Q. Liu, X. Yan, H. Chen, and M. Gong. High repetition frequency PPMgOLN mid-infrared optical parametric oscillator. *Laser Phys. Lett.*, 7(9):630, 2010.

[190] H. Vahlbruch, M. Mehmet, S. Chelkowski, B. Hage, A. Franzen, N. Lastzka, S. Goßler, K. Danzmann, and R. Schnabel. Observation of squeezed light with 10-dB quantum-noise reduction. *Phys. Rev. Lett.*, 100:033602, Jan 2008.

[191] M. Mehmet, S. Ast, T. Eberle, S. Steinlechner, H. Vahlbruch, and R. Schnabel. Squeezed light at 1550 nm with a quantum noise reduction of 12.3 dB. *Opt. Express*, 19(25):25763–25772, Dec 2011.

[192] C.E. Vollmer, C. Baune, A. Samblowski, T. Eberle, V. Händchen, J. Fiurášek, and R. Schnabel. Quantum up-conversion of squeezed vacuum states from 1550 to 532 nm. *Phys. Rev. Lett.*, 112:073602, Feb 2014.

[193] S. Zaske, A. Lenhard, and C. Becher. Efficient frequency downconversion at the single photon level from the red spectral range to the telecommunications C-band. *Opt. Express*, 19(13):12825–12836, Jun 2011.

[194] E. Waks, E. Diamanti, B.C. Sanders, S.D. Bartlett, and Y. Yamamoto. Direct observation of nonclassical photon statistics in parametric down-conversion. *Phys. Rev. Lett.*, 92:113602, Mar 2004.

[195] L. Ma, M.T. Rakher, M.J. Stevens, O. Slattery, K. Srinivasan, and X. Tang. Temporal correlation of photons following frequency up-conversion. *Opt. Express*, 19(11):10501–10510, May 2011.

[196] C. Baune, A. Schönbeck, A. Samblowski, J. Fiurášek, and R. Schnabel. Quantum non-Gaussianity of frequency up-converted single photons. *Opt. Express*, 22(19):22808–22816, Sep 2014.

[197] A. Lvovsky and J. Mlynek. Quantum-optical catalysis: generating nonclassical states of light by means of linear optics. *Phys. Rev. Lett.*, 88(25):250401, 2002.

[198] F. Marsili *et al.* Detecting single infrared photons with 93% system efficiency. *Nat. Photon.*, 7(3):210–214, 2013.

[199] F. Marsili, F. Bellei, F. Najafi, A.E. Dane, E.A. Dauler, R.J. Molnar, and K.K. Berggren. Efficient single photon detection from 500 nm to 5 μm wavelength. *Nano Lett.*, 12(9):4799–4804, 2012.